
Artificial Microswimmers in Spatio-Temporally Modulated Activating Media

by

ALEXANDER GEISELER



Institute of Physics
UNIVERSITY OF AUGSBURG

A dissertation submitted to the University of Augsburg in
accordance with the requirements of the degree of DOCTOR
RERUM NATURALIUM in the Faculty of Mathematics, Natural
Sciences, and Materials Engineering.

OCTOBER 2017

First referee: Prof. Dr. Peter Hänggi
Second referee: Prof. Dr. Thilo Kopp
Third referee: Prof. Dr. Jerzy Łuczka

Date of oral examination: December 14, 2017

ABSTRACT

Living microorganisms are capable of a directed response to external stimuli, such as light or certain chemicals, by swimming toward or away from the stimulus source. They do so by means of complex signal transduction pathways, which allow them to elaborate a physiological response to the stimulating environment. Usually, tactic stimuli are not static, but rather modulated in the form of spatio-temporal signals, like traveling wave pulses. Interestingly, many microorganisms are capable of locating the pulse source and heading toward it, irrespective of their response to a static gradient of the respective stimulus. Their biomimetic counterpart, artificial microswimmers, also propel themselves by harvesting kinetic energy from an activating medium, but in contrast lack any adaptive capacity. In the present work, we investigate the transport of such swimmers subject to traveling activation pulses and show, by means of analytical and numerical methods, that they can actually drift in either direction with respect to the propagation of the pulses, depending on the pulse speed and waveform. Moreover, chiral swimmers, which move along spiraling trajectories, may drift preferably in a direction perpendicular to the pulse propagation. Such a variety of tactic responses is explained with a combination of two mechanisms: angular fluctuations, which help the swimmer explore its surroundings and thus diffuse faster toward more active regions, and self-polarization, a mechanism inherent to (phoretic) self-propulsion, which tends to orient the swimmer's velocity parallel or anti-parallel to the local activation gradients. By determining the relative magnitude of both effects, we characterize the selective transport of artificial microswimmers in inhomogeneous activating media.

ACKNOWLEDGMENTS

The three and a half years I spent on the completion of the present thesis were, how could it be any different, a steady up and down between “great, it all makes sense” and “damned, cheered too soon”. Nevertheless, I very much enjoyed my time at the group of Theoretical Physics I (except maybe for the last few weeks of the actual writing process), due to the very pleasant and harmonious atmosphere, both on the professional and the human level. I sincerely thank the former and current group members Xue Ao, Marcelo Tozo de Araujo, Ralf Blattmann, Sergey Denisov, Michael Hartmann, Wolfgang Häusler, Gert-Ludwig Ingold, Katharina Kopper, Luca Magazzù, Colm Mulhern, Benjamin Spreng, Peter Talkner, Juzar Thingna, and Stefan Umrath for providing such an atmosphere and always being helpful at the sometimes smaller, sometimes bigger problems of academic life. My thanks go also to Ralf Utermann, who tirelessly kept our computing infrastructure alive and running.

In particular, I thank Gerhard Schmid for introducing me to the very interesting field of artificial microswimmers and always having a friendly ear. I am furthermore thankful to Thilo Kopp and Jerzy Łuczka for their time and patience to act as the second and third referee of this thesis, and to Hubert Krenner and Wolfgang Brütting for being part of the examination board.

I also gratefully acknowledge financial support from the Nanosystems Initiative Munich (NIM) and am very indebted to my supervisor Peter Hänggi for offering me the chance to work in his group, his constant support, and sharing his great expertise with me. Moreover, I owe the deepest gratitude to Fabio Marchesoni for guiding me through the process of completing this thesis, the many fruitful discussions, and the careful proofreading.

Last but not least, I thank my family and my friends for always being there for me.

Parts of this thesis have been previously published in:

- A. GEISELER, P. HÄNGGI AND G. SCHMID, *Kramers escape of a self-propelled particle*, Eur. Phys. J. B **89**, 175 (2016).
- A. GEISELER, P. HÄNGGI, F. MARCHESONI, C. MULHERN AND S. SAVEL'EV, *Chemotaxis of artificial microswimmers in active density waves*, Phys. Rev. E **94**, 012613 (2016).
- A. GEISELER, P. HÄNGGI AND F. MARCHESONI, *Self-polarizing microswimmers in active density waves*, Sci. Rep. **7**, 41884 (2017).
- A. GEISELER, P. HÄNGGI AND F. MARCHESONI, *Taxis of artificial swimmers in a spatio-temporally modulated activation medium*, Entropy **19**, 97 (2017).

TABLE OF CONTENTS

	Page
List of Figures	VII
List of Abbreviations	IX
List of Symbols	XI
1 Introduction	1
2 Artificial Microswimmers: How Dwarfs Swim	7
2.1 Swimming at Low Reynolds Number	9
2.2 Self-Phoresis of Artificial Microswimmers	11
2.2.1 Self-Diffusiophoresis	12
2.2.2 Self-Thermophoresis	21
2.2.3 Self-Electrophoresis	25
2.3 Stochastic Modeling	31
3 Artificial Microswimmers Activated by Single Pulses	39
3.1 Static Activation Gradient	39
3.2 Gaussian Activation Pulse	41
3.3 Variable Pulse Shape	46
3.4 Analytical Approach	47
3.4.1 Diffusive Regime	49
3.4.2 Ballistic Regime	54
4 Artificial Microswimmers Activated by a Periodic Pulse Sequence	59
4.1 Sinusoidal Activation Profile	59
4.1.1 Ballistic Regime	61
4.1.2 Diffusive Regime	65

TABLE OF CONTENTS

4.1.3	Influence of Translational Noise	68
4.2	Pulse Offset	70
4.3	Activation-Dependent Rotational Diffusivity	75
4.4	Chiral Swimmer Dynamics: $\Omega \neq 0$	77
4.4.1	Noiseless Regime	78
4.4.2	Diffusive Regime	82
5	Taxis of Self-Polarizing Microswimmers	89
5.1	Self-Polarization in Activation Gradients	89
5.2	Taxis of Self-Polarizing Swimmers	92
5.3	Noiseless Swimmer Dynamics	95
5.4	Influence of Noise	98
6	Conclusions and Outlook	103
A	Taxis of Artificial Microswimmers Induced by Static Stimuli	107
A.1	Artificial Chemotaxis	107
A.2	Artificial Phototaxis	109
A.3	Artificial Gravitaxis	111
A.4	Artificial Rheotaxis	113
B	Tactic Response to a Constant Activation Gradient	115
C	Tactic Shift Induced by a Soliton-Like Pulse	117
D	Numerical Methods	121
D.1	Langevin Formalism	121
D.2	Fokker-Planck Formalism	122
	Bibliography	125

LIST OF FIGURES

FIGURE	Page
2.1 Scallop Locomotion	8
2.2 Principles of Microbial Swimming	10
2.3 Self-Diffusiophoretic Propulsion Mechanism	16
2.4 Experimental Realizations of Self-Diffusiophoretic Swimmers	20
2.5 Thermophoretic Microswimmers	22
2.6 Electrophoresis of Colloidal Particles	27
2.7 Self-Electrophoretic Pt-Au Swimmer	30
2.8 Micrographs of Self-Electrophoretic Swimmers	31
2.9 Janus Microswimmer on a Substrate	33
2.10 Realization of Traveling Activation Pulses	36
3.1 Artificial Taxis in a Constant Activation Gradient	40
3.2 Tactic Shift Induced by a Gaussian Activation Pulse	41
3.3 Probability Distribution of a Swimmer's Position	42
3.4 Influence of the Pulse Width	44
3.5 Pulse Trapping	45
3.6 Variable Pulse Shape	47
3.7 Influence of the Pulse Edge Steepness	48
3.8 Tactic Shift in the Diffusive Regime: Analytics vs. Numerics	52
3.9 Influence of Translational Noise on $\Delta(\infty)$	55
3.10 Tactic Shift in the Ballistic Regime: Analytics vs. Numerics	56
4.1 Tactic Drift Induced by a Sinusoidal Swimmer Activation	60
4.2 Tactic Drift in the Ballistic Approximation	63
4.3 Tactic Drift in the Ballistic Approximation: Influence of D_0	65
4.4 Tactic Drift in the Diffusive Approximation	68
4.5 Influence of Translational Noise on v_x	69

4.6	Effect of a Pulse Offset on the Swimmer's Tactic Drift	71
4.7	Tactic Separatrix	72
4.8	Functional Dependence of v_x on the Pulse Speed and Offset	74
4.9	Activation-Dependent Rotational Diffusivity	76
4.10	Taxis of Chiral Microswimmers	77
4.11	Tactic Drift of a Chiral Swimmer in the Deterministic Limit, Pt. I	79
4.12	Tactic Drift of a Chiral Swimmer in the Deterministic Limit, Pt. II	81
4.13	Chiral Swimmer Trajectories in the Noiseless Regime	83
4.14	Drift of a Chiral Swimmer in the Diffusive Approximation	85
5.1	Self-Polarization Mechanism	90
5.2	Self-Polarization in Activating Pulses	92
5.3	Tactic Drift of Weakly Self-Polarizing Swimmers	93
5.4	Tactic Drift of Strongly Self-Polarizing Swimmers	94
5.5	Taxis of a Positively Self-Polarizing Swimmer in the Noiseless Regime	96
5.6	Taxis of a Negatively Self-Polarizing Swimmer in the Noiseless Regime	98
5.7	Role of the Rotational Noise, Pt. I	99
5.8	Role of the Rotational Noise, Pt. II	100
5.9	Role of the Translational Noise, Pt. I	101
5.10	Role of the Translational Noise, Pt. II	102
A.1	Artificial Chemotaxis: Experiment	108
A.2	Artificial Chemotaxis: Influence of Confining Walls	108
A.3	Phototaxis of Artificial Microswimmers in Optical Landscapes	110
A.4	Phototactic Artificial Nanotree	111
A.5	Artificial Gravitaxis	112
A.6	Artificial Rheotaxis	113

LIST OF ABBREVIATIONS

FPE	Fokker-Planck equation
l.h.s.	left-hand side
LE	Langevin equations
MFPT	mean first-passage time
NSE	Navier-Stokes equations
SE	Stokes equations
VdW	Van der Waals

LIST OF SYMBOLS

A, B	Chemical species
$\langle \dots \rangle$	Ensemble average
$\langle \dots \rangle_s$	Surface average
$\langle \dots \rangle_x$	Spatial average
$c_A, c_B, c_B^{(0)}, c, c_i, c_i^{(0)}$	Number density
$[\dots, \dots]$	Commutator
$D_B, D_0, D_\phi, D_s, D_x$	Diffusion constant
Δ	Laplace operator
δH	Excess or defect of a fluid's specific enthalpy near a surface
$\Delta(t), \Delta(\infty), \Delta^\phi(\infty)$	Tactic shift
D_T	Thermodiffusion coefficient
$\mathbf{E}_{\text{ex}}, \mathbf{E}_s$	Electric field
e	Elementary charge
$E_1(x)$	Exponential integral
ε	Permittivity of a dielectric medium
$\text{erfi}(x)$	Imaginary error function, $\text{erfi}(x) := (2/\sqrt{\pi}) \int_0^x \exp(y^2) dy$
η_0	Dynamic viscosity of a fluid
${}_2F_2(a_1, a_2; b_1, b_2; x)$	Generalized hypergeometric function
$\hat{\mathbb{F}}, \hat{\mathbb{F}}^\dagger$	Fokker-Planck operator
γ	Euler-Mascheroni constant
h, h_t	Thickness of a colloidal particle's interfacial layer
I	Laser intensity
$I_1(x)$	Modified Bessel function of the first kind
$\mathbb{1}$	Identity tensor
$\tilde{J}^\phi, \tilde{J}_{\text{st}}^\phi, \tilde{J}_{\text{st},y}, J_x, J_y, J_\phi$	Probability current

LIST OF SYMBOLS

j	Heat flux
K	Edge Steepness of a soliton-like activation pulse
k	Chemical reaction rate
κ	Self-diffusiophoretic source term
k_B	Boltzmann constant
L, d	Pulse width
λ_f, λ_p	Thermal conductivity
L_n	Legendre polynomial of order n
l_ϕ	Persistence length
m	Momentum flux
$\mu_d, \mu_t, \mu_e, \mu, \mu'$	Phoretic mobility
$\mathbf{n}_s, \mathbf{n}_0$	Normal vector
N_A	Avogadro constant
∇	Nabla operator
n_p	Periodicity number
\mathbf{n}	Propulsion axis
ν	Strength of a linear activation gradient
$\Omega, \Omega, \Omega_p, \Omega_p$	Rotational velocity of a self-propelled particle
$P, P^\phi, \mathcal{P}, \tilde{P}^\phi, \tilde{\mathcal{P}}, \tilde{\mathcal{P}}_{st}$	Probability density
p	Fluid pressure
Φ	Potential of mean force
Φ_e, Φ_s	Electric potential
θ, ϕ	Polar angle
$\hat{\psi}$	Backward mapping operator
$\Psi(x)$	Digamma function
Q	Electric charge
R	Particle radius
\mathcal{R}_a	Light-absorbing region on the surface of a thermophoretic swimmer
\mathcal{R}_c	Catalytic region on the surface of a diffusiophoretic swimmer
\mathbf{r}_{CM}	Center of mass
r_D	Debye length
Re	Reynolds number

ρ	Charge density
ρ_0	Fluid density
\mathcal{R}_s	Particle surface
r_{sp}	Radius of the slipping plane
$\tilde{\mathbf{r}}$	Local Cartesian coordinates on a swimmer's surface
s	Self-polarization strength
$\text{sgn}(x)$	Signum function
Σ, Σ'	Hydrodynamic stress tensor
S_T	Soret coefficient
T, T_f, T_p, T_0	Temperature
τ_ϕ	Persistence time (rotational diffusion time)
$t_c^\phi, t_c^{(n_p)}$	Ballistic pulse-crossing time
$\langle t(x_1 x_0) \rangle$	Mean first-passage time
u	Propagation speed of an activating pulse
\mathbf{u}, \mathbf{u}'	Fluid velocity
$u_s(L)$	Tactic separatrix
$\mathbf{v}_0, v_0, \mathbf{v}$	Self-propulsion velocity/speed
v_x, v_y, v_x^ϕ	Tactic drift velocity
\mathcal{V}_0	Fluid volume
\mathbf{v}_s, v_s	Phoretic slip velocity
W_x, W_y, W_ϕ	Wiener process
w	Swimmer activation profile
W_0	Laser power
w_0	Activation pulse offset
ξ_x, ξ_y, ξ_ϕ	Stochastic noise source
Z_i	Charge number
ζ	Zeta potential

INTRODUCTION

Somatic cells and microorganisms, like bacteria and certain fungi or algae, can perform a directed movement toward or away from the source of an external stimulus, a behavior which is referred to as *taxis* (plural *taxes*). If taxes did not exist, the present thesis also would not. Not only because then there would be nothing to write about, but also because there would be nobody to write it down. Actually, taxes are ubiquitous. They are categorized based on the nature of the stimulus and on whether the organisms head toward (positive taxis) or away from (negative taxis) its source [1]. Commonly, taxes are induced by certain chemicals (*chemotaxis*) or light (*phototaxis*), but other tactic mechanisms are also well known, such as, for instance, *rheotaxis*, a response to fluid flows, or *gravitaxis*, a response to the gravitational field [2]. Playing a major role in many biological processes, taxes are instrumental to the formation of cell layers and other more complex biological structures. Also most fertilization processes are governed by tactic sperm migration [3, 4], such as sperm chemotaxis [5, 6], rheotaxis [7], and also *thermotaxis*, a directed swimming of spermatozoa up a temperature gradient [8]. Moreover, many bacteria profit from pronounced tactic capabilities in their search for food or to avoid toxic substances [9, 10]. They do so by means of complex internal signal transduction pathways, which are capable of elaborating a physiological response to external stimulus gradients [11–13] and thus operate like some kind of sensor-actuator loop.

The earliest scientific observation of taxis is commonly credited to G. R. Treviranus [14], a physician and biologist, who in 1816 discovered that the zoospores of certain algae move to shady regions when exposed to sunlight [15], i.e., exhibit a negative phototactic behavior. Later, T. W. Engelmann, an animal physiologist and biologist, who pioneered the research on

photosynthesis and microbiology [16, 17], was the first to describe bacterial chemotaxis. In 1881 he observed that some bacteria are capable of detecting small changes in the surrounding oxygen concentration and move up the concentration gradient [18]. Taking advantage of this effect, he developed the “bacterial method”, a sophisticated and sensitive detection method for oxygen production in photosynthetic cells [19]. Some years later, in 1884 (and again in 1888), W. Pfeffer also reported on chemotaxis of bacteria [20, 21]. He coined the term chemotaxis (originally “chymitaxis”), and gave a decisive impulse to the experimental research in this field. Since these pioneering works, the observation and understanding of tactic effects have steadily evolved, especially in the 1930s, when the actual importance of taxis in a plethora of biological processes and in clinical pathology became apparent, and in the 1970s, when the advent of modern microbiology led to the discovery of the microbial tactic signal-transduction pathways and to a deeper understanding of the underlying physio-chemical processes.

A biomimetic counterpart of microbial motility is the self-propulsion of artificial microswimmers, also known as active or self-propelled particles, which are synthetically designed micro- or sometimes even nano-sized objects that propel themselves by converting the energy of an external activating “fuel” into kinetic energy [22–26]. Under certain operating conditions, such particles are able to generate local non-equilibrium conditions in their surrounding suspension fluid, which in turn exerts on them a thermo- [27–31], electro- [32–34], or diffusiophoretic [35–40] push. In most cases, such conditions are maintained by a functionally asymmetric particle surface consisting of at least two regions with different physio-chemical properties. With reference to the two-faced Latin deity Janus, this class of synthetic swimmers are also termed *Janus particles*. The term was coined by C. Casagrande and M. Veyssié in 1988 [41, 42], who used it as a catchword for spherical glass particles with a hydrophilic and a hydrophobic hemisphere¹. Eventually, the term became popular after P.-G. de Gennes used it in his 1991 Nobel lecture [44]. Although the early Janus particles were mainly designed as surfactants—i.e., to assemble at liquid-liquid interfaces—and did not possess any propulsive capabilities, about one decade after their discovery, the first self-propelling Janus particles were announced [36, 45, 46]. Since then, the field has steadily evolved and as of today, a considerable number of different artificial self-propulsion mechanisms have been investigated.

While the fabrication of asymmetrically structured microparticles with specific chemical and physical surface properties is still a challenging task, in recent years substantial advances have been made in this direction. To ensure a wide-spread application of artificial

¹Although not referred to as Janus particles back then, spheres with differently coated hemispheres were realized by I. Cho and K.-W. Lee already in 1985 [43].

microswimmers, three major production criteria have to be satisfied, namely (i) reliability of the particles, associated with high fabrication precision, (ii) scalability, such that a large number of microswimmers can be produced, and (iii) cost-effectiveness [24, 26]. The majority of the current fabrication techniques fall within three distinct categories, namely masking, phase separation, and self-assembly [47]. In the masking strategy, one side of an initially homogeneous “blank” particle is concealed before coating the other side with a functionalized material, which can be applied, for instance, by vapor deposition or sputtering techniques [48]. The second method, phase separation, is based on the blending of two immiscible liquid substances, such as polymer solutions, which forms a single but biphasic particle after hardening [49]. Finally, in the self-assembly approach, micellar block copolymers, designed to specifically cross-link, are brought into solution. Upon aggregation, they then form Janus-like colloidal structures [24, 50]. Needless to say that by means of the above fabrication techniques, only microswimmers of rather simple geometries (such as spheres and rods) can be produced, at least on an industrial scale. However, by employing more sophisticated and expensive cutting edge manufacturing procedures, nowadays the swimmers’ geometries can be tailored and functionalized almost at will [51, 52].

Depending on their activation mechanism, synthetic microswimmers exhibit a rich collective dynamics, from chaotic turbulence and microscopic clustering to collective oscillations and macroscopic phase separation [53–67]. More relevant to the present work is the question of how to control the transport of artificial microswimmers for nanorobotic applications [68], such as environmental monitoring [69], cleaning of polluted water [70], targeted drug delivery [71, 72], or even more challenging biomedical tasks [73–76]. Indeed, rectification of self-propelled particles is currently the focus of an intense cross-disciplinary research effort with regard to both the collective and the single particle dynamics. Various methods to control the a priori unbiased random movement of artificial microswimmers have already been reported in the recent literature, like adaptively switching on and off of the swimmer’s propulsion [77], magnetic steering [75, 78–80], or guiding swimmers along topological or optical structures [38, 81–86]. Most remarkable in this context is the recent experimental observation that tactic effects can occur also in the diffusion of artificial microswimmers, namely when exposing them to certain static stimuli [52, 87–93] (see Appendix A for a brief review). This is an interesting result, because unlike biological microorganisms, the almost structureless artificial microswimmers lack any signal-processing capability and thus seem unable to respond to an activation gradient.

Bearing in mind biomedical applications, it should however be noted that in biological systems, tactic stimuli are seldom static, but rather modulated in the form of spatio-temporal

signals, like traveling wave pulses. Some microorganisms are capable of locating the pulse source and heading toward it [94, 95]. This is an apparently paradoxical effect, because one expects rectification to naturally occur in the opposite direction, irrespective of the microorganisms' tactic response to a monotonic gradient. Indeed, on assuming a symmetric pulse waveform, a microorganism orients itself parallel to the direction of the pulse propagation on one pulse side, and opposite to it on the other side. As the swimmer then spends a longer time within the pulse when moving parallel to it, one would expect it to "surf" the pulse and effectively move away from the pulse's source (Stokes' drift [96, 97]). Experimental evidence to the contrary has been explained by invoking a finite adaption time of the microorganisms' response to temporally varying stimuli [98, 99].

By analogy with the taxis of "smart" biological swimmers induced by spatio-temporally varying stimuli, in this work we pursue the question whether similar effects can be observed also for "dumb" artificial swimmers, that is, we consider an active, self-propelled particle subjected to traveling activation wave pulses. To this purpose, in Ch. 2 we introduce the basic concepts of self-propelled motion at the microscale. We discuss the problem of swimming at low Reynolds number and briefly present the most common self-propulsion mechanisms. Based on these principles, we then set up a simplified stochastic model of an active Brownian particle that combines self-propulsion and noise-induced fluctuations within a Langevin dynamics framework. This model will be taken as a basis for the simulations and the analytical work presented in the subsequent chapters.

In Chs. 3 and 4, we investigate the tactic response of an artificial microswimmer to single and periodic sequences of traveling activation pulses, respectively. We do so by presenting and expanding the results we recently published in Refs. [100] and [101]. Two distinct regimes of the particle's dynamics are identified in which we are able to obtain explicit analytic results. Using both numerical and analytical approaches, we then investigate the impact of the pulse parameters and of the translational and rotational noise intensity on the swimmer's tactic response, and interpret the underlying physical effects. Furthermore, in Ch. 4.4 we add a chiral component to the particle's angular dynamics and study how it influences the tactic drift of a swimmer in a periodic activation pulse sequence.

In Ch. 5, we extend the findings of Chs. 3 and 4 by considering an additional hydrodynamic contribution to the swimmer's dynamics, namely its self-polarization in an activation gradient. We study the interplay between the latter effect and the purely stochastic effects reported in the preceding chapters, both in the noiseless and the noisy regime. Our main conclusion is that, as anticipated in our Ref. [102], the swimmer's tactic drift can be tuned, both in magnitude and direction, by varying the pulse parameters and/or the particle's surface properties.

In Ch. 6, we conclude with a summary of our results, briefly discuss possible extensions of our analytical methods, and elaborate on future applications.

ARTIFICIAL MICROSWIMMERS: HOW DWARFS SWIM

As mentioned in the Introduction, artificial microswimmers are micro- or sometimes even nano-sized synthetic particles, capable of propelling themselves through a surrounding fluid. Such an ability may be surprising at first sight, since swimming at the microscale generally faces a major problem: low Reynolds number hydrodynamics. Disregarding any thermal fluctuations, the motion of an object immersed in an incompressible fluid [$\nabla \cdot \mathbf{u}(\mathbf{r}, t) = 0$] of dynamic viscosity η_0 , free from external forces, is well described by the Navier-Stokes equations (NSE)

$$\rho_0 \frac{\partial \mathbf{u}(\mathbf{r}, t)}{\partial t} + \rho_0 [\mathbf{u}(\mathbf{r}, t) \cdot \nabla] \mathbf{u}(\mathbf{r}, t) = \eta_0 \nabla^2 \mathbf{u}(\mathbf{r}, t) - \nabla p(\mathbf{r}, t), \quad (2.1)$$

where ρ_0 and \mathbf{u} are, respectively, the density and velocity field of the fluid, and p is its pressure. Of course, the above statement only holds if the size of the object and the scale on which its motion is observed are significantly larger than the size of the fluid molecules, such that the fluid can be modeled as a continuous medium. As an everyday observation, swimming on the macroscale, e.g., the swimming of a human, is achieved by periodically deforming the swimmer's body, which (assuming the swimmer has already earned his/her swimming badge) results in a self-propelled motion: a good swimmer skillfully makes use of inertial and turbulent effects, which relate to the temporal derivative and the non-linear term on the left-hand side (l.h.s.) of Eq. (2.1). Upon introducing the Reynolds number [11, 103]

$$\text{Re} := \frac{\rho_0 v l}{\eta_0}, \quad (2.2)$$

where v is a characteristic speed of the fluid with respect to the immersed object and l a characteristic lengthscale of the latter, the dynamics of Eq. (2.1) admits of two limiting regimes. Since Re equals the ratio of inertial to viscous forces within the fluid, for high Reynolds numbers we observe the turbulent and inertia-dominated fluid dynamics mentioned above, whereas for low Reynolds numbers, flows are solely laminar. In fact, by an appropriate rescaling it can be shown that for $Re \ll 1$ the non-linear term on the l.h.s. of Eq. (2.1) becomes negligible and, moreover, the fluid relaxes almost instantaneously toward a stationary state. Accordingly, on timescales governing the swimmer’s motion, the temporal derivative in the latter equation can also be neglected. In that case, however, a *reciprocal* motion, that is, a deformation of the swimmer’s body from one state to another and a subsequent reversal of this process to return to the initial state, cannot lead to any propulsion through the fluid. As time does not matter anymore, the swimmer ends up exactly at the starting position after one full reciprocal cycle, no matter how fast (assuming still a low Reynolds number) the “swimming” strokes and how slow the “recovery” strokes are. This idea was formulated first by E. M. Purcell in the renowned *scallop theorem*. In his seminal talk “Life at low Reynolds number” [104], he drew inspiration from the motion of a scallop that propels itself by repeatedly opening and closing its valves [105], similar to a clapping motion sequence (Fig. 2.1). If that motion happened at low Reynolds number, the poor scallop would be stuck forever!

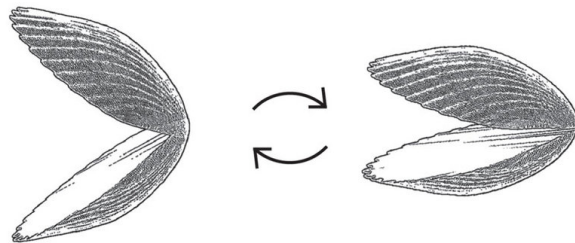


FIGURE 2.1. Schematic swimming mechanism of a scallop. By opening and quickly closing its shell, it can exhaust water jets, which propel the scallop through the fluid. Adapted from Ref. [106] under a CC BY 4.0 license.

Characteristic swimmer parameters. Looking at typical Reynolds numbers for a human swimming in water, to a rough estimate we obtain $Re \approx 10^6$ —the typical lengthscale is about 1 m, typical velocities are about 1 m/s, $\rho_0 = 10^3 \text{ kg/m}^3$, and $\eta_0 = 10^{-3} \text{ Pa s}$. For the aforementioned scallop the typical lengthscale decreases by a factor of 10, whereas the swimming speed is of the order of 0.1 m/s, leading to $Re \approx 10^4$. Therefore, swimming on macroscopic scales is clearly dominated by high Reynolds number hydrodynamics. If we however turn to microbial propulsion, the characteristic lengthscale has to be lowered to $1 \mu\text{m}$ and typical

velocities become of the order of $10\ \mu\text{m/s}$, implying that $\text{Re} \approx 10^{-5}$. With that said, life at the microscale definitely happens at low Reynolds number and thus is a hard knock one for organisms relying on autonomous motion. Luckily, Nature has contrived ways to circumvent these difficulties.

2.1 Swimming at Low Reynolds Number

Since simple reciprocal motion cycles are not an option for microorganisms to propel themselves, more sophisticated swimming techniques are required¹, most of which fall into the two broad classes of *flagellar* and *ciliary* propulsion. As a thorough in-depth review of microbial swimming—even from just a hydrodynamic point of view—would exceed the scope of the present thesis, in the following we briefly outline the underlying mechanisms and refer to the current literature for further details [25, 104, 107–121].

Flagella are thin, whip-like appendages protruding from the body of many microorganisms, see Fig. 2.2a. Whereas bacterial flagella consist of helically-shaped hollow nanotubes, formed by one single protein [125], and cannot be actively deformed, flagella of eukaryotes have a complex internal structure that allows for directed bending, thus extending the propulsion activity to the whole length of the flagellum. Bacteria swim by rotating one or more flagella that are attached to an internal motor and thus act like a propeller, performing a non-reciprocal, corkscrew-like chiral motion. In contrast, eukaryotic cells move their flagella in a whip-like beat, which produces traveling waves in the flagellum, similar to the motion of a snake [25] (see Fig. 2.2c). In either way, the problem of reciprocal motion at low Reynolds number can be bypassed, allowing for directed swimming. We note that in the case of a corkscrew-like flagellar rotation, the resulting propulsion speed is proportional to the actuation frequency, whereas for a periodic whip-like beating pattern it is proportional to the square thereof [126].

Although very similar in their structure to eukaryotic flagella, cilia implement propulsion by a different mechanism: during a swimming stroke they become rather stiff and elongated, whereas during a recovery stroke they strongly bend to minimize flow resistance [115], see Fig. 2.2d. This swimming technique slightly resembles human breaststrokes; however, microswimmers moving by ciliary propulsion usually combine an array of some ten to some hundred individual cilia to perform a coordinated beating [127] (cf. Fig. 2.2e). Such a collective behavior is mostly explained with hydrodynamic synchronization [128–131], but

¹Actually, also swimming at high Reynolds number usually takes advantage of non-reciprocal motion patterns, as these are in general more effective. For example, when rowing a boat, lifting the oar out of the water during the recovery phase certainly makes the boat faster than slowly recovering the oar through the water.

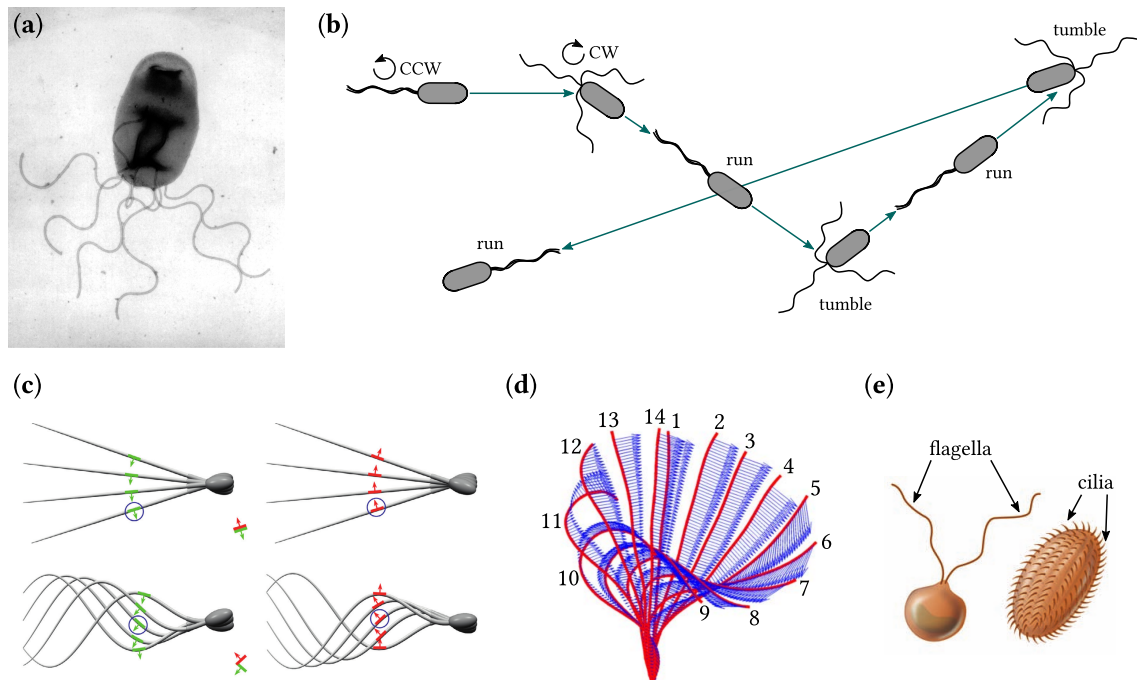


FIGURE 2.2. Principles of microbial swimming. (a) Transmission electron micrograph of the bacterium *Bartonella clarridgeiae*. Reprinted from Ref. [122] with permission. (b) Typical run-and-tumble motion of flagellated bacteria. By rotating their flagella counterclockwise (CCW), the bacteria “run” in almost straight lines, whereas by rotating the flagella clockwise (CW), they switch into a “tumbling” state. (c) Flagellar beating of eukaryotes (here sperm cells). The top line depicts a simple reciprocal beating pattern that would not allow for any self-propulsion: during the “upstroke” the flagella segments (red bars) are in exactly the same state as during the “downstroke” (green bars), solely the direction of motion is inverted. In contrast, the beating pattern depicted on the bottom line leads to self-propulsion. Due to the traveling wave generated in the flagella, the segments are in different states during the up- and downstroke, respectively. Reprinted from Ref. [123] with permission. (d) Typical ciliary beating pattern. The numbers indicate the order of the snapshots. Adapted from Ref. [121] under a CC BY 4.0 license. (e) Eukaryotic flagella versus cilia. Adapted from Ref. [124] by permission of Pearson Education, Inc., New York, New York.

other mechanisms have also been proposed, as for instance mechanical intracellular motor coupling [132–134].

While most microorganisms do not possess any direct steering mechanism to control the direction of their motion, they are nevertheless able to effectively head toward certain targets. In most cases, the ensuing tactic migration, that has already been mentioned in the Introduction, directly relates to the flagellar or ciliary propulsion mechanism. For instance, some bacteria, such as the ubiquitous *E. Coli*, can rotate their flagella clock- or counterclockwise. Due to their helicity, the flagella bundle and cause a straight propulsion when rotated counterclockwise. On the contrary, when rotated clockwise, the flagella unbundle and point in different directions, leading to a rotating, tumble-like motion [10]. By randomly switching the rotation direction of their flagella, these bacteria then perform an unbiased active diffusion via a so-called run-and-tumble mechanism [135] (Fig. 2.2b). However, in the presence of a tactic stimulus, they are able to lower (increase) the tumbling rate when moving up (down) a stimulus gradient. Such an adaptive response induces an effective, controllable drift of the bacteria toward the stimulus' source [136].

In conclusion, we see that Nature has overcome the problem of low Reynolds number hydrodynamics by designing sophisticated swimming mechanisms, allowing even rather primitive microorganisms to propel themselves through viscous media. This observation raises the question whether artificial microswimmers can be designed to swim in a similar way, as a biomimetic counterpart of biological microswimmers. Synthetically fabricated swimmers have necessarily a much simpler structure than living microorganisms and thus cannot operate by a complex propulsion mechanism. Nevertheless, over the past decade many artificial microswimmers have been reported to successfully mimic microbial swimming techniques [79, 137–150]. These are mostly based on a whip- or corkscrew-like motion of magnetic tails induced by external electromagnetic fields.

2.2 Self-Phoresis of Artificial Microswimmers

Whereas artificial microswimmers have indeed been designed to successfully mimic biological swimming techniques in recent years, their fabrication relies on a very sophisticated, cutting-edge nanotechnology, which is still far away from industrial applications. In addition, the movement of such swimmers is in general not totally autonomous, insofar as the beating or rotation of their artificial flagella is externally induced. A comparatively simpler and hence way more common method to create autonomous self-propulsion of artificial microswimmers is *self-phoresis*. As mentioned in the Introduction, swimmers of this category have much

simpler geometries and are driven by a phoretic push that originates from a local gradient they themselves create in the surrounding suspension fluid. The principle of their motion is very similar to that of classic phoresis, with the only difference that the gradients responsible for the phoretic effects are localized around each swimmer and move along with it. In the following, we explain the basic mechanisms responsible for self-phoretic swimming at the microscale and in particular focus on the three main phoretic effects presently utilized to propel synthetic microswimmers, namely self-diffusiophoresis, self-thermophoresis, and self-electrophoresis. Such phoretic effects eventually generate a directed movement of the swimmer, *as if* it were dragged by effective forces and torques [151], see Appendix A. However, we stress that these forces and torques are used there for modeling purposes only, since, as will be shown in the following section, the motion of a self-phoretic swimmer is actually force- and torque-free.

2.2.1 Self-Diffusiophoresis

The most elementary phoretic effect is diffusiophoresis. The term refers to a hydrodynamic effect caused by an external concentration gradient of a solute surrounding a colloidal particle, which leads to a slip-like motion of the fluid relative to the particle surface. By momentum conservation, this motion causes the particle to conversely move in the opposite direction, thus resulting in a particle drift without any applied external force.

For a more quantitative presentation of this mechanism, we follow the outline given by M. N. Popescu et al. [152] and consider a colloidal particle that is able to convert the solute species A to another species B at a rate k . Under most circumstances, this is accomplished by a chemical reaction, $A \xrightarrow{\text{cat}} B$, where the particle acts as a catalyst. Furthermore, for any self-diffusiophoretic motion to occur, the particle must not be catalytically active all across its surface, but break the symmetry by catalyzing the reaction only at a specific region thereof, which we denote by \mathcal{R}_c in the following. Assuming the concentration of the species A to be so high that the reaction is solely controlled by the rate k (and not by the diffusion of the A molecules toward the reaction site), we can consider the concentration of the A molecules, c_A , to be approximately constant in the vicinity of the particle. On the contrary, the concentration c_B of the B molecules, which are created at \mathcal{R}_c only, is modulated by a gradient that spans the swimmer's surface, see Fig. 2.3a. Next, we assume the species B to interact with the particle's surface by a different interaction potential than the species A and the solvent², which is the general case for different chemical species. As c_A and the fluid density are (approximately) constant across the particle's surface, we can simplify the interaction between the swimmer

²We note that also the A molecules and the solvent do not necessarily interact with the swimmer via the same potential. However, for simplicity, these two potentials are assumed to coincide in the following.

and its surrounding by introducing an effective “potential of mean force” Φ [153, 154] (see Fig. 2.3b) that describes the interaction of the B molecules with the swimmer’s surface relative to that of the solvent and the A molecules. The interactions of the latter two species with the swimmer are encoded in the fluid pressure p [152, 155] and all other interactions between the solutes and the solvent only contribute to the fluid viscosity η_0 . A more general approach that explicitly considers also the interaction of the A species with the colloidal particle is feasible along similar lines as in the present chapter; however, the relevant mathematical formulation would become considerably more complicated [156, 157], without adding much to our understanding of the basic phoretic mechanism.

Furthermore, the colloidal particle is supposed to be much larger than the solvent and the solute molecules, so that the timescale on which the diffusion of the B molecules reaches a stationary state is much smaller than the timescales governing the swimmer’s dynamics. In fact, even for a rather small spherical microparticle of radius $R = 0.1 \mu\text{m}$ immersed in water at room temperature, the diffusion constant is $D_0 = k_B T / (6\pi\eta_0 R) \approx 2.2 \mu\text{m}^2/\text{s}$, where k_B is the Boltzmann constant and T the temperature of the fluid. In contrast, the diffusion constant of a small molecular solute, such as oxygen (O_2), in water at the same temperature is about three orders of magnitude larger [158]. The timescale on which O_2 molecules diffuse across a length R is thus given by $t_{\text{diff}} = R^2 / (10^3 D_0) \approx 4.5 \mu\text{s}$. Considering a swimmer with a characteristic self-propulsion speed of the order of $10 \mu\text{m}/\text{s}$, the time it takes to travel a length R is typically $10^4 \mu\text{s}$, which is about $10^3 t_{\text{diff}}$. As the same argument applies to the ratio between the timescale of the particle’s rotational dynamics and t_{diff} , the assumption of a fast relaxation of c_B is thus validated.

Under these conditions, c_B adapts almost instantaneously to every state of the swimmer, which reduces the coupling between the diffusive dynamics of the B molecules and the swimmer’s dynamics. The solute concentration c_B can then be calculated from the stationary diffusion equation

$$\nabla \cdot \left(\nabla c_B(\mathbf{r}) + c_B(\mathbf{r}) \nabla \frac{\Phi(\mathbf{r})}{k_B T} \right) = 0, \quad (2.3)$$

with a natural boundary condition far away from the swimmer’s surface,

$$\lim_{|\mathbf{r}| \rightarrow \infty} c_B(\mathbf{r}) = 0, \quad (2.4)$$

and an influx boundary condition,

$$-D_B \mathbf{n}_s \cdot \left(\nabla c_B(\mathbf{r}) + c_B(\mathbf{r}) \nabla \frac{\Phi(\mathbf{r})}{k_B T} \right) \Big|_{\mathbf{r} \rightarrow \mathbf{r}_s} = \kappa(\mathbf{r}_s), \quad (2.5)$$

on the swimmer’s surface \mathcal{R}_s [152]. Here, $\mathbf{r}_s \in \mathcal{R}_s$ defines the particle surface, \mathbf{n}_s is the normal vector to \mathcal{R}_s , D_B denotes the diffusion constant of the species B , and κ is a source term

accounting for the catalytic creation of B molecules at \mathcal{R}_c :

$$\kappa(\mathbf{r}_s) = \begin{cases} k \left(\int_{\mathcal{R}_c} d^2r \right)^{-1} & : \mathbf{r}_s \in \mathcal{R}_c \\ 0 & : \mathbf{r}_s \notin \mathcal{R}_c. \end{cases} \quad (2.6)$$

We note that in principle also a convection term $\nabla \cdot c_B(\mathbf{r})\mathbf{u}(\mathbf{r})$ should enter Eq. (2.3), to account for the transport of the B molecules by the moving fluid—remind that \mathbf{u} denotes the velocity field of the latter. However, as discussed above, the dynamics of the colloidal particle and thus also the relevant fluid dynamics take place at a much larger timescale than the diffusive dynamics of the solute, so that the fluid’s convective contribution to Eq. (2.3) can be safely neglected.

Having dealt with the diffusion of the solvent, the next step is to consider the resulting motion of the fluid. On that account, we assume that due to the solute-solvent interactions, the force acting upon the B molecules is transferred to the solvent, which corresponds to a body force density $-c_B(\mathbf{r})\nabla\Phi(\mathbf{r})$ in the fluid [159]. Being of comparable size and propelling themselves at similar velocities as microbial swimmers, artificial microswimmers typically move at low Reynolds numbers of about 10^{-5} . Thus, the motion of the fluid is determined by the Stokes equations (SE)

$$\eta_0 \nabla^2 \mathbf{u}(\mathbf{r}) - \nabla p(\mathbf{r}) - c_B(\mathbf{r})\nabla\Phi(\mathbf{r}) = \nabla \cdot \Sigma(\mathbf{r}) - c_B(\mathbf{r})\nabla\Phi(\mathbf{r}) = 0, \quad (2.7)$$

which follow from the NSE (2.1) upon neglecting the two inertial terms on the l.h.s. and incorporating the above body force. In the latter equation, Σ is the hydrodynamic stress tensor [155],

$$\Sigma(\mathbf{r}) := \eta_0 (\nabla \mathbf{u}(\mathbf{r}) + [\nabla \mathbf{u}(\mathbf{r})]^\top) - p(\mathbf{r})\mathbb{1}, \quad (2.8)$$

with $\mathbb{1}$ denoting the identity tensor. We next impose the usual no-slip boundary condition at the particle-fluid interface [152],

$$\mathbf{u}(\mathbf{r}_s) = \mathbf{v}_0 + \boldsymbol{\Omega} \times (\mathbf{r}_s - \mathbf{r}_{\text{CM}}), \quad (2.9)$$

and assume the fluid to be at rest far away from the particle,

$$\lim_{|\mathbf{r}| \rightarrow \infty} \mathbf{u}(\mathbf{r}) = 0. \quad (2.10)$$

In Eq. (2.9), \mathbf{r}_{CM} denotes the particle’s center of mass and \mathbf{v}_0 and $\boldsymbol{\Omega}$ are, respectively, the translational and rotational angular velocity of the particle. In order to solve the coupled equations (2.3) and (2.7)—together with the respective boundary conditions (2.4), (2.5), (2.9), and (2.10)—these particle velocities have to be specified. However, \mathbf{v}_0 and $\boldsymbol{\Omega}$ are a priori not

known; in fact, they are the key result we want to obtain from the above equations. We thus have to introduce additional constraints on the swimmer's motion. To this purpose, we assume the system particle-fluid to be in a stationary state, governed by a force- and torque-free dynamics. The force and torque exerted by the fluid on the particle due to the particle-solute interaction must therefore be compensated by the force and torque originating from the viscous damping of the fluid, which leads to the auxiliary equations [83, 152]

$$\int_{\mathcal{R}_s} \boldsymbol{\Sigma}(\mathbf{r}) \cdot \mathbf{n}_s \, d^2r + \int_{\mathcal{V}_o} c_B(\mathbf{r}) \boldsymbol{\nabla} \Phi(\mathbf{r}) \, d^3r = 0, \quad (2.11)$$

$$\int_{\mathcal{R}_s} (\mathbf{r}_s - \mathbf{r}_{\text{CM}}) \times \boldsymbol{\Sigma}(\mathbf{r}) \cdot \mathbf{n}_s \, d^2r + \int_{\mathcal{V}_o} (\mathbf{r}_s - \mathbf{r}_{\text{CM}}) \times c_B(\mathbf{r}) \boldsymbol{\nabla} \Phi(\mathbf{r}) \, d^3r = 0. \quad (2.12)$$

Here, \mathcal{V}_o is the volume filled by the fluid, i.e., the complement of the particle's volume. However, computing \mathbf{v}_o and $\boldsymbol{\Omega}$ still remains a very cumbersome task, even from a numerically point of view: the particle's translational and rotational angular velocity have to be gradually adjusted, until the associated flow profile \mathbf{u} and pressure field p fulfill the conditions (2.11) and (2.12).

Phoretic slip. Fortunately, the above system of equations can be considerably simplified by taking into account that the particle-solute interactions have a very short range, which is typically of the order of 1 nm [155, 157, 160]. As discussed by J. L. Anderson in his classic review [154], the full diffusiophoretic problem, Eqs. (2.3)–(2.12), can then be divided into the particle-solute interaction problem within a thin interfacial layer of thickness h (where the influence of the potential Φ is relevant) and a force-free fluid motion and B molecule diffusion in the “outer” domain. As the swimmer is assumed to be micron-sized, $R \gg h$, the particle surface can be considered as locally flat on lengthscales of the order of h . Furthermore, the concentration c_B relaxes almost instantaneous to the particle-solute interaction potential Φ (compared to all other timescales governing the swimmer's dynamics), so that, upon introducing a local Cartesian coordinate system $\tilde{\mathbf{r}}$, within the interfacial layer it obeys the Boltzmann distribution

$$c_B(\mathbf{r}) = c_B(\mathbf{r}_s + \tilde{\mathbf{r}}) = c_B^{(0)}(\mathbf{r}_s + \tilde{x}\mathbf{e}_{\tilde{x}}) \exp\left(\frac{-\Phi(\mathbf{r}_s + \tilde{y}\mathbf{e}_{\tilde{y}})}{k_B T}\right). \quad (2.13)$$

Here, $c_B^{(0)}$ is the concentration at $\tilde{y} = h$, i.e., at the outer boundary of the interfacial layer, which is given by the free diffusion of the B molecules in the outer domain [Eqs. (2.3)–(2.6) for $\Phi(\mathbf{r}) = 0$] and $\mathbf{e}_{\tilde{x}}$ and $\mathbf{e}_{\tilde{y}}$ denote, respectively, the unit vectors in the \tilde{x} and \tilde{y} direction. Note that the local coordinate system was chosen in such a way that $\mathbf{e}_{\tilde{y}}$ is normal to the particle surface and $\mathbf{e}_{\tilde{x}}$ parallel to the projection of $\boldsymbol{\nabla} c_B^{(0)}(\mathbf{r})$ onto a plane locally tangent to the surface

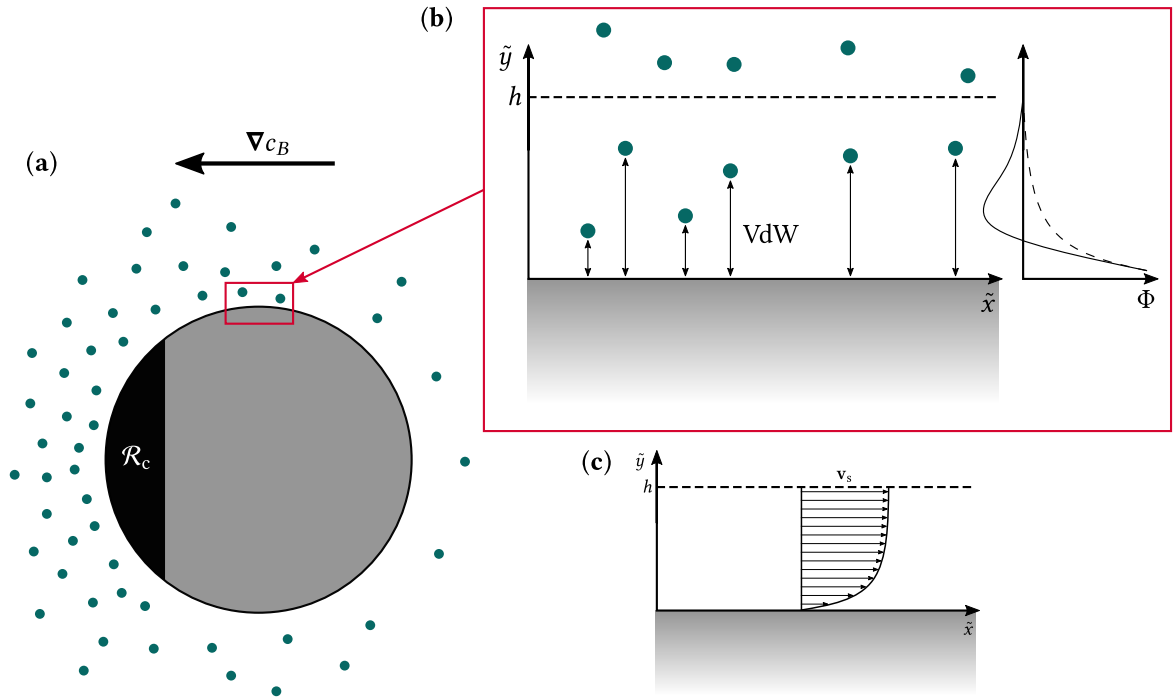


FIGURE 2.3. Self-diffusiophoretic propulsion mechanism. **(a)** Sketch of a self-diffusiophoretic swimmer. The particle is able to “release” solute molecules of the species B (green dots) at a specific region \mathcal{R}_c , which leads to a concentration gradient ∇c_B in its vicinity. **(b)** Local particle-solute interaction. The solute molecules B interact with the particle within a thin interaction layer of width h , mainly via van der Waals (VdW) forces. To the right, two examples of the resulting effective potential Φ are sketched (dashed and solid curve); the dashed potential profile implies that the solvent and the solute molecules A are always preferred over the molecules B , whereas the solid one implies that, within a certain distance from the surface, an accumulation of B molecules is favored. Note that in both examples the solvent is strongly preferred over the B molecules at very small distances. **(c)** Fluid velocity profile along the swimmer’s surface. At $\tilde{y} = h$, the potential Φ has practically vanished and the fluid velocity approaches a locally constant value v_s [see Eqs. (2.16) and (2.17)], whereas on the particle surface, $\tilde{y} = 0$, the usual no-slip boundary condition is maintained.

(cf. Fig. 2.3b). Furthermore, the variation of Φ along the latter can usually be neglected on the lengthscales considered here, which allows us to carry out the ensuing calculations in two dimensions.

Regarding the fluid motion induced by the particle-solute interaction, we revert again to the SE (2.7). However, a priori, the validity of these equations cannot be taken for granted in the interfacial region, as its thickness is so small that only a couple of solvent molecules can be layered therein and a continuum description of the solvent becomes questionable. We assume, nevertheless, the SE to be still valid; a comparison of the results thus obtained with experimental findings justifies this conjecture a posteriori [36]. Since $c_B^{(0)}$ varies on lengthscales of the order of R , the fluid velocity \mathbf{u} should also vary only on these scales in the \tilde{x} direction. On scales of the order of h we thus have $\partial_{\tilde{x}}u_{\tilde{x}} \approx 0$ and $\partial_{\tilde{x}}u_{\tilde{y}} \approx 0$, with the former relation also implying that $\partial_{\tilde{y}}u_{\tilde{y}} \approx 0$, due to the incompressibility of the fluid. The resulting SE read [154]

$$\eta_0 \frac{\partial^2 u_{\tilde{x}}}{\partial \tilde{y}^2} - \frac{\partial p}{\partial \tilde{x}} = 0, \quad \frac{\partial p}{\partial \tilde{y}} + c_B \frac{\partial \Phi}{\partial \tilde{y}} = 0, \quad (2.14)$$

which, together with the boundary conditions

$$p(\tilde{y} = h) = \text{const}, \quad u_{\tilde{x}}(\tilde{y} = 0) = 0, \quad \left. \frac{\partial u_{\tilde{x}}}{\partial \tilde{y}} \right|_{\tilde{y}=h} = 0,$$

can be solved to yield the solution

$$v_s := u_{\tilde{x}}(\tilde{y} = h) = -\frac{k_B T}{\eta_0} \int_0^h \tilde{y} \left[\exp\left(-\frac{\Phi}{k_B T}\right) - 1 \right] d\tilde{y} \frac{\partial c_B^{(0)}}{\partial \tilde{x}} \quad (2.15)$$

for the fluid velocity at $\tilde{y} = h$. The latter is also called *phoretic slip velocity*. As the potential Φ is assumed to vanish outside the interfacial layer, the upper bound of integration in the above expression can also be extended to infinity. The above result was first derived by B. V. Derjaguin et al. [161]. In a more convenient notation, Eq. (2.15) can be written as

$$\mathbf{v}_s(\mathbf{r}_s) = -\mu_d(\mathbf{r}_s) \nabla_{\parallel} c_B^{(0)}(\mathbf{r}_s), \quad (2.16)$$

where $\nabla_{\parallel} := (\mathbb{1} - \mathbf{n}_s \mathbf{n}_s) \cdot \nabla$ is the projection of the gradient operator onto a plane locally tangent to the particle surface and

$$\mu_d(\mathbf{r}_s) := \frac{k_B T}{\eta_0} \int_0^{\infty} y \left[\exp\left(-\frac{\Phi(\mathbf{r}_s + y \mathbf{n}_s)}{k_B T}\right) - 1 \right] dy \quad (2.17)$$

is called local *diffusiophoretic mobility* [162]. Note that strictly speaking, \mathbf{v}_s is not defined at \mathbf{r}_s , i.e., on the particle surface, but rather on an outer “shell” encompassing the swimmer

at a distance h from its surface. On the surface itself, the fluid is still assumed to obey the no-slip boundary condition, see Fig. 2.3c. However, as $h \ll R$, on the particle lengthscale the thickness of the interfacial layer can be neglected [163].

Looking at Eq. (2.17), we see that the phoretic mobility is proportional to the distance from the particle surface, weighted by the “excess concentration” $c_B^{(0)}(\mathbf{r}_s) \exp[-\Phi(\mathbf{r}_s + y\mathbf{n}_s)/(k_B T)] - c_B^{(0)}(\mathbf{r}_s)$ in the interfacial layer. If the attractive character of the particle-solute interaction prevails, $\mu_d(\mathbf{r}_s)$ is positive and the phoretic slip points opposite to the solute gradient $\nabla_{\parallel} c_B^{(0)}(\mathbf{r}_s)$. Vice versa, if the repulsive character prevails, \mathbf{v}_s is parallel to $\nabla_{\parallel} c_B^{(0)}(\mathbf{r}_s)$.

Having found the phoretic slip induced in the fluid by the interaction potential Φ , the total self-diffusiophoretic problem can be approached like in Eqs. (2.3)–(2.12), with the difference that now only the outer domain (where Φ has vanished) has to be considered—all dynamics in the interfacial layer are encoded in \mathbf{v}_s . We thus have to solve the system of equations [152]

$$\Delta c_B^{(0)}(\mathbf{r}) = 0, \quad \lim_{|\mathbf{r}| \rightarrow \infty} c_B^{(0)}(\mathbf{r}) = 0, \quad -D_B \mathbf{n}_s \cdot \nabla c_B^{(0)}(\mathbf{r}) \Big|_{\mathbf{r} \rightarrow \mathbf{r}_s} = \kappa(\mathbf{r}_s), \quad (2.18)$$

$$\nabla \cdot \Sigma(\mathbf{r}) = 0, \quad \lim_{|\mathbf{r}| \rightarrow \infty} \mathbf{u}(\mathbf{r}) = 0, \quad \mathbf{u}(\mathbf{r}_s) = \mathbf{v}_s(\mathbf{r}_s) + \mathbf{v}_0 + \Omega \times (\mathbf{r}_s - \mathbf{r}_{CM}), \quad (2.19)$$

where Δ is the Laplace operator. The auxiliary condition of a force-free particle motion is maintained; in the phoretic slip approximation it reads

$$\int_{\mathcal{R}_s} \Sigma(\mathbf{r}) \cdot \mathbf{n}_s \, d^2r = 0, \quad \int_{\mathcal{R}_s} (\mathbf{r}_s - \mathbf{r}_{CM}) \times \Sigma(\mathbf{r}) \cdot \mathbf{n}_s \, d^2r = 0. \quad (2.20)$$

Again, strictly speaking, Eq. (2.20) is not valid for the swimmer itself, but for the swimmer plus its (infinitesimally thin) interfacial layer. Within this layer, the particle is still subject to a viscous force arising from the no-slip boundary condition at $\tilde{y} = 0$ [see Eq. (2.14)].

Although Eqs. (2.18)–(2.20) can be solved more easily than Eqs. (2.3)–(2.12), the problem of the a priori unknown particle velocities \mathbf{v}_0 and Ω remains. However, if one is not explicitly interested in the fluid dynamics and the distribution of the B molecules, but solely in the resulting particle dynamics, a large amount of the above calculations can be bypassed by applying the Lorentz reciprocal theorem [152]. This theorem establishes a connection between two solutions of the SE [Eqs. (2.19), left equation] over the same domain \mathcal{R} , but for different boundary conditions. We thereby arrive at the equation

$$\int_{\partial\mathcal{R}} \mathbf{u}(\mathbf{r}) \cdot \Sigma'(\mathbf{r}) \cdot \mathbf{n}_0 \, d^2r = \int_{\partial\mathcal{R}} \mathbf{u}'(\mathbf{r}) \cdot \Sigma(\mathbf{r}) \cdot \mathbf{n}_0 \, d^2r, \quad (2.21)$$

where \mathbf{u}' and Σ' denote, respectively, the fluid velocity and stress tensor corresponding to a suitable auxiliary boundary value problem [83, 164, 165], $\partial\mathcal{R}$ is the surface enclosing \mathcal{R} and

\mathbf{n}_0 the unit vector normal to $\partial\mathcal{R}$. For a spherical particle with a cylindrically symmetrically applied catalytic cap, see Fig. 2.3a, this way \mathbf{v}_0 and Ω can be explicitly calculated in the bulk (i.e., away from any confining walls), yielding $\Omega = 0$ (due to the swimmer’s spatial symmetry) and

$$\mathbf{v}_0 = -\frac{1}{4\pi R^2} \int_{\mathcal{R}_s} \mathbf{v}_s(\mathbf{r}) \, d^2r, \quad (2.22)$$

where R is the particle radius [152]. That is, the swimmer’s self-propulsion velocity equals the spatial average of the phoretic slip velocity over the particle surface.

Looking again at Eqs. (2.16) and (2.17), we note that a predominance of the attractive (repulsive) character of the particle-solute interaction tends to orient \mathbf{v}_0 toward higher (lower) concentrations of the B molecules, as expected by a simple argument: if the particle-solute interaction is prevalently attractive (repulsive), the system tries to lower its free energy by moving the swimmer up (down) the gradient of $c_B^{(0)}$. As the particle is in fact “stuck” within this gradient (the distribution of the B molecules always follows its position), this mechanism results in a permanent self-propulsion³. Note that for undisturbed motion in the bulk, i.e., far away from any confining walls, and in the absence of particle fluctuations, the self-propulsion velocity is constant due to the spatial isotropy of the fluid.

Furthermore, if the swimmer or the catalytic cap had an asymmetric shape with respect to the propulsion axis, the general consequence would be a non-zero angular velocity $\Omega \neq 0$, which tries to reorient the particle in the concentration field $c_B^{(0)}$. Since the field rotates with the particle, however, this reorientation can never be accomplished, resulting in spiraling swimmer trajectories [51, 89, 166–169]. We will address the motion of such chiral microswimmers in Ch. 4.4.

Experimental realizations. The idea of self-phoretic propulsion was sketched by Anderson already in 1989 [154]. Since the first full proof of concept of a self-diffusiophoretic swimmer by R. Golestanian et al. [35], explicit results for \mathbf{v}_s (and hence for \mathbf{v}_0) have been found for various swimmer setups [160, 162, 170–172] and several groups have reported experimental demonstrations of self-diffusiophoretic propulsion [29, 36–38, 173–175]. In most cases, the swimmers are driven by the catalytic decomposition of hydrogen peroxide (H_2O_2) at a specific surface region, $2\text{H}_2\text{O}_2 \rightarrow \text{O}_2 + 2\text{H}_2\text{O}$ (Fig. 2.4), but enzymatically powered chemical reactions too have been found to induce diffusiophoretic self-propulsion [174]. The latter is an

³Although a purely thermodynamic approach on self-diffusiophoretic propulsion seems appealing, we remark that it is not suitable for calculating \mathbf{v}_0 [154]: by the thermodynamic arguments mentioned above, one might indeed calculate an effective force and torque acting upon the swimmer. However, the resulting self-propulsion velocity can only be obtained by knowing the particle’s frictional coefficient, which is determined by the dynamics of the surrounding fluid and does not obey the classic Stokes’ law. Thus, knowledge of the flow profile around the swimmer is still required.

important step toward successfully applying artificial microswimmers to tasks in biological settings, since enzymatic swimmers can be fueled by benign, biocompatible chemicals, in contrast to the toxic, very corrosive H_2O_2 .

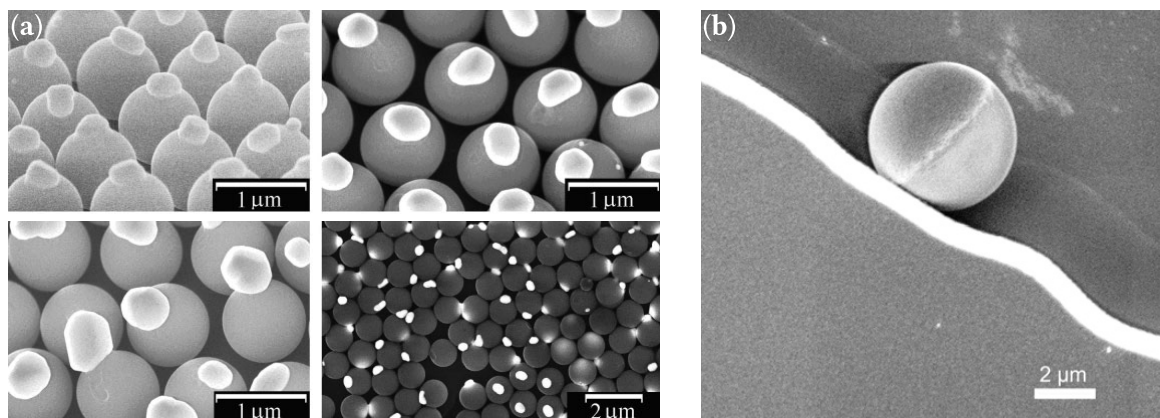


FIGURE 2.4. Scanning electron micrographs of self-diffusiophoretic swimmers. **(a)** Dimer swimmers, composed of silica spheres and small platinum ones, which catalytically decompose H_2O_2 . Adapted from Ref. [37] with permission. **(b)** Janus particle with a catalytically active platinum cap (also fueled by H_2O_2), which swims along a thin glass wall. Adapted from Ref. [176] under a CC BY 3.0 license.

We remark that the catalytic decomposition of H_2O_2 can be used to drive artificial microswimmers also by a bubble propulsion mechanism [45, 177–179], where the produced O_2 is first accumulated in cavities of the swimmer’s body and subsequently released in rather large gaseous bubbles. The ensuing recoil then results in a propulsion of the particle, similarly to a jet engine’s principle of operation. However, although fueled by H_2O_2 , as well, this propulsion mechanism is fundamentally different from self-diffusiophoresis, where no phase separation occurs.

Another self-diffusiophoretic propulsion mechanism that does not rely on chemical reactions was reported by I. Buttinoni et al. [29]. It operates on the principle of local demixing, that is, the spinodal decomposition [180, 181] of a critical mixture of two liquids at one side of the swimmer. To that purpose, one hemisphere of a spherical silica (SiO_2) particle is covered by a thin gold layer. The swimmer is then placed into a binary mixture of water and 2,6-lutidine, which is kept slightly below the critical demixing temperature [182]. Upon illuminating the particle with green light, the gold-capped hemisphere heats up, causing the surrounding fluid to exceed the critical temperature in its vicinity. As the non-capped hemisphere and the

fluid itself are not influenced directly by the irradiation (SiO_2 and H_2O hardly absorb green light), the fluid demixes only in the vicinity of the gold-capped hemisphere. Accordingly, a gradient of the lutidine-rich phase and the water-rich phase spans the swimmer, eventually causing its self-diffusiophoretic propulsion. Needless to say, this mechanism is certainly more complicated than catalytically induced diffusiophoresis, especially since here an additional temperature gradient ∇T comes into play. For their experimental setup, Buttinoni et al. [29] could rule out a prominent effect of ∇T on the swimmer's self-propulsion; in general, however, a temperature gradient can give rise to strong thermophoretic effects, which will be discussed in the forthcoming section.

2.2.2 Self-Thermophoresis

When a colloidal particle is heated non-uniformly, most commonly by coating a part of its surface with a strongly heat-absorbing material, such as gold, and irradiating it with a laser (see the end of the previous section), an asymmetric temperature gradient is established in the surrounding fluid [183]. In order to calculate this gradient due to the heat influx onto the particle's surface, we have to solve the stationary heat equations

$$\Delta T_f(\mathbf{r}) = 0, \quad \Delta T_p(\mathbf{r}) = 0, \quad (2.23)$$

for the temperature distributions T_f and T_p in the fluid and in the particle, respectively. Note that the timescales of the heat diffusion are usually much shorter than the timescales governing the swimmer's dynamics, so that the temperature distribution can be assumed to instantaneously relax to a swimmer's state. In fact, the thermal diffusivities of water and SiO_2 are $\alpha_T^{(\text{H}_2\text{O})} \approx 1.4 \cdot 10^{-7} \text{ m}^2/\text{s}$ [184] and $\alpha_T^{(\text{SiO}_2)} \approx 7.8 \cdot 10^{-7} \text{ m}^2/\text{s}$ [185]. Assuming a swimmer radius of $R = 0.1 \mu\text{m}$ (as in Ch. 2.2.1), the characteristic heat diffusion timescales are $R^2/\alpha_T^{(\text{H}_2\text{O})} \approx 0.07 \mu\text{s}$ and $R^2/\alpha_T^{(\text{SiO}_2)} \approx 0.01 \mu\text{s}$, which corroborates the above assumption. Of course, heat diffuses even faster through the metallic caps of the swimmers. We also remark that, similarly to Eq. (2.3), in Eqs. (2.23) we ignored any convective heat transport due to fluid flows, which, in the current setup, takes place on much larger timescales and thus is quite negligible with respect to heat diffusion [28, 186].

The boundary conditions for the above heat equations are

$$\lim_{|\mathbf{r}| \rightarrow \infty} T_f(\mathbf{r}) = T_0, \quad \lim_{|\mathbf{r}| \rightarrow \infty} \nabla T_f(\mathbf{r}) = 0, \quad (2.24)$$

implying that far away from the swimmer the temperature field is undisturbed (T_0 is the ambient temperature). Moreover, on the swimmer's surface the continuity conditions

$$T_f(\mathbf{r}_s) = T_p(\mathbf{r}_s), \quad -\lambda_f \mathbf{n}_s \cdot \nabla T_f(\mathbf{r}_s) + \lambda_p \mathbf{n}_s \cdot \nabla T_p(\mathbf{r}_s) = j(\mathbf{r}_s) \quad (2.25)$$

are imposed [28]. In the above equation, λ_f and λ_p are the thermal conductivities of the fluid and the swimmer, respectively. In a strict sense, the heated part of the swimmer's surface (usually a thin gold cap) must be considered explicitly by adding a third domain to Eqs. (2.23) and (2.25), with the corresponding thermal diffusivity and conductivity. However, as the laser-absorbing cap is typically very thin, the heat diffusion therein is extremely fast and we can model the heated region as an infinitesimally thin layer that injects a uniform heat flux j into the system. By analogy with Eq. (2.6), j has the form

$$j(\mathbf{r}_s) = \begin{cases} W_0 \left(\int_{\mathcal{R}_a} d^2r \right)^{-1} & : \mathbf{r}_s \in \mathcal{R}_a \\ 0 & : \mathbf{r}_s \notin \mathcal{R}_a, \end{cases} \quad (2.26)$$

where W_0 is the total laser power absorbed by the capped region \mathcal{R}_a .

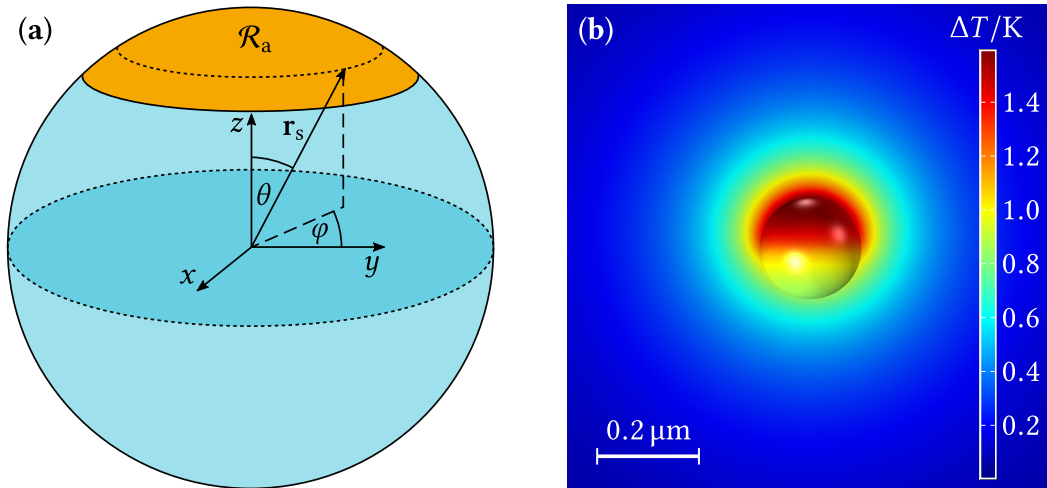


FIGURE 2.5. Thermophoretic microswimmers. (a) Sketch of a spherical thermophoretic swimmer that propels itself by absorbing laser light at a gold-coated region \mathcal{R}_a . (b) Temperature distribution on the swimmer's surface and in the surrounding fluid, obtained by numerically solving Eqs. (2.23)–(2.26), assuming water as fluid and a SiO_2 swimmer of radius $R = 0.1 \mu\text{m}$. The laser-absorbing cap was modeled to cover the whole upper hemisphere of the particle, absorbing a total power of $W_0 = 1 \mu\text{W}$. Here, ΔT denotes the difference between the measured temperature $T(\mathbf{r})$ and the constant ambient temperature, $T_0 = 293.15 \text{ K}$, at a large distance from the swimmer.

Considering an axisymmetrically coated spherical particle as in Fig. 2.5a, where the metallic cap is symmetric with respect to the z axis, j is a function of the polar angle θ only. Due to the particle's cylindrical symmetry, Eqs. (2.23)–(2.25) then formulate a two-dimensional problem in θ and the distance from the swimmer's geometric center. Upon expanding j into

the Legendre polynomials $\{L_n\}$ [187], $j(\theta) = \sum_{n=0}^{\infty} j_n L_n(\cos \theta)$, these equations can be formally solved to yield the temperature distribution on the swimmer's surface [28],

$$T(\mathbf{r}_s) = T_0 + \sum_{n=0}^{\infty} \frac{j_n |\mathbf{r}_s|^n}{(n+1)\lambda_f + n\lambda_p} L_n(\cos \theta). \quad (2.27)$$

Having found the non-uniform temperature distribution on the swimmer's surface, see also Fig. 2.5b, the next step is to find the ensuing phoretic slip. In this context, Derjaguin et al. in 1987 [188] calculated the heat flux j across a thin porous membrane, separating two fluid reservoirs, in the presence of a pressure gradient Δp . Using the relation $j = l_{12}\Delta p$, the authors subsequently determined the Onsager cross-correlation coefficient l_{12} , which relates heat transport to a prescribed pressure gradient [189]. By applying Onsager's reciprocal theorem, the momentum flux m across the membrane can then be calculated as $m = l_{21}\Delta T/T = l_{12}\Delta T/T$, where l_{21} is the Onsager cross-correlation coefficient linking mass transport to a temperature gradient. This way, Derjaguin et al. arrived at the expression

$$v_s = -\frac{2}{\eta_0} \frac{d \ln[T(x)]}{dx} \int_0^{h_t} y \delta H(y) dy \quad (2.28)$$

for the thermophoretic slip velocity along the walls of the membrane pores. In the above equation, y and x are, respectively, the coordinates perpendicular and parallel to the channel walls (assuming a circular cross section, the channels can be treated as effectively two-dimensional), δH is the excess or defect of the fluid's specific enthalpy near them, and h_t is the thickness of the interfacial layer, where δH is significantly different from zero. Making use of Eq. (2.28) to calculate the thermophoretic slip along the surface of a non-uniformly heated particle, we obtain, in the notation of Eqs. (2.16) and (2.17),

$$\mathbf{v}_s(\mathbf{r}_s) = -\mu_t(\mathbf{r}_s) \nabla_{\parallel} T(\mathbf{r}_s), \quad (2.29)$$

with the thermophoretic mobility μ_t given by

$$\mu_t(\mathbf{r}_s) := \frac{2}{\eta_0 T(\mathbf{r}_s)} \int_0^{\infty} y \delta H(\mathbf{r}_s + y \mathbf{n}_s) dy. \quad (2.30)$$

Upon inserting the thermophoretic slip velocity thus obtained into Eq. (2.19), the swimmer's self-propulsion velocity \mathbf{v}_0 can now be calculated in the same way as in Ch. 2.2.1, with the only difference that here the emergence of \mathbf{v}_s is not due to a chemical gradient, but rather to a temperature gradient induced by non-uniform particle heating.

We remark that an attractive interaction between the surface and the fluid leads to $\delta H < 0$, whereas a repulsive interaction implies that $\delta H > 0$. Thus, if the attractive part of the total interaction (weighted by the distance from the particle's surface) prevails, μ_t is negative and \mathbf{v}_0 is directed toward lower temperatures. Vice versa, for predominant fluid-surface repulsion, \mathbf{v}_0 points toward higher temperatures. This suggests a simple hand-waving interpretation of self-thermophoresis: if the swimmer is *lyophilic*, that is, if its surface attracts the fluid, it tries to move to regions where the fluid molecules are on average closer to its surface (colder regions), while, by the same argument, *lyophobic* (i.e., fluid-repelling) swimmers try to move to hotter regions.

However, despite all efforts in the field, a general microscopic model that allows for an explicit calculation of δH is still lacking; only in some special cases, the properties of δH can be derived from theory [190, 191]. As experimentally measuring the excess specific enthalpy is an extremely difficult task, as well, the self-propulsion velocity of a thermophoretic swimmer is in most cases obtained by considering the purely phenomenological convection-diffusion equation,

$$\frac{\partial c(\mathbf{r}, t)}{\partial t} = \nabla \cdot [D_0 \nabla c(\mathbf{r}, t) + D_T c(\mathbf{r}, t) \nabla T], \quad (2.31)$$

for the concentration c of non-activated swimmers in an *external* temperature gradient⁴. Here, D_0 is the swimmer's translational diffusion constant and D_T describes the phenomenological thermophoretic drift, which, for historical reasons, is called “thermodiffusion coefficient” [186, 192]. Of course, D_T has not to be confused with a real diffusion constant; it is rather another thermophoretic mobility coefficient. Upon preparing the system in a stationary state, e.g., by imposing confining boundaries and letting c relax in the presence of the temperature gradient, Eq. (2.31) becomes

$$\nabla c(\mathbf{r}, t) = -c(\mathbf{r}, t) \frac{D_T}{D_0} \nabla T. \quad (2.32)$$

The ratio $D_T/D_0 =: S_T$, which is usually referred to as Soret coefficient [193], can thus be determined by simply measuring the concentration profile. Since the thermophoretic mobility of a particle remains the same, whether ∇T is generated by the particle itself or externally imposed, the swimmers' self-phoretic velocity obeys the approximate equation $\mathbf{v}_0 = -D_0 S_T \langle \nabla_{\parallel} T(\mathbf{r}_s) \rangle_s$. Note that, because a self-generated temperature gradient can vary significantly on the lengthscale of R , here $\nabla_{\parallel} T$ has to be averaged over the particle's surface, that is,

$$\langle \nabla_{\parallel} T(\mathbf{r}_s) \rangle_s := \frac{1}{4\pi R^2} \int_{\mathcal{R}_s} \nabla_{\parallel} T(\mathbf{r}_s) d^2 r. \quad (2.33)$$

⁴Obviously, in Eq. (2.31) all particle-particle interactions are ignored, that is, strictly speaking, Eq. (2.31) is only valid for rather dilute particle mixtures.

Experimental realizations. In 2010, H.-R. Jiang et al. presented a self-thermophoretic swimmer driven by a defocused laser beam [28]. Since then, the concept of self-thermophoretic swimming has also been successfully implemented by F. Cichos' and H. Yang's groups [31, 77, 194], who considered a thermophoretic swimmer activated by laser irradiation, as well. Self-thermophoretic swimmers offer some advantages in view of possible applications in biological settings, since no (possibly poisonous) chemical fuel is required to propel them and the heating around them is extremely localized (see Fig. 2.5b), so that no noteworthy warming of the environment occurs [191]. Furthermore, the swimmers' motion can be controlled quite precisely, as switching off the laser almost immediately stops their propulsion. This excellent control, on the other hand, comes at the price of a permanent "optical access" to the particle, which hampers the usage of laser-driven swimmers for in vivo applications or autonomous tasks.

2.2.3 Self-Electrophoresis

A further common self-phoretic propulsion mechanism of artificial microswimmers is self-electrophoresis. Here, the particles are driven by a self-generated electric field resulting from a non-uniform charge density in their vicinity. This field, in turn, exerts a force on the ions in the fluid, which—due to viscous coupling—translates onto the fluid itself, resulting in a self-electrophoretic slip velocity. For a more quantitative description of this effect, we primarily discuss regular, that is, "non-self" electrophoresis, where the electric field inducing the phoretic slip is externally imposed. The generalization to the case of a self-generated electric field then follows naturally.

Let us consider, for simplicity, a spherical particle of radius R and charge Q , which is immersed in an electrolyte solution. The particle's electric field then attracts a diffusive cloud of counterions, which effectively shields the outside from its charge (see Fig. 2.6). In the Debye-Hückel approximation [195], the associated electric potential Φ_e is calculated by solving the Poisson equation outside the charged particle, where the charge density ρ of the ion cloud is assumed to obey the Boltzmann distribution,

$$\rho(\mathbf{r}) = \sum_i eZ_i c_i(\mathbf{r}) = \sum_i eZ_i c_i^{(0)} \exp\left(-\frac{eZ_i \Phi_e(\mathbf{r})}{k_B T}\right). \quad (2.34)$$

Here, e is the elementary charge, Z_i and c_i are, respectively, the charge number and number density of the electrolyte species i , and the $c_i^{(0)}$ are the corresponding bulk number densities. For weak electric potentials, namely for $eZ_i \Phi_e(\mathbf{r}_s) \ll k_B T$ (we remind that for a spherical particle, $|\mathbf{r}_s| = R$), the Taylor expansion of the exponential function in Eq. (2.34) can be

truncated after the first order and, therefore, the Poisson-Boltzmann equation becomes

$$\frac{1}{r^2} \frac{d}{dr} r^2 \frac{d\Phi_e(r)}{dr} = \frac{e^2}{\epsilon k_B T} \sum_i Z_i^2 c_i^{(0)} \Phi_e(r), \quad (2.35)$$

with ϵ denoting the permittivity of the fluid. In the above equation, the particle is located at the origin, i.e., at $\mathbf{r} = 0$, and its charge density is assumed to be spherically symmetric, so that Φ_e depends solely on $r = |\mathbf{r}|$. Furthermore, the electrolyte solution is considered to be electrically neutral, hence $\sum_i e Z_i c_i^{(0)} = 0$. Upon introducing the Debye length r_D ,

$$r_D := \sqrt{\frac{\epsilon k_B T}{e^2 \sum_i Z_i^2 c_i^{(0)}}}, \quad (2.36)$$

the solution of Eq. (2.35) reads [196]

$$\Phi_e(r) = \frac{Q}{4\pi\epsilon r} \exp\left(-\frac{r}{r_D}\right), \quad (2.37)$$

which clearly shows the screening of the particle's charge Q on a characteristic lengthscale r_D . Typical values of the Debye length depend mostly on the electrolyte concentrations. For instance, considering a (rather dilute) 0.001 molar solution of sodium chloride in water ($\Rightarrow c_{\text{Na}}^{(0)} = c_{\text{Cl}}^{(0)} = N_A \cdot 1 \text{ mol/m}^3$, where N_A is the Avogadro constant), we obtain $r_D \approx 9.6 \text{ nm}$. Thus, in general, the electric double layer around a colloidal micron-sized particle can be assumed to be very thin with respect to the particle radius, $r_D \ll R$.

A first theoretical approach to the electrophoretic motion of a charged colloidal particle was presented by M. von Smoluchowski in 1903 [197], who, in the absence of more elaborate double layer descriptions⁵, made use of the Helmholtz model of fixed counterion layers. Nevertheless, the results he obtained this way are very general and hold approximately even when assuming more complicated double layer models.

In the Smoluchowski approach, a charged colloidal particle (plus its double layer) is considered to be subject to an external electric field \mathbf{E}_{ex} . As the double layer shields the outside from the particle's charge, rendering the overall structure electrically neutral, no direct electric force acts upon the particle. The field \mathbf{E}_{ex} however acts upon the electrolyte ions, producing a body force $\rho \mathbf{E}_{\text{ex}}$ on them, which, like in Ch. 2.2.1, is assumed to be transferred to the fluid via the viscous electrolyte-fluid interactions [154]. On introducing once again the locally Cartesian coordinate system $\tilde{\mathbf{r}}$, where the \tilde{x} direction is defined by the projection of

⁵A model considering the diffusive character of the double layer was introduced only in 1910 by L. G. Gouy and in 1913 by D. L. Chapman.

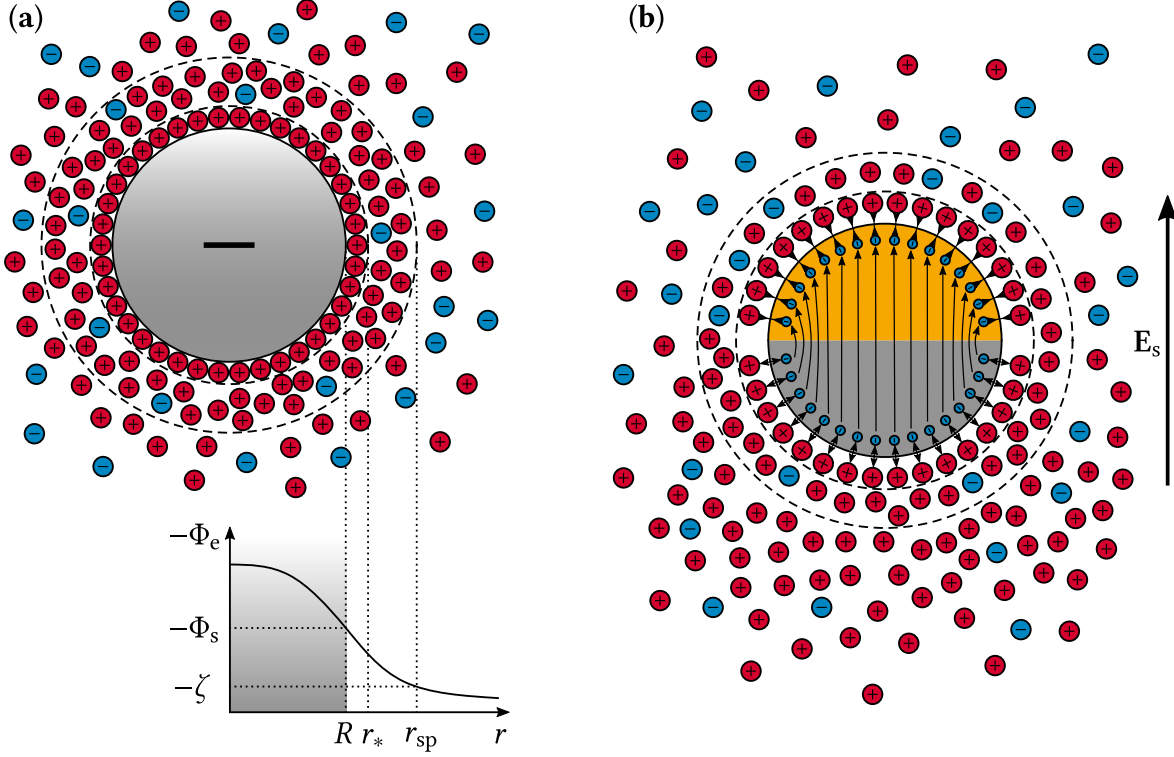


FIGURE 2.6. Electrophoresis of colloidal particles. **(a)** Electric double layer around a charged colloidal particle screening its electric field. For large surface potentials $\Phi_s := \Phi_e(R)$, that is, for $eZ_i\Phi_s \gtrsim k_B T$, the oppositely charged counterions cluster densely around the particle, generating an almost solid layer of tightly packed ions. This layer at radius r_* is called Stern layer. Moving slightly further away from the particle surface, the ionic shell exhibits a more diffusive character. However, the ions are still bound rather tightly to the particle and thus cannot be moved by (moderate) external electric fields. Only at a distance r_{sp} from the particle's center, the binding of the ions to the surface becomes so weak that they become mobile to an external forcing. This outer shell separating the mobile and the immobile part of the counterion cloud is called *slipping plane* and the corresponding electric potential is the *zeta potential* ζ . We remark that the choice of a negatively charged particle and a corresponding positive ion cloud is purely arbitrary and can also be reversed. **(b)** Electric double layer of a self-electrophoretic swimmer. A Janus particle made of two different metals is able to create positive ions at one side (gray hemisphere), normally by catalytically decomposing a certain chemical. The electrons thereby released migrate through the swimmer and recombine with the positively charged ions in another chemical reaction on the other side of the particle (yellow hemisphere). The resulting concentration gradient of ions in the surrounding fluid generates an electric field E_s outside the ion cloud, $r > r_{sp}$, which in turn propels the particle.

\mathbf{E}_{ex} onto a plane locally tangent to the particle surface \mathcal{R}_s and \tilde{y} is the coordinate normal to this plane, the corresponding SE turn out to be similar to those in Eq. (2.14), namely,

$$\eta_0 \frac{\partial^2 u_{\tilde{x}}}{\partial \tilde{y}^2} - \frac{\partial p}{\partial \tilde{x}} + \rho E_{\text{ex},\tilde{x}} = 0, \quad -\frac{\partial p}{\partial \tilde{y}} + \rho E_{\text{ex},\tilde{y}} = 0. \quad (2.38)$$

Note that the problem at hand is again effectively two-dimensional, with the spherical symmetry of the particle being broken only in the direction of the electric field \mathbf{E}_{ex} . We also remind that in Eq. (2.38), the other three components of $\nabla^2 \mathbf{u}$ were dropped, as we assumed once more a very thin interfacial layer. Furthermore, the pressure also varies at best on scales of the order of R in the \tilde{x} direction [196], so that here the term $\partial p / (\partial \tilde{x})$ can be neglected, too. Since the charge density obeys the Poisson equation $\rho = \varepsilon \Delta \Phi_e$, the electrophoretic slip can be calculated from the expression

$$\frac{\partial^2 u_{\tilde{x}}}{\partial \tilde{y}^2} = \frac{\varepsilon}{\eta_0} \frac{\partial^2 \Phi_e}{\partial \tilde{y}^2} E_{\text{ex},\tilde{x}}, \quad (2.39)$$

where $\partial^2 \Phi_e / (\partial \tilde{x}^2) = 0$, due to the symmetry of the ion cloud. Together with the boundary conditions $\partial u_{\tilde{x}} / (\partial \tilde{y})|_{\tilde{y} \rightarrow \infty} = 0$ and $u_{\tilde{x}}(\tilde{y} = r_{\text{sp}}) = 0$ (for the definition of r_{sp} , see Fig. 2.6a), the above equation can be readily integrated to yield the solution

$$v_s = \lim_{\tilde{y} \rightarrow \infty} u_{\tilde{x}} = -\frac{\varepsilon}{\eta_0} \zeta E_{\text{ex},\tilde{x}}, \quad (2.40)$$

which describes the electrophoretic slip at the outer edge of the interfacial layer where Φ_e has vanished. Formally, this requires taking the limit $\tilde{y} \rightarrow \infty$, whereas actually, Φ_e is already negligible at finite distances significantly larger than the Debye length r_D . In a more convenient vectorial notation, Eq. (2.40) can be rewritten as

$$\mathbf{v}_s(\mathbf{r}_s) = -\mu_e(\mathbf{r}_s) \mathbf{E}_{\text{ex}}^{\parallel}(\mathbf{r}_s), \quad \mu_e(\mathbf{r}_s) = \frac{\varepsilon}{\eta_0} \zeta(\mathbf{r}_s), \quad (2.41)$$

with μ_e being the electrophoretic mobility and $\mathbf{E}_{\text{ex}}^{\parallel}$ the component of the electric field locally tangent to the particle's surface. We remark that, contrary to the other phoretic mechanisms outlined in Chs. 2.2.1 and 2.2.2, here the no-slip boundary condition applied to solve Eq. (2.39) is not imposed at the particle's surface, but at the slipping plane at radius $r_{\text{sp}} > R$ (see the schematics of Fig. 2.6a). For $R < r < r_{\text{sp}}$, the electrolyte ions are tightly bound to the particle, so that in this case no ionic and, therefore, no fluid motion can be induced by (moderate) external electric fields. Accordingly, the electric potential entering μ_e is not the particle's surface potential Φ_s , but the zeta potential $\zeta := \Phi_e(r_{\text{sp}})$.

As elucidated above, an external electric field is able to induce a phoretic slip around a charged colloidal particle—and thus to move it, see Eq. (2.22). This electrophoretic motion

results from the drift of the surrounding free electrolyte ions, which is eventually transferred to the particle due to its viscous coupling with the suspension fluid. Turning to the propulsion of a self-electrophoretic swimmer, the underlying mechanisms remain the same, except for the fact that the electric field at the outer edge of the double layer is not imposed externally, but created by the swimmer itself. That is, for self-electrophoresis, Eq. (2.41) still applies in the first approximation, solely E_{ex} is replaced by a self-generated field E_s . The latter normally originates from an asymmetric, non-equilibrium electrolyte distribution around the swimmer, which is caused, in turn, by the generation and annihilation of ions at two distinct regions of its surface (see Fig. 2.6b). E_s can thus be obtained by solving the coupled convection-diffusion and Poisson equation for the ion cloud densities and the electric potential, respectively, with the creation and annihilation of ions on the swimmer's surface being modeled by appropriate boundary conditions [33]. Obviously, this renders the task of calculating E_s rather cumbersome and, therefore, theoretical results for the self-electrophoretic propulsion velocity v_0 prove elusive. Nevertheless, over the past few years, explicit results for v_0 have been found both by numerical and analytical approaches [33, 34, 198–201].

Experimental realizations. The first-ever implementation of an artificial microswimmer, reported by W. F. Paxton et al. in 2004 [46], was propelled by a self-electrophoretic mechanism. It was designed as a Janus-like bimetallic microrod with one gold (Au) and one platinum (Pt) end. Initially, Paxton et al. explained the movement of the swimmer with a reduction of the rod's surface tension by the O_2 produced at the Pt end in the catalytic decomposition of H_2O_2 , $2H_2O_2 \rightarrow O_2 + 2H_2O$. This, in turn, was supposed to drag the hydrophobic Au end toward higher O_2 concentrations due to a resulting Marangoni effect. However, that effect eventually turned out to play at best a minor role in the particle's propulsion mechanism, which is now commonly attributed to self-electrophoresis [32, 202–204]: In contrast to the self-diffusiophoretic swimmers mentioned in Ch. 2.2.1—which also propel themselves by the catalytic decomposition of H_2O_2 —here the protons (H^+) and electrons (e^-) released in the oxidation process $H_2O_2 \rightarrow 2H^+ + 2e^- + O_2$ at the swimmer's Pt end (see Fig. 2.7) do not instantly recombine with another H_2O_2 or O_2 molecule at the same site. Instead, they move toward the Au end where they fuel the separate reductions $4H^+ + O_2 + 4e^- \rightarrow 2H_2O$ and $2H^+ + 2e^- + H_2O_2 \rightarrow 2H_2O$. As the electrons migrate through the rod, whereas the protons move through the fluid, the swimmer effectively acts like a short-circuited galvanic cell [33], creating a gradient of H^+ ions in its vicinity (see Fig. 2.7). As explained above, the resulting electrical field then propels the particle electrophoretically.

Of course, the O_2 gradient thus induced must also give rise to an additional diffusiophoretic effect. However, for the above propulsion mechanism, the diffusiophoretic contribution is

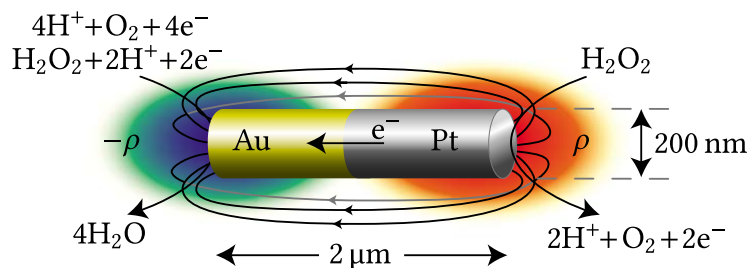


FIGURE 2.7. Sketch of the self-electrophoretic Pt-Au swimmer as reported in Ref. [46]. A reaction-induced charge density gradient gives rise to an electric field around the swimmer, which generates an electrophoretic slip along its surface. For more details, see the text. We remark that for the microrod considered here, the self-electrophoretic propulsion leads to a swimmer movement to the right, with the Pt end pointing forward [32]. Adapted from Ref. [33] with permission.

several orders of magnitude weaker than the electrophoretic contribution [32, 33], so that the influence of the non-uniform O_2 concentration around the swimmer can be safely neglected. In addition, the decomposition of H_2O_2 is an exothermic reaction, implying that strictly speaking, a temperature gradient around the swimmer should be considered, too⁶. As a matter of fact, in general self-diffusio-, -thermo-, or -electrophoretic effects do not occur separately, but in combination with each other, thus complicating the theoretical description of the swimmer's dynamics. Fortunately, the strength of the different phoretic effects is seldom of the same order of magnitude; in most experimental realizations, one phoretic mechanism prevails upon the others.

Very shortly after the publication of Ref. [46], a second paper by S. Fournier-Bidoz et al. [205] appeared, reporting on a very similar bimetallic microswimmer that was powered by catalytic H_2O_2 decomposition, as well. Since then, the model of a short-circuited galvanic cell was also applied in the fabrication of a variety of other electrophoretic microswimmers (cf. Fig. 2.8), which can be propelled by different chemical redox reactions—some involving even biocompatible organic fuels [203, 206–208].

In summary, the majority of the artificial microswimmers realized thus far are propelled by self-phoretic mechanisms, the most prominent of which are diffusio-, thermo-, and electrophoresis. Self-phoretic swimmers generate a microscopic gradient in their vicinity, which results from maintaining a field (here the number density of solutes, temperature, or electric potential) in a non-equilibrium state. The latter is established by a functional asymmetry of

⁶Of course, the same argument applies to the diffusio-phoretic swimmers in Ch. 2.2.1, which catalytically decompose H_2O_2 .

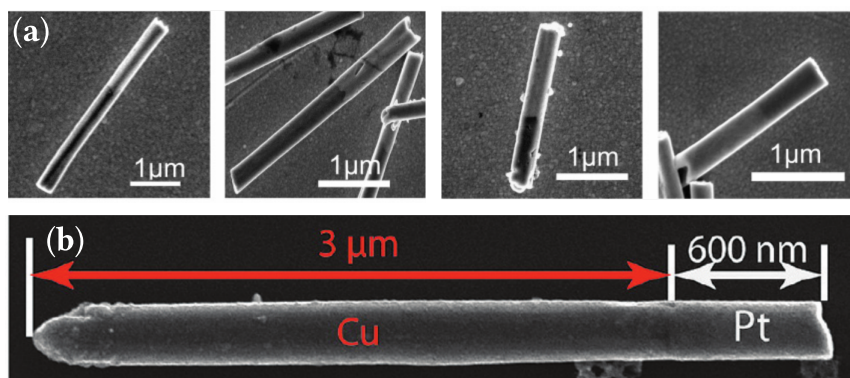


FIGURE 2.8. Micrographs of various self-electrophoretic swimmers. (a) Field emission scanning electron micrographs of bimetallic microrods, built from a (from left to right) Ni-Au, Pd-Au, Ru-Au, and Pt-Rh combination, all of which are propelled by a catalytic decomposition of H_2O_2 . Adapted from Ref. [203] with permission. Copyright 2006, American Chemical Society. (b) Scanning electron micrograph of a Cu-Pt microrod, which can be fueled by a bromine or iodine solution. Adapted from Ref. [207] with permission. Copyright 2011, American Chemical Society.

the swimmer's surface and can be sustained by heat/laser irradiation or chemical reagents. Moreover, we remark that all phoretic mechanisms described in the present chapter can be formulated in the framework of a linear theory. Accordingly, the expressions for the phoretic slip velocities (and thus also for the swimmers' self-propulsion velocities), Eqs. (2.16), (2.29), and (2.41), share the same pattern. Solely the relevant phoretic mobilities exhibit different structures, reflecting the distinct physical mechanisms underlying the interaction between the swimmer and its surrounding medium.

Thus far, we have discussed the most common propulsion mechanisms that give rise to the directed movement of an artificial microswimmer and neglected the role of fluctuations, which are intrinsic to any self-phoretic swimming mechanism. Therefore, we present now a simple stochastic model that accounts for the role of noise in the dynamics of active swimmers.

2.3 Stochastic Modeling

As stated in the previous sections, an artificial microswimmer is a microscopic particle immersed in a fluid, which is capable of propelling itself along a given direction in its reference system. Assuming a homogeneous "fuel" concentration, such as H_2O_2 concentration, laser intensity, etc., which we will refer to in the following as *activation density*, and considering

the swimmer's motion in the bulk, i.e., away from any confining walls, the modulus of its self-propulsion velocity v_0 is approximately constant. However, due to the noise that originates from the interplay of thermal fluctuations in the surrounding fluid and fluctuations caused by the self-propulsion mechanism itself⁷, the particle actually performs a free translational, "passive" Brownian motion subject to an additional "active" propulsion velocity v_0 . It is important to stress here that in the presence of noise, the modulus of v_0 is still approximately constant, but not its direction. The latter is affected by rotational fluctuations, a concept which is also known as active Brownian motion [23] and can be conveniently implemented within the Langevin formalism. In this formalism, the dynamics of a microscopic particle subject to fluctuations is modeled by incorporating one or more stochastic force terms into its deterministic, Newtonian-type equations of motion [215–217].

Furthermore, we stress that in reality, the diffusion of an artificial microswimmer always occurs in a confined geometry. For instance, in the case of negative particle buoyancy, the swimmer finally sediments at the bottom of its container, so that—no matter how large the container is—one cannot ignore at least the interaction between the particle and the bottom wall. A viable general, coarse-grained theoretical framework taking into account these interactions is almost impossible to be established, because the influence of a confining wall on the swimmer's dynamics strongly depends on the swimmer's geometry, its surface properties and the specific self-propulsion mechanism at work—and thus can be fundamentally different for distinct swimmers [38, 81–83, 85, 86, 120, 218]. For a large class of microswimmers, however, the interactions with a confining wall lead to a "pinning" of the particles' orientation parallel to it [81, 82, 85], such that their translational and rotational motion become approximately two-dimensional after approaching a planar wall (see Fig. 2.9). We will assume such a simplified two-dimensional geometry in the following, in order to avoid unnecessary algebraic complications. The extension to the three-dimensional problem can then be accomplished along similar lines [219]. Moreover, to a first approximation, the rotational and translational motion parallel to the wall are not affected by the boundary, except for an overall increase or decrease in v_0 [218].

An artificial microswimmer diffusing on a planar substrate and subjected to a homogeneous

⁷Note that any of the self-phoretic mechanisms described in Ch. 2.2 is intrinsically noisy, be it due to the diffusion of solute molecules around the swimmer or a local particle heating. Regarding the latter, we remark that maintaining a colloidal particle above its ambient temperature does not only increase thermal fluctuations in the surrounding fluid, but also reduce its viscous friction. These effects, known as hot Brownian motion [209–211], can be systematically derived from a non-isothermal fluctuating hydrodynamic theory [191, 212], yielding distinct effective temperatures for both the particle's translational and rotational fluctuations [213, 214].

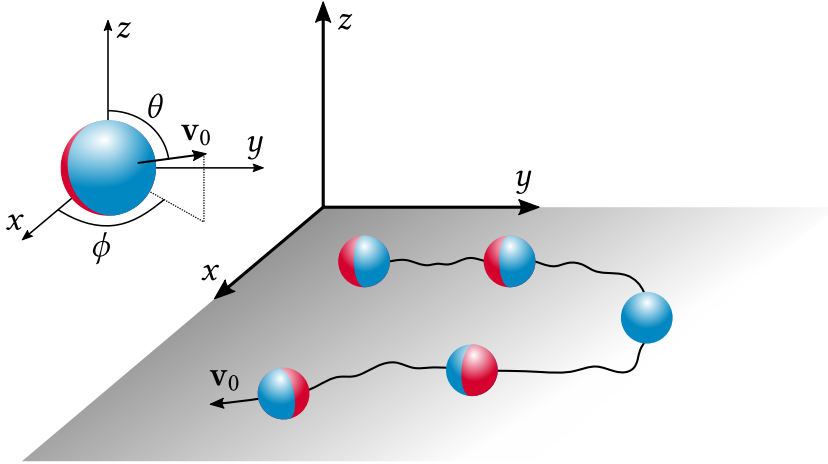


FIGURE 2.9. Schematic motion of a Janus microswimmer near a planar boundary. As reported in Refs. [81, 82, 85], many swimmers become trapped by a planar wall, with their dynamics being confined to a plane parallel to it. Hence, for the geometry supposed in the figure, we approximately have $\theta = \pi/2$ and the swimmer undergoes a two-dimensional dynamics with one orientational and two translational degrees of freedom, ϕ , x , and y .

activation density can thus be modeled by the simple Langevin equations (LE)⁸ [26]

$$\begin{aligned} \dot{x} &= v_0 \cos \phi + \sqrt{2D_0} \xi_x(t), \\ \dot{y} &= v_0 \sin \phi + \sqrt{2D_0} \xi_y(t), \\ \dot{\phi} &= \Omega + \sqrt{2D_\phi} \xi_\phi(t), \end{aligned} \tag{2.42}$$

where the swimmer's self-propulsion velocity—which acts along a specific direction in its reference system—was parametrized in terms of a variable polar angle ϕ in the xy plane (see Fig. 2.9) and a constant modulus v_0 : $\mathbf{v}_0 = v_0(\cos \phi, \sin \phi)^\top$. Note that, since the particle is supposed to swim at low Reynolds numbers, the above Langevin dynamics is formulated in the overdamped regime, i.e., inertial effects were neglected altogether.

The additive fluctuational sources—two translational of intensity D_0 and one rotational of intensity D_ϕ —are represented, for simplicity, by independent white Gaussian noises with zero mean and autocorrelation functions $\langle \xi_i(t) \xi_j(0) \rangle = \delta_{ij} \delta(t)$ for $i, j = x, y, \phi$ (where $\langle \dots \rangle$ denotes the stochastic ensemble average, obtained by taking the mean value with respect to the different realizations of a stochastic process), as usually assumed in the current literature

⁸For simplicity, here and throughout the following we assume a spherical particle geometry and model the swimmer itself as point-like.

[26]. As the noises ξ_i model the combination of independent fluctuations, namely the thermal fluctuations in the swimmer's suspension fluid and the fluctuations intrinsic to its self-propulsion mechanism, we will treat D_0 and D_ϕ as independent parameters. Note, however, that in the presence of the sole thermal fluctuations, the translational and rotational diffusion constants are related. Considering a spherical particle of radius R , for instance, one has $D_0/D_\phi = 4R^2/3$ [220].

Finally, we remind that any asymmetric slip velocity profile around the swimmer, which can, e.g., be induced by an asymmetric active cap, see Ch. 2.2.1, gives rise to an angular velocity $\Omega := \mathbf{e}_z \cdot \boldsymbol{\Omega}$ (with \mathbf{e}_z being the unit vector orthogonal to the xy plane) that makes the particle rotate counterclockwise ($\Omega > 0$) or clockwise ($\Omega < 0$). Such *chiral* effects are known to significantly impact the transport properties of both biological and synthetic microswimmers [51, 89, 166–169, 221–226].

When $\Omega = 0$, i.e., when the swimmer's rotational dynamics is purely noise-induced, the particle performs an active Brownian motion with persistence time $\tau_\phi = D_\phi^{-1}$ and corresponding persistence length $l_\phi = v_0\tau_\phi$. Indeed, a straightforward calculation [227, 228] shows that the autocorrelation functions of the angular projections $\cos \phi(t)$ and $\sin \phi(t)$ decay exponentially,

$$\begin{aligned} \langle \cos \phi(t_1) \cos \phi(t_2) \rangle &= \frac{1}{2} \exp(-D_\phi |t_1 - t_2|) \left[1 + \cos(2\phi_0) \exp(-4D_\phi \min\{t_1, t_2\}) \right], \\ \langle \sin \phi(t_1) \sin \phi(t_2) \rangle &= \frac{1}{2} \exp(-D_\phi |t_1 - t_2|) \left[1 - \cos(2\phi_0) \exp(-4D_\phi \min\{t_1, t_2\}) \right], \end{aligned} \quad (2.43)$$

where $\phi_0 := \phi(0)$. The first moments of the particle's displacement from its initial position $\mathbf{r}_0 := \mathbf{r}(0)$ can also be calculated analytically [36, 219], yielding

$$\langle \mathbf{r}(t) - \mathbf{r}_0 \rangle = \begin{pmatrix} \cos \phi_0 \\ \sin \phi_0 \end{pmatrix} \frac{v_0}{D_\phi} \left[1 - \exp(-D_\phi t) \right], \quad (2.44)$$

$$\langle [\mathbf{r}(t) - \mathbf{r}_0]^2 \rangle = 4D_0 t + \frac{2v_0^2}{D_\phi^2} \left[D_\phi t - 1 + \exp(-D_\phi t) \right]. \quad (2.45)$$

On short timescales, the swimmer's dynamics is thus characterized by a directed *ballistic* motion and on long timescales by an enhanced diffusion with zero net shift (assuming a uniformly distributed starting angle ϕ_0) and diffusion constant

$$\lim_{t \rightarrow \infty} \frac{\langle [x(t) - x_0]^2 \rangle}{2t} = \lim_{t \rightarrow \infty} \frac{\langle [y(t) - y_0]^2 \rangle}{2t} = D_0 + D_s, \quad (2.46)$$

with $D_s := v_0^2/(2D_\phi)$ [219]. We remark that in a coarse-grained description, the particle's motion can alternatively be modeled in terms of a non-Markovian driving, where the angular

dynamics is not considered explicitly and the terms $\cos \phi$ and $\sin \phi$ enter the LE (2.42) as colored noise sources instead [229–232].

In the case of a chiral swimmer dynamics with $\Omega \neq 0$, the LE (2.42) remain linear and, therefore, can still be solved analytically, resulting in

$$\begin{aligned} \langle \mathbf{r}(t) - \mathbf{r}_0 \rangle &= \frac{v_0}{D_\phi^2 + \Omega^2} \left\{ D_\phi \mathbf{n}(\phi_0) + \Omega \mathbf{t}(\phi_0) \right. \\ &\quad \left. - \exp(-D_\phi t) \left[D_\phi \mathbf{n}(\phi_0 + \Omega t) + \Omega \mathbf{t}(\phi_0 + \Omega t) \right] \right\}, \end{aligned} \quad (2.47)$$

$$\begin{aligned} \langle [\mathbf{r}(t) - \mathbf{r}_0]^2 \rangle &= 4D_0 t + \frac{2v_0^2}{(D_\phi^2 + \Omega^2)^2} \left\{ \Omega^2 - D_\phi^2 + D_\phi (D_\phi^2 + \Omega^2) t \right. \\ &\quad \left. + \exp(-D_\phi t) \left[(D_\phi^2 - \Omega^2) \cos \Omega t - 2D_\phi \Omega \sin \Omega t \right] \right\}, \end{aligned} \quad (2.48)$$

where $\mathbf{n}(x) := (\cos x, \sin x)^\top$ and $\mathbf{t}(x) := (-\sin x, \cos x)^\top$ [166]. Hence, under the repeated assumption of a uniformly distributed initial orientation ϕ_0 , a chiral swimmer does not drift, $\langle \mathbf{r}(t) - \mathbf{r}_0 \rangle = 0$, as for $\Omega = 0$, but its spatial diffusivity is reduced: taking the limit $t \rightarrow \infty$ of Eq. (2.48), one finds that [233]

$$D_s(\Omega) = \frac{D_s}{1 + (\Omega^2/D_\phi^2)}. \quad (2.49)$$

Spatio-temporally modulated activation. When the swimmer’s activation density is not homogeneous but varies in space and time, its self-propulsion speed, which is a local function of the activating “fuel” concentration, becomes likewise spatio-temporally modulated. That is, we have to replace the constant speed v_0 in Eq. (2.42) by a function of \mathbf{r} and t . As the intensity of the swimmer’s activation also impacts the strength of its fluctuations, in principle, a modulation of v_0 implies a modulation of D_0 and D_ϕ , as well. However, in most cases, the dependence of the swimmer’s diffusion constants on its activation density has been reported to be significantly weaker than that of the propulsion speed [28, 36, 55]. We thus neglect any modulation of D_0 and D_ϕ for the time being; indeed, we will show in Ch. 4.3 that extending our analysis to an activation-dependent D_ϕ would not alter the general conclusions of the present work. Assuming the activation density to vary along the x direction only, we then obtain the LE

$$\begin{aligned} \dot{x} &= v_0 w(x, t) \cos \phi + \sqrt{2D_0} \xi_x(t), \\ \dot{y} &= v_0 w(x, t) \sin \phi + \sqrt{2D_0} \xi_y(t), \\ \dot{\phi} &= \Omega + \sqrt{2D_\phi} \xi_\phi(t), \end{aligned} \quad (2.50)$$

where $w(x, t)$ represents the modulation profile of the swimmer's propulsion strength. The model equations (2.50) underlie the numerical results presented in the forthcoming chapters. Regarding this, we note that the influence of particle chirality, $\Omega \neq 0$, on the above dynamics will be studied in Ch. 4.4. Until then—that is, in Ch. 3 and at the beginning of Ch. 4—we set $\Omega = 0$, i.e., always consider achiral swimmers.

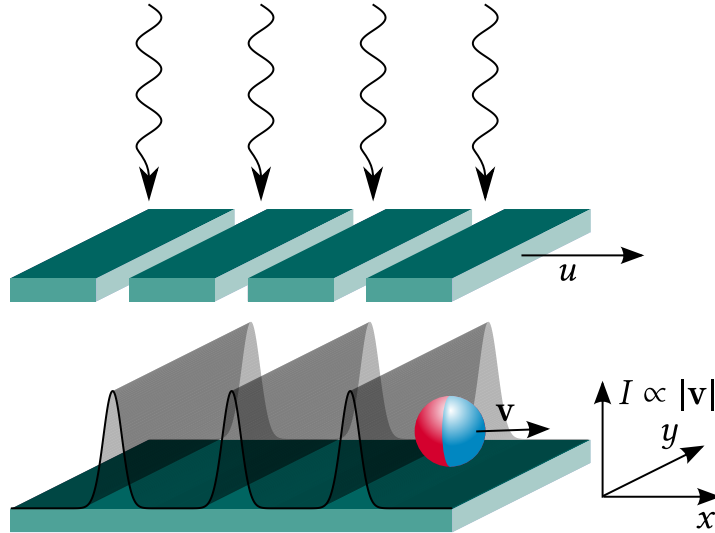


FIGURE 2.10. Artificial microswimmer subjected to traveling activation pulses. The sketch outlines an ideal setup to experimentally realize activating wave pulses. For details, see the text.

As mentioned in the Introduction and discussed in Appendix A, artificial microswimmers have been recently reported to tactically respond to several *static* (i.e., time-independent) external stimuli, such as a constant activation gradient. Motivated by the pulsating stimulus signals released in many biological systems [94], in the following we pursue the question of how these synthetic swimmers respond to a spatio-temporal modulation of the activation density in the form of traveling wave pulses. An ideal setup allowing for the creation of such activation pulses is illustrated in Fig. 2.10. In this sketch, a self-thermophoretic swimmer activated by laser light [28, 38] is placed on a planar substrate. Traveling wave pulses of laser intensity I can be generated by sliding a slit screen placed between the laser source and the particle at constant speed u . Since the swimmer's self-propulsion speed is approximately proportional to the laser intensity in a wide range of I [29], this way one can tailor any desired profile for $w(x, t)$. Although this method is probably the simplest way to experimentally realize traveling activation pulses, we remark that chemically activated swimmers represent a viable option, too. Indeed, such swimmers can be operated under the condition that their self-

propulsion speed is proportional to the concentration of the activating chemical(s), whereas, as mentioned above, their rotational diffusivity remains almost constant [36, 55]. On the other hand, traveling chemical waves can be conveniently excited in chemical reactors [234–243].

Moreover, we remind that in Eqs. (2.50) we neglected all hydrodynamic effects other than the swimmer’s phoretic slip and the pinning parallel to the bottom wall. In the absence of activation gradients, these effects are strongly suppressed by (i) restricting the swimmers’ motion to the bulk, that is, away from additional confining walls, (ii) lowering the swimmer density, so as to avoid hydrodynamically mediated particle collisions and clustering [244], and (iii) choosing spherical active particles of small size, i.e., almost point-like as in our model LE (2.50), in order to reduce hydrodynamic backflow effects [245]. However, the modulated activation gradients considered here may give rise to additional hydrodynamic contributions capable of influencing the dynamics of a unconfined single swimmer, as well. The most prominent one is a self-polarization of the swimmer, which tends to align the particle parallel or anti-parallel to the activation gradient, depending on its surface properties [91, 246]. We will address the consequences of such a self-polarization effect on the swimmer’s diffusion in Ch. 5. Until then, we limit ourselves to remark that for weak to moderate self-polarization effects, the tactic response of a swimmer behaves as reported in Chs. 3 and 4. Solely its magnitude slightly increases or decreases, subject to whether the swimmer tends to align itself parallel or anti-parallel to the gradient.

Finally, it should be kept in mind that here and in the following we neglect any internal particle structure, i.e., as mentioned above, we consider an effectively point-like swimmer, the size of which solely enters the model parameters v_0 , Ω , D_0 , and D_ϕ . Despite its simplicity, the model of Eq. (2.50) has been reported in the literature to capture and explain the prominent features of the dynamics of artificial microswimmers [26, 28, 36, 247]. However, recently also more sophisticated Langevin models have been proposed, which explicitly account for the geometry or the internal composite structure of the swimmers [51, 76, 248, 249].

ARTIFICIAL MICROSWIMMERS ACTIVATED BY SINGLE PULSES

We now consider, both numerically and analytically, the dynamics of an artificial microswimmer subjected to a single traveling activation pulse, cf. Fig. 2.10, and discuss the fundamental mechanisms underlying its resulting tactic response. In preparation for this, in Ch. 3.1 we primarily study the swimmer's taxis in a static activation gradient (see also Appendix A.1). We then proceed to consider temporally varying activation gradients in the form of a traveling Gaussian activation pulse. In Ch. 3.2, we focus on the role of the pulse speed and width, whereas the influence of the pulse waveform itself is investigated in Ch. 3.3. Finally, in Ch. 3.4, we set up a general analytical framework that allows us to obtain approximate results for the swimmer's tactic response, which compare favorably with the exact numerical outcomes.

3.1 Static Activation Gradient

Neglecting the propagation of the pulses, i.e., considering the simpler case of a static activation profile, $w(x, t) = w(x)$, artificial microswimmers have been reported to diffuse up the resulting activation gradients in the absence of confining walls [87, 88]. Indeed, for a constant activation gradient of the form $w(x) = (\nu/\nu_0)x$, where the parameter ν characterizes the strength of the gradient, the x dynamics in Eqs. (2.50) can be solved analytically, yielding for $\nu t \ll 1$ the

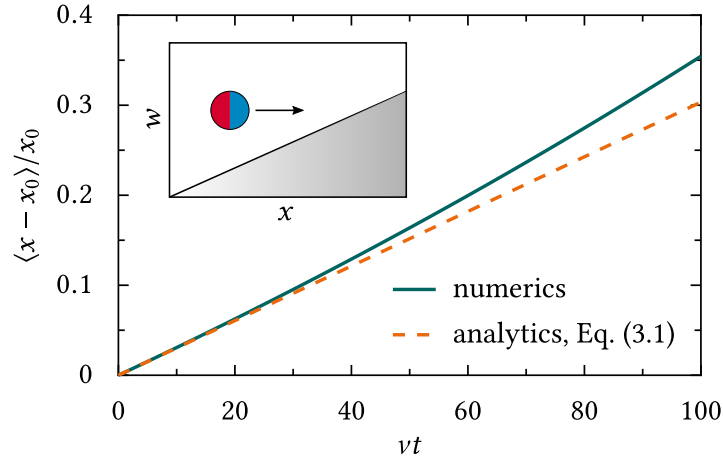


FIGURE 3.1. Taxis of an artificial microswimmer in a constant activation gradient $w(x) = (v/v_0)x$, for $v = 1 \text{ s}^{-1}$, $x_0 = 10 \text{ }\mu\text{m}$, and $D_\phi = 165 \text{ s}^{-1}$ (which equals the rotational diffusion constant of a passive, i.e., non-propelled, spherical particle of radius $R = 0.1 \text{ }\mu\text{m}$ in water at $T = 300 \text{ K}$). The solid (green) curve was obtained by numerically integrating the LE (2.50), see Appendix D for details. Clearly, the swimmer drifts up the gradient, toward regions of higher self-propulsion speeds. We remark that the activation gradient considered here is obviously rather unrealistic, as the swimmer’s self-propulsion in fact saturates at high activation densities [36, 90, 208, 250]. However, this simplified model well illustrates the tactic response of an artificial microswimmer to a static activation gradient.

result (see Appendix B)

$$\Delta(t) := \langle x(t) - x_0 \rangle \approx \frac{x_0}{2} \left(\frac{v}{D_\phi} \right)^2 \left[D_\phi t + \exp(-D_\phi t) - 1 \right]. \quad (3.1)$$

We remind that x_0 denotes the particle’s initial position, $x_0 = x(0)$. Realistically assuming a positive activation density only¹, $x_0 > 0$, the swimmer drifts to the right, i.e., toward a higher activation density, as depicted in Fig. 3.1. A simple explanation for this effect is that, due to the increase of the swimming speed to the right, during an infinitesimal time interval dt a swimmer with orientation $-\pi/2 < \phi < \pi/2$ takes a larger “step” to the right than a mirrored swimmer with $\phi \rightarrow \pi - \phi$ does to the left. Since this imbalance exists at any given position, the particle moves on average toward regions of higher self-propulsion velocities. Note that since the swimmer’s activation is modulated in the x direction only, for an achiral particle ($\Omega = 0$), we expect no net drift/position shift in the y direction. Thus, unless $\Omega \neq 0$, here and in the following we solely consider the swimmer’s *longitudinal* dynamics, that is, its

¹The hypothetical, but for the present model inevitable case of a negative activation density, $x_0 < 0$, is discussed in Appendix B.

motion parallel to the gradient(s) of the activation density—the *transversal* dynamics may be disregarded, since in Eqs. (2.50) y depends on x , but not vice versa.

3.2 Gaussian Activation Pulse

Turning to temporally varying activation gradients, we now address the question of what tactic effects are induced by propagating activation pulses. To this purpose, we initially neglect translational noise, $D_0 = 0$, and assume the pulse to have a generic Gaussian waveform, $w(x, t) = \exp[-(x - ut)^2/(2L^2)]$ (where L and u are the pulse width and propagation speed, respectively), hitting the swimmer from the left. We moreover stress that here and throughout this work, we restrict our analysis to spatially symmetric waveforms, $w(x, 0) = w(-x, 0)$, in order to avoid additional ratchet effects [93, 251, 252].

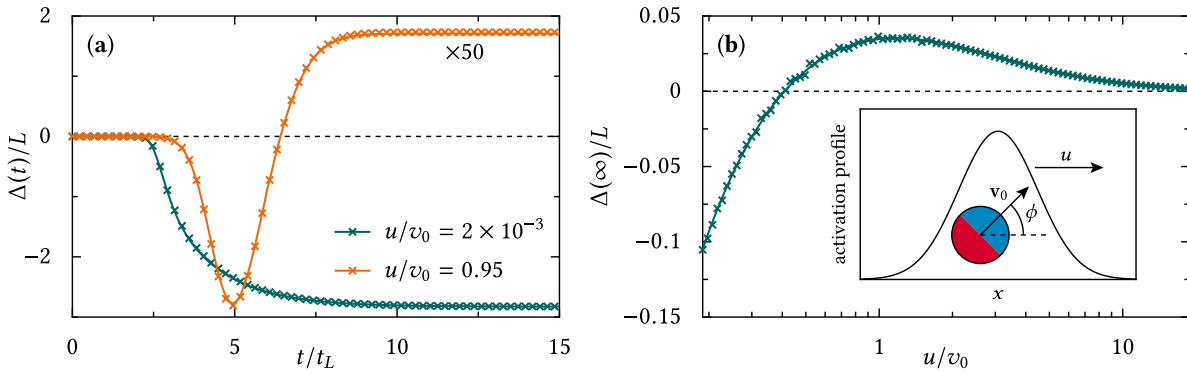


FIGURE 3.2. Taxis of an artificial microswimmer subjected to a single activation pulse.

(a) Tactic shift $\Delta(t) = \langle x(t) - x_0 \rangle$ of the swimmer's mean position generated by a Gaussian activation profile, $w(x, t) = \exp[-(x - ut)^2/(2L^2)]$ [see inset of panel (b)], versus the time t in units of the pulse crossing timescale $t_L := L/u$, for a slow and fast pulse speed u . The initial particle position was chosen to be located at a distance of $5L$ to the right of the pulse center, $x_0 = 5L$. In panel (b), the final shift $\Delta(\infty)$ is plotted as a function of the pulse speed u . The swimmer's self-propulsion parameters were set to $v_0 = 53 \mu\text{m/s}$ and $D_\phi = 165 \text{s}^{-1}$, and the pulse width, $L = 1 \mu\text{m}$, was chosen to be about three times the swimmer's persistence length $l_\phi = v_0/D_\phi$. Here, the translational noise intensity D_0 was set to zero in order to focus on the orientational mechanism responsible for the swimmer's tactic shift. In panels (a) and (b), the stochastic integration of the model LE (2.50) [crosses] is compared with the numerical solution of the corresponding Fokker-Planck equation (FPE) (3.5) [solid curves], see Appendix D for numerical details.

Influence of the pulse speed. The effect of a Gaussian activation pulse on the swimmer's dynamics is depicted in Fig. 3.2a. We observe immediately that a pulse speed $u \ll v_0$ causes the particle to shift to the left, $\Delta(t) = \langle x(t) - x_0 \rangle < 0$, whereas a pulse speed of about the same magnitude as the swimmer's maximum propulsion speed, v_0 , causes it to shift slightly to the right. Indeed, the final shift in the particle's position, $\Delta(\infty) = \lim_{t \rightarrow \infty} \Delta(t)$, attains a positive maximum at $u \simeq v_0$ and tends to large negative values for $u \rightarrow 0$, see Fig. 3.2b. As will be detailed in Ch. 3.4, $\Delta(\infty)$ actually diverges in this limit if translational noise is neglected, $D_0 = 0$.

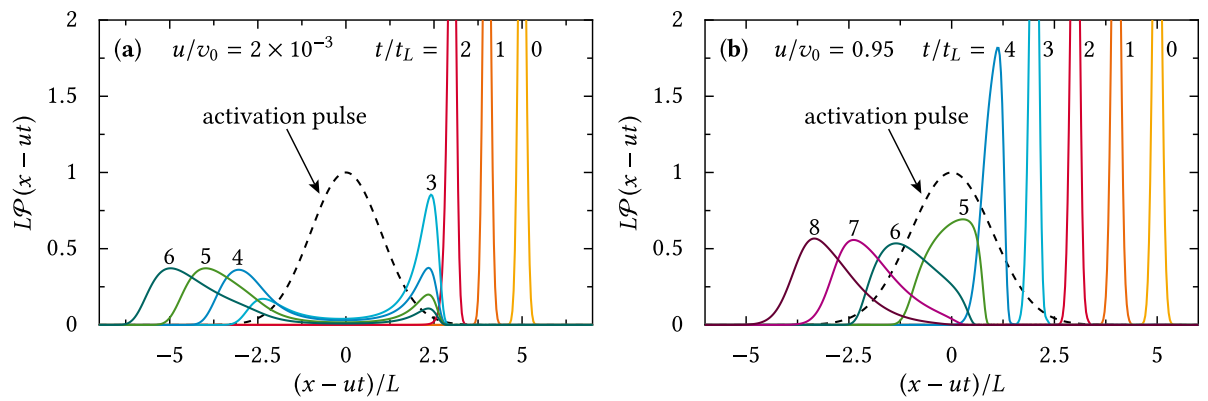


FIGURE 3.3. Probability distribution \mathcal{P} of an artificial microswimmer's position within the Gaussian activation pulse of Fig. 3.2 for various times t , assuming a rather (a) slow and (b) fast pulse propagation. The results were obtained by numerically solving the FPE (3.5) and subsequently integrating out the angular coordinate ϕ , see Ch. 3.4. Here, the model parameters were chosen as in Fig. 3.2: $x_0 = 5L$, $v_0 = 53 \mu\text{m/s}$, $D_\phi = 165 \text{ s}^{-1}$, $L = 1 \mu\text{m}$, and $D_0 = 0$. Note that for reasons of clarity and comprehensibility, in this figure we switched from the resting laboratory frame to the co-moving frame of the wave pulse, $x - ut$, where the swimmer is driven with velocity $-u$ across a static activation profile.

The existence of two opposing tactic regimes can be explained by considering the modulation of the swimmer's dynamics under the pulse crest. Assuming no translational fluctuations, $D_0 = 0$, the swimmer can only diffuse within the pulse and comes to rest outside of it. For slow pulses, $u \ll v_0$, the particle propels very fast (compared to the pulse speed) in the pulse center and thus quickly hits either of the pulse's edges, defined as the points where its self-propulsion eventually becomes slower than the pulse propagation, i.e., where $v_0 w[x(t), t]$ equals u [see Eq. (2.50)]. This is in accordance with the probability distributions of Fig. 3.3a, where the swimmer is rather unlikely to be found in the center of the pulse, corresponding to a typical

depletion of the “hot” regions. Due to the pulse’s movement to the right, however, the pulse symmetry is dynamically broken and the two edges are not equivalent: If the swimmer crosses the right edge, it becomes slower than u and is recaptured by the traveling pulse. By the same argument, once it crosses the left edge of the pulse, it is left behind for good. The right (left) edge thus behaves like a reflecting (absorbing) boundary, which allows the particle to exit the pulse on the left only, hence inducing a negative tactic shift. This mechanism can also be observed in Fig. 3.3a, where the probability distribution of the swimmer’s position piles up at the left pulse edge. For pulse speeds approaching v_0 , on the other hand, a contrasting effect comes into play, namely that within the pulse, the particle can travel a longer distance to the right than to the left. This “surfing” behavior is apparent in Fig. 3.3b, where under the pulse ($t/t_L = 5$), the probability distribution of the swimmer’s position is clearly skewed to the right. The positive shift is obviously most pronounced around $u \simeq v_0$, where the distance a highly activated swimmer can travel to the right without hitting a pulse edge is solely limited by its rotational diffusivity, D_ϕ . Accordingly, $\Delta(\infty)$ turns positive if u becomes comparable to v_0 and vanishes monotonically in the limit $u \rightarrow \infty$, where the pulse sweeps through the swimmer so fast that it has no time to surf it. In principle, the above arguments hold also for $D_0 \neq 0$: as will be discussed in Ch. 3.4, translational noise—which helps exit and enter the pulse from both sides—tends indeed to suppress the swimmer’s tactic shift, especially for slow values of u , though not completely.

Influence of the pulse width. The effect of the pulse width L on the swimmer’s tactic shift is illustrated in Fig. 3.4, where $\Delta(\infty)$ is shown to vanish for very narrow pulses if $u \geq v_0$. On the contrary, for $u < v_0$, the tactic shift apparently tends to a (positive) residual value in the limit $L \rightarrow 0$, see Fig. 3.4a. Related to this, the separatrix dividing the regions of negative and positive taxis appears to bend downward for small pulse widths, $L < l_\phi$.

We explain these observations by recalling that in the regime of negative taxis, the shift $\Delta(\infty) < 0$ is caused by a fast diffusion of the swimmer across the pulse; hence, a smaller pulse width implies a smaller negative tactic shift, as well. For small values of L/l_ϕ , the swimmer’s negative taxis is therefore strongly suppressed, to the point that another positive tactic effect starts to prevail, namely the trapping of swimmers inside traveling activation pulses with $u < v_0$. Still neglecting for the time being the finite particle size and switching to the co-moving pulse frame, $x - ut \rightarrow x$, the particle is trapped therein when $v_0 w(x) \cos \phi = u$. More precisely, for every fixed but arbitrary particle orientation with $\phi \in [-\arccos(u/v_0), \arccos(u/v_0)]$, there exists a stable trapped (or, in the laboratory frame, surfing) position x_p in the front of the pulse, such that $v_0 w(x_p) \cos \phi = u$, see Fig. 3.5. The other position in the back of the pulse, that also fulfills the above equation, is not stable. If now the swimmer is in such a trapped state in the

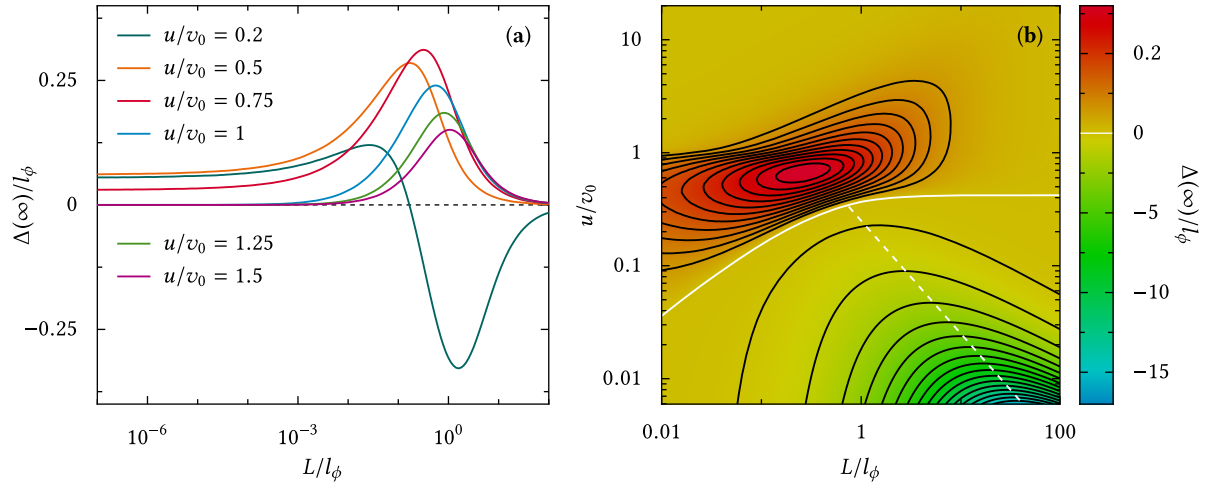


FIGURE 3.4. Influence of the pulse width L on the swimmer's taxis. **(a)** Tactic shift $\Delta(\infty)$ as a function of L (both in units of the particle's persistence length l_ϕ) for various values of u/v_0 . The curves were obtained from the stochastic integration of the LE (2.50), where the waveform and all other model parameters are the same as in Figs. 3.2 and 3.3. **(b)** $\Delta(\infty)$ versus u and L , for the same parameters as in panel (a). The solid white line denotes the contour with $\Delta(\infty) = 0$, i.e., the separatrix between the regions of negative and positive taxis, and the dashed white line depicts the analytical estimate for the position of the maximum negative shift, $L/l_\phi = v_0/(4u)$ (see the text). In the region with $L/l_\phi < 1$, the numerical data were obtained by integrating the LE (2.50), whereas for $L/l_\phi \geq 1$, we numerically solved the FPE (3.5).

pulse front, its orientation angle ϕ may fluctuate in the allowed interval without it being able to exit the pulse. That is, if ϕ changes to ϕ^* (where also $\phi^* \in [-\arccos(u/v_0), \arccos(u/v_0)]$), the swimmer immediately takes a new position x_p^* , so that $v_0 w(x_p^*) \cos \phi^* = u$. Thus, for $u < v_0$ and $L \ll l_\phi$, the duration of the particle's sojourn in the pulse and thereby the magnitude of its (positive) tactic shift are solely governed by D_ϕ , and in particular independent of the pulse width². For $u > v_0$, however, the above argument does not apply, as the pulse is always faster than the swimmer and therefore no trapped states exist. In this case, the swimmer spends indeed a longer time within the pulse when oriented parallel to the pulse propagation than when oriented opposite to it, but the magnitude of the resulting tactic shift constantly decreases when L is reduced. Thus, in the limit $L \rightarrow 0$, the shift $\Delta(\infty)$ vanishes for fast pulses, $u \geq v_0$, whereas it attains a positive residual value in the case of a slow pulse propagation,

²Of course, under realistic experimental conditions, the residual tactic shift would be offset by the inevitable translational fluctuations with $D_0 > 0$, which strongly suppress the trapping mechanism for narrow pulses.

$u < v_0$.

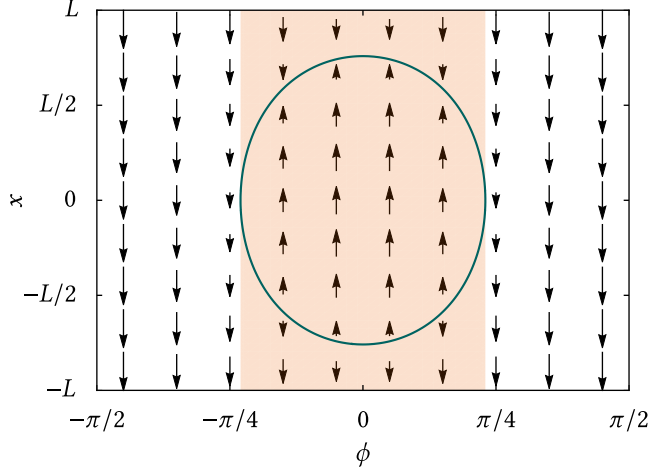


FIGURE 3.5. Trapping of an artificial microswimmer inside a traveling activation pulse for $u/v_0 = 0.75$. The arrows represent the vector field $(\dot{\phi}, \dot{x}) = (0, v_0 \exp[-x^2/(2L^2)] \cos \phi - u)$ describing the deterministic ($D_0 = D_\phi = 0$) longitudinal swimmer dynamics of Eq. (2.50). Note that here we have switched to the co-moving frame of the pulse, $x - ut \rightarrow x$. The green line denotes the x nullcline. It is obtained as the locus of all fixed points of the system, which are stable (unstable) for $x > 0$ ($x < 0$). Consequently, a swimmer entering the pulse from the right gets trapped if its orientation angle ϕ —here considered to be fixed—lies within the interval $[-\arccos(u/v_0), \arccos(u/v_0)]$, as illustrated by the orange region.

Finally, the apparent suppression of $\Delta(\infty)$ for large values of L is due to the fact that for wide pulses, the swimmer’s dynamics becomes more and more dominated by a pure bulk diffusion (where no average position shift occurs). That is, the influence of the traveling pulse edges—which are ultimately responsible for any tactic effect—gradually decreases as $L \rightarrow \infty$, because the swimmer spends relatively less and less time in their vicinity. Since in the regime of negative taxis, the magnitude of $\Delta(\infty)$ initially rises with increasing L (as long as the “bulk suppression” does not set in, a larger pulse width causes a larger tactic shift), for every chosen u an optimal pulse width exists, where the negative particle displacement is maximal. Consistently with this interpretation, we expect the “bulk suppression” to emerge when the timescale on which the swimmer diffuses across the pulse, $2L^2/D_s$ (the ad hoc factor 2 accounts for the spatial modulation of the swimmer’s self-propulsion speed under the pulse), becomes larger than the pulse crossing time L/u , namely when $L/l_\phi > v_0/(4u)$. The optimal pulse width estimated by this simple argument compares well with the numerical results in

Fig. 3.4b for small values of u/v_0 .

3.3 Variable Pulse Shape

Having studied the tactic response of an artificial microswimmer to a traveling activation pulse of Gaussian shape, we next address the question whether and, if so, how the swimmer's tactic shift depends on the actual pulse shape. To this purpose, we consider the waveform

$$w(x) = \frac{\arctan[K \operatorname{sech}(x/d)]}{\arctan(K)}, \quad (3.2)$$

which is inspired by the double soliton solutions of the sine-Gordon equation [253] and the profile of which can be conveniently tuned by varying the parameter K . As can be seen from Fig. 3.6a, K affects the steepness of the pulse edges, with $w(x)$ approaching $\operatorname{sech}(x/d)$ for $K \rightarrow 0$ and a square waveform in the limit $K \rightarrow \infty$. Note that tuning K also changes the pulse's half-width; therefore, to maintain the pulse half-width constant, the parameter d has to be adjusted accordingly. In order to compare the tactic shift induced by the pulse specified in Eq. (3.2) with the results of Ch. 3.2, we must impose that the new soliton-like waveform has the same half-width as the original Gaussian pulse $w(x) = \exp[-x^2/(2L^2)]$, $2L\sqrt{2\ln(2)}$, which implies that

$$d = \frac{L\sqrt{2\ln(2)}}{\operatorname{arcosh}(K \cot[\arctan(K)/2])}. \quad (3.3)$$

In the regime of positive taxis, i.e., for $u \simeq v_0$, no noticeable impact of K on the swimmer's tactic shift was detected; according to our expectations, the surfing effect is thus rather insensitive to the specific waveform of the activating pulse. In the regime of negative taxis, on the contrary, a moderate influence of K was observed: as depicted in Figs. 3.6b and 3.7, a smoother pulse edge implies a larger tactic shift. We explain this effect by noticing that the diffusion of the swimmer in the middle of the pulse is very fast relative to the pulse crossing timescale t_L , which causes the overall tactic shift to emerge almost instantaneously when the swimmer is hit by a rectangular activation pulse. In this case, $\Delta(\infty)$ equals approximately the total pulse width. When the edges of the activating pulse smooth out upon lowering K , the effective pulse width defined by the relation $v_0 w(x) > u$ increases, and so does the particle's tactic shift. Note that, as under the pulse tails the swimmer slows down, the time required to approach the asymptotic tactic shift $\Delta(\infty)$ increases, too.

Nevertheless, even for the very different waveforms associated with the cases $K = 1$ and $K \rightarrow \infty$ in Eq. (3.2), the resulting tactic shifts are of the same order of magnitude. We thus conclude that the effect of the actual pulse shape on $\Delta(\infty)$ is not very significant for

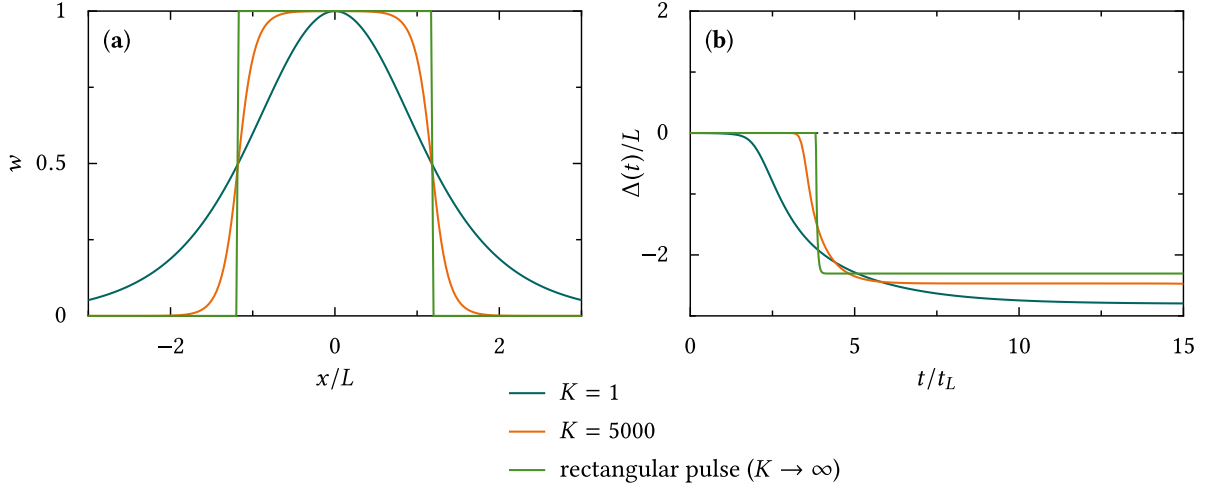


FIGURE 3.6. Tactic shift induced by a slow pulse of variable shape. **(a)** Waveform $w(x)$, as specified in Eqs. (3.2) and (3.3), for various values of the steepness parameter K . **(b)** Time evolution of the swimmer's tactic shift for the same values of K as in panel **(a)**. Again, x_0 was chosen to be located at a distance of $5L$ to the right of the pulse center. The curves for $K = 1$ and $K = 5000$ were obtained by numerically solving the FPE (3.5), whereas the tactic shift induced by a square waveform was calculated from the stochastic integration of the LE (2.50). The remaining model parameters were set to $u = 0.1 \mu\text{m/s}$, $v_0 = 53 \mu\text{m/s}$, $D_\phi = 165 \text{ s}^{-1}$, $L = 1 \mu\text{m}$, and $D_0 = 0$.

moderately small values of u/v_0 . It is only for $u/v_0 \rightarrow 0$ that the profiles of the decaying pulse tails start playing a role, as will be shown in Ch. 3.4.

3.4 Analytical Approach

In the following, we study *analytically* the tactic shift of an artificial microswimmer subjected to traveling activation pulses. We assume that the spatio-temporal modulation of the swimmer's self-propulsion speed has the form of a generic traveling wave, $w(x, t) = w[(x - ut)/L]$, with static profile $w(x/L)$. Upon changing coordinates from the laboratory frame to the co-moving pulse frame, $x - ut \rightarrow x$, the FPE for the swimmer's probability density P associated with the stochastic processes in the LE (2.50) reads

$$\frac{\partial P(\mathbf{r}, \phi, t)}{\partial t} = \left\{ D_0 \Delta - \nabla \left[v_0 w \left(\frac{x}{L} \right) \mathbf{n} - \mathbf{u} \right] + D_\phi \frac{\partial^2}{\partial \phi^2} \right\} P(\mathbf{r}, \phi, t), \quad (3.4)$$

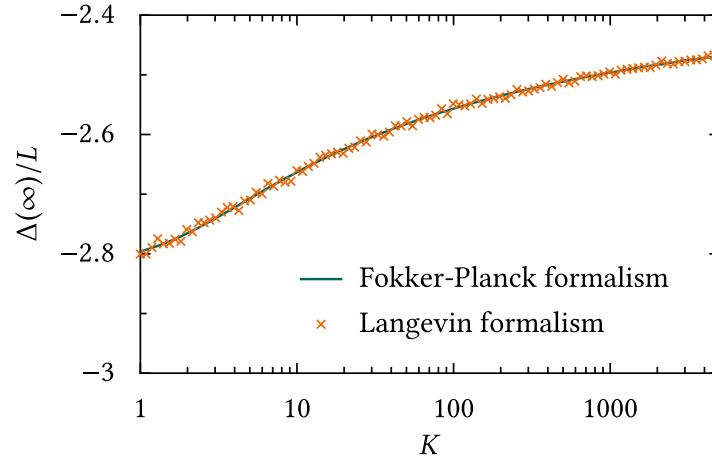


FIGURE 3.7. Influence of the pulse edge steepness on the swimmer's negative taxis. The asymptotic tactic shift $\Delta(\infty)$ is plotted as a function of K for $u = 0.1 \mu\text{m/s}$, $v_0 = 53 \mu\text{m/s}$, $D_\phi = 165 \text{s}^{-1}$, $L = 1 \mu\text{m}$, and $D_0 = 0$. Again, we compare the stochastic integration of the model LE (2.50) [crosses] with the numerical solution of the corresponding FPE (3.5) [solid curve].

where $\mathbf{r} = (x, y)^\top$, $\mathbf{u} = (u, 0)^\top$, $\mathbf{n} = (\cos \phi, \sin \phi)^\top$, and Δ and ∇ denote, respectively, the Laplace and the nabla operator in the Cartesian coordinates (x, y) . As already mentioned in Ch. 3.1, the swimmer's dynamics perpendicular to the incoming wave exhibits no tactic behavior, since the pulse does not break the spatial symmetry in the y direction. Therefore, by integrating over the y coordinate and conveniently rescaling x and t , $x =: Lx'$ and $t =: (L/v_0)t'$, we obtain a reduced FPE for the 2D marginal probability density $P(x', \phi, t')$,

$$\frac{\partial P(x', \phi, t')}{\partial t'} = \left[\frac{D_0}{Lv_0} \frac{\partial^2}{\partial x'^2} - \frac{\partial}{\partial x'} \left(w(x') \cos \phi - \frac{u}{v_0} \right) + \frac{D_\phi L}{v_0} \frac{\partial^2}{\partial \phi^2} \right] P(x', \phi, t'). \quad (3.5)$$

Here, the effective rotational diffusion constant $D_\phi L/v_0$ equals the ratio of the pulse width L to the swimmer's persistence length l_ϕ . The effective translational diffusion constant $D_0/(Lv_0)$, on the other hand, corresponds to the ratio of the time the swimmer takes to ballistically travel a pulse width L in a uniform activating medium, L/v_0 , to the time it takes to diffuse the same length subject to the sole translational noise, L^2/D_0 . This ratio characterizes the relative strength of the translational fluctuations and coincides with the reciprocal of the Péclet number for mass transport. We agree now to drop the prime signs, so that, unless stated otherwise, in the remainder of this work x and t denote the above dimensionless coordinates in the co-moving pulse frame.

3.4.1 Diffusive Regime

The activation pulse can be made wide and slow enough to regard the swimmer's motion inside it as purely diffusive. More precisely, this happens when the swimmer's rotational diffusion time, $\tau_\phi = D_\phi^{-1}$, is significantly smaller than the shortest ballistic pulse crossing time, $L/(v_0 + u)$, i.e., when $D_\phi L/v_0 \gg 1 + u/v_0$. Under this condition, we can further eliminate the orientational coordinate ϕ , so that the effects of self-propulsion merely amount to an effective one-dimensional diffusive dynamics. To this purpose, we apply to Eq. (3.5) the homogenization mapping procedure detailed in Refs. [254–257] and obtain a partial differential equation for the marginal probability density

$$\mathcal{P}(x, t) = \int_0^{2\pi} P(x, \phi, t) d\phi. \quad (3.6)$$

Following Ref. [258], we assume that the latter operation can be inverted by means of a “backward” operator $\hat{\psi}(x, \phi)$,

$$P(x, \phi, t) = \sum_{n=0}^{\infty} \epsilon^n \hat{\psi}_n(x, \phi) \frac{\mathcal{P}(x, t)}{2\pi}, \quad (3.7)$$

where $\hat{\psi}_0(x, \phi) = 1$ and $\epsilon := v_0/(D_\phi L)$. The expansion of $\hat{\psi}(x, \phi)$ in Eq. (3.7) is justified by the fact that for $\epsilon \rightarrow 0$ the swimmer rotates infinitely fast, in which case the self-propulsion can no longer contribute to its translational dynamics: the active particle behaves like a passive one, i.e., the rotational and translational dynamics decouple, and $P(x, \phi, t)$ simply becomes $\mathcal{P}(x, t)/(2\pi)$. Making use of Eqs. (3.6) and (3.7), respectively, in Eq. (3.5) and reordering all terms thus obtained according to their powers of ϵ [257, 258] yields a recurrence relation for the operators $\hat{\psi}_n$ acting upon the probability density $\mathcal{P}(x, t)$,

$$\begin{aligned} \partial_\phi^2 \hat{\psi}_{n+1}(x, \phi) &= \left[\hat{\psi}_n(x, \phi), \left(\frac{D_0}{Lv_0} \partial_x^2 + \frac{u}{v_0} \partial_x \right) \right] + \cos \phi \partial_x w(x) \hat{\psi}_n(x, \phi) \\ &\quad - \frac{1}{2\pi} \sum_{m=0}^n \hat{\psi}_{n-m}(x, \phi) \partial_x w(x) \int_0^{2\pi} \cos \phi \hat{\psi}_m(x, \phi) d\phi, \end{aligned} \quad (3.8)$$

where $\partial_x := \partial/\partial x$ and $[\dots, \dots]$ denotes the commutator of two operators. By using the aforementioned initial condition $\hat{\psi}_0(x, \phi) = 1$, the periodicity condition $\hat{\psi}_n(x, 0) = \hat{\psi}_n(x, 2\pi)$, and the normalization condition $\int_0^{2\pi} \hat{\psi}_n(x, \phi) d\phi = 2\pi \delta_{n,0}$, Eq. (3.8) can be solved iteratively, at least in principle, up to arbitrarily high orders. Yet, with increasing n this task becomes more and more laborious and the results for the $\hat{\psi}_n$ read increasingly complicated. In the

diffusive limit, however, the swimmer's rotational dynamics is significantly faster than its translational dynamics and $P(x, \phi, t)$ relaxes very fast in the ϕ direction, that is, it differs from $\mathcal{P}(x, t)/(2\pi)$ perturbatively, only. It thus suffices to collect the terms of Eq. (3.7) up to $\mathcal{O}(\epsilon)$, yielding

$$P(x, \phi, t) = \frac{1}{2\pi} \left[1 - \epsilon \cos \phi \frac{\partial}{\partial x} w(x) \right] \mathcal{P}(x, t). \quad (3.9)$$

Finally, upon inserting Eq. (3.9) into Eq. (3.5) and successively integrating with respect to ϕ , we obtain the reduced one-dimensional FPE

$$\begin{aligned} \frac{\partial \mathcal{P}(x, t)}{\partial t} &= \hat{\mathbb{F}}(x) \mathcal{P}(x, t) \\ &= \left[\frac{\partial^2}{\partial x^2} \left(\frac{v_0}{2D_\phi L} w^2(x) + \frac{D_0}{Lv_0} \right) - \frac{\partial}{\partial x} \left(\frac{v_0}{4D_\phi L} \frac{dw^2(x)}{dx} - \frac{u}{v_0} \right) \right] \mathcal{P}(x, t), \end{aligned} \quad (3.10)$$

which describes the probability density of the swimmer's longitudinal position in the diffusive regime. Here, $\hat{\mathbb{F}}(x)$ denotes the (reduced) Fokker-Planck operator, detailed in the second line.

Following Chs. 3.2 and 3.3, we consider the case of a single activating pulse hitting the swimmer and neglect translational fluctuations, $D_0 = 0$. The particle's tactic shift is then obtained by measuring its mean displacement from an initial position x_0 , placed outside the pulse, on the right. Accordingly, in the laboratory frame the tactic shift is computed as $\Delta(t) =: L \langle x(t) - x_0 + ut/v_0 \rangle$, where $\langle \dots \rangle$ denotes the ensemble average. Now, we can characterize the tactic shift in two ways: we either set a time t and calculate the corresponding average swimmer displacement in the pulse frame, $\langle x(t) \rangle$, hence

$$\Delta(t) = L \left(\langle x(t) \rangle - x_0 + \frac{u}{v_0} t \right), \quad (3.11)$$

or, vice versa, we set a longitudinal shift, $x_1 - x_0$, in the moving frame and calculate the corresponding mean first-passage time (MFPT) $\langle t(x_1|x_0) \rangle$, hence

$$\tilde{\Delta}(x_1) = L \left(x_1 - x_0 + \frac{u}{v_0} \langle t(x_1|x_0) \rangle \right). \quad (3.12)$$

We remind that $\langle t(x_1|x_0) \rangle$ denotes the average time the particle takes to reach x_1 for the first time from x_0 [259].

As long as $x_1 < x_0$, both methods are valid and equivalent, since in the co-moving frame the swimmer travels to the left and its mean position eventually takes on all values with $x < x_0$. For finite t and x_1 , though, we a priori do not know how to choose the values x_1 and t that verify the identity $\Delta(t) = \tilde{\Delta}(x_1)$. However, if we consider the full shift of the swimmer after it has completely crossed the pulse (i.e., for large enough t or for x_1 placed far enough

to the left of the pulse), both expressions yield the same result, that is, $\Delta(\infty) = \tilde{\Delta}(-\infty)$. This identity proves very helpful, since for the problem at hand, the MFPT can be calculated in a much simpler way than the average particle position. We remind that if the Fokker-Planck operator is time-independent, the MFPT is the solution of the ordinary differential equation $\hat{\mathbb{F}}^\dagger(x)\langle t(x_1|x) \rangle = -1$ [216, 260]. Here, $\hat{\mathbb{F}}^\dagger(x)$ is the adjoint Fokker-Planck operator acting upon the swimmer's starting position x , now taken as a variable, so that the differential equation for the MFPT reads explicitly:

$$-1 = \left[\frac{v_0}{2D_\phi L} w^2(x) \frac{\partial^2}{\partial x^2} + \left(\frac{v_0}{4D_\phi L} \frac{dw^2(x)}{dx} - \frac{u}{v_0} \right) \frac{\partial}{\partial x} \right] \langle t(x_1|x) \rangle. \quad (3.13)$$

Independent of the actual problem at hand, the MFPT obeys the obvious absorbing boundary condition $\langle t(x_1|x_1) \rangle = 0$. In our case, a second boundary condition follows naturally from the observation that outside of the pulse the swimmer's motion is deterministic. Namely, we know that $\dot{x} = -u/v_0$ at $x = x_0$, hence

$$\left. \frac{\partial \langle t(x_1|x) \rangle}{\partial x} \right|_{x=x_0} = \frac{v_0}{u}. \quad (3.14)$$

Note the absence of the minus sign in the above equation. This is due to fact that, since the swimmer starts at a position with $x > x_1$, to the right of the pulse, and crosses it to the left, increasing x causes likewise an increase in $\langle t(x_1|x) \rangle$. With the above boundary conditions, Eq. (3.13) returns a unique solution,

$$\langle t(x_1|x) \rangle = \int_{x_1}^x \left[\frac{v_0}{u} \exp\left(\int_y^{x_0} f(q) dq\right) + \int_y^{x_0} \frac{2}{\epsilon w^2(z)} \exp\left(\int_y^z f(q) dq\right) dz \right] dy, \quad (3.15)$$

where $\epsilon = v_0/(D_\phi L)$ and

$$f(q) := \left(\frac{\epsilon}{4} \frac{dw^2(q)}{dq} - \frac{u}{v_0} \right) \left(\frac{\epsilon}{2} w^2(q) \right)^{-1} = \frac{d \ln[w(q)]}{dq} - \frac{2u}{\epsilon v_0 w^2(q)}. \quad (3.16)$$

For a smoothly decaying pulse profile $w(x)$, the condition for the particle to sweep through the entire pulse requires taking the limits $x_0 \rightarrow \infty$ and $x_1 \rightarrow -\infty$. The tactic shift of a swimmer in the diffusive regime is thus given by the expression

$$\Delta(\infty) = L \lim_{\substack{x_1 \rightarrow -\infty \\ x_0 \rightarrow \infty}} \left\{ x_1 - x_0 + \frac{u}{v_0} \int_{x_1}^{x_0} \left[\frac{v_0}{u} \exp\left(\int_y^{x_0} f(q) dq\right) + \int_y^{x_0} \frac{2}{\epsilon w^2(z)} \exp\left(\int_y^z f(q) dq\right) dz \right] dy \right\}, \quad (3.17)$$

which contains two singularities that are supposed to cancel out. Some simple algebraic manipulations and a partial integration show that this is indeed the case and lead to the more compact result

$$\Delta(\infty) = L \int_{-\infty}^{\infty} \frac{1}{w(y)} \int_y^{\infty} \frac{dw(z)}{dz} \exp\left(-2 \frac{D_\phi L}{v_0} \frac{u}{v_0} \int_y^z \frac{1}{w^2(q)} dq\right) dz dy. \quad (3.18)$$

Note that this expression is independent of the boundary condition (3.14). Indeed, outside the pulse, i.e., when $w(x) = 0$, Eq. (3.13) reduces to a first-order differential equation and thus the boundary condition at $x = x_0$ becomes superfluous.

A comparison between the analytical prediction of Eq. (3.18) and results obtained by numerically integrating the FPE (3.5) is displayed in Fig. 3.8a. For the activating pulse, we chose the Gaussian profile of Ch. 3.2, which in rescaled units reads $w(x) = \exp(-x^2/2)$, and set a width of $L \sim 12l_\phi$.³ The analytical and numerical curves for $\Delta(\infty)$ versus u overlap in the regime of slow pulse speeds, $u \ll v_0$, thus confirming the validity of the diffusive approximation.

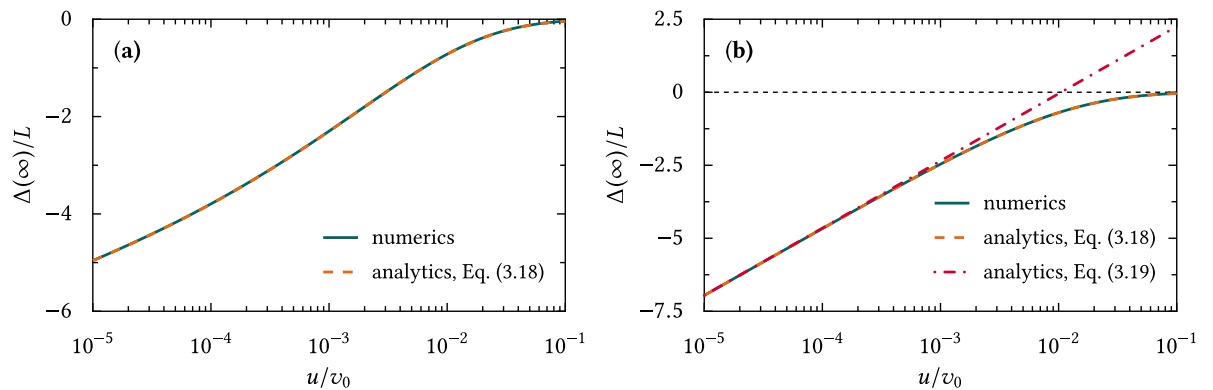


FIGURE 3.8. Tactic shift of an artificial microswimmer across a single traveling pulse of the form **(a)** $w(x) = \exp(-x^2/2)$ and **(b)** $w(x) = \text{sech}(x)$: $\Delta(\infty)$, in units of the pulse width L , versus u in units of the self-propulsion speed v_0 . The swimmer parameters are the same as in the previous figures, that is, $v_0 = 53 \mu\text{m/s}$, $D_\phi = 165 \text{ s}^{-1}$, and $D_0 = 0$. In panel **(a)**, $L = 4 \mu\text{m}$, i.e., about 12 times l_ϕ ; in panel **(b)**, L was set to $3.58 \mu\text{m}$, so that the two pulse profiles have the same half-width. The numerical results were obtained by integrating the FPE (3.5).

³We remark that due to the dimensionless scaling of x introduced at the beginning of this section, the pulse width L does not explicitly enter the waveform anymore, but instead is incorporated into the effective diffusion constants, see Eq. (3.5).

Moreover, for the soliton-like pulse profile $w(x) = \text{sech}(x)$, we succeeded to obtain an explicit analytical expression for $\Delta(\infty)$, namely (see Appendix C)

$$\Delta(\infty) = L \left[\frac{\pi}{2} + \gamma - \ln \left(\frac{v_0}{D_\phi L} \frac{v_0}{u} \right) \right], \quad (3.19)$$

where γ denotes the Euler-Mascheroni constant. As is apparent from Fig. 3.8b, here the agreement between the analytic approximation and numerical results is quite close, too. The range of validity of Eq. (3.19) however shrinks to lower values of u/v_0 compared to the general result of Eq. (3.18), which is due to the fact that in the derivation of Eq. (3.19) we repeatedly assumed a very slow pulse propagation, see Eq. (C.2).

The analytical estimate of $\Delta(\infty)$ in Eq. (3.19) lends itself to a simple heuristic interpretation. As mentioned in Ch. 3.2, in the diffusive regime, the effective pulse width x_u is defined by the identity $w(x_u) = u/v_0$. Since for $u \ll v_0$, the swimmer propels itself inside an almost static pulse until it exits for good to the left, its tactic shift must be of the order of x_u . For the soliton-like profile $w(x) = \text{sech}(x)$, this implies that

$$\Delta(\infty) \approx -L \ln \left(\frac{2v_0}{u} \right). \quad (3.20)$$

Of course, this argument cannot fully reproduce the more refined estimate of Eq. (3.19). Nevertheless, it explains why the swimmer's tactic shift diverges in the limit $u \rightarrow 0$: as the pulse nearly comes to rest, its effective width grows exceedingly large; in the diffusive regime, the effect of the pulse's fore-rear symmetry breaking is therefore steadily enhanced.

Analogously, for the slow Gaussian pulse of Figs. 3.2, 3.4b and 3.8a, the dependence of $\Delta(\infty)$ on u is expected to be of the form $\sqrt{2 \ln(v_0/u)}$, which is also in good agreement with our numerical and analytical curves. Here, the pulse tails decay faster than for the soliton-like pulse, thus leading to a smaller tactic shift in the limit $u \rightarrow 0$. Hence, contrary to the observation in Ch. 3.3 that the explicit pulse waveform plays a rather minor role for a moderately slow pulse propagation, in the case of extremely small ratios u/v_0 , the pulse shape is of key importance. This results from the fact that the swimmer's diffusion then mostly takes place in the outermost regions of the pulse's tails.

The influence of translational noise. We next consider the more realistic case of non-zero translational fluctuations, $D_0 > 0$. A very low translational noise level may be negligible in an appropriate range of pulse speeds. However, for $u \rightarrow 0$, the timescale on which the tactic shift approaches its asymptotic value, $\Delta(\infty)$, grows exceedingly long, which implies that at least in this regime, translational fluctuations cannot be ignored. To a good approximation, the translational noise intensity is independent of the spatio-temporal modulation of the swimmer's activation, see Eqs. (2.50). As a main difference with the case $D_0 = 0$, in the

presence of translational noise the pulse edges are “open”, as the swimmer can now cross them repeatedly back and forth. However, for sufficiently long observation times, the swimmer surely moves past the pulse, no matter how small u and large D_0 . Therefore, for $D_0 > 0$, we can calculate $\Delta(\infty)$ following the procedure already adopted for $D_0 = 0$. Even the (now *not* superfluous) boundary condition (3.14) remains unchanged, since at $x = x_0$, that is, outside the pulse, the particle’s longitudinal coordinate in the co-moving pulse frame obeys the simple relation $\langle \dot{x} \rangle = -u/v_0$ (instead of $\dot{x} = -u/v_0$, as was the case for $D_0 = 0$). We thus obtain

$$\Delta(\infty) = L \int_{-\infty}^{\infty} \int_y^{\infty} \frac{w(z)w'(z)}{\sqrt{[w^2(y) + \alpha][w^2(z) + \alpha]}} \exp\left(-2\frac{D_\phi L}{v_0} \frac{u}{v_0} \int_y^z \frac{1}{w^2(q) + \alpha} dq\right) dz dy, \quad (3.21)$$

where $\alpha := 2D_0D_\phi/v_0^2$ and the prime sign denotes the derivative with respect to the function’s argument. Obviously, in the limit $D_0 \rightarrow 0$, we recover Eq. (3.18).

In Fig. 3.9, the dependence of $\Delta(\infty)$ on the pulse speed u was determined both by computing the integrals in Eq. (3.21) and numerically solving Eq. (3.5). Again, the agreement between analytical and numerical results is quite close. We notice that in the presence of translational noise, the limit of $\Delta(\infty)$ for $u \rightarrow 0$ is finite. We attribute this property to the fact that translational diffusion, which tends to suppress the swimmer’s tactic rectification, prevails over self-propulsion, but only under the pulse’s tails. More precisely, the swimmer’s dynamics is dominated by translational diffusion when $D_0/(Lv_0) \gg v_0 w^2(x)/(2D_\phi L)$ [see Eq. (3.10)] or, respectively, $w^2(x) \ll \alpha$ [see Eq. (3.21)]. Under this condition, a natural definition of the effective pulse width is $\min\{x_u, x_t\}$, with x_t being the positive solution of the equation $w(x_t) \approx \sqrt{2D_0D_\phi/v_0^2}$. On decreasing u , the ratio x_u/x_t diverges, the effective pulse width coincides with x_t , and $\Delta(\infty)$ becomes a function of the sole parameter $\alpha = 2D_0D_\phi/v_0^2$.

3.4.2 Ballistic Regime

We focus now on the opposite dynamical regime, termed *ballistic*. Here, the traveling pulses are assumed to be so narrow and sweep through the swimmer so fast that the swimmer’s orientation hardly changes during the pulse crossing, i.e., the time a single activating pulse takes to pass the swimmer (which is of the order of $t_L = L/u$) is negligible with respect to the angular diffusion time τ_ϕ . In such a limit we take ϕ constant and rewrite the FPE (3.5) as

$$\frac{\partial P^\phi(x, t)}{\partial t} = \left[\frac{D_0}{Lv_0} \frac{\partial^2}{\partial x^2} - \frac{\partial}{\partial x} \left(w(x) \cos \phi - \frac{u}{v_0} \right) \right] P^\phi(x, t), \quad (3.22)$$

where $P^\phi(x, t)$ is the corresponding conditional probability density at fixed angle ϕ . In the following, we make use of Eq. (3.22) to calculate the conditional tactic shift, $\Delta^\phi(\infty)$. Since the

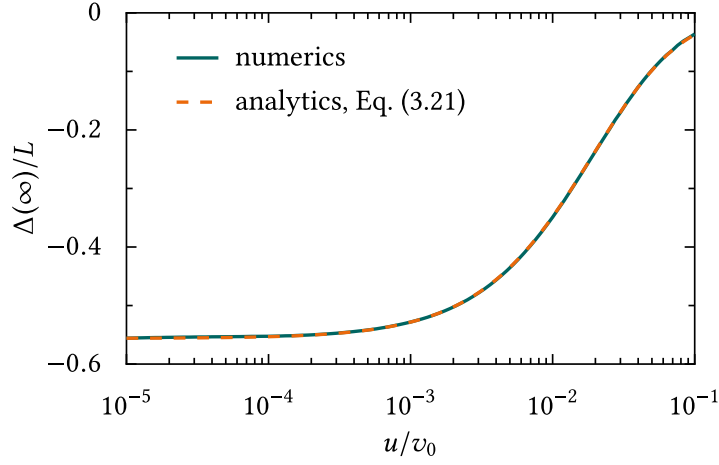


FIGURE 3.9. Tactic shift $\Delta(\infty)$ as in Fig. 3.8a, but in the presence of translational noise with intensity $D_0 = 2.2 \mu\text{m}^2/\text{s}$. The numerical results were obtained by solving the FPE (3.5).

angular coordinate is actually not fixed, but rather freely diffusing on an exceedingly long timescale (with respect to the timescale of a swimmer's pulse crossing), the overall tactic shift $\Delta(\infty)$ is eventually obtained by averaging $\Delta^\phi(\infty)$ with respect to ϕ , which is taken as uniformly distributed in the interval $[0, 2\pi]$.

Under these assumptions, the tactic shift of an artificial microswimmer hit by a single activating pulse can be calculated along similar lines as in Ch. 3.4.1. We obtain

$$\begin{aligned} \Delta(\infty) &= \frac{1}{2\pi} \int_0^{2\pi} \Delta^\phi(\infty) d\phi \\ &= \frac{L^2 v_0}{D_0} \int_{-\infty}^{\infty} \int_x^{\infty} w(y) \exp\left[-\frac{Lu}{D_0}(y-x)\right] I_1\left(\frac{Lv_0}{D_0} \int_x^y w(z) dz\right) dy dx, \end{aligned} \quad (3.23)$$

where $I_1(x) := (1/\pi) \int_0^\pi \exp(x \cos \phi) \cos \phi d\phi$ is a modified Bessel function of the first kind [187]. Although in the absence of translational fluctuations, $D_0 = 0$, the swimmer's fixed-angle dynamics is purely deterministic, we can still employ the MFPT technique to calculate $\Delta(\infty)$ for $D_0 = 0$, yielding

$$\Delta(\infty) = L \int_{-\infty}^{\infty} \left(\frac{1}{\sqrt{1 - (v_0^2/u^2) w^2(x)}} - 1 \right) dx, \quad (3.24)$$

which surely is well-defined in the ballistic regime with $u > v_0$. Here, the positive tactic shift must be exclusively attributed to the fact that swimmers oriented to the right, i.e., parallel

to the direction of the pulse propagation, “surf” the pulse for a longer time than swimmers oriented in the opposite direction.

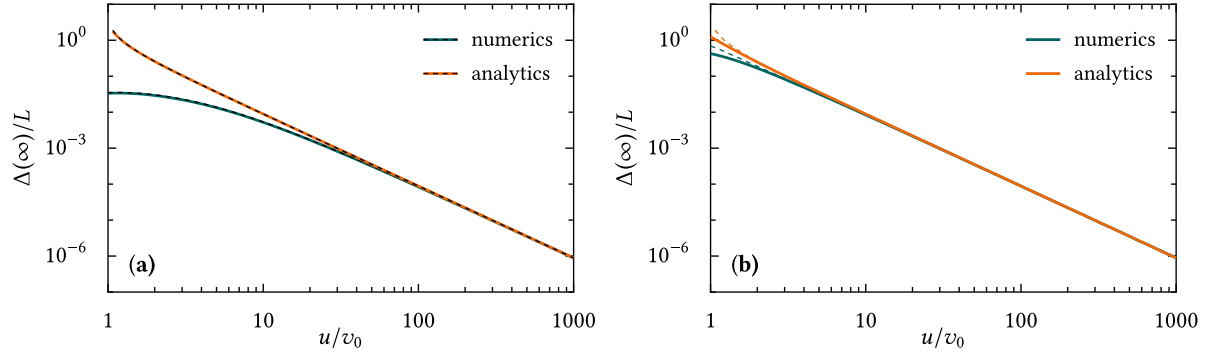


FIGURE 3.10. Tactic shift of an artificial microswimmer hit by a single Gaussian activation pulse, like in Figs. 3.8 and 3.9, but for larger values of the pulse speed u . The particle parameters are the same as in the previous figures; furthermore $L = 1 \mu\text{m}$ ($\sim 3l_\phi$) in panel (a) and $0.1 \mu\text{m}$ in panel (b). The numerical curves were obtained by solving the FPE (3.5) or integrating the LE (2.50), and the analytical ones were calculated in the ballistic approximation of Eqs. (3.23) or (3.24), as appropriate. For the sake of comparison, we plotted the curves for $D_0 = 2.2 \mu\text{m}^2/\text{s}$ (solid lines) together with the corresponding curves for $D_0 = 0$ (dashed lines).

On inspecting Fig. 3.10, we notice that the ballistic approximation holds good for fast activating pulses. One might expect it to work well only if the swimmer’s rotational diffusion time, τ_ϕ , is larger than the timescale on which a swimmer oriented to the right ($\phi = 0$) ballistically crosses the pulse, $L/(u - v_0)$. By analogy with Ch. 3.4.1, one would then end up with the condition $u/v_0 \gg 1 + L/l_\phi$. This argument however totally disregards the influence of translational fluctuations and thus only applies when $D_0/(Lv_0)$ can be safely neglected (see Fig. 3.10a). More in general, we must require that τ_ϕ is larger than the pulse crossing timescale in the ballistic regime, $L/(u - v_0)$, or the timescale of a pulse crossing due to the sole translational fluctuations, L^2/D_0 , whichever is smaller. This leads to the weaker condition for the validity of the ballistic approximation, $l_\phi/L \gg \min \left\{ (u/v_0 - 1)^{-1}, Lv_0/D_0 \right\}$.

By comparing the data for $D_0 = 0$ and $D_0 > 0$ in Fig. 3.10, we also observe that translational fluctuations only marginally affect the tactic response of a ballistic swimmer. Contrary to the diffusive regime, here the swimmer crosses the pulse quite fast, so that the translational noise has almost no time to act on it—provided the pulse is not too narrow, as in the limit $L \rightarrow 0$ the effective translational noise intensity $D_0/(Lv_0)$ diverges, see Eq. (3.5). The simple

expression of Eq. (3.24) can thus be safely employed to predict the tactic shift of a swimmer in the ballistic regime also in the presence of translational noise.

In summary, the tactic shift of an artificial microswimmer induced by a traveling activation pulse is a purely stochastic effect, resulting from the spatio-temporal modulation of its self-propulsion speed inside the pulse. Contrary to the case of a monotonic activation gradient, here the swimmer's taxis does not arise from a steady drift toward higher activation densities, as discussed in Ch. 3.1, but rather from the broken spatial symmetry associated with the pulse propagation.

ARTIFICIAL MICROSWIMMERS ACTIVATED BY A PERIODIC PULSE SEQUENCE

Having understood the basic mechanisms underlying an artificial microswimmer's tactic shift induced by a single traveling activation pulse, in the following we consider the effect of a periodic sequence of such pulses. In Ch. 4.1, we first investigate the swimmer's tactic response to a sinusoidal activation sequence and characterize the space of the system parameters. In Ch. 4.2, we then introduce an offset in the activation pulses and determine its impact on the swimmer's taxis. Finally, in Chs. 4.3 and 4.4 we study, respectively, the influence of an activation-dependent rotational diffusion coefficient and of particle chirality.

4.1 Sinusoidal Activation Profile

Let us initially consider a periodic pulse sequence of a simple sinusoidal form, $w(x) = \sin^2(\pi x)$, hitting the swimmer from the left¹. The resulting tactic response is then no longer characterized by a finite shift in the mean particle position, but rather by a steady-state tactic drift velocity, $v_x = \lim_{t \rightarrow \infty} v_0(\dot{x}) + u$, which is most conveniently obtained by calculating the swimmer's average velocity in the co-moving pulse frame and subsequently transforming it

¹We remind that here x and t are expressed in the dimensionless units introduced in Ch. 3.4 and $w(x)$ is defined in the co-moving frame of the wave pulses. Correspondingly, in the laboratory frame and unscaled units, the pulse sequence has the explicit representation $w(x, t) = \sin^2[\pi(x - ut)/L]$.

back to the laboratory frame. Again, we keep the particle parameters v_0 and D_ϕ fixed, and vary the pulse parameters L and u .

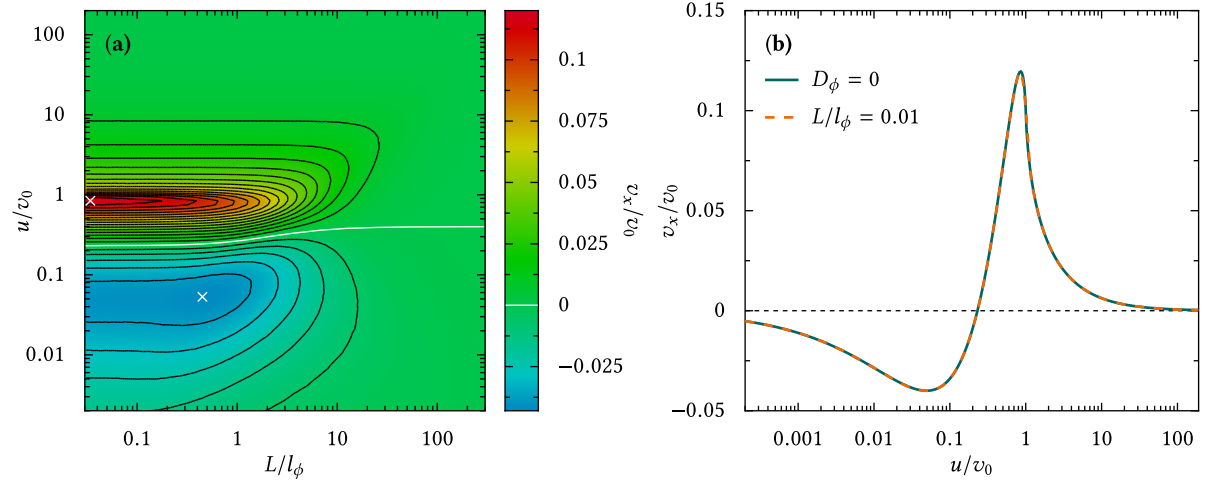


FIGURE 4.1. Tactic drift v_x of an artificial microswimmer induced by a sinusoidal activation sequence, $w(x) = \sin^2(\pi x)$. In panel (a), v_x is plotted as a function of the pulse width L and speed u , with the swimmer parameters being chosen as in the previous figures, $v_0 = 53 \mu\text{m/s}$, $D_\phi = 165 \text{ s}^{-1}$, and $D_0 = 0$. The position of the maximum positive drift and the maximum negative drift, respectively, is marked by white crosses and the white contour depicts the separatrix dividing the regions of positive and negative taxis. In panel (b), a cut of the contour plot of panel (a) in the u direction is shown for a very small pulse width, $L = 0.01l_\phi$. As discussed in the text, for small values of L/l_ϕ , the swimmer's tactic drift can be described within the purely deterministic framework with $D_0 = D_\phi = 0$ (green line). All results were obtained by numerically integrating the LE (2.50).

In the absence of translational noise, Fig. 4.1, we observe a behavior reminiscent of the case of a single activation pulse: v_x is negative for $u \ll v_0$ and turns positive as u approaches v_0 , exhibiting a pronounced maximum at $u \simeq v_0$. However, the ratio of the maximum positive to the maximum negative tactic speed appears to be inverted—for a single pulse, the negative shift at low values of u is markedly larger than the positive shift at $u \simeq v_0$. To this regard, we remind that in Fig. 4.1 we plotted the net tactic drift, i.e., the velocity defined as the average tactic shift divided by the relevant observation time. Since the large negative shift observed in Ch. 3—see e.g. Figs. 3.4b and 3.8—occurs over a long time (the time needed by the swimmer to fully cross the Gaussian pulse is proportional to L/u), we thus expect the tactic drift velocity in Fig. 4.1 to be less pronounced in the negative regime. Moreover, the

characteristic down-bending of the tactic separatrix for narrow single activation pulses, cf. Fig. 3.4, does not occur in the case of a periodic swimmer stimulation.

These general features can be qualitatively explained as follows. While the positive particle drift observed for $u \simeq v_0$ is induced by the same effect as already discussed in Ch. 3.2 (swimmers oriented to the right spend on average a longer time within the pulses than those oriented to the left), the fact that the separatrix does not bend downward is a unique feature of a periodic swimmer activation: For $u < v_0$, swimmers with $-\arccos(u/v_0) < \phi < \arccos(u/v_0)$ still get trapped within the pulses and thus drift to the right with speed u . However, now swimmers oriented to the left can cross not just one single pulse [which for $L \ll l_\phi$ leads to an extremely small negative tactic shift, causing $\Delta(\infty)$ in Fig. 3.4 to become positive for every choice of u] but an entire sequence of them, so that the vanishingly small single-pulse shifts may add up to a finite negative drift. As a consequence, if u is suitably smaller than v_0 , the trapped swimmers may happen to move considerably slower to the right than the swimmers with $|\phi| > \pi/2$ travel to the left, eventually causing the overall tactic drift to become negative.

Finally, looking at the left side of Fig. 4.1a and at Fig. 4.1b, we identify the swimmer's tactic drift to be a primarily deterministic effect, resulting from the distinct dynamics of swimmers oriented parallel and opposite to the pulse propagation direction (see Ch. 3.2). To this regard we remind that, as is apparent from Eq. (3.5), the natural units of D_0 and D_ϕ are, respectively, v_0L and v_0/L . This implies that upon decreasing the pulse width L , the effect of the translational noise increases, whereas the effect of the rotational noise is suppressed. Therefore, if $D_0 = 0$, the particle's dynamics in the limit $L \rightarrow 0$ equals the deterministic dynamics with $D_\phi = 0$.

4.1.1 Ballistic Regime

In order to quantitatively support the above arguments, in the following we analytically study the swimmer's tactic drift in the ballistic regime. To this purpose, we initially neglect both translational and angular fluctuations, $D_0 = D_\phi = 0$. The longitudinal LE (2.50) then simplifies to a purely deterministic fixed-angle equation of motion, $\dot{x} = w(x) \cos \phi - u/v_0$. For a sinusoidal pulse sequence, $w(x) = \sin^2(\pi x)$, this equation can be solved analytically, yielding

$$x(t) = \begin{cases} -\frac{1}{\pi} \arctan \left[\frac{\tan\left(\frac{\pi t u / v_0 \sqrt{1-(v_0/u) \cos \phi}}{\sqrt{1-(v_0/u) \cos \phi}}\right)}{\sqrt{1-(v_0/u) \cos \phi}} \right] & : t \leq \frac{v_0}{2u \sqrt{1-(v_0/u) \cos \phi}} \\ -\frac{1}{\pi} \arctan \left[\frac{\tan\left(\frac{\pi t u / v_0 \sqrt{1-(v_0/u) \cos \phi}}{\sqrt{1-(v_0/u) \cos \phi}}\right)}{\sqrt{1-(v_0/u) \cos \phi}} \right] - 1 & : t > \frac{v_0}{2u \sqrt{1-(v_0/u) \cos \phi}}, \end{cases} \quad (4.1)$$

with x being restricted to the interval $[-1, 0]$, $u > v_0$, and the initial condition $x_0 = 0$. The ballistic pulse crossing time t_c^ϕ for a fixed orientation angle, defined by the relation $x(t_c^\phi) = -1$, thus reads $t_c^\phi = v_0 / (u \sqrt{1 - (v_0/u) \cos \phi})$. Now, the swimmer's conditional tactic drift v_x^ϕ can be calculated by transforming the dimensionless particle drift in the co-moving frame, $-1/t_c^\phi$, back to the dimensional coordinates in the laboratory frame, i.e., $v_x^\phi = -v_0/t_c^\phi + u$. The net particle drift is then obtained by averaging v_x^ϕ with respect to ϕ , which is again assumed to be uniformly distributed in the interval $[0, 2\pi]$. However, if u grows smaller than v_0 , one has to take into account the already mentioned trapping of swimmers with $-\arccos(u/v_0) < \phi < \arccos(u/v_0)$. Since in the co-moving pulse frame, the velocity of trapped swimmers is zero, the ϕ -averaged drift velocity eventually turns out to be

$$v_x = \begin{cases} -u \left(\frac{1}{2\pi} \int_0^{2\pi} \sqrt{1 - \frac{v_0}{u} \cos \phi} d\phi - 1 \right) & : \frac{u}{v_0} \geq 1 \\ -u \left(\frac{1}{2\pi} \int_{\arccos(u/v_0)}^{2\pi - \arccos(u/v_0)} \sqrt{1 - \frac{v_0}{u} \cos \phi} d\phi - 1 \right) & : \frac{u}{v_0} < 1. \end{cases} \quad (4.2)$$

It is interesting to remark that we can now refine the validity criterion for the ballistic approximation discussed in Ch. 3.4.2, owing to the more precise estimate of the ballistic pulse crossing time derived above. Following the relevant argument of Ch. 3.4.2, we thus expect the ballistic approximation to hold for $l_\phi/L > \min \{t_c^{\phi=0}, Lv_0/D_0\}$. Furthermore, since for $u < v_0$, a swimmer with $\phi = 0$ is in a “locked” state inside a pulse, i.e., $t_c^{\phi=0} = \infty$, the ballistic approach should also approximately hold in the regime of $u/v_0 < 1$ and $l_\phi/L > \min \{t_c^{\phi=\pi}, Lv_0/D_0\}$.

A comparison between exact numerics and the ballistic approximation is illustrated in Fig. 4.2. As expected, its range of validity in the parameter u shrinks on increasing L/l_ϕ , and the refined validity condition just introduced provides an estimate of that range. The above approach is thus confirmed to accurately predict the swimmer's tactic response to a periodic sequence of rather narrow activating pulses. The ballistic approximation even appears to yield correct results at the very left of Fig. 4.2a, where the validity criterion does not apply. Furthermore, like in Fig. 4.2b, the sign inversion of v_x from positive to negative values upon decreasing the pulse speed u can clearly be detected. As a rough estimate and in line with the previous considerations, in the ballistic regime we expect the swimmer's tactic drift v_x to become negative once the drift velocity of a particle with $\phi = \pi$, $-u(\sqrt{1 + v_0/u} - 1)$, attains a larger absolute value than the drift velocity of a trapped particle, u . This argument predicts the sign inversion of v_x to occur when $u/v_0 \simeq 1/3$, which is in good agreement with the analytical and numerical curves of Figs. 4.1 and 4.2.

Moreover, we can extract the asymptotic behavior of v_x for a very slow and a very fast pulse propagation from Eq. (4.2). In the limit $u \rightarrow 0$ we obtain $v_x/v_0 \propto -\sqrt{u/v_0}$, whereas for

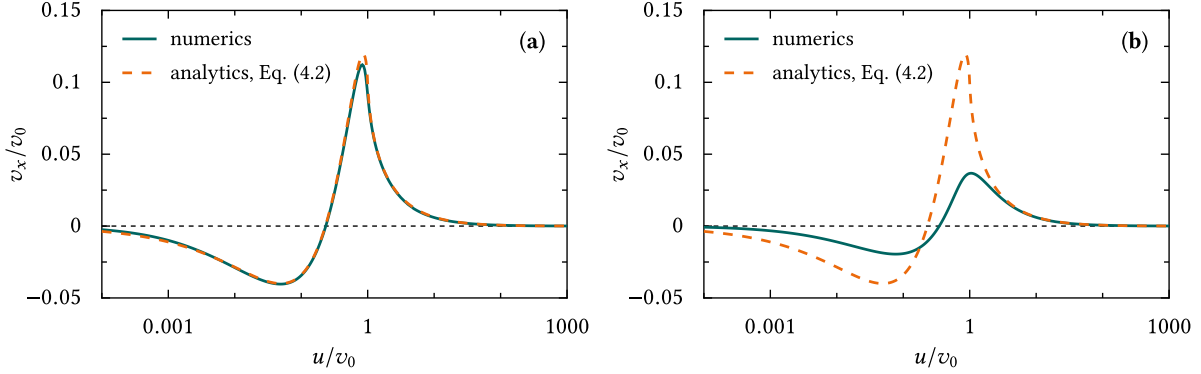


FIGURE 4.2. Tactic drift of an artificial microswimmer induced by the sinusoidal pulse sequence of Fig. 4.1: v_x versus u in units of v_0 . In panel (a), we chose a rather small pulse periodicity, $L = 0.2l_\phi$, whereas in panel (b), L was set to $5l_\phi$. The swimmer parameters v_0 and D_ϕ have the same values as in the previous figures and we set $D_0 = 0$. The numerical curves were again obtained by numerically integrating the LE (2.50) or solving the FPE (3.5).

$u \rightarrow \infty$ we find $v_x/v_0 \propto v_0/u$. We anticipate that the power law fits reported in Fig. 4.8a seem to confirm our predictions.

We extend now our approach to incorporate the translational fluctuations with $D_0 > 0$. To this purpose, we revert to the fixed-angle FPE (3.22) and consider a general periodic sequence of activating pulses, $w(x+n) = w(x) \forall n \in \mathbb{Z}$, with unit period². In order to calculate the resulting longitudinal drift velocity, $v_x = v_0/(2\pi) \int_0^{2\pi} \lim_{t \rightarrow \infty} \langle \dot{x}(\phi) \rangle d\phi + u$ from Eq. (3.22), we introduce the reduced conditional one-zone probability

$$\tilde{P}^\phi(x, t) = \sum_{n=-\infty}^{\infty} P^\phi(x+n, t), \quad (4.3)$$

which maps the overall conditional probability density $P^\phi(x, t)$ onto one period of the pulse sequence [261, 262]. That is, instead of considering the time-evolution of the swimmer probability density along an infinite periodic pulse sequence, we focus on a single wave period and impose periodic boundary conditions to ensure the existence of a stationary state. Accordingly, we define the corresponding reduced conditional probability current, $\tilde{J}^\phi(x, t)$, and write down the continuity equation

$$\frac{\partial \tilde{P}^\phi(x, t)}{\partial t} = -\frac{\partial \tilde{J}^\phi(x, t)}{\partial x}. \quad (4.4)$$

²We remind that a spatial period of one in the dimensionless units introduced in Ch. 3.4 corresponds to a period of L in the unscaled notation.

Upon introducing the auxiliary function $h(x) := (Lv_0/D_0)[w(x) \cos \phi - u/v_0]$, the implicit solution for $\tilde{J}^\phi(x, t)$ reads

$$\tilde{J}^\phi(x, t) = -\frac{D_0}{Lv_0} \exp\left(\int_0^x h(y) dy\right) \frac{\partial}{\partial x} \exp\left(-\int_0^x h(y) dy\right) \tilde{P}^\phi(x, t), \quad (4.5)$$

which in the stationary limit, $t \rightarrow \infty$, tends to a constant that can be explicitly calculated [262],

$$\tilde{J}_{\text{st}}^\phi := \lim_{t \rightarrow \infty} \tilde{J}^\phi(x, t) = \frac{D_0}{Lv_0} \left[1 - \exp\left(-\int_0^1 h(x) dx\right) \right] \left[\int_0^1 \int_x^{x+1} \exp\left(-\int_x^y h(z) dz\right) dy dx \right]^{-1}. \quad (4.6)$$

Finally, on transforming back to the laboratory frame and averaging with respect to ϕ , we obtain the swimmer's tactic drift velocity,

$$\begin{aligned} v_x &= \frac{v_0}{2\pi} \int_0^{2\pi} \int_0^1 \tilde{J}_{\text{st}}^\phi dx d\phi + u = \frac{v_0}{2\pi} \int_0^{2\pi} \tilde{J}_{\text{st}}^\phi d\phi + u \\ &= \frac{D_0}{2\pi L} \int_0^{2\pi} \left\{ 1 - \exp\left[\frac{Lv_0}{D_0} \left(\frac{u}{v_0} - \cos \phi \int_0^1 w(x) dx\right)\right] \right\} \\ &\quad \times \left\{ \int_0^1 \int_0^1 \exp\left[\frac{Lv_0}{D_0} \left(\frac{u}{v_0} y - \cos \phi \int_x^{x+y} w(z) dz\right)\right] dy dx \right\}^{-1} d\phi + u. \end{aligned} \quad (4.7)$$

In Fig. 4.3, the tactic drift obtained by means of Eq. (4.7) is compared with exact numerical results. A good agreement is observed again for small values of L/l_ϕ ; in fact, the ballistic approximation holds for about the same parameter range as in the case $D_0 = 0$. Furthermore, on comparing Figs. 4.3 and 4.2, translational fluctuations are revealed to suppress the swimmer's tactic drift overall, though their impact is more pronounced for small pulse widths. This is to be expected, since we know that the natural unit of D_0 is v_0L . Moreover, we also notice that translational noise has a stronger impact at slow pulse speeds, so that the negative tactic drift occurring for $u \ll v_0$ is totally quenched for small pulse widths. We explain this effect by reminding that a slow pulse propagation implies a long pulse crossing time, which enhances the influence of the translational noise. In particular, the trapping of swimmers inside slow pulses is suppressed, as translational fluctuations quickly “free” them from a trapped state. Since this way the mechanism accounting for the negative tactic drift in the ballistic regime—swimmers oriented to the right get trapped and move slower to the right than swimmers

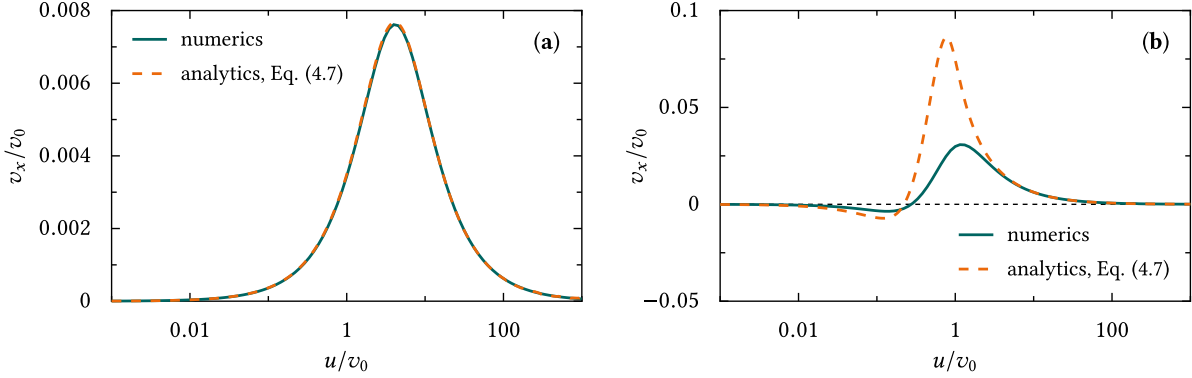


FIGURE 4.3. Influence of the translational noise intensity D_0 on the swimmer's tactic drift in the ballistic regime. The plots are the same as in Fig. 4.2, with the only difference that here we set $D_0 = 2.2 \mu\text{m}^2/\text{s}$. The numerical curves were obtained by solving the FPE (3.5).

with opposite orientation move to the left—becomes ineffective, solely the positive surfing effect³ (though weak for $u \ll v_0$) remains at work and v_x turns overall positive.

As a further difference with the case $D_0 = 0$, the asymptotic behavior of v_x for a very slow pulse propagation becomes linear in u under the influence of translational fluctuations. Indeed, by expanding the result in Eq. (4.7) in powers of u/v_0 , the tactic drift velocity is shown to behave like $v_x/v_0 \propto u/v_0$, with the sign of the proportionality factor turning from negative to positive upon raising $D_0/(Lv_0)$ above a certain threshold. This change of sign, which is displayed also in Fig. 4.8a, marks the onset of the regime where negative taxis is suppressed by translational noise and will be discussed in more detail in Ch. 4.1.3.

4.1.2 Diffusive Regime

On moving from the left to the right side of Fig. 4.1a, that is, for wider pulses, the influence of rotational noise becomes significant. As a consequence, upon increasing L , the swimmer eventually enters the diffusive regime inside the sweeping pulses. Figure 4.1a shows that the dependence of the swimmer's tactic drift on L and u in the diffusive regime is qualitatively the same as in the ballistic regime, i.e., v_x is negative (positive) for a slow (fast) pulse propagation. Like in the case of a single activation pulse, here the negative drift results from the fact that due to the pulses' movement to the right, the swimmers—which actively diffuse under

³As already discussed, swimmers spend a longer time inside a single pulse when moving in the direction of the pulse propagation than when moving in the opposite direction.

the pulse crests—are more likely to exit the pulses to the left. The positive drift, on the other hand, is again a consequence of the already discussed surfing effect. However, for exceedingly large values of L we again approach the bulk dynamics discussed in Ch. 3.2 and v_x is suppressed overall. Moreover, the separatrix dividing the regions of positive and negative taxis remains approximately a function of the pulse speed only, although shifted to slightly higher values of u . As a matter of fact, in the diffusive regime we can estimate the separatrix position by assuming that the dynamical effect of the angular fluctuations (which is eventually responsible for the negative tactic drift) gets suppressed with respect to the dragging action of the activation pulses after u growing larger than the average of the swimmer's self-propulsion speed, $v_0 \langle w(x) | \cos \phi | \rangle$ [cf. Eq. (3.5)]. Thus, the sign of v_x is predicted to turn from negative to positive at $u/v_0 \gtrsim 1/(2\sqrt{2})$, which, consistently with our numerics, is slightly larger than the corresponding value in the ballistic regime, $u/v_0 \gtrsim 1/3$.

In order to analytically substantiate the above arguments, we again consider the generic periodic waveform of Ch. 4.1.1, $w(x+n) = w(x) \forall n \in \mathbb{Z}$. The swimmer's tactic drift can then be calculated in the same way as in the ballistic approximation, this time starting from Eq. (3.10). We obtain

$$v_x = \frac{v_0^2}{2D_\phi L} \left[1 - \exp \left(2 \frac{D_\phi L}{v_0} \frac{u}{v_0} \int_0^1 \frac{1}{w^2(x) + \alpha} dx \right) \right] \times \left[\int_0^1 \int_0^1 \frac{1}{\sqrt{[w^2(x) + \alpha][w^2(x+y) + \alpha]}} \exp \left(2 \frac{D_\phi L}{v_0} \frac{u}{v_0} \int_x^{x+y} \frac{1}{w^2(z) + \alpha} dz \right) dy dx \right]^{-1} + u, \quad (4.8)$$

with $\alpha = 2D_0 D_\phi / v_0^2$, as was defined in Ch. 3.4.1.

Taking the limit $D_0 \rightarrow 0$ and assuming $w(0) = w(1) = 0$, as is the case for $w(x) = \sin^2(\pi x)$, Eq. (4.8) can be given the more convenient form

$$v_x = u \left[\int_0^1 \int_0^1 \frac{w'(x+y)}{w(x)} \exp \left(-2 \frac{D_\phi L}{v_0} \frac{u}{v_0} \int_{x+y}^{x+1} \frac{1}{w^2(z)} dz \right) dy dx - 1 \right]^{-1} + u, \quad (4.9)$$

where the prime sign denotes the derivative of a function with respect to its argument.

In Fig. 4.4 we compare the analytical approximations of Eqs. (4.8) and (4.9) with the exact values for v_x , computed by numerically integrating the FPE (3.5) or the LE (2.50). Once again, we notice the tactic drift to be directed opposite to the propagation direction of the activating pulse sequence if the pulses are slow and wide. Moreover, as expected, a close agreement between the numerical and analytical curves is achieved if the conditions of wide ($D_\phi L / v_0 \gg 1$) and slow ($u / v_0 \ll 1$) pulses are *simultaneously* fulfilled. Yet, in contrast to our

initial conjecture about the range of validity of the diffusive approximation at the beginning of Ch. 3.4.1, under the weaker condition $D_\phi L/v_0 \gg 1 + u/v_0$, the motion of an artificial microswimmer inside a traveling activation pulse may well be regarded as purely diffusive, but the corresponding diffusive approximation fails to correctly predict its tactic drift when $u \gtrsim v_0$ (see Figs. 4.4b and d). Thus, although the ballistic nature of the swimmer's dynamics is less prominent for wide pulses, $L \gg l_\phi$, it still cannot be neglected if $u \gtrsim v_0$, which suggests that the *positive* branches of the v_x curves are purely determined by these ballistic properties. This conclusion is supported by Figs. 4.4a and c, where for $L/l_\phi \lesssim 10$, the influence of D_0 is observed to gradually take over. However, in the diffusive approximation (dashed curves), the effect of the translational fluctuations is predicted to just prevent the drift from growing more negative, whereas in the full dynamics treatment (solid curves) the influence of D_0 causes v_x to change sign.

Considering the asymptotic behavior of v_x for $u \rightarrow 0$, as we already did in the ballistic regime, the swimmer's drift velocity can now be shown to decay proportional to u if $D_0 \neq 0$. However, in the diffusive regime, the corresponding proportionality factor is negative for every choice of L , as discussed above. Since an expansion of the expression in Eq. (4.9) around $u/v_0 = 0$ would take lengthy algebraic manipulations, we restrict ourselves to consider the asymptotic behavior of v_x for $D_0 = 0$ from a more intuitive point of view. To this purpose, we remind that in the absence of translational noise, the swimmer's tactic drift can be calculated from the relation

$$\frac{v_x}{v_0} = \frac{-1}{\langle t(0|1) \rangle} + \frac{u}{v_0}, \quad (4.10)$$

i.e., by dividing the dimensionless shift caused by a single activation pulse in the co-moving frame, -1 , by the corresponding observation time (which in this case is the MFPT $\langle t(0|1) \rangle$ from a starting point at $x = 1$ to an absorbing point at $x = 0$) and finally transforming back to the laboratory frame. This approach is legitimate, since for $D_0 = 0$, the swimmer surely enters every pulse from the right and exits it to the left. Making use of Eq. (3.12), we rewrite the above equation as

$$\frac{v_x}{v_0} = \frac{u}{v_0} \left(1 - \frac{1}{\Delta(\infty)/L + 1} \right), \quad (4.11)$$

where $\Delta(\infty)$ is the tactic shift induced by a single sinusoidal activation pulse, cf. Ch. 3. Following the derivation of Eq. (3.20), we now approximate $\Delta(\infty)$ for $u/v_0 \ll 1$, yielding $\Delta(\infty) \approx -L + (2L/\pi) \arcsin(\sqrt{u/v_0})$. Thus, in the limit $u/v_0 \rightarrow 0$, we obtain $v_x/v_0 \propto \sqrt{u/v_0}$ also in the diffusive regime, which is again in agreement with Fig. 4.8a.

Summarizing the results of Chs. 4.1.1 and 4.1.2, we conclude that the positive tactic drift is a purely ballistic effect, entirely due to the finite persistence of the swimmer's active Brownian

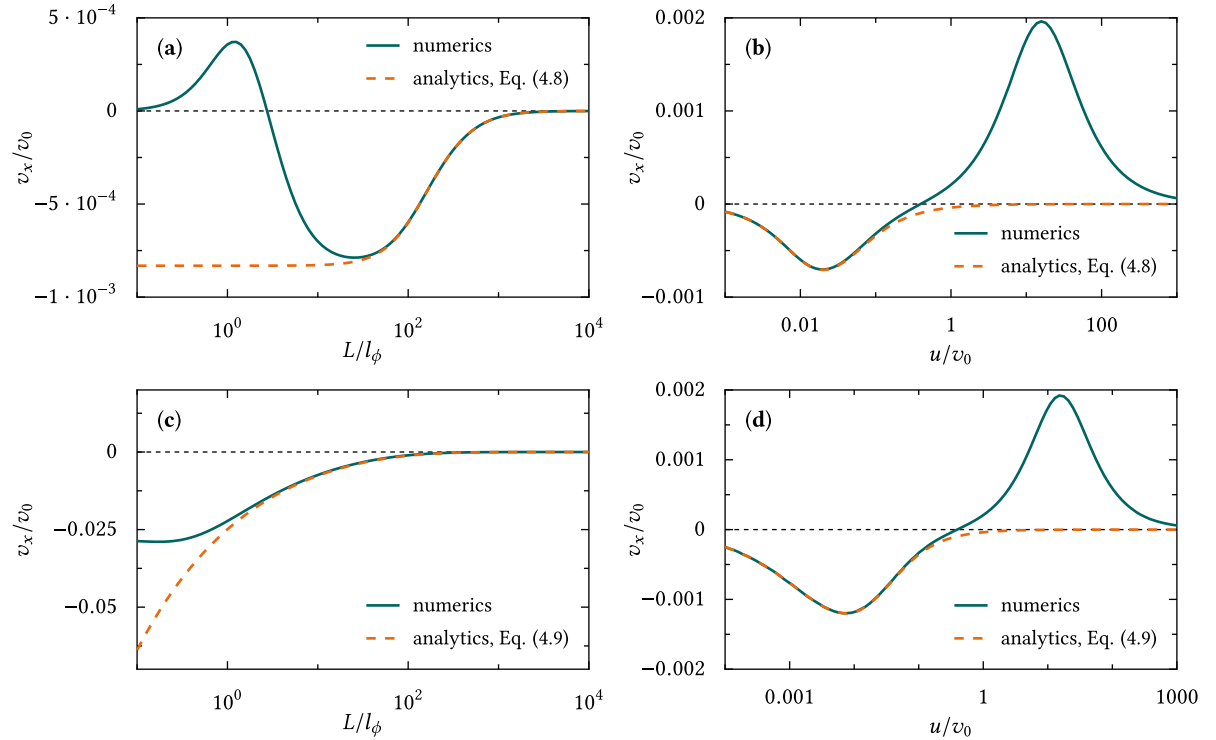


FIGURE 4.4. Tactic drift velocity of an artificial microswimmer in the diffusive regime, assuming the sinusoidal activation sequence of Fig. 4.1: v_x versus the pulse width L (a,c) and speed u (b,d). The swimmer parameters are the same as in the previous figures, $v_0 = 53 \mu\text{m/s}$ and $D_\phi = 165 \text{ s}^{-1}$; $D_0 = 2.2 \mu\text{m}^2/\text{s}$ in panels (a,b) and $D_0 = 0$ in panels (c,d). Furthermore, $u = 0.01v_0$ in panels (a,c) and $L = 100l_\phi$ in panels (b,d). The numerical data plotted here have been obtained by numerically integrating the LE (2.50) or, equivalently, the FPE (3.5).

motion, whereas the negative tactic drift results from the combination of the diffusive and ballistic properties of the swimmer's dynamics. In line with this argument, the position of the maximum negative value of v_x in Fig. 4.1a is located at lower values of u and higher values of L than the position of the maximum positive value. Moreover, contrary to Stokes' drift [97], v_x was shown to grow with a power of u clearly smaller than 2 for $u/v_0 \ll 1$, which can also be attributed to the ballistic nature of the swimmer's dynamics.

4.1.3 Influence of Translational Noise

As already discussed in the previous sections, translational fluctuations strongly suppress the swimmer's negative tactic drift in the bottom-left quadrant of Fig. 4.1a, to the point that

v_x eventually turns positive. Accordingly, in Fig. 4.5a (which is essentially the same plot as in Fig. 4.1a, but for a finite translational noise level), the separatrix dividing the regions of positive and negative taxis bends downward at a critical value of L . Moreover, as expected, the swimmer's tactic drift diminishes overall under the influence of translational fluctuations. In particular, negative taxis is suppressed more effectively than positive taxis, since for $D_0 \neq 0$, only the diffusive rectification effect at $L \gtrsim l_\phi$ can contribute to the swimmer's negative drift.

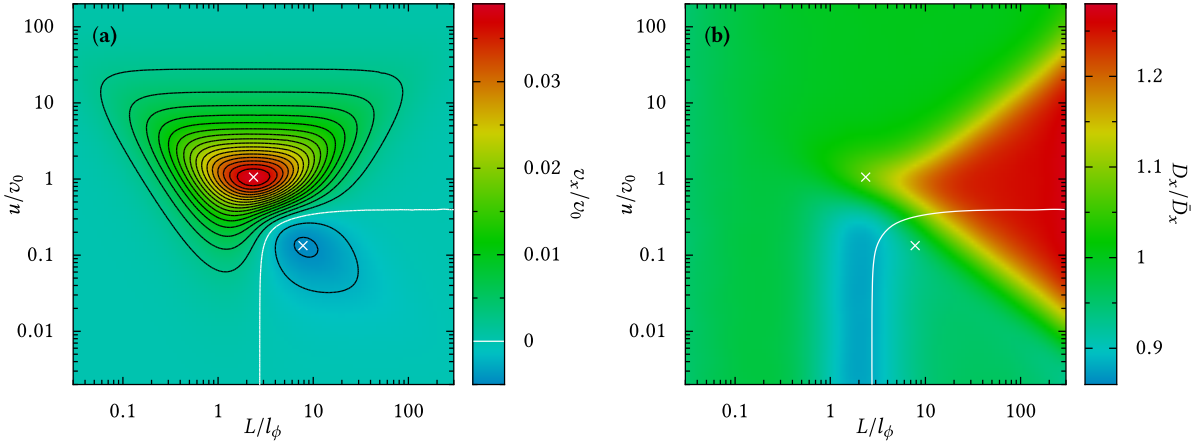


FIGURE 4.5. Influence of translational noise on the swimmer's tactic drift. **(a)** Same plot as in Fig. 4.1a, but for the finite translational noise intensity $D_0 = 2.2 \mu\text{m}^2/\text{s}$. **(b)** Contour plot of the spatial diffusion constant $D_x = \lim_{t \rightarrow \infty} [\langle x^2 \rangle - \langle x \rangle^2] / (2t)$ for the model parameters of panel **(a)**. The scaling factor \bar{D}_x is the swimmer's spatial diffusion constant in the average velocity field $v_0 \langle w(x) \rangle_x$, see the text. All data were obtained by numerically solving the FPE (3.5) **(a)** and integrating the LE (2.50) **(b)**.

As anticipated before, the influence of translational fluctuations increases as L is lowered (we remind that the natural unit of D_0 is v_0/L) and therefore the threshold value of L , below which negative taxis is suppressed, ought to be proportional to D_0/v_0 . Indeed, we observe that the vertical branch of the separatrix in Fig. 4.7a shifts linearly to the right upon increasing D_0 . Consistently with the sign change of the asymptotic behavior of v_x in the limit $u/v_0 \rightarrow 0$ for $D_0/(Lv_0)$ exceeding a certain threshold (see the end of Ch. 4.1.1), we thus postulate the existence of a critical value of $D_0/(Lv_0)$, $(D_0/Lv_0)_{\text{cr}}$, above which negative taxis is suppressed. In Chs. 4.1.1 and 4.1.2, the positive particle drift occurring in the bottom-left quadrant of Fig. 4.5a was related with the ballistic properties of the swimmer's active Brownian motion. Accordingly, $(D_0/Lv_0)_{\text{cr}}$ is expected to be a "ballistic quantity", as well, i.e., to be independent of D_ϕ . Numerical simulations (not shown here) confirm that the magnitude of $(D_0/Lv_0)_{\text{cr}}$ can

indeed be estimated by a very simple ballistic argument: we assume that the influence of translational noise prevails (and accordingly v_x turns positive) once the time required by a swimmer to travel a half pulse width due to the sole translational fluctuations, $(L/2)^2/(2D_0)$, becomes shorter than the time $2L/v_0$, which is required to cross a pulse ballistically with an average speed of $v_0/2$. This argument results in the rough estimate $(D_0/Lv_0)_{cr} \approx 0.06$, which is in good agreement with the numerical data of Fig. 4.5a.

The role of the tactic separatrix is further illustrated by the contour plot of Fig. 4.5b, where we plotted the swimmer's spatial diffusion constant $D_x := \lim_{t \rightarrow \infty} [\langle x^2 \rangle - \langle x \rangle^2]/(2t)$ for the model parameters of Fig. 4.5a. Note that the computed values of D_x are compared with the swimmer's spatial diffusion constant in the average velocity field $v_0 \langle w(x) \rangle_x = v_0/2$,⁴ which is given by $\bar{D}_x = D_0 + v_0^2/(8D_\phi)$. One can see immediately that $D_x/\bar{D}_x \approx 1$ almost everywhere in the (L, u) plane, except along the (hot) horizontal and (cold) vertical branches of the separatrix, where $D_x/\bar{D}_x > 1$ and $D_x/\bar{D}_x < 1$, respectively. Indeed, the sign change of the tactic drift observed upon increasing the pulse speed u corresponds to a locked-running transition in the ballistic particle dynamics [see Ch. 4.1.1 and in particular Eq. (4.2)], a mechanism known to produce excess diffusion [263–265]. The tactic sign inversion at the vertical separatrix branch, on the other hand, is governed by translational noise, which suppresses the trapped/locked swimmer states and strongly favors the pulse-crossing, i.e., running states. It thus acts there as a sort of lubricant, resulting in a slight suppression of the swimmer's spatial diffusivity. However, we remark that in any case, D_x is of the same order of magnitude as \bar{D}_x , implying that the tactic effects studied here are not much more dispersive than regular swimmer transport in the bulk.

4.2 Pulse Offset

Thus far, the swimmer's self-propulsion velocity has been assumed to vanish outside the activating pulses, i.e., $w(x)$ has been supposed to decay to zero at an appropriate distance from the pulse center. However, in realistic experimental setups, a perfect control of v_0 is hard, if not impossible, to realize. Indeed, real swimmers are expected to exhibit a sort of “ground activation” due to, e.g., stray light from the activating laser pulses or a residual fuel concentration in the presence of chemical stimulation. Therefore, in a more realistic approach one should not expect the swimmer to come to a complete halt outside the pulses, but rather to propel itself at a slow residual speed. In our model, such a rest propulsion can be accounted

⁴Here, $\langle w(x) \rangle_x := \int_0^1 w(x) dx$ denotes the spatial average of a single activation pulse.

for by introducing an offset $w_0 \in [0, 1]$ in the activation profile of Ch. 4.1,

$$w(x) = w_0 + (1 - w_0) \sin^2(\pi x), \quad (4.12)$$

where the amplitude of the pulses, $1 - w_0$, was scaled so that $w(x) \leq 1 \forall x$ and, therefore, v_0 remains the swimmer's maximum self-propulsion speed.

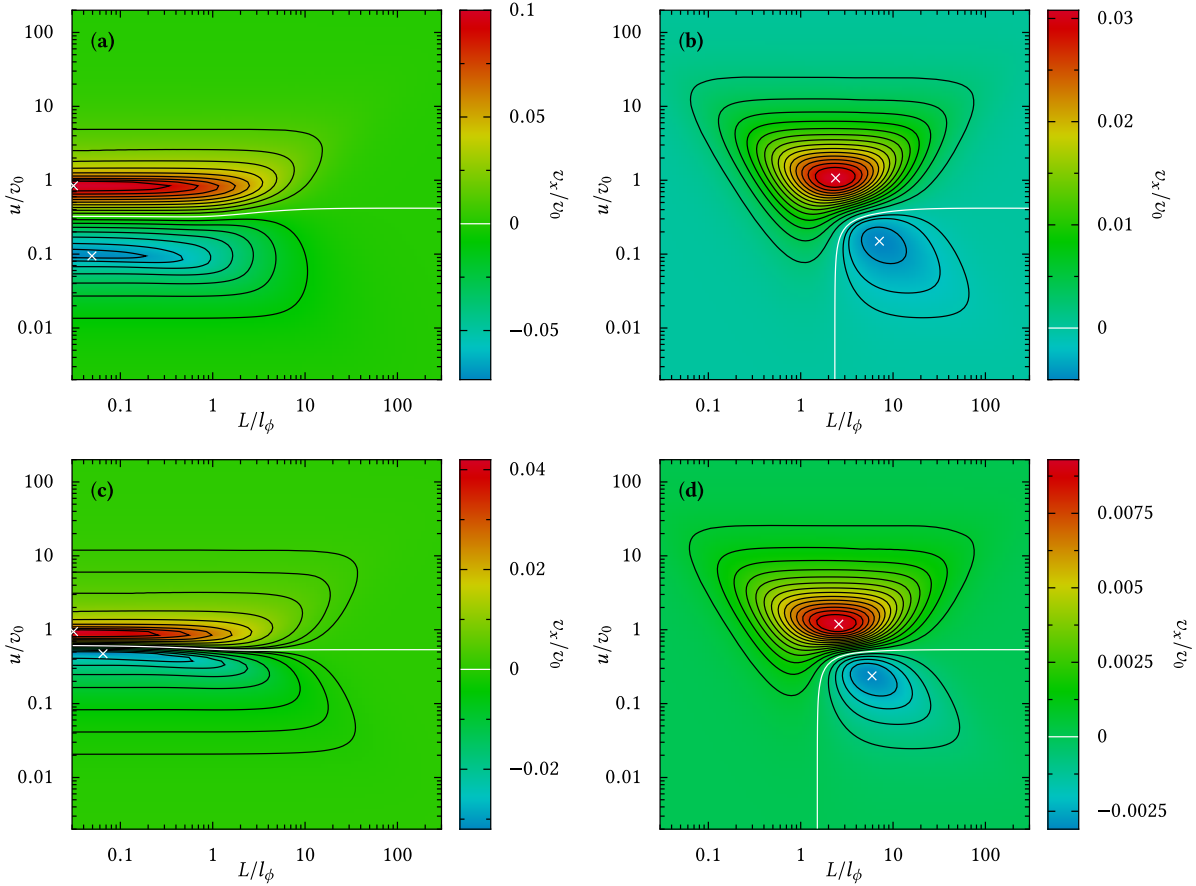


FIGURE 4.6. Influence of a pulse offset w_0 [see Eq. (4.12)] on the swimmer's tactic response to a sinusoidal activation sequence. The tactic drift v_x is plotted as a function of the width L and propagation speed u of the activating pulses, for a pulse offset of $w_0 = 0.1$ (a,b) and $w_0 = 0.5$ (c,d). The swimmer parameters D_ϕ and v_0 are the same as in the previous figures, and the translational noise intensity was set to $D_0 = 0$ in panels (a,c) and $D_0 = 2.2 \mu\text{m}^2/\text{s}$ in panels (b,d). All results were obtained by numerically integrating the FPE (3.5).

Looking at Fig. 4.6, we observe that the swimmer's tactic drift persists even for a very large pulse offset (in panels c and d, w_0 was set to 0.5, so as to equal the pulse amplitude), though its

magnitude generally diminishes. This is a natural consequence of the fact that upon raising w_0 , the swimmer's dynamics is increasingly governed by pure bulk diffusion—which is the only remaining dynamics in the limit $w_0 \rightarrow 1$. On a closer inspection we further notice that v_x is suppressed more strongly in the positive regime than in the negative regime, an effect that will be discussed in more detail below. Consistently with this observation, the region of negative tactic drift in the (L, u) plane is enlarged upon increasing w_0 : the horizontal (vertical) branches of the separatrix shift upward (to the left), as is also apparent in Fig. 4.7a.

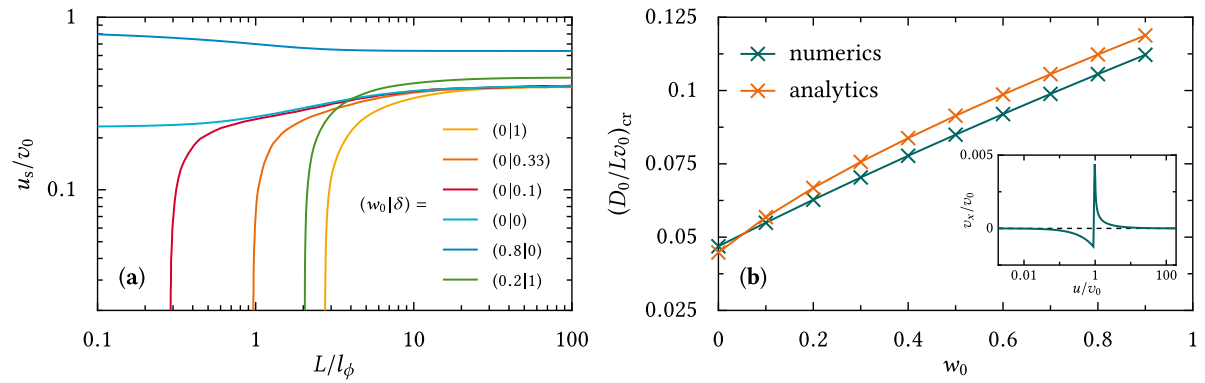


FIGURE 4.7. (a) Separatrix $u_s(L)$ dividing the regions of positive and negative tactic drift in the (L, u) plane, see Figs. 4.1a, 4.5a, and 4.6, for different values of the pulse offset w_0 and translational noise intensity D_0 . Here, $\delta := D_0/(2.2 \mu\text{m}^2/\text{s})$ describes the strength of the actual noise intensity, relative to its standard value used in the previous figures. We observe the vertical separatrix branch to shift toward lower values of L upon increasing w_0 and decreasing D_0 . The separatrices were obtained by locating the zeros of the swimmer's tactic drift v_x in the (L, u) plane, calculated from the FPE (3.5). (b) Critical value $(D_0/Lv_0)_{cr}$ determining the position of the vertical separatrix branch as a function of w_0 . The curves were again obtained by finding the zeros of v_x , either from the integration of the exact FPE (3.5) [green crosses] or from the ballistic approximation, Eq. (4.7) [orange crosses]. In the inset, the result of Eq. (4.13) is plotted versus u for $w_0 = 0.9$. The model parameters D_ϕ and v_0 are the same as in the previous figures and the pulse waveform is given by Eq. (4.12).

In the ballistic regime⁵, the dependence of the tactic separatrix $u_s(L)$ on w_0 can be explained by noting that in the presence of a finite pulse offset, the swimmer is actually “free”, i.e.,

⁵Like in Ch. 4.1.1, we expect the ballistic properties of the swimmer's dynamics to prevail when $l_\phi/L > \min\{t_c^{\phi=0}, Lv_0/D_0\}$. Again, for pulse speeds allowing the existence of trapped swimmer states with $t_c^{\phi=0} = \infty$, the latter condition weakens to $l_\phi/L > \min\{t_c^{\phi=\pi}, Lv_0/D_0\}$. For the calculation of the fixed-angle pulse crossing time t_c^ϕ in the presence of a pulse offset w_0 , see the text.

able to exit a pulse to the left *and* right, when the pulses propagate slower than its residual self-propulsion speed, $u/v_0 < w_0$. For u slightly below this threshold value, $w_0 - u/v_0 \ll 1$, a swimmer with a fixed orientation parallel to the pulse propagation direction thus crosses the activation troughs to the right, though with a low relative velocity of $v_0 w_0 - u$. A swimmer oriented into the opposite direction, on the other hand, crosses the troughs with a much higher relative velocity of $v_0 w_0 + u$. Hence, in a given timespan, a particle with $\phi = \pi$ hits many more “accelerating” pulse crests than a particle with $\phi = 0$. True is that these accelerating stages are shorter in time and, therefore, less effective for swimmers oriented to the left, see the discussion in Chs. 3.2 and 4.1; this effect, however, is outweighed by the much higher rate of activation pulse crossings. As a consequence, for moderate to large pulse offsets, the overall drift velocity v_x turns from positive to negative with a very steep slope upon lowering u , just before attaining its minimum at $u/v_0 \simeq w_0$ (see Fig. 4.6c and the inset of Fig. 4.7b).

In order to further investigate the impact of w_0 on the swimmer’s dynamics, we analytically calculate v_x once again in the ballistic regime, but now for a finite pulse offset, $w_0 > 0$. Analogously to Ch. 4.1.1, the swimmer’s longitudinal equation of motion can be solved exactly for a fixed orientation angle ϕ and $D_0 = 0$, yielding the ballistic pulse crossing time $t_c^\phi = v_0/\sqrt{(u - v_0 \cos \phi)(u - v_0 w_0 \cos \phi)}$ in the running states. Now, the main difference with the case $w_0 = 0$ is that, as already mentioned above, swimmers with orientation $-\arccos[u/(v_0 w_0)] < \phi < \arccos[u/(v_0 w_0)]$ travel to the right in the co-moving pulse frame (provided $u < v_0 w_0$) and hence only swimmers with $\phi \in [-\arccos(u/v_0), \arccos(u/v_0)] \setminus [-\arccos(u/(v_0 w_0)), \arccos(u/(v_0 w_0))]$ are in a locked state. The overall particle drift thus reads

$$v_x = \begin{cases} -\frac{1}{2\pi} \int_0^{2\pi} \sqrt{(u - v_0 \cos \phi)(u - v_0 w_0 \cos \phi)} d\phi + u & : \frac{u}{v_0} \geq 1 \\ -\frac{1}{2\pi} \int_{\arccos(u/v_0)}^{2\pi - \arccos(u/v_0)} \sqrt{(u - v_0 \cos \phi)(u - v_0 w_0 \cos \phi)} d\phi + u & : w_0 \leq \frac{u}{v_0} < 1 \\ \left[-\frac{1}{2\pi} \int_{\arccos(u/v_0)}^{2\pi - \arccos(u/v_0)} \sqrt{(u - v_0 \cos \phi)(u - v_0 w_0 \cos \phi)} d\phi \right. \\ \left. + \frac{1}{2\pi} \int_{-\arccos[u/(v_0 w_0)]}^{\arccos[u/(v_0 w_0)]} \sqrt{(u - v_0 \cos \phi)(u - v_0 w_0 \cos \phi)} d\phi + u \right] & : \frac{u}{v_0} < w_0. \end{cases} \quad (4.13)$$

Based on Eq. (4.13) we now remark the following: (i) For large pulse offsets, the negative tactic drift is most pronounced at $u/v_0 = w_0$, as the positive contribution of the second integral (see the last line of the above equation) steadily increases upon further lowering u . (ii) Moreover, by the same argument as in Ch. 4.1.1— v_x is supposed to turn negative once $v_x^{\phi=\pi}$ outweighs u in magnitude—we predict the horizontal separatrix branch for $D_0 = 0$ to be located at $u/v_0 = (1 + w_0 + \sqrt{w_0^2 + 14w_0 + 1})/6$, an expression that approaches w_0 from above

for $w_0 \rightarrow 1$ (cf. Fig. 4.7b, inset) and, furthermore, allows us to recover the value $u/v_0 = 1/3$ in the limit $w_0 \rightarrow 0$. (iii) In the presence of a finite pulse offset, $w_0 > 0$, the asymptotic behavior of v_x for $u \rightarrow 0$ and $D_0 = 0$ changes from $v_x/v_0 \propto -\sqrt{u/v_0}$ to $v_x/v_0 \propto -u/v_0$. This effect, clearly illustrated Fig. 4.8a, is caused by the suppression of the locked swimmer states in the limit of a very slow pulse propagation.

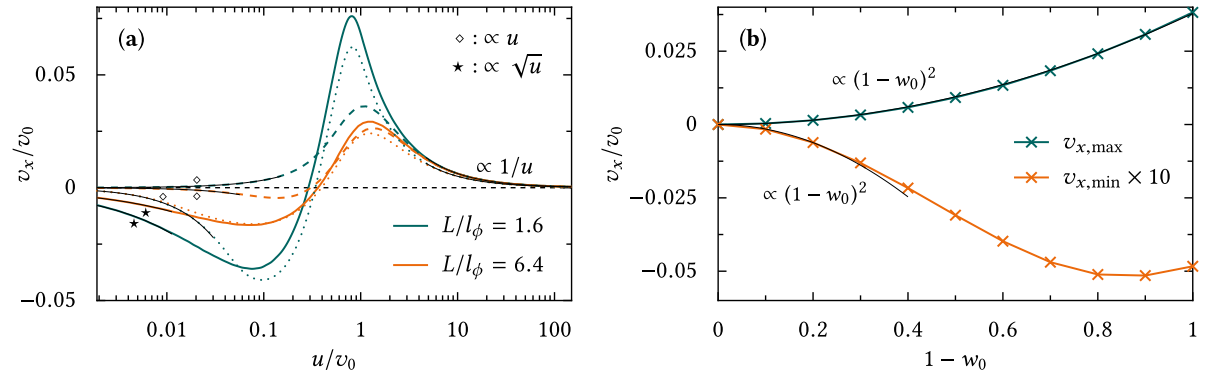


FIGURE 4.8. **(a)** Tactic drift of an artificial microswimmer as a function of the activation pulse speed, both in the predominantly ballistic regime, $L/l_\phi = 1.6$, and diffusive regime, $L/l_\phi = 6.4$. By way of comparison, we plotted v_x versus u (each in units of the swimmer's self-propulsion speed v_0) for $D_0 = 2.2 \mu\text{m}^2/\text{s}$ and $w_0 = 0$ (dashed lines), $D_0 = 0$ and $w_0 = 0.1$ (dotted lines), and $D_0 = 0$ and $w_0 = 0$ (solid lines). All curves decay asymptotically according to power laws, as indicated. **(b)** Maximum and minimum tactic swimmer drift, $v_{x,\text{max}}$ and $v_{x,\text{min}}$, respectively, as a function of the activation pulse amplitude, $1 - w_0$. Both $v_{x,\text{max}}$ and $v_{x,\text{min}}$ increase faster than linearly with $1 - w_0$; note, however, that the modulus of $v_{x,\text{min}}$ increases with the pulse offset w_0 for $w_0 \ll 1$, as also discernible in panel (a). The numerical data underlying the plots were obtained by solving the FPE (3.5) or integrating the LE (2.50) for $v_0 = 53 \mu\text{m}/\text{s}$, $D_\phi = 165 \text{s}^{-1}$, and $w(x) = w_0 + (1 - w_0) \sin^2(\pi x)$.

We now consider the case of non-zero translational fluctuations, $D_0 > 0$. As the suppression of the positive tactic drift caused by the pulse offset does not only enlarge the regime of negative v_x toward higher values of u , but in the presence of translational noise also toward lower values of L , the vertical branch of the tactic separatrix shifts to the left upon increasing w_0 . The corresponding critical value of $D_0/(Lv_0)$ can be estimated by the argument we gave in Ch. 4.1.3, namely, v_x is expected to turn positive when the translational diffusion time $(L/2)^2/(2D_0)$ becomes shorter than the ballistic pulse crossing time $2L/(v_0 + v_0 w_0)$. This criterion yields the threshold value $(D_0/Lv_0)_{\text{cr}} \approx 0.06(1 + w_0)$, which is in rather good agreement with the data of Fig. 4.7b. However, as mentioned earlier, $(D_0/Lv_0)_{\text{cr}}$ is a ballistic

quantity and therefore we should be able to calculate it even more precisely within the ballistic approximation. Indeed, the vertical branch of the separatrix is located quite accurately by Eq. (4.7), see Fig. 4.7b, which confirms the effectiveness of the analytical approaches discussed in the previous sections.

For wide pulses, $L \gg l_\phi$, the position of the horizontal separatrix branch can be estimated by applying the argument of Ch. 4.1.2. In the presence of a finite pulse offset w_0 , we obtain $\langle w(x) | \cos \phi | \rangle \approx (1 + w_0)/2(\sqrt{2})$ and, accordingly, the horizontal separatrix branch ought to be located at $u/v_0 \approx (1 + w_0)/(2\sqrt{2})$. The latter condition yields, for instance, $u/v_0 \approx 0.64$ for $w_0 = 0.8$, which is in excellent agreement with Fig. 4.7a.

Finally, in Fig. 4.8b we investigated the quantitative influence of w_0 on the magnitude of the swimmer's tactic drift. As observed before, v_x is suppressed by w_0 , with its maximum and minimum value, $v_{x,\max}$ and $v_{x,\min}$, scaling proportional to the square of the pulse amplitude $1 - w_0$. We notice, though, that a small offset, $w_0 \ll 1$, may even enhance the swimmer's negative drift, which is due to the expansion of the region of negative v_x toward both lower L and higher u values in the (L, u) plane. However, for larger values of w_0 , the suppressive effect of the pulse offset prevails and $v_{x,\min}$ decreases again.

4.3 Activation-Dependent Rotational Diffusivity

In Ch. 2.3 we remarked that in principle, a modulation of the swimmer's activation and, therefore, of v_0 implies a modulation of D_0 and D_ϕ , as well. However, both the swimmer's translational and rotational diffusivity have been observed to depend rather weakly on the activation density, with the former being even less sensitive to it than the latter [36]. For this reason, the modulation of D_0 and D_ϕ was assumed to be negligible in the present work. In the following we investigate whether such an approximation is justified, i.e., whether the tactic effects as reported in the previous sections still persist if D_ϕ , too, depends on the swimmer's activation density.

The rotational diffusivity of highly activated microswimmers has been reported to be either increased [36] or decreased [55] compared to the corresponding value of a passive particle, depending on the specific self-propulsion mechanism at work. In any case, D_ϕ is typically altered by a factor of about 0.4. Therefore, on assuming that under the pulse crests, $w(x) = 1$, the swimmer's rotational diffusivity is reduced/increased relative to the residual value in the pulse troughs by such a factor, and on further assuming for simplicity a linear dependence of D_ϕ on $w(x)$, the swimmer dynamics considered thus far ought to be modified

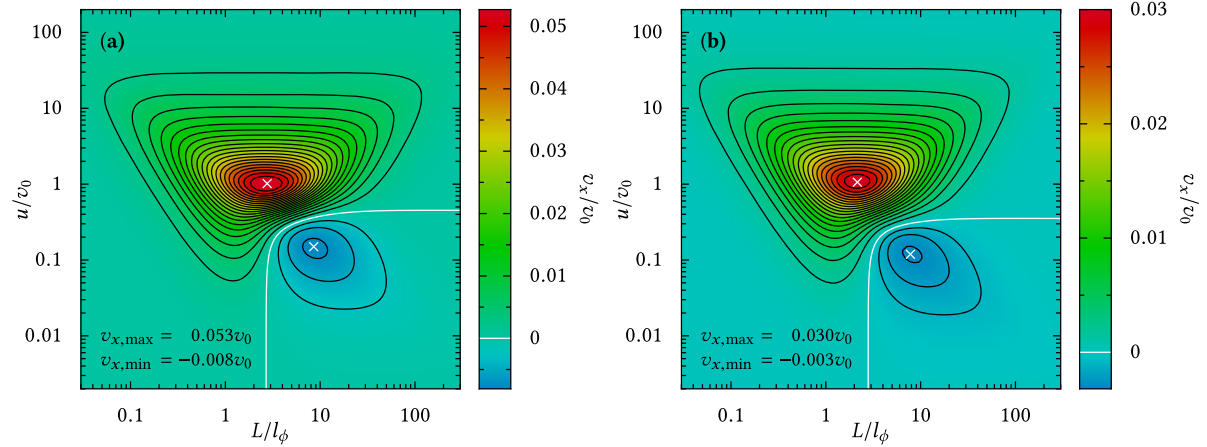


FIGURE 4.9. Effect of an activation-dependent rotational diffusion coefficient on the tactic drift of an artificial microswimmer. The plots are the same as in Fig. 4.5a, except that here the particle's rotational diffusivity was modified according to Eq. (4.14): $D_\phi \rightarrow D_\phi[1 - 0.4w(x)]$ in panel (a) and $D_\phi \rightarrow D_\phi[1 + 0.4w(x)]$ in panel (b).

by the substitution

$$D_\phi \rightarrow D_\phi[1 \pm 0.4w(x)]. \quad (4.14)$$

Upon comparing Fig. 4.9 to Fig. 4.5a, we clearly see that the tactic effects discussed in the previous sections persist in the case of an activation-dependent rotational diffusivity. Solely the overall magnitude of v_x gets slightly enhanced or diminished, according to whether the rotational diffusion coefficient decreases or increases with the strength of the swimmer's activation. This is a direct consequence of the fact that in general, a lower (higher) value of D_ϕ strengthens (suppresses) the swimmer's taxis, as implied by Eq. (3.5) and Fig. 4.1a: for $D_0 = 0$, a change in D_ϕ equals an analog change in L . Hence, for small values of D_ϕ (left side of Fig. 4.1a), v_x is strongly enhanced, whereas it vanishes monotonically in the limit $D_\phi \rightarrow \infty$ (except for the slight amplification of the negative tactic drift at around $L/l_\phi = LD_\phi/v_0 \simeq 1$). The overall enhancement of v_x caused by the substitution $D_\phi \rightarrow D_\phi[1 - 0.4w(x)]$, Fig. 4.9a, can thus be explained with a simple reduction of the swimmer's average rotational diffusivity. For $D_\phi \rightarrow D_\phi[1 + 0.4w(x)]$, Fig. 4.9b, the situation is reversed. Besides that, an activation-dependent rotational diffusivity does not significantly impact the swimmer's tactic response, so that our initial assumption of a constant rotational diffusion coefficient is reasonable and will be maintained in the forthcoming sections.

4.4 Chiral Swimmer Dynamics: $\Omega \neq 0$

We now consider the more general case of chiral swimmers with rotational velocity $\Omega \neq 0$. As already mentioned in Ch. 2.3, such an angular dynamics results from an asymmetric slip velocity profile around the swimmer and may be either the accidental result of fabrication defects or a deliberate effect. It can, for instance, be provoked by applying an asymmetric active cap on a spherical swimmer or bending a self-propelled microrod [266].

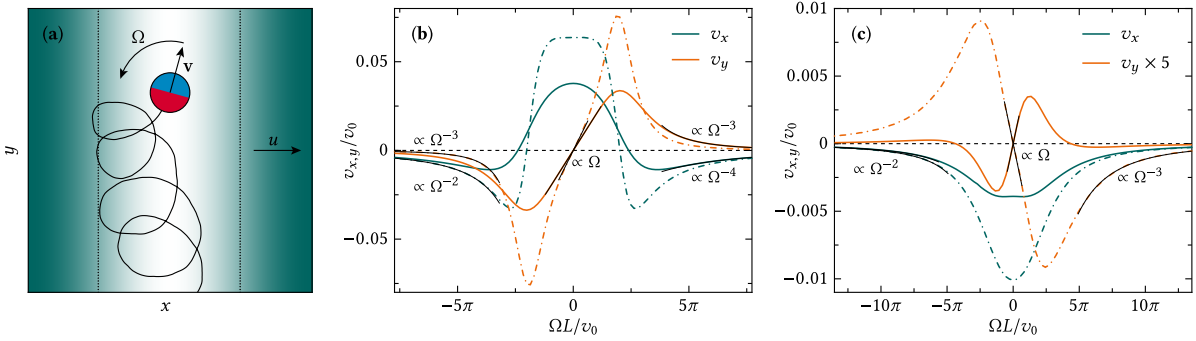


FIGURE 4.10. Taxis of a chiral microswimmer with $\Omega \neq 0$ induced by a sinusoidal activation pulse sequence, $w(x) = \sin^2(\pi x)$. Unless stated differently, all model parameters were chosen as in Fig. 4.5a. (a) Sketch of the upward spiraling swimmer trajectory evolving at the left pulse edge (cf. Fig. 4.13b), where the dotted black line indicates the pulse half-width. In panels (b) and (c), the longitudinal and transverse drift velocities, $v_x = v_0 \lim_{t \rightarrow \infty} \langle x(t) - x_0 \rangle / t + u$ and $v_y = v_0 \lim_{t \rightarrow \infty} \langle y(t) - y_0 \rangle / t$, respectively, are plotted versus the chiral frequency Ω in units of v_0/L for (b) $L/l_\phi = 2$, $u/v_0 = 1$ and (c) $L/l_\phi = 7$, $u/v_0 = 0.2$. We calculated the swimmer's tactic drift by numerically integrating the LE (2.50) or solving the FPE (4.16), both for $D_0 = 2.2 \mu\text{m}^2/\text{s}$ (solid lines) and $D_0 = 0$ (dashed lines). The thin black lines represent the fitted power laws for $\Omega L/v_0 \ll 1$ and $\Omega L/v_0 \gg 1$.

In the following, we study how a chiral angular velocity Ω influences the swimmer's tactic response to the sinusoidal activation sequence of Ch. 4.1. To this purpose, in Figs. 4.10b and c, respectively, the longitudinal and transversal drift velocities $v_x = \langle \dot{x} \rangle$ and $v_y = \langle \dot{y} \rangle$ are plotted against Ω . The pulse parameters L and u were chosen so as to capture the regime of the strongest positive (b) and negative (c) longitudinal tactic drift for $\Omega = 0$ and $D_0 = 2.2 \mu\text{m}^2/\text{s}$ (marked by white crosses in the contour plot of Fig. 4.5a). We immediately realize that a finite rotational velocity, $\Omega \neq 0$, induces a transverse tactic drift—which we observe to be most pronounced in the regime of positive achiral taxis—and in return tends to

suppress v_x . That is, the swimmer's longitudinal tactic drift, which is caused by the pulses' broken spatial symmetry, is "transferred" to the transversal direction by means of a second symmetry-breaking mechanism associated with particle chirality. This effect is best noticeable in Fig. 4.10b, where for $\Omega L/v_0 \simeq 2\pi$, v_x drops to zero, while v_y attains a maximum of about the same magnitude as $v_x(\Omega = 0)$. On further increasing Ω , the longitudinal tactic drift changes sign from positive to negative. Moreover, in the regime of negative achiral taxis, Fig. 4.10c, the curve $v_y(\Omega)$ has no zeros (besides the obvious one at $\Omega = 0$) and the same sign as Ω for $D_0 = 0$. On raising D_0 , however, transversal taxis is suppressed and its sign starts to vary with increasing Ω . More precisely, we observe that $\text{sgn}(v_y) = \text{sgn}(\Omega)$ for $|\Omega L/v_0| \lesssim 5\pi$, while $\text{sgn}(v_y) = -\text{sgn}(\Omega)$ for $|\Omega L/v_0| \gtrsim 5\pi$. It also becomes apparent from Fig. 4.10 that v_x and v_y are, respectively, even and odd functions of Ω , in agreement with the symmetry of the x and y dynamics in the LE (2.50) under the transformation $\phi \rightarrow -\phi$. For this reason, we can restrict the discussion of the following two sections to the case of *levorotary* swimmers ($\Omega > 0$); the dynamics of *dextrorotary* swimmers ($\Omega < 0$) then ensues immediately from the latter by symmetry considerations.

Finally, we remark that, analogously to the tactic response of achiral swimmers, a finite pulse offset w_0 tends to suppress the longitudinal and transversal tactic drift of chiral swimmers, too (not shown here).

4.4.1 Noiseless Regime

Since in the regime of positive taxis of achiral swimmers, the particle dynamics is governed by ballistic effects (see the previous sections), the dependence of the longitudinal and transversal drift on Ω in Fig. 4.10b should also be dominated by ballistic mechanisms and, therefore, be interpreted within the framework of a deterministic analysis. To this regard, in Fig. 4.11 we report the results obtained by integrating the LE (2.50)⁶ in the noiseless case (i.e., for $D_0 = D_\phi = 0$),

$$\dot{x} = \sin^2(\pi x) \cos \phi - \frac{u}{v_0}, \quad \dot{y} = \sin^2(\pi x) \sin \phi, \quad \dot{\phi} = \frac{L\Omega}{v_0}, \quad (4.15)$$

for the pulse parameters of Fig. 4.10b, $L = 2l_\phi$ and $u = v_0$. From a qualitative point of view, we observe a behavior similar to the swimmer's tactic drift in the noisy regime (Fig. 4.10b), namely $v_x > 0$ for $\Omega = 0$, while v_y vanishes at this point. Vice versa, at $\Omega = 2\pi v_0/L$, v_x is equal to zero, whereas the swimmer's transversal drift attains a maximum. However, in the

⁶We remind that in Eq. (4.15), x , y and t denote the dimensionless spatial and temporal particle coordinates in the co-moving pulse frame, which were introduced in Ch. 3.4.

noiseless limit, v_x and v_y are no longer smooth functions of Ω , but rather band-like structures made of piecewise continuously differentiable branches. Most notably, v_y is different from zero only in certain ranges of Ω (which are shaded in gray in Fig. 4.11).

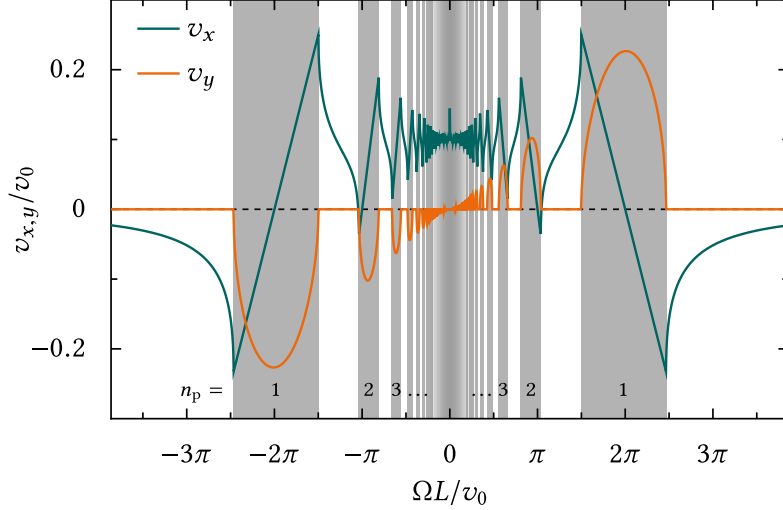


FIGURE 4.11. Tactic drift of a chiral microswimmer as a function of Ω (in units of v_0/L) in the deterministic limit, $D_\phi = D_0 = 0$. All other parameters were chosen as in Fig. 4.10b. The swimmer's drift is governed by the synchronization of rotational and translational dynamics occurring in the gray-shaded regions, where the periodicity number n_p denotes the number of pulse crossings required to complete a full particle rotation (see the text). The numerical data were obtained by integrating the system of equations (4.15) and subsequently averaging with respect to the starting angle ϕ_0 , which was assumed to be uniformly distributed in the interval $[0, 2\pi]$.

We explain these findings with the observation that in those Ω ranges, the swimmer's rotational and translational dynamics synchronize, i.e., during one full rotation, the particle exactly crosses an integer number of activation pulses, thus tracing quasi-periodic trajectories. Such a synchronization mechanism can be characterized by the periodicity number n_p that indicates the number of pulse crossings required to complete one full particle rotation. More precisely, for every integer $n_p \geq 1$, there exists a certain range of Ω where $v_y \neq 0$, which is determined by the solutions of the equation $t_c^{(n_p)}(\Omega) = 2\pi/\Omega$. Here, $t_c^{(n_p)}$ denotes the time required by a noise-free swimmer to cross n_p pulses, which has to equal the period of a full swimmer rotation, $2\pi/\Omega$.

In such a synchronized state, a levorotary swimmer tends to spiral upward, orthogonal to the propagation direction of the pulses (see, e.g., Fig. 4.10a). Samples of trajectories corresponding to the $n_p = 1$ mode for the pulse parameters of Figs. 4.10b and 4.11 are drawn

in panels a–c of Fig. 4.13. It is apparent that different choices of Ω result in trajectories with the same periodicity number n_p , but distinct drift directions. At the very left of the synchronization window with $n_p = 1$ for $\Omega > 0$ in Fig. 4.11, $\Omega \simeq (3\pi/2)v_0/L$, the swimmer rotates so slowly that it barely manages to complete a full rotation during a single pulse crossing. In this case, the corresponding trajectory is directed fully to the right (Fig. 4.13a) and thus v_x attains a maximum, while $v_y = 0$. Upon further increasing Ω , the effective direction of the swimmer’s path rotates counterclockwise, until for $\Omega = 2\pi v_0/L$ an ideal synchronization sets in, totally suppressing v_x and, in turn, maximizing v_y (cf. Fig. 4.13b). Here we recover the already mentioned transformation of longitudinal to transversal tactic drift caused by the additional symmetry breaking induced by particle chirality. Vice versa, once Ω exceeds the ideal synchronization condition, the swimmer’s rotational dynamics slightly “outruns” its translational dynamics and the drift of the particle trajectory becomes directed to the left, Fig. 4.13c. As a consequence, the longitudinal drift v_x turns negative and v_y is suppressed.

In the higher synchronization modes at lower values of Ω , $n_p > 1$, the mechanism accounting for the swimmer’s tactic drift remains the same, except a higher number of pulse crossings occurs during a full particle rotation. The dependence of v_x and v_y on Ω is thus qualitatively the same as for $n_p = 1$; however, the tactic drift is less and less modulated with respect to the residual value at $\Omega = 0$. This is due to fact that with rising n_p , the timescale on which the chiral symmetry breaking occurs becomes longer—and so does the observation time required to detect any chirality-induced shift of the mean particle position. Accordingly, v_x is positive at the center of the synchronization windows with $n_p > 1$, that is, even when the swimmer’s rotational dynamics is ideally in tune with the pulse periodicity (resulting in a maximal transversal drift), the effective direction of the trajectories points slightly to the right, as a consequence of the ballistic surfing effect discussed before. Related to this, we observe that the modes with $n_p > 1$ are not centered around $\Omega \simeq (2\pi/n_p)v_0/L$, but increasingly shifted toward lower values of Ω .

We also notice that all trajectories corresponding to a synchronized state are “attractive”, in the sense that for each choice of Ω (that allows for the existence of such a state), only one stable quasi-periodic trajectory exists, independent of the initial conditions ϕ_0 and x_0 . These starting values indeed influence the swimmer’s transient dynamics, but after a few pulse crossings, all trajectories converge to the same quasi-periodic orbit.

On the contrary, when Ω is chosen such that the swimmer’s rotational dynamics is not synchronized with the pulse periodicity, the particle trajectories exhibit a chaotic behavior. Hence, in the long-time limit, the symmetry in the y direction is restored and $v_y = 0$.

Last but not least, we remark that no synchronization modes exist when the swimmer

is able to complete n full rotations during a single pulse crossing (where $n > 1$), which would correspond to a fractional periodicity number, $n_p = 1/n$. Indeed, for each of these periodicity numbers, there exists an angular frequency such that the particle trajectories are quasi-periodic; this occurs, however, only for one specific value (i.e., not over a finite interval) of Ω . Moreover, the quasi-periodic particle paths for $n_p = 1/n$ are directed fully to the left, so that the transversal drift vanishes, $v_y = 0$. In the limit of an extremely fast particle rotation, $\Omega \rightarrow \infty$, the swimmer finally spins so fast that the self-propulsion mechanism can no longer contribute to its translational dynamics. Since this assimilates the active particle to a passive one and suppresses any tactic response, v_x vanishes monotonically for $\Omega \rightarrow \infty$.

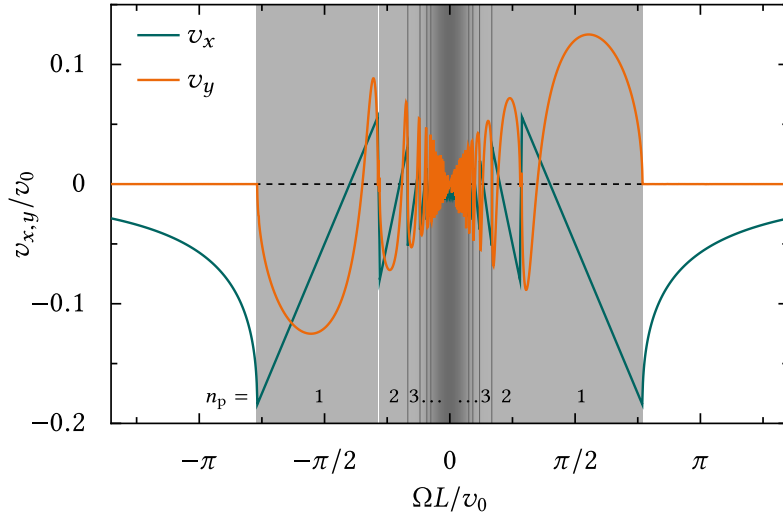


FIGURE 4.12. Same plot as in Fig. 4.11, but for the pulse parameters of Fig. 4.10c: $L/l_\phi = 7$ and $u/v_0 = 0.2$.

With decreasing u , Fig. 4.12, the swimmer's taxis in the noiseless limit exhibits a similar behavior as before, yet, we notice several differences in comparison with the case $u = v_0$: (i) As discussed in the previous sections, the longitudinal tactic drift of achiral particles becomes negative for slow pulse propagation speeds and, therefore, v_x is biased toward negative values for $\Omega \neq 0$, as well. (ii) Moreover, the transversal drift v_y is now a slightly asymmetric function of Ω in each synchronization window, that is, it reverses its sign for $|\Omega|$ being smaller than the central value of the relevant window. Trajectory samples corresponding to the $n_p = 1$ mode are displayed in panels d–f of Fig. 4.13. (iii) Most notably, the swimmer's tactic effects take place at lower values of Ω if u is lowered. This is a direct consequence of the fact that the particle's pulse crossing time is increased upon decreasing the pulse propagation speed. Thus, in order to allow for a synchronization between translational and rotational dynamics,

its angular frequency has to be lowered, too. Accordingly, the synchronization windows concentrate within a smaller range of Ω ; indeed, in Fig. 4.12 they seamlessly adjoin one another for $n_p > 1$.

4.4.2 Diffusive Regime

Comparing Fig. 4.10b and Fig. 4.11, we notice that the tactic drift of a chiral microswimmer in the regime of positive achiral taxis can be well explained, at least qualitatively, by the noiseless swimmer dynamics discussed in the previous section. Rotational fluctuations, $D_\phi > 0$, which in this regime have a rather weak effect, then tend to smear the discrete synchronization windows of Fig. 4.11, effectively applying a sort of moving average to the $v_{x,y}(\Omega)$ curves. Both rotational and translational noise also contribute, as to be expected, to the overall suppression of the tactic drift. However, comparing Fig. 4.10c and Fig. 4.12, we realize that the noiseless dynamics fail to explain the tactic response of a chiral swimmer in the regime of negative achiral taxis⁷. This is due to the fact that the pulses are now so wide and slow that, as in the case $\Omega = 0$, the swimmer's tactic drift is mainly induced by diffusive effects.

More precisely, in the latter regime, $L = 7l_\phi$ and $u = 0.2v_0$, the particle actively diffuses within the pulses, whose right (left) edges are reflective (absorbing) in the absence of translational fluctuations. The swimmer thus spends on average a longer time in the vicinity of the right pulse edge, where, for $\Omega > 0$, its spiraling trajectories are directed downward, i.e., in the negative y direction (cf. Fig. 4.10a). This implies a negative transversal tactic drift for $D_0 = 0$ and $\Omega > 0$, as displayed in Fig. 4.10c. Since the swimmer's spatial diffusivity $D_s(\Omega)$ is a monotonically decreasing function of its chiral frequency, see Eq. (2.49), the longitudinal drift v_x attains a maximum at $\Omega = 0$ and smoothly decays in the limits $\Omega \rightarrow \pm\infty$.

In the presence of translational fluctuations with $D_0 > 0$, the reflective (absorbing) character of the right (left) pulse edge is partly lost, such that the above diffusive rectification mechanism and the ensuing negative transversal drift are heavily suppressed. As a consequence, the tactic effects related to the ballistic nature of the swimmer's dynamics (see Fig. 4.12) may dominate again, causing v_y to change sign. Since the tactic drift originating from the diffusive character of the swimmer's dynamics occurs at significantly larger angular frequencies than the tactic drift induced by the ballistic character, compare Fig. 4.10c for $D_0 = 0$ with Fig. 4.12, this change of sign occurs for small to moderate values of $|\Omega|$ only. On the other hand, although strongly suppressed, the diffusive rectification effect still governs the tactic response of very quickly rotating swimmers.

⁷For instance, the swimmer's transversal drift is found to be negative for $\Omega > 0$ and $D_0 = 0$ in Fig. 4.10c, while the purely deterministic model predicts the opposite.

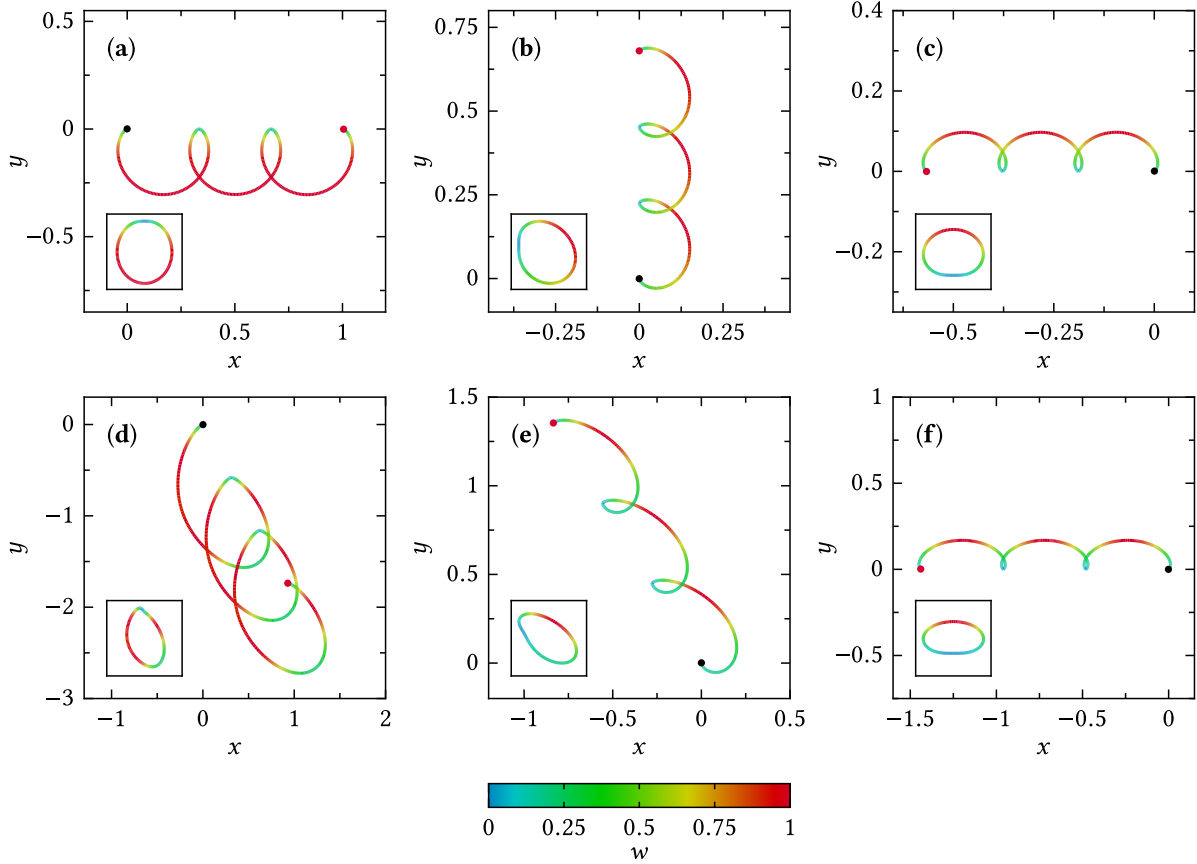


FIGURE 4.13. Samples of stationary trajectories of a chiral swimmer calculated from Eq. (2.50) in the noiseless regime, for the model parameters of Fig. 4.11 (a–c) and Fig. 4.12 (d–f). Here, x and y denote the swimmer’s dimensionless coordinates in the laboratory frame. In panels (a–c), the chiral frequency Ω was selected from Fig. 4.11, corresponding to (a) the left edge of the synchronization window with $n_p = 1$ of a levorotary swimmer ($\Omega > 0$), where v_x is maximally positive; (b) the position of the maximal transversal drift, $\Omega L/v_0 = 2\pi$; and (c) the right edge of the synchronization window with $n_p = 1$ for $\Omega > 0$, where v_x becomes maximally negative. Similarly, in panels (d–f), Ω was chosen from Fig. 4.12, to correspond to the position of the maximally negative (d) and positive (e) transversal and the maximally negative longitudinal drift (f) for $\Omega > 0$. For graphic reasons, the starting point of each trajectory sample (marked by a black dot) was set to the center of a pulse trough located at the origin, that is, $w(x_0) = x_0 = y_0 = 0$. The red dots label the endpoints of the sample paths, which were cut after three quasi-periodic cycles. In the inset, we subtracted the swimmer’s tactic drift, in order to better visualize the periodic nature of the trajectories. The coloring of the curves encodes the actual swimmer activation w along the sample paths (see bottom legend).

In order to give a more quantitative account of the tactic effects occurring in the diffusive regime, we apply again the mapping procedure of Ch. 3.4.1, this time to the FPE of a chiral swimmer with $\Omega \neq 0$,

$$\begin{aligned} \frac{\partial P(x, y, \phi, t)}{\partial t} = & \left[\frac{D_0}{Lv_0} \frac{\partial^2}{\partial x^2} + \frac{D_0}{Lv_0} \frac{\partial^2}{\partial y^2} - \frac{\partial}{\partial x} \left(w(x) \cos \phi - \frac{u}{v_0} \right) \right. \\ & \left. - w(x) \sin \phi \frac{\partial}{\partial y} + \frac{D_\phi L}{v_0} \frac{\partial^2}{\partial \phi^2} - \frac{\Omega L}{v_0} \frac{\partial}{\partial \phi} \right] P(x, y, \phi, t), \end{aligned} \quad (4.16)$$

cf. Eq. (3.5). In doing so, the full swimmer dynamics of Eq. (4.16) can be approximated to a FPE for the marginal one-zone probability density

$$\tilde{\mathcal{P}}(x, y, t) = \sum_{n=-\infty}^{\infty} \sum_{m=-\infty}^{\infty} \mathcal{P}(x+n, y+m, t) \quad (4.17)$$

[see also Eq. (4.3)], where $\mathcal{P}(x, y, t) = \int_0^{2\pi} P(x, y, \phi, t) d\phi$. This way, we obtain the equation

$$\begin{aligned} \frac{\partial \tilde{\mathcal{P}}(x, y, t)}{\partial t} = & \left[\left(\frac{\partial^2}{\partial x^2} + \frac{\partial^2}{\partial y^2} \right) \left(\frac{v_0 D_\phi}{2L(D_\phi^2 + \Omega^2)} w^2(x) + \frac{D_0}{Lv_0} \right) \right. \\ & \left. - \frac{\partial}{\partial x} \left(\frac{v_0 D_\phi}{4L(D_\phi^2 + \Omega^2)} \frac{dw^2(x)}{dx} - \frac{u}{v_0} \right) - \frac{v_0 \Omega}{4L(D_\phi^2 + \Omega^2)} \frac{dw^2(x)}{dx} \frac{\partial}{\partial y} \right] \tilde{\mathcal{P}}(x, y, t), \end{aligned} \quad (4.18)$$

which we know to be valid in the diffusive regime, i.e., for $D_\phi L/v_0 \gg 1$ and $u/v_0 \ll 1$.

Since for any arbitrary but fixed value of x , the swimmer performs a free diffusion with constant drift and diffusion coefficients in the y direction, a stationary solution of the FPE (4.18) obeying periodic boundary conditions in y has the form $\tilde{\mathcal{P}}_{\text{st}}(x, y) = \tilde{\mathcal{P}}_{\text{st}}(x)$, i.e., it is constant in the transversal direction. Accordingly, upon comparing Eqs. (4.18) and (3.10), we find the longitudinal tactic drift v_x of chiral swimmers to be given by the same expressions as in the case $\Omega = 0$ [Eqs. (4.8) and (4.9)], except the rotational diffusivity is replayed by an effective, Ω -dependent value, $D_\phi \rightarrow D_\phi(1 + \Omega^2/D_\phi^2)$.

Interpreting now Eq. (4.18) as a continuity equation, the implicit expression for the swimmer's transversal drift reads

$$v_y = v_0 \int_0^1 \int_0^1 \tilde{J}_{\text{st},y}(x) dy dx = \frac{v_0^2 \Omega}{4L(D_\phi^2 + \Omega^2)} \int_0^1 \frac{dw^2(x)}{dx} \tilde{\mathcal{P}}_{\text{st}}(x) dx, \quad (4.19)$$

where $\tilde{J}_{\text{st},y}$ is the stationary probability current in the y direction. Following step by step the procedure of Ch. 4.1.1, we also derived an explicit expression for the stationary probability

distribution $\tilde{\mathcal{P}}_{\text{st}}(x)$ [262] and thus obtained our final expression for v_y ,

$$v_y = \frac{v_0^2 \Omega}{4L(D_\phi^2 + \Omega^2)} \int_0^1 \int_0^1 \frac{dx dy (dw^2(x)/dx)}{\sqrt{[w^2(x) + \alpha][w^2(x+y) + \alpha]}} \exp\left(\frac{2(D_\phi^2 + \Omega^2)Lu}{D_\phi v_0^2} \int_x^{x+y} \frac{dz}{w^2(z) + \alpha}\right) \\ \times \left[\int_0^1 \int_0^1 \frac{dx dy}{\sqrt{[w^2(x) + \alpha][w^2(x+y) + \alpha]}} \exp\left(\frac{2(D_\phi^2 + \Omega^2)Lu}{D_\phi v_0^2} \int_x^{x+y} \frac{dz}{w^2(z) + \alpha}\right) \right]^{-1}, \quad (4.20)$$

with $\alpha := 2D_0(D_\phi^2 + \Omega^2)/(D_\phi v_0^2)$. Similarly to Eq. (4.8), Eq. (4.20) can be further simplified in the absence of translational fluctuations, $D_0 = 0$, yielding

$$v_y = \frac{v_0^2 \Omega}{2L(D_\phi^2 + \Omega^2)} \int_0^1 \int_0^1 w'(x+y) w'(x) \exp\left(-\frac{2(D_\phi^2 + \Omega^2)Lu}{D_\phi v_0^2} \int_{x+y}^{x+1} \frac{1}{w^2(z)} dz\right) dy dx \\ \times \left[\int_0^1 \int_0^1 \frac{w'(x+y)}{w(x)} \exp\left(-\frac{2(D_\phi^2 + \Omega^2)Lu}{D_\phi v_0^2} \int_{x+y}^{x+1} \frac{1}{w^2(z)} dz\right) dy dx - 1 \right]^{-1}. \quad (4.21)$$

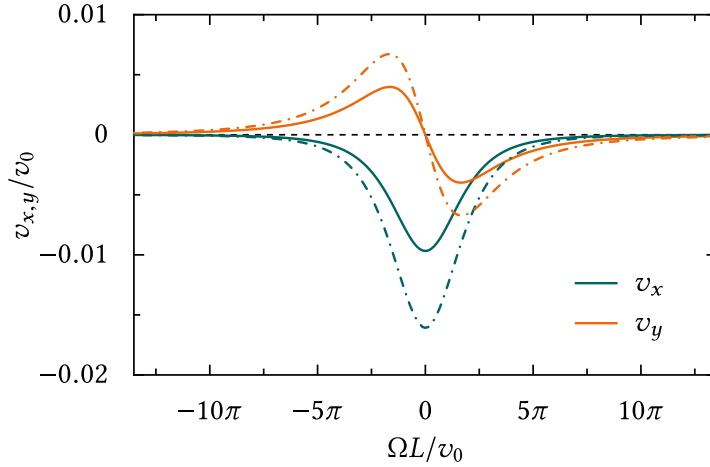


FIGURE 4.14. Longitudinal, v_x , and transversal tactic drift, v_y , of a chiral microswimmer as a function of Ω , calculated within the diffusive approximation. The curves for v_x were obtained from Eq. (4.8) for $D_0 = 2.2 \mu\text{m}^2/\text{s}$ (solid lines) and Eq. (4.9) for $D_0 = 0$ (dashed lines), where in both equations the substitution $D_\phi \rightarrow D_\phi(1 + \Omega^2/D_\phi^2)$ has to be made (see the text). Analogously, v_y was calculated from Eqs. (4.20) and (4.21) for $D_0 = 2.2 \mu\text{m}^2/\text{s}$ (solid lines) and $D_0 = 0$ (dashed lines), respectively. The values of all other model parameters are identical to the ones in Fig. 4.10c.

In Fig. 4.14, we plotted the swimmer's tactic drift in the diffusive approximation for the pulse parameters of Fig. 4.10c. The comparison of these two figures supports our previous

conjecture that in the absence of translational fluctuations, $D_0 = 0$, the drift of chiral swimmers in the regime of negative achiral taxis is primarily induced by rotational fluctuations⁸. For $D_0 > 0$, on the other hand, the diffusive approximation merely predicts a suppression of v_x and v_y , whereas the full particle dynamics reveals a more drastic impact of translational noise. Thus, as in Fig. 4.4, the sign inversion of the tactic drift is essentially a ballistic effect: translational and rotational fluctuations in a way compensate for each other and thus “restore” the deterministic effects associated with the particle’s finite persistence length.

Moreover, from the above expressions we were also able to derive the asymptotic behavior of v_x and v_y in the limits $\Omega \rightarrow 0$ and $\Omega \rightarrow \infty$. In the diffusive regime, v_x decays proportional to Ω^{-4} and v_y proportional to Ω^{-3} for $\Omega \rightarrow \infty$, independent of the translational noise intensity D_0 . Furthermore, in the case of a very weak chirality, $\Omega L/v_0 \ll 1$, the swimmer’s transversal drift grows proportional to Ω , again irrespective of D_0 . Upon comparing the above results with the fitted power laws in Fig. 4.10, we conclude that the asymptotic behavior of v_y remains the same both in the ballistic and the diffusive regime of the swimmer’s dynamics, whereas the decay of the longitudinal drift v_x for $\Omega \rightarrow \infty$ obeys different power laws in Ω , depending on the translational noise level and the pulse parameters L and u .

In summary we proved, both numerically and analytically, that chiral microswimmers, which move along spiraling trajectories, can drift preferably in a direction perpendicular to the pulse propagation, depending on their actual angular frequency Ω . This effect results from the spatial symmetry breaking due to the particles’ chirality and exhibits distinct properties in the diffusive and the ballistic regime.

Finally, we remark that the setup of a traveling activation pulse sequence hitting an artificial microswimmer, as considered in the present chapter, bears resemblance to the model investigated in Ref. [93], where a swimmer was placed in a static, periodically modulated activation landscape (see Appendix A.2). However, a main difference between the two setups is how the system’s spatial symmetry is broken. In the present setup, the pulse symmetry is broken by the stationary propagation of the pulses to the right, whereas in Ref. [93] the asymmetry of the static activation profile was tailored ad hoc. A tactic drift can be observed in both cases, yet, the underlying mechanisms are quite different: in our model, the swimmer’s tactic drift results from the modulation of its active diffusion inside the traveling wave pulses, while the tactic effect reported in Ref. [93] is explained with a saturated self-polarization

⁸The quantitative discrepancy between the curves for $D_0 = 0$ in both figures is attributed to the fact that for $L = 7l_\phi$ and $u = 0.2v_0$, the diffusive properties of the swimmer’s dynamics prevails indeed, though, its ballistic component cannot yet be completely neglected (cf. Fig. 4.4). However, we found a favorable agreement between the results obtained within the diffusive approximation and exact numerics for larger values of L/l_ϕ and v_0/u (not shown here).

of the particle—see Ch. 2.3 and Appendix A.2. In the following chapter, we will incorporate such a self-polarization effect into our model and investigate to what extent it influences a swimmer’s tactic drift induced by a traveling activation pulse sequence.

TAXIS OF SELF-POLARIZING MICROSWIMMERS

When the density of the activating medium surrounding a self-phoretic microswimmer is not uniform, a polarizing angular velocity may occur, which tends to align the swimmer parallel or opposite to the activation gradient [59, 91, 246]. We refer to this mechanism, respectively, as positive or negative self-polarization of the swimmer. In this chapter, we incorporate such a self-polarizing angular effect into our model and discuss its influence on the properties of the tactic response studied in Ch. 4. To this purpose, we initially consider the phoretic mechanisms underlying the swimmer's self-polarization. We then investigate how the tactic drift induced by a sinusoidal activation pulse sequence is modified by the particle's alignment with the activation gradients. In particular, we focus on the interplay between self-polarization and the effects of translational and rotational fluctuations. Finally, upon estimating the relative magnitude of these possibly competing mechanisms, we fully characterize the selective transport of artificial microswimmers in inhomogeneous activating media.

5.1 Self-Polarization in Activation Gradients

Let us consider, for simplicity, a spherical self-phoretic microswimmer, which is subjected to a non-uniform activation density with gradient ∇w . The local self-generated gradient in the vicinity of the particle and the associated phoretic slip profile (green arrows in Fig. 5.1) are then in general asymmetric with respect to the swimmer's propulsion axis. In this case, a

rotational velocity,

$$\Omega_p = \frac{3}{2R} \langle \mathbf{v}_s \times \mathbf{n}_s \rangle_s, \quad (5.1)$$

is induced [154], where R is the particle radius. We also remind that $\langle \dots \rangle_s$ denotes the average over the particle surface and \mathbf{n}_s the unit vector normal to it. As the slip velocity \mathbf{v}_s is larger on the side of higher activation density, see Fig. 5.1, the angular velocity of Eq. (5.1) tends to orient the swimmer opposite to the gradient ∇w . However, there is a second component (orange arrows in Fig. 5.1) to the phoretic slip profile around the swimmer, which is not caused by the self-generated gradient, but rather by the external activation gradient itself. When the swimmer's phoretic mobility is not uniform, $\mu' \neq \mu$, this component gives rise to an additional angular velocity, which forces an orientation of the particle opposite *or* parallel to ∇w . The actual direction of this alignment depends on the interaction between the particle's surface and the surrounding medium, that is, the swimmer tends to orient itself so that the side of larger phoretic mobility faces a higher activation density, cf. Eqs. (2.16) and (2.29).

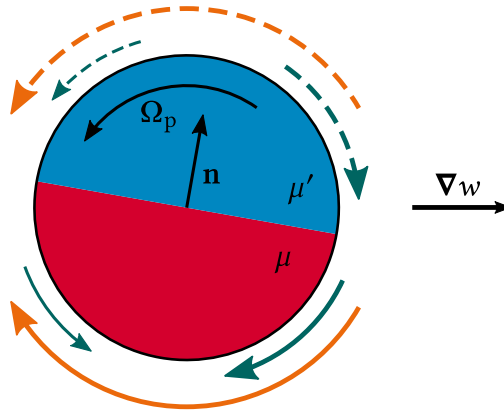


FIGURE 5.1. Schematics of the self-polarization mechanism underlying Eq. (5.2), see also Ref. [246]. A swimmer with two (in general different) phoretic surface motilities μ and μ' aligns its propulsion direction \mathbf{n} (anti-)parallel to the activation gradient ∇w with angular velocity Ω_p . The effect is caused by an asymmetric slip profile (represented by green and orange arrows) around the particle.

It was found in Ref. [246] that upon taking into account these two effects, the overall angular velocity is of the form

$$\Omega_p = v_0 [Y_1 (\mu' - \mu) + Y_2 (\mu' + \mu)] \mathbf{n} \times \nabla w, \quad (5.2)$$

where \mathbf{n} denotes the swimmer's propulsion direction and Y_1 and Y_2 are material-dependent coefficients accounting for the deformation of the external activation medium due to the

presence of the particle [246]. We note that in the above equation, ∇ denotes the gradient operator in the natural (i.e., unscaled and dimensional) Cartesian coordinates. The term proportional to $\mu' + \mu$ corresponds to the polarization effect induced by the self-generated gradient, whereas the term proportional to $\mu' - \mu$ represents the swimmer's self-polarization in the external activation gradient. From Eq. (5.2) it becomes evident that the alignment of the particle with ∇w can be controlled in strength *and* direction by varying the surface mobilities μ and μ' . In principle, μ and μ' can even be chosen so as to make Ω_p vanish, at least approximately, which justifies the assumption $\Omega_p = 0$ introduced for simplicity in the previous chapters.

We now replace the dimensionless and material-dependent term $[Y_1(\mu' - \mu) + Y_2(\mu' + \mu)]$ by a single phenomenological parameter s , which effectively characterizes the strength of the swimmer's self-polarization and is typically of the order of 1 [246]. Moreover, it should be remarked that an activation gradient not only gives rise to the above angular dynamics, but also to an additional contribution to the particle's self-propulsion velocity, namely $\mathbf{v} \rightarrow \mathbf{v} + \delta\mathbf{v}$, with $\delta\mathbf{v} = v_0\sigma\nabla w$. The parameter σ here describes the effective coupling of the local self-propulsion velocity \mathbf{v} to the activation gradient. However, as typically $|\delta\mathbf{v}| \ll |\mathbf{v}|$ [246], we neglect this contribution altogether in the remainder of this work. Finally, we remind that in the derivation of the model Eqs. (2.50), we assumed the activation density to be so low that the swimmer's self-propulsion speed is proportional to it, i.e., in the linear regime. Likewise, we assume that the activation gradients are weak enough, too, such that the saturation of the self-polarizing angular speed predicted in Ref. [93] can be neglected.

Returning to our model, in the presence of an activation gradient ∇w , the angular dynamics of the LE (2.50) comprises now the additional velocity $\Omega_p := \mathbf{e}_z \cdot \Omega_p$ (with \mathbf{e}_z being the unit vector orthogonal to the xy plane), that is,

$$\dot{\phi} = \Omega_p + \sqrt{2D_\phi} \xi_\phi(t), \quad \text{where} \quad \Omega_p = -v_0 s \sin \phi \frac{\partial w(x, t)}{\partial x}. \quad (5.3)$$

In the above equation, like in Eq. (2.50), x and t refer to the unscaled, dimensional spatial and temporal swimmer coordinates. Moreover, here and in the following we consider an achiral particle, $\Omega = 0$, that is, the swimmer's angular dynamics is assumed to be governed by a mere self-polarization effect. Since Ω_p does *not* break the symmetry of the swimmer's dynamics in the transversal direction, we thus expect that $v_y = 0$, which allows us to restrict our analysis again to the particle's longitudinal dynamics.

The angular velocity Ω_p vanishes for $\sin \phi = 0$, causing the swimmer to orient itself either parallel ($\phi = 0$) or anti-parallel ($\phi = \pi$) to the gradient $\partial_x w(x, t)$. Here, the stable orientation is *positive* (i.e., directed toward a higher activation density) for $s > 0$ and *negative*

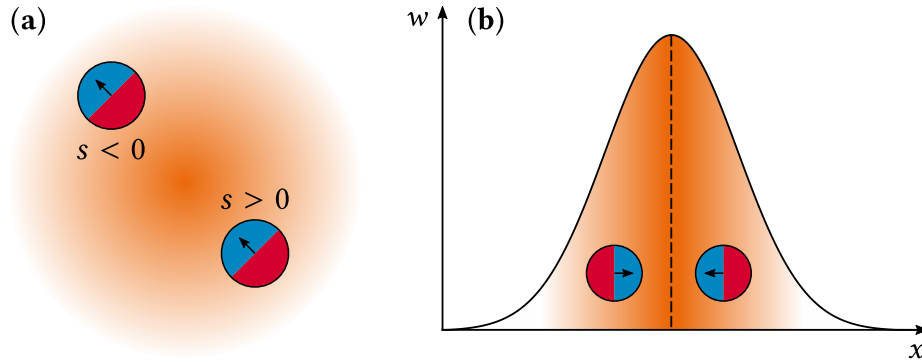


FIGURE 5.2. **(a)** Self-polarization of swimmers with $s > 0$ and $s < 0$ in a radially symmetric activating spot. **(b)** Sketch of a possible trapping mechanism, where a positively self-polarizing swimmer, $s > 0$, is sucked inside a traveling activation pulse.

(i.e., directed toward a lower activation density) for $s < 0$, as illustrated in Fig. 5.2a. We now return to the dimensionless scaling introduced at the beginning of Ch. 3.4, $x \rightarrow x/L$ and $t \rightarrow (v_0/L)t$, and assume once again the sinusoidal activation profile $w(x) = \sin^2(\pi x)$. Due to its self-polarization, a swimmer now tends to orient itself inward (outward) the pulses for $s > 0$ ($s < 0$), see Fig. 5.2b.

5.2 Taxis of Self-Polarizing Swimmers

To investigate the influence of self-polarization on a swimmer's tactic drift induced by the sinusoidal activation sequence of Ch. 4.1, we numerically integrated the LE (2.50) with Eq. (5.3) and solved the associated FPE

$$\frac{\partial P(x, \phi, t)}{\partial t} = \left[\frac{D_0}{Lv_0} \frac{\partial^2}{\partial x^2} - \frac{\partial}{\partial x} \left(\cos \phi w(x) - \frac{u}{v_0} \right) + \frac{D_\phi L}{v_0} \frac{\partial^2}{\partial \phi^2} + s \frac{dw(x)}{dx} \frac{\partial}{\partial \phi} \sin \phi \right] P(x, \phi, t). \quad (5.4)$$

The qualitative effect of a moderate self-polarization on the swimmer's tactic response is summarized in Fig. 5.3. Upon comparing the latter with Fig. 4.1a, we find that a negative self-polarization with $s < 0$ strongly enhances the magnitude of the positive tactic drift described in Ch. 4.1 and, in return, suppresses negative taxis. Vice versa, for $s > 0$, the drift is suppressed (enhanced) in the regime with $v_x > 0$ ($v_x < 0$), without much affecting the sign of v_x . This behavior can be explained with the fact that, as anticipated above, for $s > 0$ ($s < 0$) the self-polarization mechanism favors an orientation of the particle inward (outward) the pulses, which shortens (prolongs) the mean time a swimmer can surf an advancing pulse front. By contrast, as the positive surfing effect is destabilized (stabilized) for $s > 0$

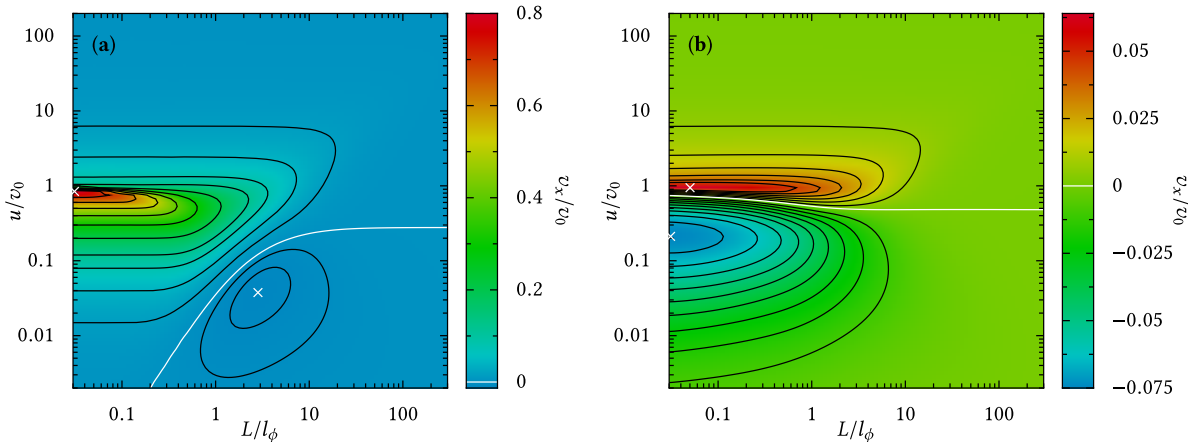


FIGURE 5.3. Taxis of a self-polarizing microswimmer induced by a sinusoidal activation sequence, $w(x) = \sin^2(\pi x)$. The model parameters were chosen as before, $v_0 = 53 \mu\text{m/s}$ and $D_\phi = 165 \text{ s}^{-1}$. Only D_0 was set to zero, in order to focus on the fundamental effects underlying the swimmer's tactic response. All results were obtained by combining the numerical integration of the model LE (2.50) and (5.3) with the numerical solution of the corresponding FPE (5.4). The contour plots of the longitudinal drift velocity v_x have been obtained for both a positive and negative particle self-polarization; $s = -0.5$ in panel (a) and $s = 0.5$ in panel (b).

($s < 0$), the competing effects responsible for the negative tactic drift, see Ch. 4.1, gain (lose) influence. Accordingly, the tactic separatrix shifts slightly upward in the case of a positive self-polarization, $s > 0$. For $s < 0$, on the other hand, the separatrix not only shifts toward slightly lower values of u [compare the right branch of the separatrix, $u_s(L \rightarrow \infty)$, in Figs. 4.1a and 5.3a], but slants downward as L is decreased. In this regard, we remind that the negative tactic drift of a non-polarizing swimmer ($s = 0$) for small values of u/v_0 , $D_0 = 0$, and $L/l_\phi \ll 1$ is due to the fact that trapped particles with $|\phi| < \arccos(u/v_0)$ move slower to the right than particles with $\pi/2 < \phi < 3\pi/2$ cross the pulses to the left. When $s < 0$, however, a swimmer with $\pi/2 < \phi < 3\pi/2$ cannot simply cross one pulse after another to the left, as in the front of each pulse it is forced to reorient to the right by the self-polarization mechanism. Hence, most trajectories that would contribute to a negative tactic drift for $s = 0$ end up in a trapped state and thus contribute to a positive overall drift for $s < 0$. Since rotational fluctuations hamper the swimmer's alignment with the activation gradients, this effect becomes increasingly prominent as the influence of rotational noise is lowered and, as a result, the tactic separatrix bends downward with decreasing L .

For a stronger negative self-polarization, $s < -0.5$, the tactic drift v_x remains qualitatively the same as in Fig. 5.3a. The only difference is that, as expected, the amplification of the positive tactic drift is even more pronounced. If s is raised above 0.5, on the other hand, the swimmer's tactic response is quickly suppressed overall, to the point that it completely vanishes in the limit $s \rightarrow 1$. The latter can be readily proven by setting $s = 1$ in the FPE (5.4), which after some simple algebraic manipulations of the rotational and translational drift term can then be rewritten as

$$\frac{\partial P(x, \phi, t)}{\partial t} = \left[\frac{D_0}{Lv_0} \frac{\partial^2}{\partial x^2} - \left(\cos \phi w(x) - \frac{u}{v_0} \right) \frac{\partial}{\partial x} + \frac{D_\phi L}{v_0} \frac{\partial^2}{\partial \phi^2} + \sin \phi \frac{dw(x)}{dx} \frac{\partial}{\partial \phi} \right] P(x, \phi, t). \quad (5.5)$$

Upon considering the stationary state, $P(x, \phi, t) \rightarrow P_{\text{st}}(x, \phi)$, and imposing the usual periodic boundary conditions in x and ϕ , $P_{\text{st}}(x + 1, \phi + 2\pi) = P_{\text{st}}(x, \phi)$ [cf. Ch. 4.1.1], one immediately obtains $P_{\text{st}}(x, \phi) = 1/(2\pi)$, i.e., a uniform probability density. The corresponding tactic drift thus must vanish, that is, $v_x = 0$ for any choice of the activation pulse parameters L and u .

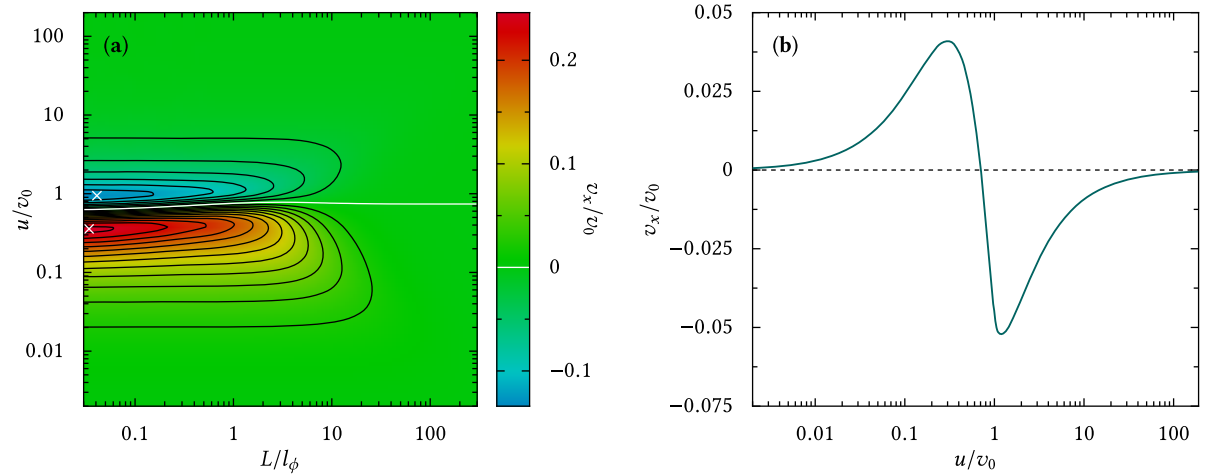


FIGURE 5.4. **(a)** Same plot as in Fig. 5.3, but for a strongly positive self-polarization strength, $s = 2.5$. **(b)** Tactic drift v_x as a function of the pulse propagation speed u (both in units of v_0) in the noiseless regime, $D_\phi = D_0 = 0$. The data underlying the curve were obtained by numerically integrating the system of ordinary differential equations (5.6) for $s = 2.5$. The results were then averaged with respect to the initial conditions ϕ_0 and x_0 , which were assumed to be uniformly distributed, respectively, in the intervals $[0, 2\pi]$ and $[0, 1]$.

When s is raised above 1, however, the tactic drift velocity v_x changes sign in the entire (L, u) plane, as illustrated in Fig. 5.4a. It thus becomes obvious that a positive self-polarization, $s > 0$, exerts a distinct, partly competing tactic effect on the swimmer's dynamics. Looking at

the right side of the contour plot in Fig. 5.4a, we notice that a high translational noise level ($L/l_\phi = D_\phi L/v_0 \gg 1$) suppresses this effect, as well. Upon comparing the left side of Fig. 5.4a with Fig. 5.4b, we thus conclude that, like in the case $s = 0$, the origin of such an additional tactic effect must be found in the purely deterministic regime with $D_\phi = D_0 = 0$.

5.3 Noiseless Swimmer Dynamics

In order to clarify the interplay between the tactic mechanisms of Ch. 4 and self-polarization, we address now in more detail the deterministic swimmer dynamics in the noiseless regime, $D_0 = D_\phi = 0$. The dimensionless form of the LE (2.50), combined with Eq. (5.3), then boils down to a set of (in general non-linear) ordinary differential equations, which for the sinusoidal activation sequence of Ch. 4.1 read

$$\dot{\phi} = -s\pi \sin \phi \sin(2\pi x), \quad \dot{x} = \cos \phi \sin^2(\pi x) - u/v_0. \quad (5.6)$$

As anticipated before, here the transverse coordinate y has been ignored due to symmetry considerations.

The tactic drift velocity of a self-polarizing deterministic swimmer with $s = 2.5$ and $s = -0.5$ is plotted, respectively, in Figs. 5.7a and 5.7b. We interpret the displayed dependence of v_x on the pulse speed u as follows.

Positive self-polarization. In the co-moving pulse frame with $u \rightarrow \infty$, the particle is pulled through the activating pulses so fast that its dynamics is insensitive to the modulation of the activation density. In such a limit, the velocity field $(\dot{\phi}, \dot{x})$ consists of parallel lines with $\dot{\phi} = 0$ and $\dot{x} = -u/v_0$, see Fig. 5.5a; hence, $v_x \rightarrow 0$.

Upon lowering the pulse propagation speed u , the swimmer begins to perceive the modulated gradients as it crosses the activation pulses. Accordingly, the velocity field gets progressively distorted, as shown in panels b–d of Fig. 5.5. As long as $u > v_0$, Fig. 5.5b, the field lines are no longer parallel, but still cross the reduced pulse unit cell $[0, 1]$ from top to bottom with $\dot{x} < 0$, while the majority of field lines starting at $x = 1$ cross the centerline, $x = 1/2$, with $|\phi| > \pi/2$. This means that a positively self-polarizing swimmer points preferably to the left ($\Rightarrow \dot{x} < -u/v_0$) under the pulse crests and to the right ($\Rightarrow \dot{x} > -u/v_0$) in the troughs. Since the regions where the particle preferably points to the left (right) correspond to high (low) self-propulsion velocities, for $u > v_0$ the swimmer's net drift in the laboratory frame is expected to be negative, in agreement with the data reported in Figs. 5.4b and 5.7a. This is an unavoidable effect of the particle's finite reorientation time.

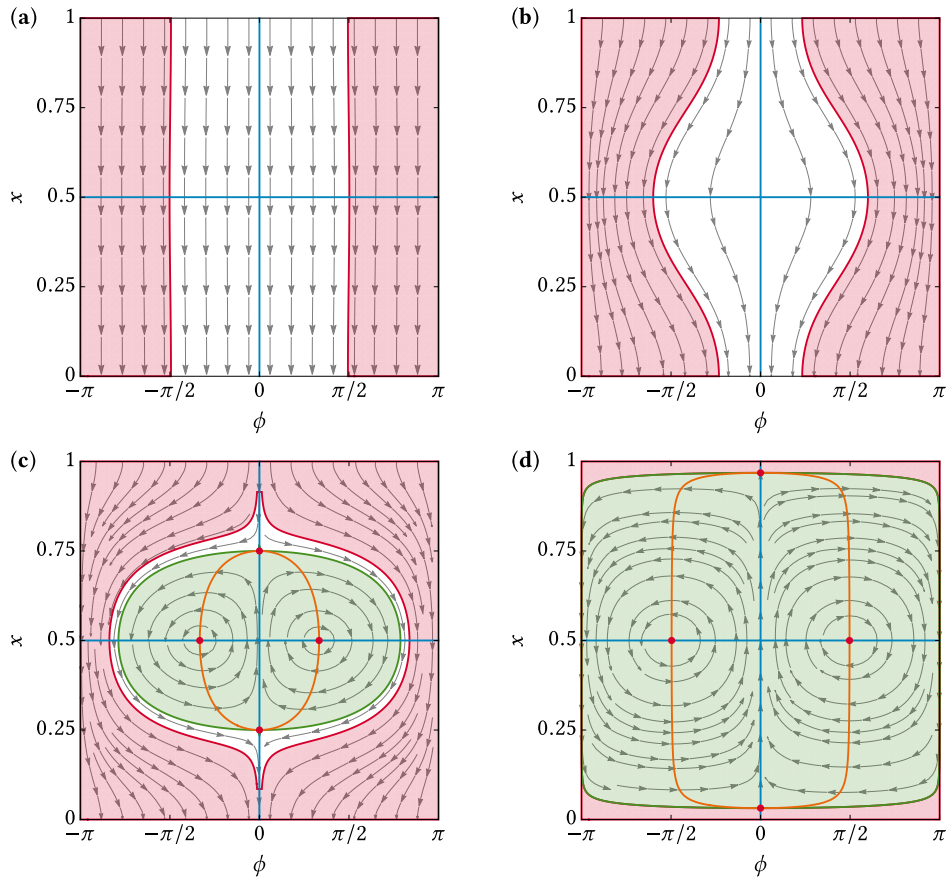


FIGURE 5.5. Swimmer taxis in the noiseless regime, $D_\phi = D_0 = 0$. In the panels, the velocity field $(\dot{\phi}, \dot{x})$ [see Eq. (5.6)] is plotted for $s = 2.5$ and $u/v_0 = 100$ **(a)**, 2 **(b)**, 0.5 **(c)**, and 0.01 **(d)**. The blue and orange curves denote, respectively, the existing ϕ and x nullclines of Eq. (5.6); their intersections (red dots) locate two stable ($x = 1/2$) and unstable ($\phi = 0$) fixed points. The region shaded in red marks the initial conditions corresponding to a negative drift velocity, $v_x = \lim_{t \rightarrow \infty} v_0[x(t) - x_0]/t + u < 0$, and the green region the trapping states with $v_x = u$, where the particle oscillates inside a pulse in the co-moving frame (see the text for further details).

If the pulse propagation becomes slower than the swimmer's self-propulsion speed, $u < v_0$, the particle can get trapped by the traveling pulses with either positive or negative orientation, as sketched in Fig. 5.2b. Such a mechanism is marked by the emergence of two periodic bound solutions of Eq. (5.6) for $s > 0$, see Figs. 5.5c and d. Closed swimmer trajectories wind up around the stable fixed points $(\phi_f, x_f) = (\pm \arccos[u/v_0], 1/2)$ with frequencies $\pm \pi \sqrt{2s [1 - (u/v_0)^2]}$, as one can easily prove by rewriting the system of equations (5.6) in linear approximation,

$$\frac{d}{dt} \begin{pmatrix} \tilde{\phi} \\ \tilde{x} \end{pmatrix} = \pm \sqrt{1 - \left(\frac{u}{v_0}\right)^2} \begin{pmatrix} 0 & 2\pi^2 s \\ -1 & 0 \end{pmatrix} \begin{pmatrix} \tilde{\phi} \\ \tilde{x} \end{pmatrix}, \quad (5.7)$$

where $\tilde{\phi} := \phi - \phi_f$ and $\tilde{x} := x - x_f$.

Of course, initial conditions in the region of the configuration space (ϕ, x) corresponding to such closed trajectories contribute the maximum positive amount, u , to the net drift velocity of the noiseless swimmer. Moreover, as illustrated in Fig. 5.5d, upon lowering u , the trapping region becomes larger and larger, until finally v_x turns positive. Accordingly, we predict that the overall tactic drift velocity must tend to zero proportional to u in the limit $u \rightarrow 0$, as confirmed by Fig. 5.4b.

Negative self-polarization. By the same argument as put forth above for a positively self-polarizing swimmer, also the tactic drift of a swimmer with $s < 0$ is predicted to vanish in the limit $u \rightarrow \infty$ (Fig. 5.6a). Upon decreasing the pulse propagation speed, the rectification mechanism just described for $s > 0$ sets in, but in a reversed manner: swimmers preferably point to the left (right) in regions of low (high) self-propulsion speeds, as illustrated in Fig. 5.6b. Hence, v_x grows increasingly positive, see Fig. 5.7b.

If u becomes smaller than v_0 , again four fixed points emerge in the (ϕ, x) phase space, as visualized in Fig. 5.6c. In the case of a negatively self-polarizing swimmer, the positions $(\pm \arccos[u/v_0], 1/2)$ become saddle points, whereas the fixed points at $(0, \arcsin[\sqrt{u/v_0}]/\pi)$ and $(0, 1 - \arcsin[\sqrt{u/v_0}]/\pi)$ turn, respectively, into a repeller and an attractor. As mentioned in the previous section, the latter is responsible for the strong enhancement of the positive tactic drift, cf. the steep slope of the curves $v_x(u)$ for $(L/v_0)D_\phi \ll 1$ and $u/v_0 \simeq 1$ in Fig. 5.7b.

Finally, when $u \ll v_0$, Fig. 5.6d, the swimmer's phase space mostly consists of pulse-trapped states, which contribute a positive amount u to the overall net drift. However, in contrast to the case $s > 0$ (compare Fig. 5.6d with Fig. 5.5d), here some swimmer trajectories still cross the pulses to the left, which corresponds to a negative particle drift. If u now becomes small enough, the contribution of these few states to the swimmer's overall tactic response may outweigh the positive contribution of the trapped states, to the point that v_x eventually turns negative. This is confirmed in Fig. 5.7b, where the tactic drift of a noiseless

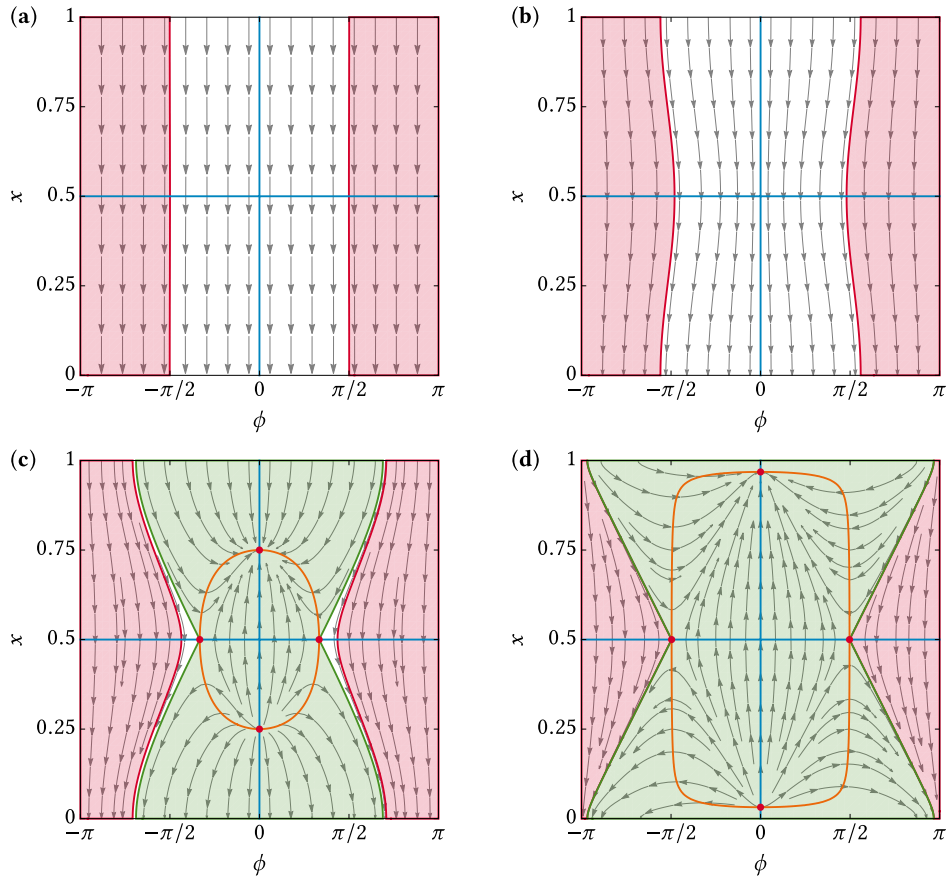


FIGURE 5.6. Same plots as in Fig. 5.5, except that the self-polarization strength is now set to $s = -0.5$. The velocity field $(\dot{\phi}, \dot{x})$ is then characterized by two symmetric saddle points at $(\phi, x) = (\pm \arccos[u/v_0], 1/2)$, one attractor at $(\phi, x) = (0, 1 - \arcsin[\sqrt{u/v_0}]/\pi)$, and one repeller at $(\phi, x) = (0, \arcsin[\sqrt{u/v_0}]/\pi)$.

swimmer with $D_\phi = 0$ changes sign at $u/v_0 \simeq 0.08$. Of course, in the limit of a vanishing pulse propagation, $u \rightarrow 0$, the swimmer is not able to leave a pulse anymore, independent of its actual trajectory and, therefore, $v_x \rightarrow 0$.

5.4 Influence of Noise

The role of rotational fluctuations. We now consider the more realistic case when the rotational noise, $\xi_\phi(t)$ in Eq. (5.3), has a finite intensity, $D_\phi > 0$, and the translational noises in the LE (2.50) are comparatively so weak to be safely neglected, i.e., $D_0 = 0$. The swimmer then tends to rotate as a combined effect of the polarizing angular velocity Ω_p and the angular fluctuations due to thermal Brownian motion in the suspension fluid and, possibly,

the particle's self-propulsion mechanism itself. In dimensionless units, the time constant of the swimmer's self-polarization can be readily estimated from Eq. (5.6), $\tau_s^{-1} = \pi s$. Regarding the second orientational process, we remind that the particle's rotational diffusion time is $\tau_\phi = D_\phi^{-1}$ or, in dimensionless units, $\tau_\phi = v_0/(LD_\phi)$. Note that as long as the tactic mechanisms due to self-polarization and rotational noise can be regarded as independent, the effective rotational time constant is of the order of $\tau = \tau_s \tau_\phi / (\tau_s + \tau_\phi)$, with $\tau \rightarrow \tau_s$ for $D_\phi \rightarrow 0$ and $\tau \rightarrow \tau_\phi$ for $D_\phi \rightarrow \infty$.

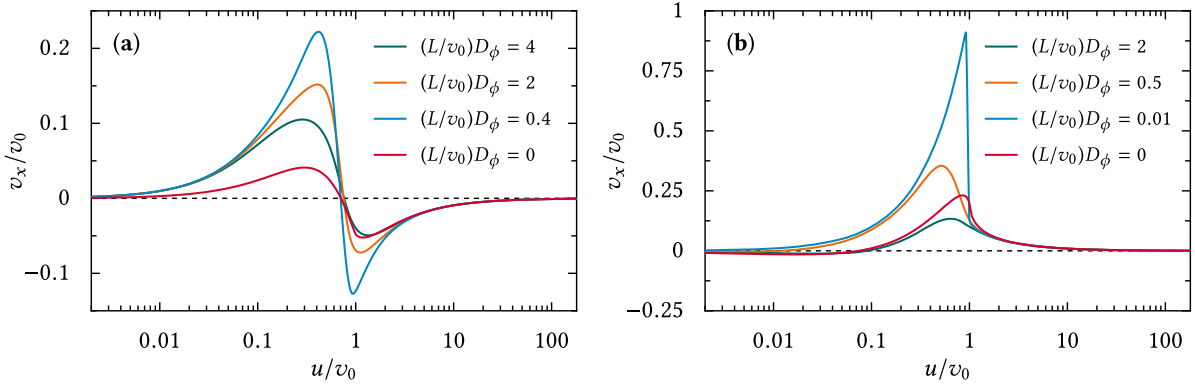


FIGURE 5.7. Influence of the rotational noise. Drift velocity v_x of the self-polarizing swimmers of Figs. 5.4 [$s = 2.5$, panel (a)] and 5.3a [$s = -0.5$, panel (b)] versus u , both in units of v_0 . The curves were obtained by integrating the LE (2.50) and (5.3) or numerically solving the FPE (5.4), for different values of the dimensionless noise intensity $(L/v_0)D_\phi$ (see legends) and $D_0 = 0$.

The influence of the rotational noise intensity on a self-polarizing swimmer's tactic drift is illustrated in Figs. 5.7 and 5.8. For both $s > 0$ and $s < 0$, the rotational fluctuations clearly suppress v_x at high values of D_ϕ , $D_\phi \gg v_0/L$, whereas at low intensities, they significantly enhance the particle's tactic response. Moreover, adding any amount of rotational noise barely changes the sign of v_x , except for the suppression of the swimmer's negative tactic drift when $s < 0$. The drift velocity v_x thus exhibits a prominent resonant behavior as a function of D_ϕ , both in the positive and negative regime of the swimmer's taxis.

Such a remarkable noise dependence has a certain similarity with the phenomenology of stochastic resonance [267–272]. A small amount of rotational noise acts as a *lubricant*, meaning that it favors the swimmer's reorientation with respect to the activation gradients. In particular, for a positively self-polarizing swimmer, this anticipates the onset of the trapping mechanism described above in the noiseless limit. Also in the case of negative self-polarization, $s < 0$, a low rotational noise level facilitates the swimmer's trapping, this time by the attractor

in the front of the pulses. Accordingly, the pulse-crossing trajectories corresponding to running states (red regions in Figs. 5.6c and d) finally end up in a trapped state, as well, and the tactic drift turns overall positive. The strong enhancement of the trapping mechanism is apparent from the curve $v_x(u)$ for $(L/v_0)D_\phi = 0.01$ in Fig. 5.7b, where (i) $v_x > 0$ throughout the range of u we explored, and (ii) the tactic drift suddenly jumps to large positive values once the locked swimmer states emerge (i.e., when u becomes smaller than v_0).

On the contrary, large angular fluctuations tend to randomize the swimmer's trajectories, so that the regular field line patterns displayed in Figs. 5.5 and 5.6 get blurred until they eventually become undiscernible. Under these circumstances, noise acts rather as a *suppressant* of the tactic response and, accordingly, the modulus of the swimmer's drift velocity vanishes.

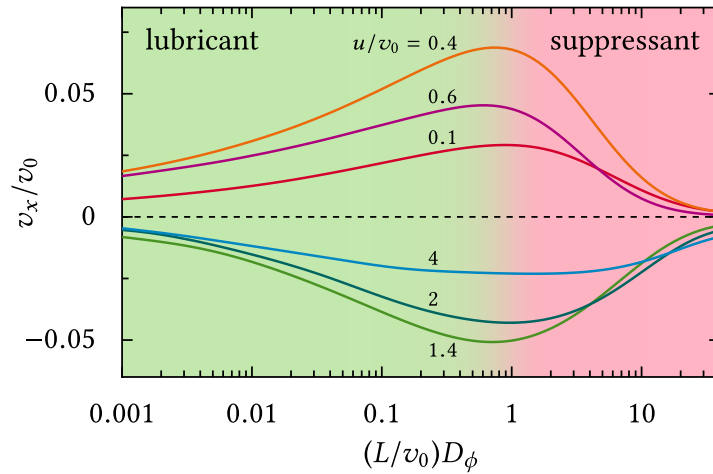


FIGURE 5.8. Tactic drift velocity of the strongly self-polarizing swimmer of Fig. 5.10 ($s = 2.5$, $v_0 = 53 \mu\text{m/s}$, and $D_0 = 2.2 \mu\text{m}^2/\text{s}$) versus D_ϕ , both in dimensionless units, for $L = 1.3 \mu\text{m}$ and different values of u . The data plotted here have been obtained by numerically integrating the LE (2.50) combined with Eq. (5.3).

The resonant behavior of v_x persists also in the presence of translational fluctuations with $D_0 > 0$, as can be seen from Fig. 5.8. However, here the tactic drift quickly vanishes for $D_\phi \rightarrow 0$, as a decreasing rotational noise level implies an increasing timescale on which the swimmer's tactic response is established. In this case, the translational noise has more time to exert its randomizing action on the particle, until eventually the swimmer's tactic response is completely suppressed.

The role of translational fluctuations. The influence of translational noise on the tactic drift v_x is displayed in Figs. 5.9 and 5.10. In the regime where the impact of rotational fluctuations outweighs the effect of self-polarization, that is, in the absence of the tactic

sign inversion mentioned in Ch. 5.2, $s < 1$, translational noise expectedly suppresses the swimmer's tactic drift, as it did for $s = 0$. Accordingly, the tactic separatrix bends downward at a critical pulse width L corresponding to the threshold value $(D_0/Lv_0)_{\text{cr}}$, see Ch. 4.1.3. Since the negative tactic drift is enhanced compared to the positive drift as the swimmer's self-polarization strength is raised from negative to positive values (still assuming $s < 1$), the vertical separatrix branches shift to the left with increasing s .

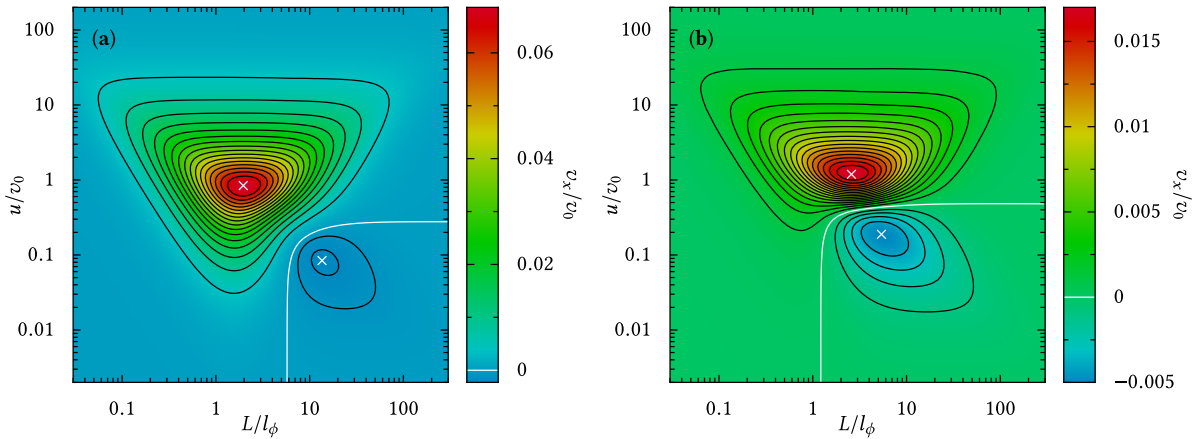


FIGURE 5.9. Influence of the translational noise. Contour plots of the longitudinal drift velocity v_x for the same model parameters as in Fig. 5.3, but for a finite translational noise intensity, $D_0 = 2.2 \mu\text{m}^2/\text{s}$. We remind that $s = -0.5$ in panel (a) and $s = 0.5$ in panel (b).

After the tactic sign inversion at $s = 1$ has occurred, Fig. 5.10, the effect of the translational fluctuations is in a sense reversed, as well. Translational noise indeed still suppresses the swimmer's tactic response overall, but it now favors the negative drift: v_x is definitely negative in the regime with $D_0/(Lv_0) > (D_0/Lv_0)_{\text{cr}}$. Accordingly, for $D_0 > 0$, the positive tactic drift is then restricted to the bottom-right quadrants of the $v_x(L, u)$ contour plots. This is a simple consequence of the fact that translational noise suppresses the tactic mechanisms more effectively at lower pulse propagation speeds u , which imply a longer observation time for any tactic drift to set in. However, we notice (not shown here) that the vertical separatrix branches still shift slightly to the left on increasing the self-polarization strength, even for $s > 1$. This suggests that a larger value of s stabilizes the trapped oscillating swimmer states against translational noise at the expense of the running pulse-crossing states.

In conclusion, the tactic response of an artificial microswimmer to traveling activation pulses persists even in the presence of self-polarization effects induced by the activation

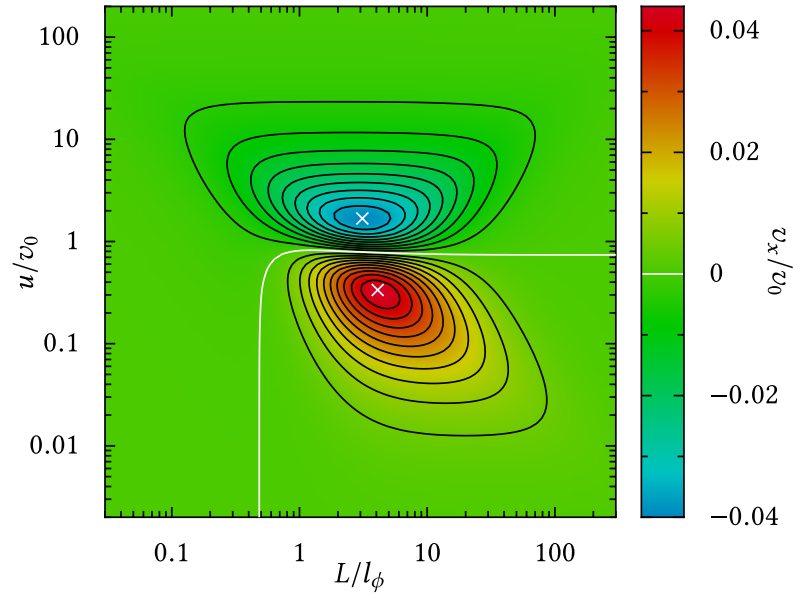


FIGURE 5.10. Influence of the translational noise on the tactic response of a strongly self-polarizing swimmer with $s = 2.5$. The contour plot of v_x versus L and u is the same as in Fig. 5.4a, except here the translational noise intensity was set to $D_0 = 2.2 \mu\text{m}^2/\text{s}$.

gradients. The interplay between such a hydrodynamically induced polarization and angular fluctuations of the swimmer's self-propulsion velocity gives rise to diverse tactic behaviors, the magnitude and direction of which can be selectively controlled by tuning the particle's (surface-dependent) self-polarization strength.

CONCLUSIONS AND OUTLOOK

Inspired by the tactic response of biological microorganisms to traveling stimulus pulses, in the present work we have investigated the (tactic) transport of artificial microswimmers in spatio-temporally modulated activating media. To this purpose, in Ch. 2 we explained the principles of swimming at the microscale, in particular by means of *self-phoretic* effects, and set up a stochastic model incorporating translational and rotational fluctuations into the dynamics of a self-phoretic microswimmer. After having analyzed the impact of a non-uniform activation density on the swimmer's dynamics, we focused on a spatio-temporal modulation of this density in the form of traveling wave pulses.

Single activation pulse. In Ch. 3, we considered a swimmer hit by a single activation pulse and studied, both numerically and analytically, its tactic shift induced thereby. We focused in particular on the role of the pulse parameters and determined the influence of the actual pulse shape. As a result, we found that a swimmer may drift in *either* direction with respect to the pulse propagation, depending on the pulse's speed and width. This is due to the fact that the ballistic and the diffusive properties of the swimmer's self-propulsion dynamics inside the pulse give rise to opposite tactic responses, which are both induced by the broken spatial symmetry associated with the pulse propagation. The tactic shift thus can be controlled in magnitude *and* direction by enhancing or suppressing either of these properties. This strategy is most conveniently implemented by tuning the pulse speed u and width L . In the two dynamical regimes corresponding to a predominantly ballistic or diffusive swimmer dynamics, we also established an analytical framework that allowed us to obtain approximate

analytic results for the swimmer's tactic response.

Periodic activation sequence. In Ch. 4, we next focused on the more realistic case of a periodic pulse sequence and studied the resulting tactic drift of the swimmer. Again, the latter can drift either parallel or opposite to the pulse propagation direction, with the underlying mechanisms being similar to those discussed in Ch. 3. We identified the positive tactic drift as being a purely ballistic effect, i.e., to stem solely from the finite persistence time of the swimmer's active Brownian motion, whereas the negative tactic drift results from the combination of diffusive and ballistic properties of its dynamics. Moreover, we analyzed the influence of the inevitable translational fluctuations on the tactic drift. Translational noise suppresses the latter overall, but is also able to reverse its sign in a certain range of the pulse parameters L and u . An activation offset was incorporated into the pulse sequence, too, so that swimmers do not come to a complete halt outside the pulses, but rather propel themselves at a residual speed. In the presence of such an offset, the tactic effects reported before proved to persist, although slightly suppressed in magnitude. Finally, we investigated the effect of an activation-dependent rotational diffusivity of the swimmer (which turned out to be rather minor) and particle chirality. Chiral swimmers, which move along spiraling trajectories due to some asymmetry of the self-propulsion mechanism, were found to drift in a direction *perpendicular* to the pulse propagation, as a consequence of a further symmetry breaking associated with the swimmer's chiral angular dynamics.

Swimmer self-polarization. In Ch. 5, we considered an additional hydrodynamic contribution to the swimmer's dynamics, namely an alignment of its orientation (anti-)parallel to the activation gradients, which we referred to as *self-polarization*. We discussed the origins of such an effect and investigated its impact on the tactic response of Ch. 4. It was found to exert an additional, partly competing tactic effect on the swimmer's dynamics, due to a deterministic mechanism. Furthermore, this mechanism proved to be amplified by low rotational noise levels, such that it exhibits a prominent resonant behavior. As a consequence, the magnitude and direction of the swimmer's tactic drift are tunable by varying not only the pulse speed and width, but also the particle's (surface-dependent) polarization strength.

Outlook

We conclude this work by underscoring that taxis of artificial microswimmers in spatio-temporally modulated activating media is a *robust* phenomenon that lends itself to accessible laboratory demonstrations [28, 87, 89, 90, 92, 93, 273] and promising applications to nanotechnology and medical sciences [55]. In the following, we sketch possible future implementations of the effects predicted in the present work and outline some extensions of our model that are expected to lead to new and useful results.

Tactic steering. As summarized above, the direction and magnitude of the tactic response are extremely sensitive to the swimmer's self-propulsion mechanism, which suggests the design of tactic devices to control the production and transport of artificial microswimmers. Here we have considered mostly fixed swimmer properties, such as self-propulsion speed and rotational diffusivity, and varied the pulse parameters to control the swimmer's drift. However, in the same way one could also specify a fixed activation sequence and vary the swimmer parameters. As swimmers with different self-propulsion speeds and different rotational diffusivities then can exhibit opposite tactic responses, the results presented in this work might inspire new and efficient particle separation techniques. Moreover, our analytical approach provides a valuable framework for future studies of the dynamics of artificial microswimmers in spatio-temporally modulated activating media.

Multiple interacting swimmers. The generalization of our single-particle model to multiple interacting swimmers, for instance similar to the setup considered in Ref. [66] for macroscopic phototactic robots, could help explore interesting new collective effects, as well. These are expected to emerge due to a coupling of the hydrodynamic swimmer-swimmer interactions to the activation gradient [91, 246].

Swimmer transport in corrugated channels. Upon further investigating the hydrodynamic interactions between artificial microswimmers and confining walls, in particular for curved geometries, our model can also be extended to the diffusion of such swimmers in narrow channels with corrugated walls [274], as the next step toward the design and operation of microfluidic devices powered by spatio-temporally modulated activation densities. We expect that the combination of self-polarization and hydrodynamic swimmer-wall interactions is likely to provide an additional and possibly competing orientational mechanism [168, 275], which can contribute to controlling the swimmers' flow in microfluidic circuits.

Asymmetric activation profile. Finally, we point out that in the present work we have considered solely spatially symmetric activation profiles with anti-symmetric gradients at the front and the rear of the pulses, in order to avoid additional ratchet effects [93]. However, a generalization of our results to traveling activation pulses with asymmetric waveforms is straightforward and might prove useful to design more sophisticated experimental setups.



TAXIS OF ARTIFICIAL MICROSWIMMERS INDUCED BY STATIC STIMULI

Artificial self-phoretic microswimmers—the operating principles of which have been discussed in Ch. 2—have been reported in recent years to tactically respond to various static (i.e., time-independent) external stimuli, such as activation gradients, gravitation, or flows in the surrounding fluid. Here we briefly review the current literature on the tactic response of artificial microswimmers to static external stimuli, as a supplement to the discussion of their response to the spatio-temporally varying signals considered in the main text.

A.1 Artificial Chemotaxis

A tactic behavior of artificial microswimmers was first observed by Y. Hong et al. in 2007 [87], who noticed an accumulation of self-electrophoretic Pt-Au microrods fueled by H_2O_2 , see Ch. 2.2.3, in regions of high H_2O_2 concentrations (Fig. A.1). Similar findings were reported later by other authors in several experimental and computational studies [92, 273, 276, 277].

Although the Pt-Au rods had no sophisticated internal structure and hence possessed no specific sensing capabilities, they responded chemotactically to the H_2O_2 gradient, which the authors explained by a purely stochastic effect induced by the swimmers' active diffusion in an external activation gradient. Indeed, it is shown in Ch. 3.1 that within the simple Langevin dynamics framework of Eq. (2.50), an artificial microswimmer is predicted to drift up a constant activation gradient of the form $w(x, t) \propto x$. However, the latter result holds

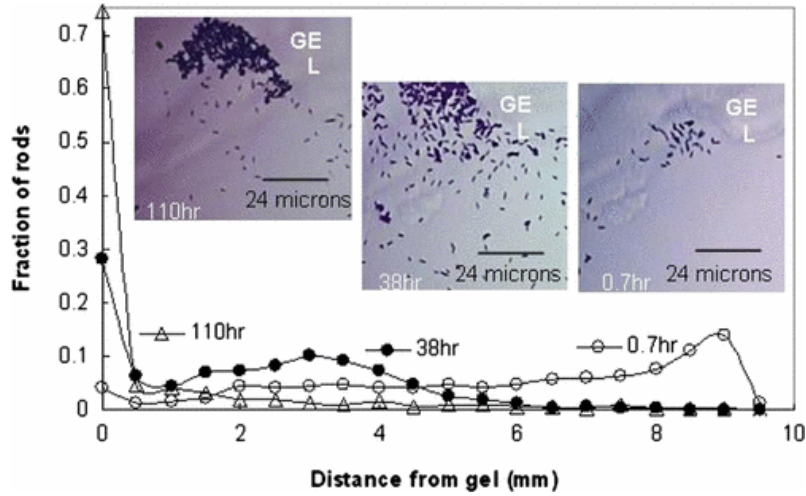


FIGURE A.1. Time evolution of the spatial distribution of rod-like Pt-Au microswimmers placed in an activation gradient, which was created by inserting a H_2O_2 -soaked gel into the system at $t = 0$. The insets depict micrographs of the actual particle accumulation near the gel at different times. Reprinted from Ref. [87] with permission.

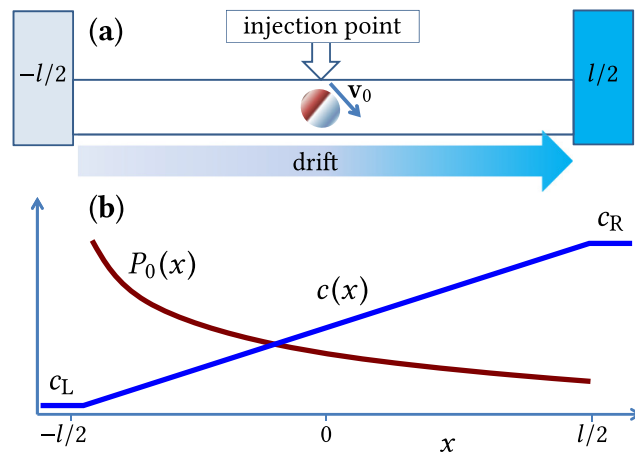


FIGURE A.2. Chemotaxis of an artificial microswimmer in a confined geometry. (a) Sketch of the considered setup. A swimmer is placed in the middle of a channel of length l , the ends of which are maintained at a constant fuel concentration c_L and c_R , respectively. The resulting linear fuel concentration gradient is described by the function $c(x)$, see panel (b). An initial drift of the particle toward the “hotter” right side (where the fuel concentration is higher) is observed; in the long-time limit, however, the influence of the confining walls prevails, causing the swimmer to be more likely located near the “cold” left end of the channel [cf. the particle’s probability density $P_0(x)$ in panel (b)]. Adapted from Ref. [88] with permission.

only in an unbounded geometry, i.e., in an infinitely extended gradient, where—independent of its actual position—the swimmer can always move toward a higher activation density. For a confined geometry, on the other hand, artificial microswimmers have been recently reported to accumulate in regions of low fuel concentrations [88] (see Fig. A.2), as suggested by the classic hot-cold argument.

The accumulation of swimmers in regions of high fuel concentrations observed in Ref. [87] thus cannot be explained by the stochastic single particle dynamics as discussed above; instead, it must either be a collective aggregation effect or arise from a (weak) self-polarization of the rods in the H_2O_2 gradient. The latter was indeed observed for similar rod-shaped artificial microswimmers in Ref. [277] and might very well also play a role in the accumulation pattern of the Pt-Au swimmers of Ref. [87]. Actually, self-polarization in an activation gradient was found to be the key factor governing the phototactic drift of self-diffusiophoretic microswimmers in an optical activation landscape, as addressed in the forthcoming section.

A.2 Artificial Phototaxis

C. Lozano et al. in 2016 studied the dynamics of artificial microswimmers activated by light¹, which were placed in a static, non-uniform illumination landscape as depicted in panels a and b of Fig. A.3 [93].

The resulting strong spatial modulation of the swimmers' activation, see Fig. A.3b, then gives rise to a self-polarization of the particles, which in the setup of Ref. [93] aligns them anti-parallel to the activation gradients². As a consequence, the swimmers tend to orient themselves to the left (right) in the red (blue) regions of Fig. A.3b. Depending on the actual self-polarization strength, this mechanism causes either their oscillating motion around the profile troughs (implying a vanishing net drift) or their successive crossing of the profile barriers to the left or to the right. Yet, an explicit calculation shows [93] that under the assumption that the self-polarizing angular speed is proportional to the strength of the activation gradient, swimmers move to the right and to the left with the same average speed and, moreover, the same probability. Hence, despite the ratchet-like shape of the activation profile, no overall particle drift should occur, in apparent contradiction to the experimental observations of Fig. A.3c.

The authors resolve this paradoxical situation by noticing that the self-polarizing angular velocity saturates at large values of $|\nabla I|$, for what reason the swimmers cannot react sufficiently

¹More precisely, the swimmers were driven by the local demixing mechanism described in Ch. 2.2.1.

²For a more detailed discussion of the underlying hydrodynamic effects, see Ch. 5.

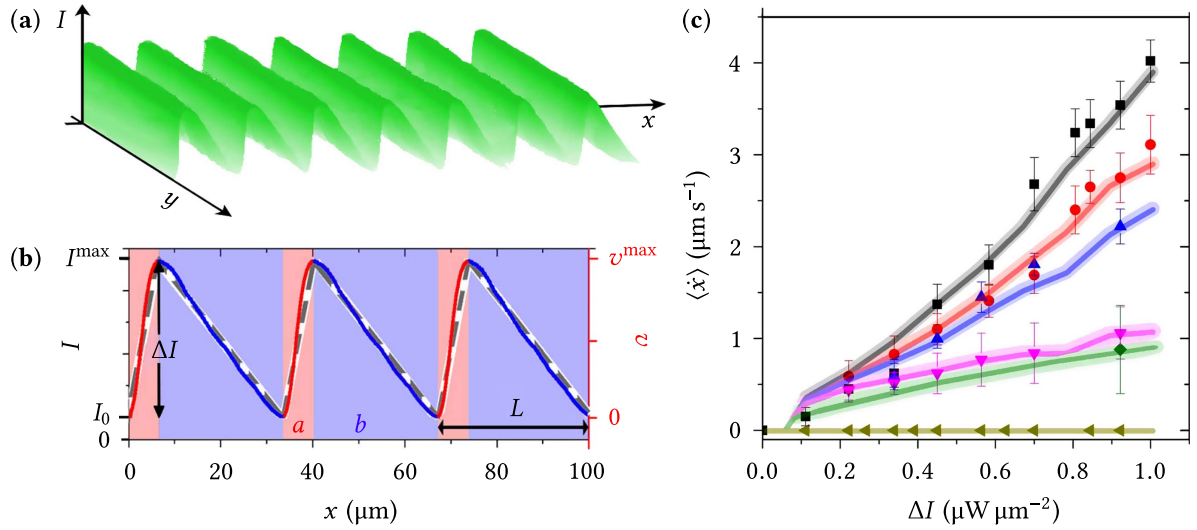


FIGURE A.3. Phototaxis of artificial microswimmers in optical landscapes [93]. (a) Measured intensity profile of the effectively one-dimensional, non-uniform light field activating the local demixing swimmers of Ch. 2.2.1. From panel (b), the profile asymmetry, characterized by the ratio a/b , becomes evident. The swimmers' self-propulsion sets in only after the light intensity I is raised above a certain threshold value I_0 and (for the considered intensities) then is proportional to $I - I_0$; see the right (red) axis of panel (b). Below I_0 , the light-absorbing region on the swimmers' surface is not heated above the critical temperature at which the local demixing in the surrounding fluid takes place and hence no propulsion is induced. In panel (c), the particle drift velocity $\langle \dot{x} \rangle$ is plotted versus the intensity amplitude $\Delta I := I^{\max} - I_0$, obtained both from experiments (symbols) and numerical simulations (solid lines), for $a/b = 1$ (khaki), $a/b = 0.75$ (pink), $a/b = 0.55$ (green), $a/b = 0.33$ (blue), $a/b = 0.28$ (red), and $a/b = 0.22$ (black). Adapted from Ref. [93] under a CC BY 4.0 license.

fast to the steeper edge of the activation profile. More precisely, their mean sojourn time in the red regions of Fig. A.3b is smaller than their reorientation time due to the self-polarization mechanism, so that particles can cross these regions with the “wrong” orientation [93]. This explains the net drift to the right displayed in Fig. A.3c.

By a similar principle, a rod-like phototactic “nanotree” was reported by B. Dai in 2016 to align itself (anti-)parallel to the illumination direction of an activating light source [52]: When irradiated, the particle catalyzes a photoelectrochemical redox reaction on its surface, see Fig. A.4a, which generates an asymmetric ion distribution in the surrounding fluid and eventually induces a self-electrophoretic propulsion along the swimmer's symmetry axis. If now the illumination direction is not parallel to this axis, the particle's brush-like end is

asymmetrically shaded and, since in the shaded regions fewer ions are produced, the overall ion distribution is also asymmetric perpendicularly to the rod's axis (see Fig. A.4b). As a consequence, the resulting electric field has a component perpendicular to the swimmer's propulsion direction that tends to align the latter (anti-)parallel to the illumination direction and causes a directed motion of the particle away from (toward) the activating light source.

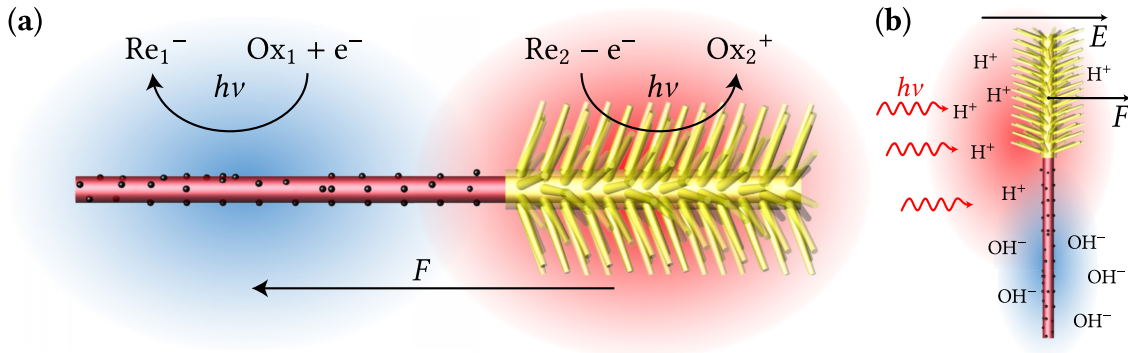


FIGURE A.4. Sketch of a phototactic artificial nanotree-swimmer [52]. **(a)** An assembly of TiO_2 nanowires (yellow) and platinum nanoparticles (black) are attached to a silicon microwire (red). When illuminated, both ends of the swimmer catalyze a photoelectrically induced chemical reaction: photoexcited holes in the TiO_2 wires oxidize a certain chemical Re_2 , while the thereby created electrons migrate through the rod and fuel an electrochemical reduction, $\text{Ox}_1 + e^- \rightarrow \text{Re}_1^-$, at the Pt-coated end. The electric field induced by the non-uniform ion distribution in the vicinity of the swimmer then propels the latter self-electrophoretically, as if an *effective* force F would act upon it. **(b)** Visualization of the particle's phototactic alignment toward or away from the activating light source (see the text). Here, for the sake of concreteness, the photoelectrochemical reaction is supposed to be a classic H_2O_2 decomposition, $\text{H}_2\text{O}_2 - 2e^- \rightarrow \text{O}_2 + 2\text{H}^+$ (TiO_2 end) and $\text{H}_2\text{O}_2 + 2e^- \rightarrow 2\text{OH}^-$ (Pt end). Adapted from Ref. [52] with permission.

A.3 Artificial Gravitaxis

Another type of tactic response of an artificial microswimmer, namely a directed drift parallel or opposite to the gravitational field, was reported in 2014 by B. ten Hagen et al. [89]. The authors again considered a self-diffusiophoretic swimmer operated by the mechanism of local demixing, which was developed earlier by C. Bechinger's group [38]. The particle geometry, however, was not spherical but L-shaped (as depicted in Fig. A.5a), which gives rise to an anisotropic hydrodynamic friction tensor. As a consequence, the swimmer aligned itself relative to the gravitational field when sedimenting (see Fig. A.5b), so that upon activation, it

moved up or down the gravitational field, depending on its self-propulsion strength and the magnitude of the gravitational force. A phase diagram of the possible swimmer trajectories is shown in Fig. A.5c. We note that due to its inherent asymmetry, the particle itself is subject to a chiral angular dynamics; hence, it starts to swim in a spiraling, trochoid-like manner (termed “TLM” in Fig. A.5c) once the self-propulsion becomes so strong that the associated effective chiral torque outweighs the restoring effect of the gravitational force.

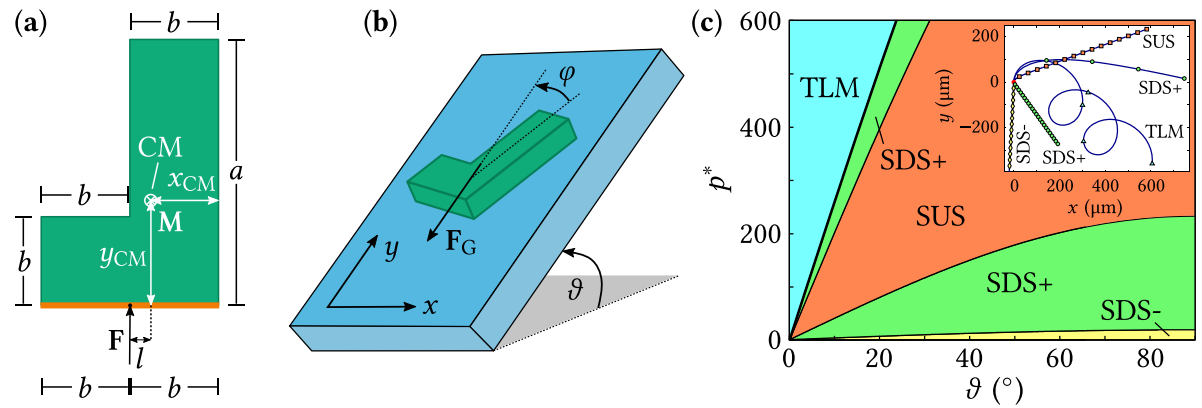


FIGURE A.5. Artificial gravitaxis [89]. (a) Sketch of the L-shaped microswimmer described in the text, where the orange line indicates a gold-coated region on the particle’s surface that is heated by laser irradiation. The resulting self-diffusiophoretic propulsion can again be described in terms of an effective force F acting upon the swimmer. Note that due to the asymmetric particle geometry, the point of origin of this force in general does not coincide with the swimmer’s center of mass, which gives rise to an effective chiral torque M . (b) Sketch of the particle’s alignment with the gravitational field F_G when sedimenting with disabled self-propulsion. By varying the inclination angle ϑ between the substrate and the horizontal plane, the effective gravitational force acting upon the swimmer can be tuned at the experimenter’s convenience. (c) State diagram of the possible trajectory types of a L-shaped microswimmer in the setup of panel (b) for $a = 9 \mu\text{m}$, $b = 3 \mu\text{m}$, and $l = -0.75 \mu\text{m}$, calculated by numerical simulations. Depending on the substrate inclination angle ϑ and the dimensionless parameter p^* , which determines the strength of the swimmer’s self-propulsion, a straight downward swimming with drift in the negative/positive x direction (SDS-/SDS+), a straight upward swimming (SUS), or a trochoid-like motion (TLM) can be observed; see the inset for a sample of noise-free swimmer trajectories. Adapted from Ref. [89] with permission.

A.4 Artificial Rheotaxis

By analogy with the above gravitactic drift, artificial microswimmers have also been observed to align themselves opposite to a stationary shear flow and thus effectively perform an upstream migration [90]. Again, an appropriate asymmetric particle shape—the authors of Ref. [90] considered sphere dimers driven by catalytic H_2O_2 decomposition—may result in a rectification of the swimmers against the fluid flow, which eventually leads to a directed upstream motion.

However, an asymmetric swimmer geometry is not even required for a rheotactic response to occur, as was reported by W. E. Uspal et al. in 2015 [91]. In a theoretical study, the authors found that, when subjected to a shear flow near a planar wall, spherical self-phoretic swimmers may drift upstream, too. Here, the hydrodynamic particle-wall interactions, together with the drag from the shear flow, were shown to lock the swimmer's orientation in a stable dynamical state near the wall, such that, as sketched in Fig. A.6, a constant particle migration opposite to the flow direction may occur.

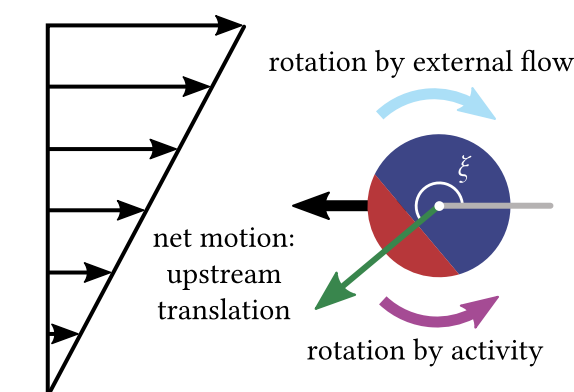


FIGURE A.6. Schematic illustration of the tactic response of a spherical, self-diffusiophoretic microswimmer to a shear flow near a planar wall [91]. The phoretic slip profile around the particle, induced by a catalytically active cap (blue), gets perturbed in the vicinity of the wall, which gives rise to an angular velocity component (magenta) that can counterbalance the rotation due to the external flow profile (cyan). In this case, the swimmer's orientation (illustrated by the green arrow and measured by the angle ξ) is in a rheotactic steady state, which, provided the self-propulsion is strong enough to overcome the drift induced by the external flow, leads to an upstream particle migration. Adapted from Ref. [91] with permission from The Royal Society of Chemistry.

In summary, a variety of tactic responses has been observed in recent years when subjecting artificial microswimmers to static stimuli, such as activation gradients (which can be

of optical or chemical nature), external forces, or fluid flows. The underlying mechanisms range from purely stochastic effects to rather complex hydrodynamic interactions and often manifest themselves even for very simple spherical particle geometries. Inspired by tactic effects in biological systems, see the Introduction, a natural generalization of the above setups is to consider not only static, but time-dependent tactic stimuli. This program is carried out in Chs. 3–5 of the main text.

TACTIC RESPONSE TO A CONSTANT ACTIVATION GRADIENT

In the following, we consider an artificial microswimmer diffusing in a static activation gradient, which, for simplicity, is supposed to be of the form $w(x) = (v/v_0)x$. Neglecting any saturation effects of the swimmer's self-propulsion speed (see the caption below Fig. 3.1) and assuming an achiral particle dynamics, $\Omega = 0$, the swimmer's longitudinal motion is then described by the linear LE

$$\dot{x} = v_0 w(x) \cos \phi + \sqrt{2D_0} \xi_x(t), \quad w(x) = \frac{v}{v_0} x, \quad \dot{\phi} = \sqrt{2D_\phi} \xi_\phi(t), \quad (\text{B.1})$$

cf. Eq. (2.50). The above system of equations can readily be solved, yielding

$$\phi(t) = \phi_0 + \sqrt{2D_\phi} W_\phi(t), \quad (\text{B.2})$$

$$x(t) = x_0 \exp\left(v \int_0^t \cos[\phi(\tau)] d\tau\right) + \sqrt{2D_0} \int_0^t \exp\left(v \int_\tau^t \cos[\phi(\tau')] d\tau'\right) \xi_x(\tau) d\tau, \quad (\text{B.3})$$

where $\phi_0 = \phi(0)$, $x_0 = x(0)$, and W_ϕ is the rotational Wiener process corresponding to the Gaussian white noise ξ_ϕ , $W_i(t) := \int_0^t \xi_i(\tau) d\tau$ for $i = x, \phi$. As ξ_x and ξ_ϕ are assumed to be independent of each other, upon averaging over Eq. (B.3) we obtain $[\forall t, \langle \xi_x(t) \rangle = \langle \xi_\phi(t) \rangle = 0]$:

$$\langle x(t) \rangle = x_0 \left\langle \exp\left(v \int_0^t \cos\left[\phi_0 + \sqrt{2D_\phi} W_\phi(\tau)\right] d\tau\right) \right\rangle. \quad (\text{B.4})$$

Here, we have assumed the swimmer's initial position x_0 to be a deterministic variable. By expanding the exponential function in Eq. (B.4) up to the second order, which surely is valid

for $\nu t \ll 1$, the expression for the swimmer's mean position simplifies to

$$\begin{aligned} \langle x(t) \rangle \approx x_0 & \left[1 + \nu \left\langle \int_0^t \cos \left[\phi_0 + \sqrt{2D_\phi} W_\phi(\tau) \right] d\tau \right\rangle \right. \\ & \left. + \frac{\nu^2}{2} \left\langle \left(\int_0^t \cos \left[\phi_0 + \sqrt{2D_\phi} W_\phi(\tau) \right] d\tau \right)^2 \right\rangle \right]. \end{aligned} \quad (\text{B.5})$$

Assuming ϕ_0 to be uniformly distributed in the interval $[0, 2\pi]$, the explicit calculation of the above moments eventually yields the compact result [227]

$$\langle x(t) \rangle = x_0 \left[1 + \frac{1}{2} \left(\frac{\nu}{D_\phi} \right)^2 \left[D_\phi t + \exp(-D_\phi t) - 1 \right] \right], \quad (\text{B.6})$$

as stated in Eq. (3.1). Note that in principle, also higher moments of the stochastic integral in Eq. (B.5) can be computed [227]. However, the results become increasingly complex (and thus more and more laborious to obtain), while not providing any significantly new insight into the current problem.

For $x_0 > 0$, Eq. (B.6) predicts a swimmer to drift to the right, that is, toward a higher activation density, as discussed in Ch. 3.1. Yet, for the sake of completeness, we remark that a negative starting value, $x_0 < 0$, implies a drift of the swimmer to the left, which might be surprising at first glance. Note, however, that for $x < 0$ the self-propulsion speed νx becomes increasingly negative. Nevertheless, its sign is of no consequence, as $\cos \phi$ takes on positive and negative values anyway, depending on the actual particle orientation. The swimmer's dynamics in the negative half-space is thus just the mirror-symmetric image of its dynamics in the positive half-space, why the drift to the left occurring for $x_0 < 0$ also corresponds to a drift toward higher activation densities.



TACTIC SHIFT INDUCED BY A SOLITON-LIKE PULSE

Let the activating pulse have a simple exponentially decaying symmetric profile, $w(x) = \text{sech}(x)$, and $D_0 = 0$. Starting from Eq. (3.10), we further rescale the time, $t =: (v_0/u)\tau$, which leaves only one effective parameter, $\eta := v_0^2/(2D_\phi Lu)$, in the resulting FPE. Upon introducing the auxiliary coordinate χ , $x =: \text{arsinh}(\sqrt{\eta}\chi)$, we rewrite the new FPE as

$$\frac{\partial \mathcal{P}(\chi, \tau)}{\partial \tau} = \left(\frac{\partial^2}{\partial \chi^2} + \frac{\partial}{\partial \chi} \sqrt{\frac{1}{\eta} + \chi^2} \right) \mathcal{P}(\chi, \tau), \quad (\text{C.1})$$

which for slow wave pulses, $u \ll v_0^2/(2D_\phi L)$ or $\eta \gg 1$, respectively, can be approximated by

$$\frac{\partial \mathcal{P}(\chi, \tau)}{\partial \tau} = \left(\frac{\partial^2}{\partial \chi^2} + \frac{\partial}{\partial \chi} |\chi| \right) \mathcal{P}(\chi, \tau). \quad (\text{C.2})$$

For $\chi \geq 0$ [$\chi < 0$], the corresponding Fokker-Planck operator is associated with a Hermitian operator, $\hat{\mathcal{F}}(\chi) \rightarrow \exp(\chi^2/4)\hat{\mathcal{F}}(\chi)\exp(-\chi^2/4)$ [$\hat{\mathcal{F}}(\chi) \rightarrow \exp(-\chi^2/4)\hat{\mathcal{F}}(\chi)\exp(\chi^2/4)$] [216]. Accordingly, the FPE (C.2) can be mapped onto the Schrödinger equation for a particle in the piecewise harmonic potential

$$V(\chi) = \begin{cases} \frac{1}{4}(\chi^2 - 2) : & \chi \geq 0 \\ \frac{1}{4}(\chi^2 + 2) : & \chi < 0. \end{cases}$$

The probability density $\mathcal{P}(\chi, \tau)$ could therefore be expressed, at least in principle, in terms of the eigenvalues and eigenfunctions of such Schrödinger equation. However, in view of the potential cusp at $\chi = 0$, that would be a challenging task. We thus resort once more to

computing the MFPT, $\langle \tau(\chi_1|\chi) \rangle$, by solving the relevant differential equation associated with the FPE (C.2), namely

$$-1 = \left(\frac{\partial^2}{\partial \chi^2} - |\chi| \frac{\partial}{\partial \chi} \right) \langle \tau(\chi_1|\chi) \rangle, \quad (\text{C.3})$$

with the boundary and continuity conditions

$$\begin{aligned} \text{i)} \quad & \langle \tau(\chi_1|\chi_1) \rangle = 0, \\ \text{ii)} \quad & \langle \tau(\chi_1|0^+) \rangle = \langle \tau(\chi_1|0^-) \rangle, \\ \text{iii)} \quad & \left. \frac{\partial \langle \tau(\chi_1|\chi) \rangle}{\partial \chi} \right|_{\chi=0^+} = \left. \frac{\partial \langle \tau(\chi_1|\chi) \rangle}{\partial \chi} \right|_{\chi=0^-}, \\ \text{iv)} \quad & \left. \frac{\partial \langle \tau(\chi_1|\chi) \rangle}{\partial \chi} \right|_{\chi \rightarrow \infty} = 0. \end{aligned}$$

Its solution for $\chi \geq 0$ reads

$$\langle \tau(\chi_1|\chi) \rangle = \frac{\pi}{2} \left[\operatorname{erfi} \left(\frac{\chi}{\sqrt{2}} \right) - \operatorname{erf} \left(\frac{\chi_1}{\sqrt{2}} \right) \right] - \frac{\chi^2}{2} {}_2F_2 \left(1, 1; \frac{3}{2}, 2; \frac{\chi^2}{2} \right) + \frac{\chi_1^2}{2} {}_2F_2 \left(1, 1; \frac{3}{2}, 2; -\frac{\chi_1^2}{2} \right), \quad (\text{C.4})$$

where $\operatorname{erfi}(x) := (2/\sqrt{\pi}) \int_0^x \exp(y^2) dy$ is the imaginary error function and

$${}_2F_2 \left(1, 1; \frac{3}{2}, 2; x \right) = \frac{\sqrt{\pi}}{x} \int_0^{\sqrt{x}} \operatorname{erf}(y) \exp(y^2) dy \quad (\text{C.5})$$

is a generalized hypergeometric function [278]. Thus, since in the present notation the particle displacement in the laboratory frame is calculated as $L[x(t) - x_0 + \tau]$, the swimmer's tactic shift is formally given by the expression

$$\begin{aligned} \Delta(\infty) = L \lim_{\substack{x_1 \rightarrow -\infty \\ x_0 \rightarrow \infty}} \left\{ x_1 - x_0 + \frac{\pi}{2} \left[\operatorname{erfi} \left(\frac{\sinh(x_0)}{\sqrt{2\eta}} \right) - \operatorname{erf} \left(\frac{\sinh(x_1)}{\sqrt{2\eta}} \right) \right] \right. \\ \left. - \frac{\sinh^2(x_0)}{2\eta} {}_2F_2 \left(1, 1; \frac{3}{2}, 2; \frac{\sinh^2(x_0)}{2\eta} \right) + \frac{\sinh^2(x_1)}{2\eta} {}_2F_2 \left(1, 1; \frac{3}{2}, 2; -\frac{\sinh^2(x_1)}{2\eta} \right) \right\}. \end{aligned} \quad (\text{C.6})$$

In order to explicitly take the above limits, one must now determine the asymptotic expansions of the special functions in Eq. (C.6). For $\operatorname{erfi}(x)$, this can be easily accomplished [279],

$$\operatorname{erfi}(x) \sim \frac{\exp(x^2)}{\sqrt{\pi} x} \quad (x \rightarrow \infty). \quad (\text{C.7})$$

The expansion of the hypergeometric function ${}_2F_2$ for $x \rightarrow \pm\infty$ is somewhat more elaborate. We start by considering its integral representation for *negative* arguments,

$${}_2F_2 \left(1, 1; \frac{3}{2}, 2; -x \right) = \frac{\sqrt{\pi}}{x} \int_0^{\sqrt{x}} \operatorname{erfi}(y) \exp(-y^2) dy \quad (x > 0), \quad (\text{C.8})$$

which follows directly from Eq. (C.5). By means of some algebraic substitutions and a binomial series expansion, the latter expression can then be brought to the form

$$\begin{aligned} {}_2F_2\left(1, 1; \frac{3}{2}, 2; -x\right) &= \frac{1}{2x} \int_0^x \frac{1 - \exp(-y)}{y \sqrt{1 - \frac{y}{x}}} dy \\ &= \frac{1}{2} \sum_{n=0}^{\infty} \binom{-\frac{1}{2}}{n} (-1)^n x^{-(n+1)} \int_0^x y^{n-1} [1 - \exp(-y)] dy. \end{aligned} \quad (\text{C.9})$$

The last integral in the above equation yields for $n = 0$:

$$\int_0^x \frac{1 - \exp(-y)}{y} dy = \lim_{y \rightarrow 0} [\ln(x) - \ln(y) + E_1(x) - E_1(y)], \quad (\text{C.10})$$

where $E_1(x) := \int_x^{\infty} e^{-y}/y dy$ is the exponential integral [187]. Upon considering the asymptotic behavior of $E_1(x)$ in the limits $x \rightarrow 0$ and $x \rightarrow \infty$ [187], we finally obtain

$$\int_0^x \frac{1 - \exp(-y)}{y} dy \sim \gamma + \ln(x) \quad (x \rightarrow \infty), \quad (\text{C.11})$$

with $\gamma \approx 0.577$ denoting the Euler-Mascheroni constant. For $n \geq 1$, the integral in the second line of Eq. (C.9) can readily be calculated [280], namely

$$\int_0^x y^{n-1} [1 - \exp(-y)] dy = \frac{x^n}{n} + \exp(-x) \sum_{i=0}^{n-1} \binom{n-1}{i} i! x^{n-1-i} \quad (n \geq 1). \quad (\text{C.12})$$

In conclusion, the asymptotic expansion of the hypergeometric function of Eq. (C.8) for large negative arguments reads, to the lowest orders,

$${}_2F_2\left(1, 1; \frac{3}{2}, 2; -x\right) \sim \frac{1}{2x} \left[\ln(x) + \gamma + \sum_{n=1}^{\infty} \binom{-\frac{1}{2}}{n} \frac{(-1)^n}{n} \right]. \quad (\text{C.13})$$

To sum the series of Eq. (C.13), we start from the integral representation of the digamma function $\Psi(x)$ [280],

$$\Psi(x) = -\gamma + \int_0^1 \frac{y^{x-1} - 1}{y - 1} dy, \quad (\text{C.14})$$

which, in turn, can be expanded into a Newton series, yielding

$$\Psi(x) = -\gamma - \sum_{n=1}^{\infty} \binom{x-1}{n} \frac{(-1)^n}{n}. \quad (\text{C.15})$$

Upon setting $x = 1/2$ in Eq. (C.15), one obtains the identity [187]

$$\sum_{n=1}^{\infty} \binom{-\frac{1}{2}}{n} \frac{(-1)^n}{n} = -\gamma - \Psi\left(\frac{1}{2}\right) = \ln(4), \quad (\text{C.16})$$

which, replaced into Eq. (C.13), leads to our final result,

$${}_2F_2\left(1, 1; \frac{3}{2}, 2; -x\right) \sim \frac{\ln(4x) + \gamma}{2x} \quad (x \rightarrow \infty). \quad (\text{C.17})$$

The asymptotic expansion of the ${}_2F_2$ function for large *positive* arguments follows immediately from the identity

$${}_2F_2\left(1, 1; \frac{3}{2}, 2; x\right) = \frac{\pi}{2x} \operatorname{erf}(\sqrt{x}) \operatorname{erfi}(\sqrt{x}) - {}_2F_2\left(1, 1; \frac{3}{2}, 2; -x\right), \quad (\text{C.18})$$

which one derives from Eq. (C.5) by partial integration. Hence, for $x \rightarrow \infty$,

$${}_2F_2\left(1, 1; \frac{3}{2}, 2; x\right) \sim \frac{\sqrt{\pi} \exp(x)}{2x^{3/2}} - \frac{\ln(4x) + \gamma}{2x}. \quad (\text{C.19})$$

By inserting the asymptotic expansions of Eqs. (C.7), (C.17), and (C.19) into Eq. (C.6), one verifies that the singularities for $x_0 \rightarrow \infty$ and $x_1 \rightarrow -\infty$ cancel out as expected ($\ln[4 \sinh^2(x)] \sim 2|x|$ for $x \rightarrow \pm\infty$) and the final result simplifies to the tractable expression in Eq. (3.19).



NUMERICAL METHODS

The numerical results of Chs. 3–5, namely the tactic response of an artificial microswimmer to traveling activation pulses, were obtained by numerically integrating the LE (2.50)¹ or the corresponding FPE, which is Eq. (3.5) for $s = \Omega = 0$, Eq. (4.16) for $s = 0$ and $\Omega \neq 0$, and Eq. (5.4) for $s \neq 0$ and $\Omega = 0$. Both numerical approaches yield—within their respective accuracy—the same results, so that we can adopt either of them, as more convenient. In general, solving the FPE is advantageous, since numerically integrating the LE for an ensemble of particles is rather time-consuming. For certain parameter ranges however, namely when the probability density P is sharply peaked, the spatial grid, on which the temporal evolution of the FPE has to be solved, would grow extremely fine. Memory consumption and computation time then explode, so that the numerical integration of the LE proves more effective.

D.1 Langevin Formalism

In the Langevin formalism, we numerically integrated the stochastic differential equations (2.50) by means of a standard Euler-Maruyama scheme [281], where the random numbers representing Gaussian white noise were generated using the *Mersenne twister* algorithm [282]. The stochastic averages were then taken over an ensemble of swimmer trajectories with random initial orientations, $\phi_0 \in [0, 2\pi]$. In order to reduce the stochastic errors, we applied the variance reduction technique of anti-thetic variates [283] and implemented the

¹We remind that for a self-polarizing swimmer, $s \neq 0$, the angular Langevin dynamics follows from Eq. (5.3).

multilevel Monte Carlo method [284, 285]. The latter allows to control both the stochastic *and* the discretization error of the numerical integration. Finally, the computation time was significantly shortened by parallelizing the simulation of the swimmer trajectories on a graphics processing unit using CUDA [286].

D.2 Fokker-Planck Formalism

An alternative (and usually faster) way to calculate the swimmer’s tactic shift or drift is based on the Fokker-Planck formalism. Here, the appropriate FPE is numerically solved for the probability density P , from which the moments of any function f of the swimmer state (x, y, ϕ) can be calculated by simple integration:

$$\langle f(x, y, \phi)^n \rangle = \int_{-\infty}^{\infty} \int_{-\infty}^{\infty} \int_0^{2\pi} f(x, y, \phi)^n P(x, y, \phi, t) d\phi dy dx. \quad (\text{D.1})$$

Note that, as mentioned in Ch. 3, the transverse coordinate y is dispensable for achiral swimmers with $\Omega = 0$, such that the integration over y can be performed *before* solving the FPE. This reduces the latter to a partial differential equation for the two-dimensional probability density $P(x, \phi, t)$ and, therefore, significantly saves memory and computation time.

For the numerical solution of the FPE we applied the method of lines [287], where the “spatial” discretization in the coordinates x , ϕ and, if necessary, y was performed using a central differencing scheme of varying order [288]. The resulting system of coupled ordinary differential equations in time was then integrated by means of a second-order backward differentiation formula [289]. However, in some situations the latter approach became numerically unstable, so that we had recourse to the finite volume method implemented within FiPy [290]. Here, the discretization in the coordinates x , ϕ , and y was realized by applying the power-law scheme [291] and the subsequent temporal integration was performed using an adaptive first-order backward differentiation formula.

In order to calculate the tactic shift discussed in Ch. 3, $\Delta(t)$, the FPE (3.5) was solved numerically for periodic boundary conditions in the angular coordinate ϕ and natural boundary conditions in the spatial coordinate x . The latter condition requires that $\lim_{x \rightarrow \pm\infty} P(x, \phi, t) = \lim_{x \rightarrow \pm\infty} J_x(x, \phi, t) = 0$, where J_x denotes the probability current in the x direction. Since we used the dimensionless coordinates in the co-moving pulse frame (see Ch. 3.4) also in our

numerical code, we eventually obtained $\Delta(t)$ from Eq. (3.11), that is,

$$\Delta(t) = L \left(\int_{-\infty}^{\infty} \int_0^{2\pi} x P(x, \phi, t) d\phi dx - x_0 + \frac{u}{v_0} t \right). \quad (\text{D.2})$$

Accordingly, the swimmer's final tactic shift $\Delta(\infty)$ follows from the above equation in the limit $t \rightarrow \infty$.

For the computation of the tactic drift v_x or v_y , we recast the FPE into a continuity equation, which in its most general form (i.e., accounting also for particle chirality and self-polarization) reads

$$\frac{\partial P(x, y, \phi, t)}{\partial t} = - \frac{\partial J_x(x, y, \phi, t)}{\partial x} - \frac{\partial J_y(x, y, \phi, t)}{\partial y} - \frac{\partial J_\phi(x, y, \phi, t)}{\partial \phi}, \quad (\text{D.3})$$

with

$$\begin{aligned} J_x(x, y, \phi, t) &= \left(-\frac{D_0}{Lv_0} \frac{\partial}{\partial x} + w(x) \cos \phi - \frac{u}{v_0} \right) P(x, y, \phi, t), \\ J_y(x, y, \phi, t) &= \left(-\frac{D_0}{Lv_0} \frac{\partial}{\partial y} + w(x) \sin \phi \right) P(x, y, \phi, t), \\ J_\phi(x, y, \phi, t) &= \left(-\frac{D_\phi L}{v_0} \frac{\partial}{\partial \phi} + \frac{\Omega L}{v_0} - s \frac{dw(x)}{dx} \sin \phi \right) P(x, y, \phi, t). \end{aligned} \quad (\text{D.4})$$

Here, J_y and J_ϕ are, respectively, the probability current in the y and ϕ direction. Periodic boundary conditions were assumed for all three variables x , y , and ϕ , with relevant periods 1, 1, and 2π . This amounts to the one-zone reduced formulation of the probability density [262],

$$\tilde{P}(x, y, \phi, t) = \sum_{i=-\infty}^{\infty} \sum_{n=-\infty}^{\infty} \sum_{m=-\infty}^{\infty} P(x+i, y+n, \phi+2\pi m, t), \quad (\text{D.5})$$

see Chs. 4.1.1 and 4.4.2. Finally, upon numerically calculating the swimmer's probability density P , the tactic drift velocities were computed as the stationary probability currents in the x and y direction, transformed back to the laboratory frame,

$$\begin{aligned} v_x &= v_0 \int_0^1 \int_0^1 \int_0^{2\pi} \lim_{t \rightarrow \infty} J_x(x, y, \phi, t) d\phi dy dx + u, \\ v_y &= v_0 \int_0^1 \int_0^1 \int_0^{2\pi} \lim_{t \rightarrow \infty} J_y(x, y, \phi, t) d\phi dy dx. \end{aligned} \quad (\text{D.6})$$

BIBLIOGRAPHY

- [1] J. D. MURRAY, *Mathematical Biology*, Springer, Berlin/Heidelberg, 2 ed., 1993.
- [2] J. P. ARMITAGE, *Bacterial tactic responses*, *Adv. Microb. Physiol.* **41**, 229 (1999).
- [3] M. EISENBACH AND L. C. GIOJALAS, *Sperm guidance in mammals — an unpaved road to the egg*, *Nat. Rev. Mol. Cell Biol.* **7**, 276 (2006).
- [4] M. MORISAWA, *Cell signaling mechanisms for sperm motility*, *Zool. Sci.* **11**, 647 (1994).
- [5] M. EISENBACH, *Sperm chemotaxis*, *Rev. Reprod.* **4**, 56 (1999).
- [6] B. M. FRIEDRICH AND F. JÜLICHER, *Chemotaxis of sperm cells*, *Proc. Natl. Acad. Sci.* **104**, 13256 (2007).
- [7] K. MIKI AND D. E. CLAPHAM, *Rheotaxis guides mammalian sperm*, *Curr. Biol.* **23**, 443 (2013).
- [8] S. PÉREZ-CEREZALES, S. BORYSHPOLETS, O. AFANZAR, A. BRANDIS, R. NEVO, V. KISS AND M. EISENBACH, *Involvement of opsins in mammalian sperm thermotaxis*, *Sci. Rep.* **5**, 16146 (2015).
- [9] J. ADLER, *Chemotaxis in bacteria*, *Science* **153**, 708 (1966).
- [10] H. C. BERG, *E. coli in Motion*, Springer, New York, 2004.
- [11] H. C. BERG AND E. M. PURCELL, *Physics of chemoreception*, *Biophys. J.* **20**, 193 (1977).
- [12] J. P. ARMITAGE AND M. C. W. EVANS, *The reaction centre in the phototactic and chemotactic response of photosynthetic bacteria*, *FEMS Microbiol. Lett.* **11**, 89 (1981).
- [13] G. H. WADHAMS AND J. P. ARMITAGE, *Making sense of it all: Bacterial chemotaxis*, *Nat. Rev. Mol. Cell Biol.* **5**, 1024 (2004).
- [14] S. W. BENDIX, *Phototaxis*, *Bot. Rev.* **26**, 145 (1960).

- [15] G. R. TREVIRANUS AND L. C. TREVIRANUS, *Vermischte Schriften anatomischen und physiologischen Inhalts, Bd. 2*, Johann Georg Heyse, Bremen, 1817.
- [16] H. GEST, *Phototaxis and other sensory phenomena in purple photosynthetic bacteria*, FEMS Microbiol. Rev. **16**, 287 (1995).
- [17] G. DREWS, *Contributions of Theodor Wilhelm Engelmann on phototaxis, chemotaxis, and photosynthesis*, Photosyn. Res. **83**, 25 (2005).
- [18] T. W. ENGELMANN, *Neue Methode zur Untersuchung der Sauerstoffausscheidung pflanzlicher und thierischer Organismen*, Pflügers Arch. Gesamte Physiol. Menschen Tiere **25**, 285 (1881).
- [19] ———, *Über Sauerstoffausscheidung von Pflanzenzellen im Mikrospektrum*, Pflügers Arch. Gesamte Physiol. Menschen Tiere **27**, 485 (1882).
- [20] W. PFEFFER, *Locomotorische Richtungsbewegungen durch chemische Reize*, Untersuchungen aus dem Botanischen Institut zu Tübingen **1**, 363 (1884).
- [21] ———, *Über chemotaktische Bewegungen von Bacterien, Flagellaten und Volvocineen*, Untersuchungen aus dem Botanischen Institut zu Tübingen **2**, 582 (1888).
- [22] F. SCHWEITZER, *Brownian Agents and Active Particles*, Springer, Berlin/Heidelberg, 2003.
- [23] P. ROMANCZUK, M. BÄR, W. EBELING, B. LINDNER AND L. SCHIMANSKY-GEIER, *Active Brownian particles: From individual to collective stochastic dynamics*, Eur. Phys. J. ST **202**, 1 (2012).
- [24] A. WALTHER AND A. H. E. MÜLLER, *Janus particles: Synthesis, self-assembly, physical properties, and applications*, Chem. Rev. **113**, 5194 (2013).
- [25] J. ELGETI, R. G. WINKLER AND G. GOMPPER, *Physics of microswimmers—single particle motion and collective behavior: A review*, Rep. Prog. Phys. **78**, 056601 (2015).
- [26] C. BECHINGER, R. DI LEONARDO, H. LÖWEN, C. REICHHARDT, G. VOLPE AND G. VOLPE, *Active particles in complex and crowded environments*, Rev. Mod. Phys. **88**, 045006 (2016).
- [27] A. WÜRGER, *Thermophoresis in colloidal suspensions driven by Marangoni forces*, Phys. Rev. Lett. **98**, 138301 (2007).

-
- [28] H.-R. JIANG, N. YOSHINAGA AND M. SANO, *Active motion of a Janus particle by self-thermophoresis in a defocused laser beam*, Phys. Rev. Lett. **105**, 268302 (2010).
- [29] I. BUTTINONI, G. VOLPE, F. KÜMMEL, G. VOLPE AND C. BECHINGER, *Active Brownian motion tunable by light*, J. Phys. Condens. Matter **24**, 284129 (2012).
- [30] M. YANG AND M. RIPOLL, *Thermophoretically induced flow field around a colloidal particle*, Soft Matter **9**, 4661 (2013).
- [31] G. FALASCO, R. PFALLER, A. P. BREGULLA, F. CICHOS AND K. KROY, *Exact symmetries in the velocity fluctuations of a hot Brownian swimmer*, Phys. Rev. E **94**, 030602 (2016).
- [32] W. F. PAXTON, A. SEN AND T. E. MALLOUK, *Motility of catalytic nanoparticles through self-generated forces*, Chem. Eur. J. **11**, 6462 (2005).
- [33] J. L. MORAN, P. M. WHEAT AND J. D. POSNER, *Locomotion of electrocatalytic nanomotors due to reaction induced charge autoelectrophoresis*, Phys. Rev. E **81**, 065302 (2010).
- [34] S. J. EBBENS, D. A. GREGORY, G. DUNDERDALE, J. R. HOWSE, Y. IBRAHIM, T. B. LIVERPOOL AND R. GOLESTANIAN, *Electrokinetic effects in catalytic platinum-insulator Janus swimmers*, EPL **106**, 58003 (2014).
- [35] R. GOLESTANIAN, T. B. LIVERPOOL AND A. AJDARI, *Propulsion of a molecular machine by asymmetric distribution of reaction products*, Phys. Rev. Lett. **94**, 220801 (2005).
- [36] J. R. HOWSE, R. A. L. JONES, A. J. RYAN, T. GOUGH, R. VAFABAKHSH AND R. GOLESTANIAN, *Self-motile colloidal particles: From directed propulsion to random walk*, Phys. Rev. Lett. **99**, 048102 (2007).
- [37] L. F. VALADARES, Y.-G. TAO, N. S. ZACHARIA, V. KITAEV, F. GALEMBECK, R. KAPRAL AND G. A. OZIN, *Catalytic nanomotors: Self-propelled sphere dimers*, Small **6**, 565 (2010).
- [38] G. VOLPE, I. BUTTINONI, D. VOGT, H.-J. KÜMMERER AND C. BECHINGER, *Microswimmers in patterned environments*, Soft Matter **7**, 8810 (2011).
- [39] A. WÜRGER, *Self-diffusiophoresis of Janus particles in near-critical mixtures*, Phys. Rev. Lett. **115**, 188304 (2015).
- [40] M.-J. HUANG, J. SCHOFIELD AND R. KAPRAL, *A microscopic model for chemically-powered Janus motors*, Soft Matter **12**, 5581 (2016).

- [41] C. CASAGRANDE AND M. VEYSSIÉ, «*Grains Janus*» : *Réalisation et premières observations des propriétés interfaciales*, C. R. Acad. Sci. Paris, Série II **306**, 1423 (1988).
- [42] C. CASAGRANDE, P. FABRE, E. RAPHAËL AND M. VEYSSIÉ, “*Janus beads*”: *Realization and behaviour at water/oil interfaces*, Europhys. Lett. (EPL) **9**, 251 (1989).
- [43] I. CHO AND K.-W. LEE, *Morphology of latex particles formed by poly(methyl methacrylate)-seeded emulsion polymerization of styrene*, J. Appl. Polym. Sci. **30**, 1903 (1985).
- [44] P.-G. DE GENNES, *Soft matter (Nobel lecture)*, Angew. Chemie Int. Ed. Engl. **31**, 842 (1992).
- [45] R. F. ISMAGILOV, A. SCHWARTZ, N. BOWDEN AND G. M. WHITESIDES, *Autonomous movement and self-assembly*, Angew. Chemie Int. Ed. **41**, 652 (2002).
- [46] W. F. PAXTON, K. C. KISTLER, C. C. OLMEDA, A. SEN, S. K. ST. ANGELO, Y. CAO, T. E. MALLOUK, P. E. LAMMERT AND V. H. CRESPI, *Catalytic nanomotors: Autonomous movement of striped nanorods*, J. Am. Chem. Soc. **126**, 13424 (2004).
- [47] M. LATTUADA AND T. A. HATTON, *Synthesis, properties and applications of Janus nanoparticles*, Nano Today **6**, 286 (2011).
- [48] J. C. LOVE, B. D. GATES, D. B. WOLFE, K. E. PAUL AND G. M. WHITESIDES, *Fabrication and wetting properties of metallic half-shells with submicron diameters*, Nano Lett. **2**, 891 (2002).
- [49] K.-H. ROH, D. C. MARTIN AND J. LAHANN, *Biphasic Janus particles with nanoscale anisotropy*, Nat. Mater. **4**, 759 (2005).
- [50] A. WALTHER, A. GÖLDEL AND A. H. E. MÜLLER, *Controlled crosslinking of polybutadiene containing block terpolymer bulk structures: A facile way towards complex and functional nanostructures*, Polymer (Guildf.) **49**, 3217 (2008).
- [51] F. KÜMMEL, B. TEN HAGEN, R. WITTKOWSKI, I. BUTTINONI, R. EICHHORN, G. VOLPE, H. LÖWEN AND C. BECHINGER, *Circular motion of asymmetric self-propelling particles*, Phys. Rev. Lett. **110**, 1 (2013).
- [52] B. DAI, J. WANG, Z. XIONG, X. ZHAN, W. DAI, C.-C. LI, S.-P. FENG AND J. TANG, *Programmable artificial phototactic microswimmer*, Nat. Nanotechnol. **11**, 1087 (2016).

-
- [53] F. PERUANI, A. DEUTSCH AND M. BÄR, *Nonequilibrium clustering of self-propelled rods*, Phys. Rev. E **74**, 030904 (2006).
- [54] E. BERTIN, M. DROZ AND G. GRÉGOIRE, *Hydrodynamic equations for self-propelled particles: Microscopic derivation and stability analysis*, J. Phys. A **42**, 445001 (2009).
- [55] Y. HONG, D. VELEGOL, N. CHATURVEDI AND A. SEN, *Biomimetic behavior of synthetic particles: From microscopic randomness to macroscopic control*, Phys. Chem. Chem. Phys. **12**, 1423 (2010).
- [56] A. PESHKOV, I. S. ARANSON, E. BERTIN, H. CHATÉ AND F. GINELLI, *Nonlinear field equations for aligning self-propelled rods*, Phys. Rev. Lett. **109**, 268701 (2012).
- [57] J. BIALKÉ, H. LÖWEN AND T. SPECK, *Microscopic theory for the phase separation of self-propelled repulsive disks*, EPL **103**, 30008 (2013).
- [58] M. E. CATES AND J. TAILLEUR, *When are active Brownian particles and run-and-tumble particles equivalent? Consequences for motility-induced phase separation*, EPL **101**, 20010 (2013).
- [59] S. SAHA, R. GOLESTANIAN AND S. RAMASWAMY, *Clusters, asters, and collective oscillations in chemotactic colloids*, Phys. Rev. E **89**, 062316 (2014).
- [60] T. SPECK, J. BIALKÉ, A. M. MENZEL AND H. LÖWEN, *Effective Cahn-Hilliard equation for the phase separation of active Brownian particles*, Phys. Rev. Lett. **112**, 218304 (2014).
- [61] A. WYSOCKI, R. G. WINKLER AND G. GOMPPER, *Cooperative motion of active Brownian spheres in three-dimensional dense suspensions*, EPL **105**, 48004 (2014).
- [62] A. ZÖTTL AND H. STARK, *Hydrodynamics determines collective motion and phase behavior of active colloids in quasi-two-dimensional confinement*, Phys. Rev. Lett. **112**, 118101 (2014).
- [63] R. GROSSMANN, P. ROMANCZUK, M. BÄR AND L. SCHIMANSKY-GEIER, *Pattern formation in active particle systems due to competing alignment interactions*, Eur. Phys. J. ST **224**, 1325 (2015).
- [64] S. WEITZ, A. DEUTSCH AND F. PERUANI, *Self-propelled rods exhibit a phase-separated state characterized by the presence of active stresses and the ejection of polar clusters*, Phys. Rev. E **92**, 012322 (2015).

- [65] A. DOMÍNGUEZ, P. MALGARETTI, M. N. POPESCU AND S. DIETRICH, *Collective dynamics of chemically active particles trapped at a fluid interface*, *Soft Matter* **12**, 8398 (2016).
- [66] M. MIJALKOV, A. MCDANIEL, J. WEHR AND G. VOLPE, *Engineering sensorial delay to control phototaxis and emergent collective behaviors*, *Phys. Rev. X* **6**, 011008 (2016).
- [67] S. C. TAKATORI AND J. F. BRADY, *Forces, stresses and the (thermo?) dynamics of active matter*, *Curr. Opin. Colloid Interface Sci.* **21**, 24 (2016).
- [68] J. KATURI, K. D. SEO, D. S. KIM AND S. SÁNCHEZ, *Artificial micro-swimmers in simulated natural environments*, *Lab Chip* **16**, 1101 (2016).
- [69] L. SOLER AND S. SÁNCHEZ, *Catalytic nanomotors for environmental monitoring and water remediation*, *Nanoscale* **6**, 7175 (2014).
- [70] L. SOLER, V. MAGDANZ, V. M. FOMIN, S. SÁNCHEZ AND O. G. SCHMIDT, *Self-propelled micromotors for cleaning polluted water*, *ACS Nano* **7**, 9611 (2013).
- [71] L. K. E. A. ABDELMOHSEN, F. PENG, Y. TU AND D. A. WILSON, *Micro- and nano-motors for biomedical applications*, *J. Mater. Chem. B* **2**, 2395 (2014).
- [72] U. KEI CHEANG, K. LEE, A. A. JULIUS AND M. J. KIM, *Multiple-robot drug delivery strategy through coordinated teams of microswimmers*, *Appl. Phys. Lett.* **105**, 083705 (2014).
- [73] W. F. PAXTON, S. SUNDARARAJAN, T. E. MALLOUK AND A. SEN, *Chemical locomotion*, *Angew. Chemie Int. Ed.* **45**, 5420 (2006).
- [74] S. SUNDARARAJAN, P. E. LAMMERT, A. W. ZUDANS, V. H. CRESPI AND A. SEN, *Catalytic motors for transport of colloidal cargo*, *Nano Lett.* **8**, 1271 (2008).
- [75] L. BARABAN, D. MAKAROV, R. STREUBEL, I. MÖNCH, D. GRIMM, S. SÁNCHEZ AND O. G. SCHMIDT, *Catalytic Janus motors on microfluidic chip: Deterministic motion for targeted cargo delivery*, *ACS Nano* **6**, 3383 (2012).
- [76] D. DEBNATH, P. K. GHOSH, Y. LI, F. MARCHESONI AND B. LI, *Communication: Cargo towing by artificial swimmers*, *J. Chem. Phys.* **145**, 191103 (2016).
- [77] B. QIAN, D. MONTIEL, A. P. BREGULLA, F. CICHOS AND H. YANG, *Harnessing thermal fluctuations for purposeful activities: The manipulation of single micro-swimmers by adaptive photon nudging*, *Chem. Sci.* **4**, 1420 (2013).

- [78] J. BURDICK, R. LAOCHAROENSUK, P. M. WHEAT, J. D. POSNER AND J. WANG, *Synthetic nanomotors in microchannel networks: Directional microchip motion and controlled manipulation of cargo*, J. Am. Chem. Soc. **130**, 8164 (2008).
- [79] A. GHOSH AND P. FISCHER, *Controlled propulsion of artificial magnetic nanostructured propellers*, Nano Lett. **9**, 2243 (2009).
- [80] S. AHMED, W. WANG, L. O. MAIR, R. D. FRALEIGH, S. LI, L. A. CASTRO, M. HOYOS, T. J. HUANG AND T. E. MALLOUK, *Steering acoustically propelled nanowire motors toward cells in a biologically compatible environment using magnetic fields*, Langmuir **29**, 16113 (2013).
- [81] D. TAKAGI, J. PALACCI, A. B. BRAUNSCHWEIG, M. J. SHELLEY AND J. ZHANG, *Hydrodynamic capture of microswimmers into sphere-bound orbits*, Soft Matter **10**, 1784 (2014).
- [82] S. DAS, A. GARG, A. I. CAMPBELL, J. R. HOWSE, A. SEN, D. VELEGOL, R. GOLESTANIAN AND S. J. EBBENS, *Boundaries can steer active Janus spheres*, Nat. Commun. **6**, 8999 (2015).
- [83] W. E. USPAL, M. N. POPESCU, S. DIETRICH AND M. TASINKEVYCH, *Self-propulsion of a catalytically active particle near a planar wall: From reflection to sliding and hovering*, Soft Matter **11**, 434 (2015).
- [84] S. PALAGI, A. G. MARK, S. Y. REIGH, K. MELDE, T. QIU, H. ZENG, C. PARMEGGIANI, D. MARTELLA, A. SANCHEZ-CASTILLO, N. KAPERNAUM, F. GIESSELMANN, D. S. WIERSMA, E. LAUGA AND P. FISCHER, *Structured light enables biomimetic swimming and versatile locomotion of photoresponsive soft microrobots*, Nat. Mater. **15**, 647 (2016).
- [85] J. SIMMCHEN, J. KATURI, W. E. USPAL, M. N. POPESCU, M. TASINKEVYCH AND S. SÁNCHEZ, *Topographical pathways guide chemical microswimmers*, Nat. Commun. **7**, 10598 (2016).
- [86] W. E. USPAL, M. N. POPESCU, S. DIETRICH AND M. TASINKEVYCH, *Guiding catalytically active particles with chemically patterned surfaces*, Phys. Rev. Lett. **117**, 048002 (2016).
- [87] Y. HONG, N. M. K. BLACKMAN, N. D. KOPP, A. SEN AND D. VELEGOL, *Chemotaxis of nonbiological colloidal rods*, Phys. Rev. Lett. **99**, 178103 (2007).
- [88] P. K. GHOSH, Y. LI, F. MARCHESONI AND F. NORI, *Pseudochemotactic drifts of artificial microswimmers*, Phys. Rev. E **92**, 012114 (2015).

- [89] B. TEN HAGEN, F. KÜMMEL, R. WITTKOWSKI, D. TAKAGI, H. LÖWEN AND C. BECHINGER, *Gravitaxis of asymmetric self-propelled colloidal particles*, Nat. Commun. **5**, 4829 (2014).
- [90] J. PALACCI, S. SACANNA, A. ABRAMIAN, J. BARRAL, K. HANSON, A. Y. GROSBERG, D. J. PINE AND P. M. CHAIKIN, *Artificial rheotaxis*, Sci. Adv. **1**, e1400214 (2015).
- [91] W. E. USPAL, M. N. POPESCU, S. DIETRICH AND M. TASINKEVYCH, *Rheotaxis of spherical active particles near a planar wall*, Soft Matter **11**, 6613 (2015).
- [92] J.-X. CHEN, Y.-G. CHEN AND Y.-Q. MA, *Chemotactic dynamics of catalytic dimer nanomotors*, Soft Matter **12**, 1876 (2016).
- [93] C. LOZANO, B. TEN HAGEN, H. LÖWEN AND C. BECHINGER, *Phototaxis of synthetic microswimmers in optical landscapes*, Nat. Commun. **7**, 12828 (2016).
- [94] J. P. ARMITAGE AND J. M. LACKIE, eds., *Biology of the Chemotactic Response*, Cambridge University Press, Cambridge, 1990.
- [95] D. WESSELS, J. MURRAY AND D. R. SOLL, *Behavior of Dictyostelium amoebae is regulated primarily by the temporal dynamic of the natural cAMP wave*, Cell Motil. Cytoskeleton **23**, 145 (1992).
- [96] G. G. STOKES, *On the theory of oscillatory waves*, Trans. Cambridge Philos. Soc. **8**, 441 (1847).
- [97] C. VAN DEN BROECK, *Stokes' drift: An exact result*, Europhys. Lett. (EPL) **46**, 1 (1999).
- [98] T. HÖFER, P. K. MAINI, J. A. SHERRATT, M. A. J. CHAPLAIN, P. CHAUVET, D. METEVIER, P. C. MONTES AND J. D. MURRAY, *A resolution of the chemotactic wave paradox*, Appl. Math. Lett. **7**, 1 (1994).
- [99] R. E. GOLDSTEIN, *Traveling-wave chemotaxis*, Phys. Rev. Lett. **77**, 4 (1996).
- [100] A. GEISELER, P. HÄNGGI, F. MARCHESONI, C. MULHERN AND S. SAVEL'EV, *Chemotaxis of artificial microswimmers in active density waves*, Phys. Rev. E **94**, 012613 (2016).
- [101] A. GEISELER, P. HÄNGGI AND F. MARCHESONI, *Taxis of artificial swimmers in a spatio-temporally modulated activation medium*, Entropy **19**, 97 (2017).
- [102] —, *Self-polarizing microswimmers in active density waves*, Sci. Rep. **7**, 41884 (2017).

-
- [103] A. SOMMERFELD, *Ein Beitrag zur hydrodynamischen Erklärung der turbulenten Flüssigkeitsbewegungen*, in *Atti del IV Congresso Internazionale dei Matematici*, volume 3, Rome, 1908, pp. 116–124.
- [104] E. M. PURCELL, *Life at low Reynolds number*, *Am. J. Phys.* **45**, 3 (1977).
- [105] J.-Y. CHENG, I. G. DAVISON AND M. E. DEMONT, *Dynamics and energetics of scallop locomotion*, *J. Exp. Biol.* **199**, 1931 (1996).
- [106] T. QIU, T.-C. LEE, A. G. MARK, K. I. MOROZOV, R. MÜNSTER, O. MIERKA, S. TUREK, A. M. LESHANSKY AND P. FISCHER, *Swimming by reciprocal motion at low Reynolds number*, *Nat. Commun.* **5**, 5119 (2014).
- [107] W. LUDWIG, *Zur Theorie der Flimmerbewegung (Dynamik, Nutzeffekt, Energiebilanz)*, *Z. Vgl. Physiol.* **13**, 397 (1930).
- [108] M. E. J. HOLWILL, *Physical aspects of flagellar movement*, *Physiol. Rev.* **46**, 698 (1966).
- [109] J. Lighthill, *Mathematical Biofluidynamics*, Society for Industrial and Applied Mathematics, Philadelphia, 1975.
- [110] ———, *Flagellar hydrodynamics: The John von Neumann lecture, 1975*, *SIAM Rev.* **18**, 161 (1976).
- [111] C. BRENNEN AND H. WINET, *Fluid mechanics of propulsion by cilia and flagella*, *Annu. Rev. Fluid Mech.* **9**, 339 (1977).
- [112] S. CHILDRESS, *Mechanics of Swimming and Flying*, Cambridge University Press, Cambridge, 1981.
- [113] G. T. YATES, *How microorganisms move through water: The hydrodynamics of ciliary and flagellar propulsion reveal how microorganisms overcome the extreme effect of the viscosity of water*, *Am. Sci.* **74**, 358 (1986).
- [114] H. C. BERG, *Motile behavior of bacteria*, *Phys. Today* **53**, 24 (2000).
- [115] J. BLAKE, *Fluid Mechanics of Ciliary Propulsion*, in *Computational Modeling in Biological Fluid Dynamics*, L. J. Fauci and S. Gueron, eds., Springer, New York, 2001, pp. 1–51.
- [116] L. J. FAUCI AND R. DILLON, *Biofluidmechanics of reproduction*, *Annu. Rev. Fluid Mech.* **38**, 371 (2006).

- [117] A. DAUPTAIN, J. FAVIER AND A. BOTTARO, *Hydrodynamics of ciliary propulsion*, J. Fluids Struct. **24**, 1156 (2008).
- [118] E. LAUGA AND T. R. POWERS, *The hydrodynamics of swimming microorganisms*, Rep. Prog. Phys. **72**, 096601 (2009).
- [119] G. K. TAYLOR, M. S. TRIANTAFYLLOU AND C. TROPEA, eds., *Animal Locomotion*, Springer, Berlin/Heidelberg, 2010.
- [120] S. E. SPAGNOLIE AND E. LAUGA, *Hydrodynamics of self-propulsion near a boundary: Predictions and accuracy of far-field approximations*, J. Fluid Mech. **700**, 105 (2012).
- [121] D. R. BRUMLEY, K. Y. WAN, M. POLIN AND R. E. GOLDSTEIN, *Flagellar synchronization through direct hydrodynamic interactions*, eLife **3**, e02750 (2014).
- [122] S. G. E. ANDERSSON AND C. DEHIO, *Rickettsia prowazekii and Bartonella henselae: Differences in the intracellular life styles revisited*, Int. J. Med. Microbiol. **290**, 135 (2000).
- [123] L. ALVAREZ, B. M. FRIEDRICH, G. GOMPPER AND U. B. KAUPP, *The computational sperm cell*, Trends Cell Biol. **24**, 198 (2014).
- [124] M. T. MADIGAN, J. M. MARTINKO, K. S. BENDER, D. H. BUCKLEY AND D. A. STAHL, *Brock Biology of Microorganisms*, Pearson, Boston, 14 ed., 2015.
- [125] R. M. MACNAB, *How bacteria assemble flagella*, Annu. Rev. Microbiol. **57**, 77 (2003).
- [126] R. D. ASTUMIAN AND P. HÄNGGI, *Brownian motors*, Phys. Today **55**, 33 (2002).
- [127] L. GHEBER AND Z. PRIEL, *Synchronization between beating cilia*, Biophys. J. **55**, 183 (1989).
- [128] S. GUERON, K. LEVIT-GUREVICH, N. LIRON AND J. J. BLUM, *Cilia internal mechanism and metachronal coordination as the result of hydrodynamical coupling*, Proc. Natl. Acad. Sci. **94**, 6001 (1997).
- [129] P. LENZ AND A. RYSKIN, *Collective effects in ciliar arrays*, Phys. Biol. **3**, 285 (2006).
- [130] A. VILFAN AND F. JÜLICHER, *Hydrodynamic flow patterns and synchronization of beating cilia*, Phys. Rev. Lett. **96**, 058102 (2006).
- [131] B. GUIRAO AND J.-F. JOANNY, *Spontaneous creation of macroscopic flow and metachronal waves in an array of cilia*, Biophys. J. **92**, 1900 (2007).

- [132] M. E. WERNER, P. HWANG, F. HUISMAN, P. TABOREK, C. C. YU AND B. J. MITCHELL, *Actin and microtubules drive differential aspects of planar cell polarity in multiciliated cells*, J. Cell Biol. **195**, 19 (2011).
- [133] E. R. BROOKS AND J. B. WALLINGFORD, *Multiciliated cells*, Curr. Biol. **24**, R973 (2014).
- [134] G. QUARANTA, M.-E. AUBIN-TAM AND D. TAM, *Hydrodynamics versus intracellular coupling in the synchronization of eukaryotic flagella*, Phys. Rev. Lett. **115**, 238101 (2015).
- [135] J. ELGETI AND G. GOMPPER, *Run-and-tumble dynamics of self-propelled particles in confinement*, EPL **109**, 58003 (2015).
- [136] B. E. SCHARF, K. A. FAHRNER, L. TURNER AND H. C. BERG, *Control of direction of flagellar rotation in bacterial chemotaxis*, Proc. Natl. Acad. Sci. **95**, 201 (1998).
- [137] R. DREYFUS, J. BAUDRY, M. L. ROPER, M. FERMIGIER, H. A. STONE AND J. BIBETTE, *Microscopic artificial swimmers*, Nature **437**, 862 (2005).
- [138] P. TIERNO, R. GOLESTANIAN, I. PAGONABARRAGA AND F. SAGUÉS, *Magnetically actuated colloidal microswimmers*, J. Phys. Chem. B **112**, 16525 (2008).
- [139] L. ZHANG, J. J. ABBOTT, L. DONG, K. E. PEYER, B. E. KRATOCHVIL, H. ZHANG, C. BERGELES AND B. J. NELSON, *Characterizing the swimming properties of artificial bacterial flagella*, Nano Lett. **9**, 3663 (2009).
- [140] J. DO, R. SCHREIBER, A. A. LUTICH, T. LIEDL, J. RODRÍGUEZ-FERNÁNDEZ AND J. FELDMANN, *Design and optical trapping of a biocompatible propeller-like nanoscale hybrid*, Nano Lett. **12**, 5008 (2012).
- [141] E. E. KEAVENY, S. W. WALKER AND M. J. SHELLEY, *Optimization of chiral structures for microscale propulsion*, Nano Lett. **13**, 531 (2013).
- [142] W. GAO, X. FENG, A. PEI, C. R. KANE, R. TAM, C. HENNESSY AND J. WANG, *Bioinspired helical microswimmers based on vascular plants*, Nano Lett. **14**, 305 (2014).
- [143] A. GHOSH, D. PARIJA, G. RANGARAJAN AND A. GHOSH, *Velocity fluctuations in helical propulsion: How small can a propeller be*, J. Phys. Chem. Lett. **5**, 62 (2014).
- [144] D. SCHAMEL, A. G. MARK, J. G. GIBBS, C. MIKSCH, K. I. MOROZOV, A. M. LESHANSKY AND P. FISCHER, *Nanopropellers and their actuation in complex viscoelastic media*, ACS Nano **8**, 8794 (2014).

- [145] P. MANDAL, V. CHOPRA AND A. GHOSH, *Independent positioning of magnetic nanomotors*, ACS Nano **9**, 4717 (2015).
- [146] P. J. VACH, P. FRATZL, S. KLUMPP AND D. FAIVRE, *Fast magnetic micropropellers with random shapes*, Nano Lett. **15**, 7064 (2015).
- [147] D. AHMED, T. BAASCH, B. JANG, S. PANE, J. DUAL AND B. J. NELSON, *Artificial swimmers propelled by acoustically activated flagella*, Nano Lett. **16**, 4968 (2016).
- [148] K. KIM, Z. LIANG, M. LIU AND D. E. FAN, *Biobased high-performance rotary micromotors for individually reconfigurable micromachine arrays and microfluidic applications*, ACS Appl. Mater. Interfaces **9**, 6144 (2017).
- [149] A. M. MAIER, C. WEIG, P. OSWALD, E. FREY, P. FISCHER AND T. LIEDL, *Magnetic propulsion of microswimmers with DNA-based flagellar bundles*, Nano Lett. **16**, 906 (2016).
- [150] Y. TU, F. PENG, A. ADAWY, Y. MEN, L. K. E. A. ABDELMOHSEN AND D. A. WILSON, *Mimicking the cell: Bio-inspired functions of supramolecular assemblies*, Chem. Rev. **116**, 2023 (2016).
- [151] B. TEN HAGEN, R. WITTKOWSKI, D. TAKAGI, F. KÜMMEL, C. BECHINGER AND H. LÖWEN, *Can the self-propulsion of anisotropic microswimmers be described by using forces and torques?*, J. Phys. Condens. Matter **27**, 194110 (2015).
- [152] M. N. POPESCU, W. E. USPAL AND S. DIETRICH, *Self-Diffusiophoresis of Chemically Active Colloids*, in *Microswimmers – From Single Particle Motion to Collective Behaviour*. Lecture Notes of the DFG SPP 1726 Summer School 2015, G. Gompper, C. Bechinger, S. Herminghaus, R. Isele-Holder, U. B. Kaupp, H. Löwen, H. Stark and R. G. Winkler, eds., Forschungszentrum Jülich GmbH Zentralbibliothek, Verlag, Jülich, 2015, ch. C1.
- [153] J. G. KIRKWOOD, *Statistical mechanics of fluid mixtures*, J. Chem. Phys. **3**, 300 (1935).
- [154] J. L. ANDERSON, *Colloid transport by interfacial forces*, Annu. Rev. Fluid Mech. **21**, 61 (1989).
- [155] B. SABASS AND U. SEIFERT, *Dynamics and efficiency of a self-propelled, diffusiophoretic swimmer*, J. Chem. Phys. **136**, 064508 (2012).
- [156] N. SHARIFI-MOOD, J. KOPLIK AND C. MALDARELLI, *Diffusiophoretic self-propulsion of colloids driven by a surface reaction: The sub-micron particle regime for exponential and van der Waals interactions*, Phys. Fluids **25**, 012001 (2013).

-
- [157] J. DE GRAAF, G. REMPFER AND C. HOLM, *Diffusiophoretic self-propulsion for partially catalytic spherical colloids*, IEEE Trans. Nanobioscience **14**, 272 (2015).
- [158] F. C. TSE AND O. C. SANDALL, *Diffusion coefficients for oxygen and carbon dioxide in water at 25°C by unsteady state desorption from a quiescent liquid*, Chem. Eng. Commun. **3**, 147 (1979).
- [159] M. N. POPESCU, S. DIETRICH AND G. OSHANIN, *Confinement effects on diffusiophoretic self-propellers*, J. Chem. Phys. **130**, 194702 (2009).
- [160] M. N. POPESCU, S. DIETRICH, M. TASINKEVYCH AND J. RALSTON, *Phoretic motion of spheroidal particles due to self-generated solute gradients*, Eur. Phys. J. E **31**, 351 (2010).
- [161] B. V. DERJAGUIN, G. P. SIDORENKOV, E. A. ZUBASHCHENKOV AND E. V. KISELEVA, *Kinetic phenomena in boundary films of liquids*, Kolloidn. Zh. **9**, 335 (1947).
- [162] R. GOLESTANIAN, T. B. LIVERPOOL AND A. AJDARI, *Designing phoretic micro- and nano-swimmers*, New J. Phys. **9**, 126 (2007).
- [163] M. N. POPESCU, M. TASINKEVYCH AND S. DIETRICH, *Pulling and pushing a cargo with a catalytically active carrier*, EPL **95**, 28004 (2011).
- [164] J. HAPPEL AND H. BRENNER, *Low Reynolds Number Hydrodynamics*, Nijhoff, The Hague, 1983.
- [165] H. K. KUIKEN, ed., *The Centenary of a Paper on Slow Viscous Flow by the Physicist H. A. Lorentz*, Springer Netherlands, Dordrecht, 1996.
- [166] S. VAN TEEFFELN AND H. LÖWEN, *Dynamics of a Brownian circle swimmer*, Phys. Rev. E **78**, 020101 (2008).
- [167] X. AO, P. K. GHOSH, Y. LI, G. SCHMID, P. HÄNGGI AND F. MARCHESONI, *Active Brownian motion in a narrow channel*, Eur. Phys. J. ST **223**, 3227 (2014).
- [168] Y. LI, P. K. GHOSH, F. MARCHESONI AND B. LI, *Manipulating chiral microswimmers in a channel*, Phys. Rev. E **90**, 062301 (2014).
- [169] X. AO, P. K. GHOSH, Y. LI, G. SCHMID, P. HÄNGGI AND F. MARCHESONI, *Diffusion of chiral Janus particles in a sinusoidal channel*, EPL **109**, 10003 (2015).

- [170] S. J. EBBENS, M.-H. TU, J. R. HOWSE AND R. GOLESTANIAN, *Size dependence of the propulsion velocity for catalytic Janus-sphere swimmers*, Phys. Rev. E **85**, 020401 (2012).
- [171] S. MICHELIN AND E. LAUGA, *Phoretic self-propulsion at finite Péclet numbers*, J. Fluid Mech. **747**, 572 (2014).
- [172] S. Y. REIGH AND R. KAPRAL, *Catalytic dimer nanomotors: Continuum theory and microscopic dynamics*, Soft Matter **11**, 3149 (2015).
- [173] J. PALACCI, S. SACANNA, A. P. STEINBERG, D. J. PINE AND P. M. CHAIKIN, *Living crystals of light-activated colloidal surfers*, Science **339**, 936 (2013).
- [174] X. MA, A. JANNASCH, U.-R. ALBRECHT, K. HAHN, A. MIGUEL-LÓPEZ, E. SCHÄFFER AND S. SÁNCHEZ, *Enzyme-powered hollow mesoporous Janus nanomotors*, Nano Lett. **15**, 7043 (2015).
- [175] X. MA, K. HAHN AND S. SÁNCHEZ, *Catalytic mesoporous Janus nanomotors for active cargo delivery*, J. Am. Chem. Soc. **137**, 4976 (2015).
- [176] J. PARMAR, X. MA, J. KATURI, J. SIMMCHEN, M. M. STANTON, C. TRICHET-PAREDES, L. SOLER AND S. SÁNCHEZ, *Nano and micro architectures for self-propelled motors*, Sci. Technol. Adv. Mater. **16**, 014802 (2015).
- [177] A. A. SOLOVEV, Y. MEI, E. BERMÚDEZ UREÑA, G. HUANG AND O. G. SCHMIDT, *Catalytic microtubular jet engines self-propelled by accumulated gas bubbles*, Small **5**, 1688 (2009).
- [178] S. SÁNCHEZ, A. N. ANANTH, V. M. FOMIN, M. VIEHRIG AND O. G. SCHMIDT, *Superfast motion of catalytic microjet engines at physiological temperature*, J. Am. Chem. Soc. **133**, 14860 (2011).
- [179] D. A. WILSON, R. J. M. NOLTE AND J. C. M. VAN HEST, *Autonomous movement of platinum-loaded stomatocytes*, Nat. Chem. **4**, 268 (2012).
- [180] J. W. CAHN, *On spinodal decomposition*, Acta Metall. **9**, 795 (1961).
- [181] K. BINDER AND D. STAUFFER, *Theory for the slowing down of the relaxation and spinodal decomposition of binary mixtures*, Phys. Rev. Lett. **33**, 1006 (1974).

- [182] C. A. GRATTONI, R. A. DAWE, C. Y. SEAH AND J. D. GRAY, *Lower critical solution coexistence curve and physical properties (density, viscosity, surface tension, and interfacial tension) of 2,6-lutidine + water*, J. Chem. Eng. Data **38**, 516 (1993).
- [183] T. BICKEL, A. MAJEE AND A. WÜRGER, *Flow pattern in the vicinity of self-propelling hot Janus particles*, Phys. Rev. E **88**, 012301 (2013).
- [184] D. W. JAMES, *The thermal diffusivity of ice and water between -40 and +60° C*, J. Mater. Sci. **3**, 540 (1968).
- [185] T. KATSURA, *Thermal diffusivity of silica glass at pressures up to 9 GPa*, Phys. Chem. Miner. **20**, 201 (1993).
- [186] S. DUHR AND D. BRAUN, *Thermophoretic depletion follows Boltzmann distribution*, Phys. Rev. Lett. **96**, 168301 (2006).
- [187] M. ABRAMOWITZ AND I. A. STEGUN, eds., *Handbook of Mathematical Functions*, U.S. Government Printing Office, Washington, D.C., 10 ed., 1972.
- [188] B. V. DERJAGUIN, N. V. CHURAEV AND V. M. MULLER, *Surface Forces*, Springer US, Boston, 1987.
- [189] L. ONSAGER, *Reciprocal relations in irreversible processes. I.*, Phys. Rev. **37**, 405 (1931).
- [190] A. WÜRGER, *Thermal non-equilibrium transport in colloids*, Rep. Prog. Phys. **73**, 126601 (2010).
- [191] F. CICHOS AND K. KROY, *Self-Thermophoretic Swimming*, in *Microswimmers – From Single Particle Motion to Collective Behaviour*. Lecture Notes of the DFG SPP 1726 Summer School 2015, G. Gompper, C. Bechinger, S. Herminghaus, R. Isele-Holder, U. B. Kaupp, H. Löwen, H. Stark and R. G. Winkler, eds., Forschungszentrum Jülich GmbH Zentralbibliothek, Verlag, Jülich, 2015, ch. C3.
- [192] R. PIAZZA AND A. PAROLA, *Thermophoresis in colloidal suspensions*, J. Phys. Condens. Matter **20**, 153102 (2008).
- [193] A. PAROLA AND R. PIAZZA, *Particle thermophoresis in liquids*, Eur. Phys. J. E **15**, 255 (2004).
- [194] A. P. BREGULLA, H. YANG AND F. CICHOS, *Stochastic localization of microswimmers by photon nudging*, ACS Nano **8**, 6542 (2014).

- [195] P. DEBYE AND E. HÜCKEL, *Zur Theorie der Elektrolyte. I. Gefrierpunktserniedrigung und verwandte Erscheinungen.*, Phys. Z. **24**, 185 (1923).
- [196] P. C. HIEMENZ AND R. RAJAGOPALAN, *Principles of Colloid and Surface Chemistry*, Marcel Dekker, Inc., New York, 3 ed., 1997.
- [197] M. VON SMOLUCHOWSKI, *Contribution à la théorie de l'endosmose électrique et de quelques phénomènes corrélatifs*, Bull. Int. Acad. Sci. Cracovie, Cl. Sci. Math. **3**, 182 (1903).
- [198] J. L. MORAN AND J. D. POSNER, *Electrokinetic locomotion due to reaction-induced charge auto-electrophoresis*, J. Fluid Mech. **680**, 31 (2011).
- [199] E. YARIV, *Electrokinetic self-propulsion by inhomogeneous surface kinetics*, Proc. Royal Soc. A **467**, 1645 (2011).
- [200] A. NOURHANI, P. E. LAMMERT, V. H. CRESPI AND A. BORHAN, *A general flux-based analysis for spherical electrocatalytic nanomotors*, Phys. Fluids **27**, 012001 (2015).
- [201] A. NOURHANI, V. H. CRESPI, P. E. LAMMERT AND A. BORHAN, *Self-electrophoresis of spheroidal electrocatalytic swimmers*, Phys. Fluids **27**, 092002 (2015).
- [202] W. F. PAXTON, P. T. BAKER, T. R. KLINE, Y. WANG, T. E. MALLOUK AND A. SEN, *Catalytically induced electrokinetics for motors and micropumps*, J. Am. Chem. Soc. **128**, 14881 (2006).
- [203] Y. WANG, R. M. HERNANDEZ, D. J. BARTLETT, J. M. BINGHAM, T. R. KLINE, A. SEN AND T. E. MALLOUK, *Bipolar electrochemical mechanism for the propulsion of catalytic nanomotors in hydrogen peroxide solutions*, Langmuir **22**, 10451 (2006).
- [204] S. SENGUPTA, M. E. IBELE AND A. SEN, *Fantastic voyage: Designing self-powered nanorobots*, Angew. Chemie Int. Ed. **51**, 8434 (2012).
- [205] S. FOURNIER-BIDOZ, A. C. ARSENAULT, I. MANNERS AND G. A. OZIN, *Synthetic self-propelled nanorobots*, Chem. Commun., 441 (2005).
- [206] N. MANO AND A. HELLER, *Bioelectrochemical propulsion*, J. Am. Chem. Soc. **127**, 11574 (2005).
- [207] R. LIU AND A. SEN, *Autonomous nanomotor based on copper-platinum segmented nanobattery*, J. Am. Chem. Soc. **133**, 20064 (2011).

-
- [208] T.-C. LEE, M. ALARCÓN-CORREA, C. MIKSCH, K. HAHN, J. G. GIBBS AND P. FISCHER, *Self-propelling nanomotors in the presence of strong Brownian forces*, Nano Lett. **14**, 2407 (2014).
- [209] D. RINGS, R. SCHACHOFF, M. SELMKE, F. CICHOS AND K. KROY, *Hot Brownian motion*, Phys. Rev. Lett. **105**, 090604 (2010).
- [210] D. CHAKRABORTY, M. V. GNANN, D. RINGS, J. GLASER, F. OTTO, F. CICHOS AND K. KROY, *Generalised Einstein relation for hot Brownian motion*, EPL **96**, 60009 (2011).
- [211] D. RINGS, M. SELMKE, F. CICHOS AND K. KROY, *Theory of hot Brownian motion*, Soft Matter **7**, 3441 (2011).
- [212] G. FALASCO AND K. KROY, *Nonisothermal fluctuating hydrodynamics and Brownian motion*, Phys. Rev. E **93**, 032150 (2016).
- [213] D. RINGS, D. CHAKRABORTY AND K. KROY, *Rotational hot Brownian motion*, New J. Phys. **14**, 053012 (2012).
- [214] G. FALASCO, M. V. GNANN, D. RINGS AND K. KROY, *Effective temperatures of hot Brownian motion*, Phys. Rev. E **90**, 032131 (2014).
- [215] P. LANGEVIN, *Sur la théorie du mouvement brownien*, C. R. Acad. Sci. Paris **146**, 530 (1908).
- [216] H. RISKEN, *The Fokker-Planck Equation*, Springer, Berlin/Heidelberg, 2 ed., 1989.
- [217] W. T. COFFEY, Y. P. KALMYKOV AND J. T. WALDRON, *The Langevin Equation*, World Scientific, Singapore, 2 ed., 2004.
- [218] D. G. CROWDY, *Wall effects on self-diffusiophoretic Janus particles: A theoretical study*, J. Fluid Mech. **735**, 473 (2013).
- [219] B. TEN HAGEN, S. VAN TEEFFELN AND H. LÖWEN, *Brownian motion of a self-propelled particle*, J. Phys. Condens. Matter **23**, 194119 (2011).
- [220] I. N. SERDYUK, N. R. ZACCAI AND J. ZACCAI, *Methods in Molecular Biophysics: Structure, Dynamics, Function*, Cambridge University Press, New York, 2007.
- [221] H. S. JENNINGS, *On the significance of the spiral swimming of organisms*, Am. Nat. **35**, 369 (1901).

- [222] H. C. BERG AND L. TURNER, *Chemotaxis of bacteria in glass capillary arrays. Escherichia coli, motility, microchannel plate, and light scattering*, Biophys. J. **58**, 919 (1990).
- [223] E. LAUGA, W. R. DiLUZIO, G. M. WHITESIDES AND H. A. STONE, *Swimming in circles: Motion of bacteria near solid boundaries*, Biophys. J. **90**, 400 (2006).
- [224] B. M. FRIEDRICH AND F. JÜLICHER, *The stochastic dance of circling sperm cells: Sperm chemotaxis in the plane*, New J. Phys. **10**, 123025 (2008).
- [225] M. MIJALKOV AND G. VOLPE, *Sorting of chiral microswimmers*, Soft Matter **9**, 6376 (2013).
- [226] B.-Q. AI, Y.-F. HE AND W.-R. ZHONG, *Chirality separation of mixed chiral microswimmers in a periodic channel*, Soft Matter **11**, 3852 (2015).
- [227] B. TEN HAGEN, S. VAN TEEFFELEN AND H. LÖWEN, *Non-Gaussian behaviour of a self-propelled particle on a substrate*, Condens. Matter Phys. **12**, 725 (2009).
- [228] P. K. GHOSH, V. R. MISKO, F. MARCHESONI AND F. NORI, *Self-propelled Janus particles in a ratchet: Numerical simulations*, Phys. Rev. Lett. **110**, 1 (2013).
- [229] T. F. F. FARAGE, P. KRINNINGER AND J. M. BRADER, *Effective interactions in active Brownian suspensions*, Phys. Rev. E **91**, 042310 (2015).
- [230] Y. FILY, A. BASKARAN AND M. F. HAGAN, *Equilibrium mappings in polar-isotropic confined active particles*, Eur. Phys. J. E **40**, 61 (2017).
- [231] U. M. B. MARCONI, A. PUGLISI AND C. MAGGI, *Heat, temperature and Clausius inequality in a model for active Brownian particles*, Sci. Rep. **7**, 46496 (2017).
- [232] P. HÄNGGI AND P. JUNG, *Colored Noise in Dynamical Systems*, in Advances in Chemical Physics, Vol. 89, I. Prigogine and S. A. Rice, eds., Wiley, New York, 1994, pp. 239–326.
- [233] S. J. EBBENS, R. A. L. JONES, A. J. RYAN, R. GOLESTANIAN AND J. R. HOWSE, *Self-assembled autonomous runners and tumblers*, Phys. Rev. E **82**, 015304 (2010).
- [234] S. KOGA AND Y. KURAMOTO, *Localized patterns in reaction-diffusion systems*, Prog. Theor. Phys. **63**, 106 (1980).
- [235] Y. KURAMOTO, *Instability and turbulence of wavefronts in reaction-diffusion systems*, Prog. Theor. Phys. **63**, 1885 (1980).
- [236] ———, *Chemical Oscillations, Waves, and Turbulence*, Springer, Berlin/Heidelberg, 1984.

-
- [237] V. S. ZYKOV AND A. T. WINFREE, *Simulation of Wave Processes in Excitable Media*, Wiley, New York, 1992.
- [238] R. KAPRAL AND K. SHOWALTER, eds., *Chemical Waves and Patterns*, Springer Netherlands, Dordrecht, 1995.
- [239] A. S. MIKHAILOV AND K. SHOWALTER, *Control of waves, patterns and turbulence in chemical systems*, Phys. Rep. **425**, 79 (2006).
- [240] V. K. VANAG AND I. R. EPSTEIN, *Design and control of patterns in reaction-diffusion systems*, Chaos **18**, 026107 (2008).
- [241] H. DIERCKX, O. BERNUS AND H. VERSCHELDE, *Accurate eikonal-curvature relation for wave fronts in locally anisotropic reaction-diffusion systems*, Phys. Rev. Lett. **107**, 108101 (2011).
- [242] S. THAKUR, J.-X. CHEN AND R. KAPRAL, *Interaction of a chemically propelled nanomotor with a chemical wave*, Angew. Chemie Int. Ed. **50**, 10165 (2011).
- [243] J. LÖBER, S. MARTENS AND H. ENGEL, *Shaping wave patterns in reaction-diffusion systems*, Phys. Rev. E **90**, 062911 (2014).
- [244] R. M. NAVARRO AND S. M. FIELDING, *Clustering and phase behaviour of attractive active particles with hydrodynamics*, Soft Matter **11**, 7525 (2015).
- [245] T. A. WITTEN AND P. A. PINCUS, *Structured Fluids. Polymers, Colloids, Surfactants*, Oxford University Press, New York, 2004.
- [246] T. BICKEL, G. ZECUA AND A. WÜRGER, *Polarization of active Janus particles*, Phys. Rev. E **89**, 050303 (2014).
- [247] X. ZHENG, B. TEN HAGEN, A. KAISER, M. WU, H. CUI, Z. SILBER-LI AND H. LÖWEN, *Non-Gaussian statistics for the motion of self-propelled Janus particles: Experiment versus theory*, Phys. Rev. E **88**, 032304 (2013).
- [248] P. K. GHOSH, Y. LI, G. MARCHEGANI AND F. MARCHESONI, *Communication: Memory effects and active Brownian diffusion*, J. Chem. Phys. **143**, 211101 (2015).
- [249] G. MARCHEGANI AND F. MARCHESONI, *Driven microswimmers on a 2D substrate: A stochastic towed sled model*, J. Chem. Phys. **143**, 184901 (2015).

- [250] A. ERBE, M. ZIENTARA, L. BARABAN, C. KREIDLER AND P. LEIDERER, *Various driving mechanisms for generating motion of colloidal particles*, J. Phys. Condens. Matter **20**, 404215 (2008).
- [251] M. BORROMEO AND F. MARCHESONI, *Brownian surfers*, Phys. Lett. A **249**, 199 (1998).
- [252] P. HÄNGGI AND F. MARCHESONI, *Artificial Brownian motors: Controlling transport on the nanoscale*, Rev. Mod. Phys. **81**, 387 (2009).
- [253] R. RAJARAMAN, *Solitons and Instantons*, North Holland (Elsevier), Amsterdam, 1989.
- [254] P. KALINAY AND J. K. PERCUS, *Corrections to the Fick-Jacobs equation*, Phys. Rev. E **74**, 041203 (2006).
- [255] ———, *Approximations of the generalized Fick-Jacobs equation*, Phys. Rev. E **78**, 021103 (2008).
- [256] ———, *Mapping of diffusion in a channel with soft walls*, Phys. Rev. E **83**, 031109 (2011).
- [257] P. KALINAY, *Effective transport equations in quasi 1D systems*, Eur. Phys. J. ST **223**, 3027 (2014).
- [258] A. GEISELER, P. HÄNGGI AND G. SCHMID, *Kramers escape of a self-propelled particle*, Eur. Phys. J. B **89**, 175 (2016).
- [259] S. REDNER, *A Guide to First-Passage Processes*, Cambridge University Press, Cambridge, 2001.
- [260] N. S. GOEL AND N. RICHTER-DYN, *Stochastic Models in Biology*, Academic Press, New York, 1974.
- [261] P. S. BURADA, G. SCHMID, D. REGUERA, J. M. RUBÍ AND P. HÄNGGI, *Biased diffusion in confined media: Test of the Fick-Jacobs approximation and validity criteria*, Phys. Rev. E **75**, 051111 (2007).
- [262] P. S. BURADA, G. SCHMID AND P. HÄNGGI, *Entropic transport: A test bed for the Fick-Jacobs approximation*, Philos. Trans. A. Math. Phys. Eng. Sci. **367**, 3157 (2009).
- [263] G. COSTANTINI AND F. MARCHESONI, *Threshold diffusion in a tilted washboard potential*, Europhys. Lett. (EPL) **48**, 491 (1999).

-
- [264] P. REIMANN, C. VAN DEN BROECK, H. LINKE, P. HÄNGGI, J. M. RUBÍ AND A. PÉREZ-MADRID, *Giant acceleration of free diffusion by use of tilted periodic potentials*, Phys. Rev. Lett. **87**, 010602 (2001).
- [265] ———, *Diffusion in tilted periodic potentials: Enhancement, universality, and scaling*, Phys. Rev. E **65**, 031104 (2002).
- [266] D. TAKAGI, A. B. BRAUNSCHWEIG, J. ZHANG AND M. J. SHELLEY, *Dispersion of self-propelled rods undergoing fluctuation-driven flips*, Phys. Rev. Lett. **110**, 038301 (2013).
- [267] R. BENZI, A. SUTERA AND A. VULPIANI, *The mechanism of stochastic resonance*, J. Phys. A **14**, L453 (1981).
- [268] P. JUNG AND P. HÄNGGI, *Amplification of small signals via stochastic resonance*, Phys. Rev. A **44**, 8032 (1991).
- [269] K. WIESENFELD AND F. MOSS, *Stochastic resonance and the benefits of noise: From ice ages to crayfish and SQUIDS*, Nature **373**, 33 (1995).
- [270] L. GAMMAITONI, P. HÄNGGI, P. JUNG AND F. MARCHESONI, *Stochastic resonance*, Rev. Mod. Phys. **70**, 223 (1998).
- [271] P. HÄNGGI, *Stochastic resonance in biology: How noise can enhance detection of weak signals and help improve biological information processing*, ChemPhysChem **3**, 285 (2002).
- [272] I. GOYCHUK AND P. HÄNGGI, *Non-Markovian stochastic resonance*, Phys. Rev. Lett. **91**, 070601 (2003).
- [273] L. BARABAN, S. M. HARAZIM, S. SÁNCHEZ AND O. G. SCHMIDT, *Chemotactic behavior of catalytic motors in microfluidic channels*, Angew. Chemie Int. Ed. **52**, 5552 (2013).
- [274] X. YANG, C. LIU, Y. LI, F. MARCHESONI, P. HÄNGGI AND H. P. ZHANG, *Hydrodynamic and entropic effects on colloidal diffusion in corrugated channels*, Proc. Natl. Acad. Sci. **114**, 9564 (2017).
- [275] W. E. USPAL, H. B. ERAL AND P. S. DOYLE, *Engineering particle trajectories in microfluidic flows using particle shape*, Nat. Commun. **4**, 2666 (2013).
- [276] K. K. DEY, S. BHANDARI, D. BANDYOPADHYAY, S. BASU AND A. CHATTOPADHYAY, *The pH taxis of an intelligent catalytic microbot*, Small **9**, 1916 (2013).

- [277] A. R. MORGAN, A. B. DAWSON, H. S. MCKENZIE, T. S. SKELHON, R. BEANLAND, H. P. W. FRANKS AND S. A. F. BON, *Chemotaxis of catalytic silica-manganese oxide "matchstick" particles*, Mater. Horizons **1**, 65 (2014).
- [278] A. P. PRUDNIKOV, Y. A. BRYCHKOV AND O. I. MARICHEV, *Integrals and Series. Volume 2: Special Functions*, Gordon and Breach, New York, 1992.
- [279] R. B. DINGLE, *Asymptotic expansions and converging factors. II. Error, Dawson, Fresnel, exponential, sine and cosine, and similar integrals*, Proc. Royal Soc. A **244**, 476 (1958).
- [280] I. S. GRADSHTEYN AND I. M. RYZHIK, *Table of Integrals, Series, and Products*, Academic Press, Amsterdam, 7 ed., 2007.
- [281] P. E. KLOEDEN AND E. PLATEN, *Numerical Solution of Stochastic Differential Equations*, Springer, Berlin/Heidelberg, 1992.
- [282] M. MATSUMOTO AND T. NISHIMURA, *Mersenne twister: A 623-dimensionally equidistributed uniform pseudo-random number generator*, ACM Trans. Model. Comput. Simul. **8**, 3 (1998).
- [283] J. M. HAMMERSLEY AND K. W. MORTON, *A new Monte Carlo technique: Antithetic variates*, Math. Proc. Cambridge Philos. Soc. **52**, 449 (1956).
- [284] M. B. GILES, *Multilevel Monte Carlo path simulation*, Oper. Res. **56**, 607 (2008).
- [285] ———, *Multilevel Monte Carlo methods*, Acta Numer. **24**, 259 (2015).
- [286] N. WILT, *The CUDA Handbook: A Comprehensive Guide to GPU Programming*, Addison-Wesley, Upper Saddle River, NJ, 2013.
- [287] W. E. SCHIESSER, *The Numerical Method of Lines: Integration of Partial Differential Equations*, Academic Press, San Diego, 1991.
- [288] J. D. ANDERSON, *Computational Fluid Dynamics: The Basics with Applications*, McGraw-Hill, New York, 1995.
- [289] E. HAIRER AND G. WANNER, *Solving Ordinary Differential Equations II: Stiff and Differential-Algebraic Problems*, Springer Series in Computational Mathematics, Springer, Berlin/Heidelberg, 1996.
- [290] J. E. GUYER, D. WHEELER AND J. A. WARREN, *FiPy: Partial differential equations with Python*, Comput. Sci. Eng. **11**, 6 (2009).

- [291] S. V. PATANKAR, *Numerical Heat Transfer and Fluid Flow*, McGraw-Hill, New York, 1980.